Escola de Camins
Escola Tècnica Superior d'Enginyeria de Camins, Canals i Ports
UPC BARCELONATECH

ANALYSIS OF THE BEHAVIOUR OF THE LILLA TUNNEL CIRCULAR LINING

Treball realitzat per:
Laura Verda

Dirigit per:
Eduardo Alonso Pérez de Agreda
Anna Ramon Tarragona

Màster en:
Enginyeria de Camins, Canals i Ports

Barcelona, 15 juny 2018

Departament d'Enginyeria Civil i Ambiental

TREBALL FINAL DE MÀSTER

Acknowledgements

I would like to especially thank my supervisors, Professors Eduardo Alonso and Anna Ramon. I offer them my sincerest gratitude for their guidance, expert advice and constructive comments throughout my research. Their passion toward the geotechnical word is fascinating.

I owe a debt of gratitude also to my former colleagues at BAC, with whom I have enjoyed working and having good times. My thanks for having supported and helped me constantly.

Furthermore, I would like to thank all my friends in Imperia, Milano and Barcelona, my housemates and my family for their support and kindness.

Finally, I am very grateful to my parents and my grandma for their unconditional love and patience during these years of study.

There is one person to whom I am eternally grateful. He stayed with me throughout and his encouragement for me never stopped. Thank you.

Abstract

The Lilla tunnel suffered significant expansive displacement and swelling pressures during construction and consequent operation due to gypsum crystals growth in rock massif discontinuities. The heaves severely affected the tunnel and led to the construction of a circular section with a highly reinforced high-strength concrete lining. The thesis analyses the behaviour of the definitive circular lining of the well-documented case history of Lilla tunnel, excavated in Tertiary sulfated claystones. The aim of the thesis is to predict Lilla tunnel circular lining behaviour through the development of numerical models for the simulation of rock mass expansion phenomena and the reproduction of swelling pressure action against the circular lining. The research presents two different modelling procedures to address the resisting structure response under extreme swelling pressure. Model capabilities have been checked against long-term monitoring of the reinforced tunnel in terms of stresses developed in the support and heave pressures exerting on the lining.

The performance of a two-dimensional plane strain analysis permits to achieve better knowledge of the recorded swelling pressure extreme variability across the width of a particular section and along the length of the tunnel. Various distributions of loads have been considered to explain the anhydritic rock behaviour and its interaction with the Lilla tunnel circular lining. The sets of imposed loads in all the analyses performed follow the same distribution observed in the pressures measured along the tunnel. Three different circular cross sections represent the benchmarks to test formulation assumptions and suitability of the model; specifically, the comparison relates the estimated stresses from simulations with measured stresses in reinforcement. The results lead to discrepancies between monitoring data and model predictions and show the importance of the three-dimensional effects in the problem analysed. The model loading distributions do not capture the stresses developed in the lining due to rock expansive behaviour.

Afterwards, a three-dimensional numerical model simulates the Lilla tunnel circular lining when subjected to localized swelling loads. Different swelling loads allocations, obtained through a statistic distribution deriving from measured stresses, have been reproduced to model the real swelling pressure pattern exerting on the invert of the tunnel. Numerical analyses focus on the structural behaviour of the circular lining in terms of stresses. The outcome provides information on the spatial distribution of the swelling pressure. Measured hoop stresses in the resisting structure have been used to verify the accuracy of the results. Model calculations and measurements agree reasonably well and provide a valuable information on the distribution that swelling punctual loads have to assume to reproduce stresses in the field. To give a reliable interpretation of measured stresses loads should be applied at 0,5 m.

Resumen

El túnel de Lilla sufrió importantes deformaciones de expansión y presiones de hinchamiento durante su construcción y consecuente operación debido a la precipitación de cristales de yeso en las discontinuidades del macizo rocoso. El caso del túnel de Lilla está muy bien documentado. Los hinchamientos afectaron severamente el túnel y condujeron a la construcción de una sección circular con un revestimiento de hormigón de alta resistencia altamente armado. La tesis analiza el comportamiento del revestimiento circular del túnel de Lilla, excavado en roca arcillosa sulfatada del Terciario. El objetivo de la tesis es predecir el comportamiento del revestimiento circular del túnel a través de modelos numéricos que permiten la simulación del fenómeno de expansión de la roca y la reproducción de la acción de la presión de hinchamiento contra el revestimiento circular. La investigación presenta dos modelizaciones diferentes para abordar la respuesta de la estructura sometida a presiones de hinchamiento. Las capacidades de los modelos se comparan con las medidas de auscultación del túnel a largo plazo del túnel en términos de tensiones desarrolladas en el revestimiento y de presiones de hinchamiento.

El estudio de un análisis en deformación plana proporciona un mejor conocimiento del efecto de la variabilidad extrema de la presión de hinchamiento registrada en una misma sección transversal y a lo largo de la longitud del túnel. Se consideran varias distribuciones de cargas para reproducir el comportamiento de la roca anhídritica y su interacción con el revestimiento. Los conjuntos de cargas impuestas en los análisis siguen la misma distribución observada en las presiones medidas en el túnel. Tres secciones transversales circulares instrumentadas del túnel de Lilla representan secciones de referencia para validar las hipótesis y la idoneidad del modelo mediante la comparación de los esfuerzos calculados en el revestimiento con los cálculos con los esfuerzos medidos en el armado. Los resultados conducen a discrepancias entre los datos de monitoreo y las predicciones del modelo y muestran la importancia de los efectos tridimensionales del problema analizado. El modelo no captura los esfuerzos en el revestimiento debidos a los hinchamientos de la roca.

Posteriormente, se considera un modelo numérico tridimensional para simular el revestimiento circular del túnel de Lilla sometido a cargas de hinchamiento localizadas. Se consideran diferentes combinaciones de cargas, obtenidas a través de una distribución estadística de las presiones de hinchamiento medidas contra el revestimiento, para modelar el patrón de presión de hinchamiento que ejerce el macizo rocoso contra el túnel. Los análisis numéricos se centran en el estudio de las tensiones del revestimiento circular. Los resultados de la simulación tridimensional proporcionan información sobre la distribución espacial de la presión de hinchamiento. Las tensiones circunferenciales medidas en el revestimiento definitivo se utilizan para verificar la precisión de los resultados numéricos. Los resultados obtenidos mediante el modelo y las medidas de auscultación concuerdan razonablemente bien y proporcionan una información valiosa sobre la distribución que las cargas puntuales de hinchamiento tienen que tener para reproducir las tensiones medidas en campo. El estudio muestra que se deben aplicar cargas de hinchamiento distanciadas 0,5 m para dar una interpretación confiable de los esfuerzos medidos.

Table of contents

ANALYSIS OF THE BEHAVIOUR OF THE LILLA TUNNEL CIRCULAR LINING ..I

ACKNOWLEDGEMENTS III

ABSTRACT IV

RESUMEN VI

TABLE OF CONTENTS VIII

LIST OF FIGURES XI

LIST OF TABLES XVII

CHAPTER 1 INTRODUCTION 21

1.1 INTRODUCTION 21
1.2 OBJECTIVES OF THE THESIS 22

CHAPTER 2 CASE HISTORY: THE LILLA TUNNEL 23

2.1 BACKGROUND 23
2.2 SWELLING MECHANISM OF ANHYDRITIC-GYPSIFEROUS CLAYSTONES 26
2.3 LILLA TUNNEL 32
2.3.1 Geology 33
2.3.2 Design and construction of the original section 36
2.3.3 Expansive phenomena in the Lilla tunnel 39
2.3.4 Performance of flat-slab floor 42
2.3.5 Performance of the curved invert 46
2.3.6 Performance of circular test sections 49
2.3.7 Tunnel reinforcement 54
2.3.8 Performance of the reinforced tunnel 55

CHAPTER 3 2D FINITE ELEMENT METHOD ANALYSIS 67

3.1 GEOTECHNICAL MODEL 67
3.1.1 Soil *69*
3.1.2 Mohr-Coulomb model *70*
3.2 TUNNEL GEOMETRY AND LINING PROPERTIES 72
3.3 CALCULATION PHASES 74
3.4 SWELLING PRESSURE DISTRIBUTION 77
3.4.1 Case a *83*
3.4.2 Results *84*
3.4.3 Case b *89*
3.4.4 Results *90*
3.4.5 Case c *95*
3.4.6 Results *96*
3.4.7 Case d *100*
3.4.8 Results *101*
3.4.9 Case e *105*
3.4.10 Results *106*
3.5 CONCLUSIONS 110

CHAPTER 4 3D FINITE ELEMENT METHOD ANALYSIS 113

4.1 FIRST MODEL DEFINITION 113
4.2 SWELLING LOADS DEFINITION 118
4.3 METHODOLOGY 124
4.4 RESULTS AND DISCUSSION 132
4.5 SECOND MODEL DEFINITION 137
4.6 SWELLING LOADS DEFINITION 137
4.7 RESULTS AND DISCUSSION 139
4.8 THIRD MODEL DEFINITION 143
4.9 SWELLING LOADS DEFINITION 143
4.10 RESULTS AND DISCUSSION 144

CHAPTER 5 CONCLUSIONS AND FUTURE RESEARCH 149

5.1 CONCLUSIONS 149
5.2 FUTURE RESEARCH 151

REFERENCES 153

APPENDIX A 155

APPENDIX B 171

APPENDIX C **173**

List of figures

Figure 2.1. Field observations of extreme expansive phenomena in tunnels, caverns, deep excavations and foundations in swelling rocks and soils: (a) Heave (b) Swelling pressure Berdugo (2007) 24
Figure 2.2. Classic interpretation of swelling in sulphate argillaceous rocks (Alonso et al., 2007) 26
Figure 2.3. Chemical and physical basics of the anhydrite-gypsum conversion (M=molar mass, =density, V=volume) (modified after Amstad & Kovari 2001) 28
Figure 2.4. Swelling stress vs clay content (after Hauber et al.2005, with data from Madsen and Nüesch 1991) 29
Figure 2.5. Schematic diagram illustrating gypsum-anhydrite-gypsum cycle (according to Murray 1964) 30
Figure 2.6. Conceptual model for swelling by crystal growth (gypsum precipitation) (from Alonso 2011; Ramon 2014) 31
Figure 2.7. High-speed railway Madrid-Barcelona-French border (Adif Alta Velocidad, 2006) 32
Figure 2.8. (a) Main Tertiary basins in Iberian Peninsula (modified after Salvany, 1989); (b) distribution of evaporite formations in Tertiary Ebro Basin (Ortı et al., 1989) and location of Lilla tunnel. (Alonso et al.,2013) 34
Figure 2.9. Geological longitudinal section of Lilla tunnel. 35
Figure 2.10. Details of Lilla claystone: (a) cross-shaped fibrous gypsum veins into the clayey matrix, (b) slickenside surfaces. 35
Figure 2.11. Original cross section of Lilla tunnel (Berdugo, 2007) 36
Figure 2.12. Excavation stages in Lilla tunnel: (a) schematic representation of head and bench, (b) head section in station 412+474, (c) key dates during excavation, (d) presence of water during excavation (Berdugo,2007) 37
Figure 2.13. Evolution of the excavation process in Lilla tunnel (Berdugo, 2007) 38
Figure 2.14. Groundwater level and distribution of heave affecting the flat-slab in October 2002 (Berdugo, 2007) 39
Figure 2.15. Summary of field activities to study the expansive phenomena in Lilla tunnel Berdugo (2007) 40

Figure 2.16. Core specimens of chainage 411+600. (a) Active zone, depth 2.8 – 3.0 m (Tarragó, 2006). (b) Stable zone, depth 6.9 – 7.2 m. (Berdugo, 2007) 40
Figure 2.17. Geotechnical and mineralogical characterisation of rock at chainage 411+600 (invert arch), and vertical displacements measured by sliding micrometer installed in the axis. (Alonso, E. E. et al.,2013) 41
Figure 2.18. (a) Gypsum needles on an open slickenside surface located into the active zone, (b) gypsiferous aggregations in a confined discontinuity located in the lower part of the active zone (Alonso & Olivella, 2008) 42
Figure 2.19. Distortion, heave and failure of flat-slabs in photos taken in March 2003. (Berdugo, 2007) 42
Figure 2.20. Evolution of the heave and failure of the flat-slab in station 411+880: (a) March 2003, (b) May 2003, (c) September 2003 (Berdugo, 2007) 43
Figure 2.21. Heave of the flat-slab between October 2002 and December 2003 and their connection with conditions of the rock in October 2002 and the depth of the active zone (Berdugo,2007) 44
Figure 2.22. Evolution of floor heave between September 2002 and December 2003 in critical sections with flat-slab (Berdugo, 2007) 45
Figure 2.23. Relationship between the depth of the active zone below test sections with flat-slab and the maximum radius of excavation (Berdugo, 2007) 45
Figure 2.24. Design of the cross-section with invert-arch (Berdugo, 2007) 46
Figure 2.25. Evolution of floor heave between January and December 2003 in test sections with invert-arch (Berdugo, 2007) 47
Figure 2.26. Distribution of the floor heave and the total radial pressures in test sections with invert-arch in December 2003 (Berdugo, 2007) 48
Figure 2.27. Sliding micrometer readings below test section 411 + 600 with invert arch of 400 mm; strains recorded February–December 2003 (Berdugo, 2007) 48
Figure 2.28. Initial cross sections and testing sections in the longitudinal section of Lilla tunnel 49
Figure 2.29. Distribution and typical characteristics of circular test sections with resisting and yielding supports (Berdugo, 2007) 50
Figure 2.30. Details of the system for the flooding in circular sections with resisting and yielding supports: (a) design of cross-section and boreholes to allow wetting the rock; (b) test section before the start of the test; (c) flooded test section (Ramon, 2014) 51
Figure 2.31. Total radial pressure against inverts and instrumentation of a test section (Alonso et al.,2013) 52
Figure 2.32. Sliding micrometers' readings (Alonso et al.,2013) 52

Figure 2.33. Evolution of calculated swelling strains in critical expansive layers below circular test sections: (a) below the resisting support, (b) below the yielding support-slots (Berdugo, 2007) 53
Figure 2.34. Resisting support adopted for the reinforcement of Lilla tunnel (ADIF, 2006; Alonso et al.,2013) 54
Figure 2.35. Typical instrumented section of reinforced tunnel with instruments in vault and invert (Ramon, 2014) 57
Figure 2.36. Typical instrumented section of reinforced tunnel with instruments installed only in invert (Ramon, 2014) 57
Figure 2.37. Maximum radial pressures recorded from January 2005 to December 2011 (Alonso et al.,2013) 57
Figure 2.38. Monitoring results for reinforced Lilla tunnel, chainage 411 + 348: (a) pressure cells; (b) stresses in reinforcement. (Alonso et al.,2013) 58
Figure 2.39. Monitoring results for reinforced Lilla tunnel, chainage 411 + 468:(a) pressure cells; (b) stresses in reinforcement. (Alonso et al.,2013) 59
Figure 2.40. Monitoring results for reinforced Lilla tunnel, chainage 411 + 590: (a) pressure cells; (b) stresses in reinforcement. (Alonso et al.,2013) 60
Figure 2.41. Monitoring results for reinforced Lilla tunnel, chainage 411 + 707: (a) pressure cells; (b) stresses in reinforcement. (Alonso et al.,2013) 61
Figure 2.42. Monitoring results for reinforced Lilla tunnel, chainage 411 + 826: (a) pressure cells; (b) stresses in reinforcement. (Alonso et al.,2013) 62
Figure 2.43. Monitoring results for reinforced Lilla tunnel, chainage 412 + 080: (a) radial pressures against vault; (b) radial pressures against invert; (c) hoop stresses in vault; (d) stresses in vault reinforcement; (e), (f) stresses in invert reinforcement. (Alonso et al.,2013) 63
Figure 2.44. Monitoring results for reinforced Lilla tunnel, chainage 412 + 680: (a) radial pressures against vault; (b) radial pressures against invert; (c) hoop stresses in vault; (d) hoop stresses in invert; (e) stresses in vault reinforcement; (f), (g) stresses in invert reinforcement. (Alonso et al.,2013) 64
Figure 2.45. Measured distributions of radial pressure in the three sections indicated in December 2011 (Alonso et al.,2013) 65
Figure 3.1. Geometry and boundary conditions of the analysis domain 68
Figure 3.2. Finite element mesh 69
Figure 3.3. Definition of tunnel subdivisions 72
Figure 3.4. Comparison between model and real lining (*d* is the thickness of the lining segment measured in m) 73
Figure 3.5. Definition of tunnel subdivision with negative interfaces 74

Figure 3.6. K0 procedure phase 75
Figure 3.7. Excavation phase 76
Figure 3.8. Tunnel construction phase 76
Figure 3.9. Swelling pressure application phase 77
Figure 3.10. Internal forces acting on stress points in the plate are imposed on rectangular cross-section in the same positions 81
Figure 3.11. Rectangular cross-section properties 81
Figure 3.12. Measured stresses in invert reinforcement at chainage 411+348 82
Figure 3.13. Measured stresses in invert reinforcement at chainage 411+468 82
Figure 3.14. Measured stresses in invert reinforcement at chainage 411+707 83
Figure 3.15. Continuous heterogeneous distribution of section at chainage 411 + 348 83
Figure 3.16. Continuous heterogeneous distribution of section at chainage 411 + 468 84
Figure 3.17. Continuous heterogeneous distribution of section at chainage 411 + 707 84
Figure 3.18. Calculated stresses in reinforcement bars at chainage 411+348 with case a swelling distribution 88
Figure 3.19. Calculated stresses in reinforcement bars at chainage 411+468 with case a swelling distribution 88
Figure 3.20. Calculated stresses in reinforcement bars at chainage 411+707 with case a swelling distribution 89
Figure 3.21. Uniform distributions extended 40 cm in section at chainage 411 + 348 89
Figure 3.22. Uniform distributions extended 40 cm in section at chainage 411 + 468 90
Figure 3.23. Uniform distributions extended 40 cm in section at chainage 411 + 707 90
Figure 3.24. Calculated stresses in reinforcement bars at chainage 411+348 with case b swelling distribution 93
Figure 3.25. Calculated stresses in reinforcement bars at chainage 411+468 with case b swelling distribution 94
Figure 3.26. Calculated stresses in reinforcement bars at chainage 411+707 with case b swelling distribution 94
Figure 3.27. Uniform distributions extended 30 cm in section at chainage 411 + 348 95
Figure 3.28. Uniform distributions extended 30 cm in section at chainage 411 + 468 95
Figure 3.29. Uniform distributions extended 30 cm in section at chainage 411 + 707 96
Figure 3.30. Calculated stresses in reinforcement bars at chainage 411+348 with case c swelling distribution 99
Figure 3.31. Calculated stresses in reinforcement bars at chainage 411+468 with case c swelling distribution 99
Figure 3.32. Calculated stresses in reinforcement bars at chainage 411+707 with case c swelling distribution 100

Figure 3.33. Uniform distributions extended 20 cm in section at chainage 411 + 348 100
Figure 3.34. Uniform distributions extended 20 cm in section at chainage 411 + 468 101
Figure 3.35. Uniform distributions extended 20 cm in section at chainage 411 + 707 101
Figure 3.36. Calculated stresses in reinforcement bars at chainage 411+348 with case d swelling distribution 104
Figure 3.37. Calculated stresses in reinforcement bars at chainage 411+468 with case d swelling distribution 104
Figure 3.38. Calculated stresses in reinforcement bars at chainage 411+707 with case d swelling distribution 105
Figure 3.39. Uniform distributions extended 10 cm in section at chainage 411 + 348 105
Figure 3.40. Uniform distributions extended 10 cm in section at chainage 411 + 468 106
Figure 3.41. Uniform distributions extended 10 cm in section at chainage 411 + 707 106
Figure 3.42. Calculated stresses in reinforcement bars at chainage 411+348 with case e swelling distribution 109
Figure 3.43. Calculated stresses in reinforcement bars at chainage 411+468 with case e swelling distribution 109
Figure 3.44. Calculated stresses in reinforcement bars at chainage 411+707 with case e swelling distribution 110
Figure 4.1. Tunnel cylindrical structure 114
Figure 4.2. Geometrical model of the tunnel 115
Figure 4.3. Boundary conditions 116
Figure 4.4. Spring stiffness condition 117
Figure 4.5. Histogram of observed radial pressures 118
Figure 4.6. Probability density function and exponential distribution 119
Figure 4.7. Grid of 36 swelling loads from x-z plane 120
Figure 4.8. Forces components with respect to the perpendicular to the lining 122
Figure 4.9. x-y plane view 123
Figure 4.10. Grid of swelling forces in the x-z plane 124
Figure 4.11. Global view of the swelling forces grid 124
Figure 4.12. Measured hoop stresses at ECV-1 at different cross sections 125
Figure 4.13. Measured hoop stresses at ECV-2 at different cross sections 125
Figure 4.14. Measured hoop stresses at ECV-3 at different cross sections 125
Figure 4.15. Measured hoop stresses at ECV-4 at different cross sections 126
Figure 4.16. Measured hoop stresses at ECV-5 at different cross sections 126
Figure 4.17. Measured hoop stresses at ECV-6 at different cross sections 126

Figure 4.18. Measured hoop stresses at ECV-7 at different cross sections 127
Figure 4.19. Measured hoop stresses at ECV-8 at different cross sections 127
Figure 4.20. Measured hoop stresses at ECV-9 at different cross sections 127
Figure 4.21. Measured hoop stresses at ECV-10 at different cross sections 128
Figure 4.22. Measured hoop stresses at ECV-11 at different cross sections 128
Figure 4.23. Measured hoop stresses at ECV-12 at different cross sections 128
Figure 4.24. Measured mean hoop stresses values 130
Figure 4.25. Global axes x,y (a). Local axes n,t rotated by θ with respect to x,y 131
Figure 4.26. Calculated hoop stresses with 6x6 grid model and k=0,3333 10^9 134
Figure 4.27. Calculated hoop stresses with 6x6 grid model and k=0,16667 10^9 134
Figure 4.28. Calculated hoop stresses with 6x6 grid model and k=0,3333 10^8 135
Figure 4.29. Comparison between measured and calculated stresses with the 6x6 grid model 136
Figure 4.30. Grid of 108 swelling loads from x-z plane 138
Figure 4.31. Calculated hoop stresses with 6x18 grid model and k=0,3333 10^9 141
Figure 4.32. Calculated hoop stresses with 6x18 grid model and k=0,16667 10^9 141
Figure 4.33. Calculated hoop stresses with 6x18 grid model and k=0,3333 10^8 142
Figure 4.34. Comparison between calculated stress with 6x6 grid model and 18x6 grid model 142
Figure 4.35. Grid of 676 loads from x-z plane 144
Figure 4.36. Calculated hoop stresses with 26x26 grid model and k=0,3333 10^9 146
Figure 4.37. Calculated hoop stresses with 26x26 grid model and k=0,16667 10^9 146
Figure 4.38. Calculated hoop stresses with 26x26 grid model and k=0,3333 10^8 147
Figure 4.39. Comparison between measured and calculated stresses with the 26x26 grid model 148

List of tables

Table 2.1. Mineralogy and geotechnical indices of undisturbed Lilla 27
Table 2.2. General features of construction (Berdugo,2007) 36
Table 3.1. Soil properties 69
Table 3.2. Generalised Hoek–Brown strength parameters 71
Table 3.3. Mohr-Coulomb parameters 72
Table 3.4. Plates parameters 73
Table 3.5. Cross-sections dimensional values 82
Table 3.6. Stresses in the reinforcement at position ECV 12-11-10-9. Chainage 411+348 85
Table 3.7. Stresses in the reinforcement at position ECV 8-7-6-5. Chainage 411+348 85
Table 3.8. Stresses in the reinforcement at position ECV 4-3-2-1. Chainage 411+348 85
Table 3.9. Stresses in the reinforcement at position ECV 12-11-10-9. Chainage 411+468 85
Table 3.10. Stresses in the reinforcement at position ECV 8-7-6-5. Chainage 411+468 86
Table 3.11. Stresses in the reinforcement at position ECV 4-32-1. Chainage 411+468 86
Table 3.12. Stresses in the reinforcement at position ECV 12-11-10-9. Chainage 411+707 86
Table 3.13. Stresses in the reinforcement at position ECV 8-7-6-5. Chainage 411+707 86
Table 3.14. Stresses in the reinforcement at position ECV 4-3-2-1. Chainage 411+707 87
Table 3.15. Stresses in the reinforcement at position ECV 12-11-10-9. Chainage 411+348 91
Table 3.16. Stresses in the reinforcement at position ECV 8-7-6-5. Chainage 411+348 91
Table 3.17. Stresses in the reinforcement at position ECV 4-3-2-1. Chainage 411+348 91
Table 3.18. Stresses in the reinforcement at position ECV 8-7-6-5. Chainage 411+468 91
Table 3.19. Stresses in the reinforcement at position ECV 8-7-6-5. Chainage 411+468 92
Table 3.20. Stresses in the reinforcement at position ECV 4-3-2-1. Chainage 411+468 92

Table 3.21. Stresses in the reinforcement at position ECV 12-11-10-9. Chainage 411+707 92
Table 3.22. Stresses in the reinforcement at position ECV 8-7-6-5. Chainage 411+707 92
Table 3.23. Stresses in the reinforcement at position ECV 4-3-2-1. Chainage 411+707 93
Table 3.24. Stresses in the reinforcement at position ECV 12-11-10-9. Chainage 411+348 96
Table 3.25. Stresses in the reinforcement at position ECV 8-7-6-5. Chainage 411+348 96
Table 3.26. Stresses in the reinforcement at position ECV 4-3-2-1. Chainage 411+348 97
Table 3.27. Stresses in the reinforcement at position ECV 12-11-10-9. Chainage 411+468 97
Table 3.28. Stresses in the reinforcement at position ECV 8-7-6-5. Chainage 411+468 97
Table 3.29. Stresses in the reinforcement at position ECV 4-3-2-1. Chainage 411+468 97
Table 3.30. Stresses in the reinforcement at position ECV 12-11-10-9. Chainage 411+707 98
Table 3.31. Stresses in the reinforcement at position ECV 8-7-6-5. Chainage 411+707 98
Table 3.32. Stresses in the reinforcement at position ECV 4-3-2-1. Chainage 411+707 98
Table 3.33. Stresses in the reinforcement at position ECV 12-11-10-9. Chainage 411+348 101
Table 3.34. Stresses in the reinforcement at position ECV 8-7-6-5. Chainage 411+348 102
Table 3.35. Stresses in the reinforcement at position ECV 4-3-2-1. Chainage 411+348 102
Table 3.36. Stresses in the reinforcement at position ECV 12-11-10-9. Chainage 411+468 102
Table 3.37. Stresses in the reinforcement at position ECV 8-7-6-5. Chainage 411+348 102
Table 3.38. Stresses in the reinforcement at position ECV 4-3-2-1. Chainage 411+348 103
Table 3.39. Stresses in the reinforcement at position ECV 12-11-10-9. Chainage 411+707 103

Table 3.40. Stresses in the reinforcement at position ECV 8-7-6-5. Chainage 411+707 103
Table 3.41. Stresses in the reinforcement at position ECV 4-3-2-1. Chainage 411+707 103
Table 3.42. Stresses in the reinforcement at position ECV 12-11-10-9. Chainage 411+348 106
Table 3.43. Stresses in the reinforcement at position ECV 8-7-6-5. Chainage 411+348 107
Table 3.44. Stresses in the reinforcement at position ECV 4-3-2-1. Chainage 411+348 107
Table 3.45. Stresses in the reinforcement at position ECV 12-11-10-9. Chainage 411+468 107
Table 3.46. Stresses in the reinforcement at position ECV 8-7-6-5. Chainage 411+468 107
Table 3.47. Stresses in the reinforcement at position ECV 4-3-2-1. Chainage 411+468 108
Table 3.48. Stresses in the reinforcement at position ECV 12-11-10-9. Chainage 411+707 108
Table 3.49. Stresses in the reinforcement at position ECV 8-7-6-5. Chainage 411+707 108
Table 3.50. Stresses in the reinforcement at position ECV 4-3-2-1. Chainage 411+707 108
Table 4.1. Concrete's properties 115
Table 4.2. Values of shear modulus and spring coefficient considered 117
Table 4.3. Set of random numbers 121
Table 4.4. Set of swelling pressures in MPa 121
Table 4.5. Set of swelling forces in N 122
Table 4.6. Set of swelling forces x component in N 123
Table 4.7. Set of swelling forces y component in N 123
Table 4.8. Hoop stress values in MPa at ECV – 1-2-3-4 129
Table 4.9. Hoop stress values in MPa at ECV – 5-6-7-8 129
Table 4.10. Hoop stress values in MPa at ECV – 9-10-11-12 129
Table 4.11. Calculated stress values with 6x6 grid model and k=0,3333 10^9 132
Table 4.12. Calculated stress with 6x6 grid model and k=0,16667 10^9 133
Table 4.13. Calculated stress values with 6x6 grid model and k=0,3333 10^8 133
Table 4.14. Set of 108 swelling forces in N 138
Table 4.15. Calculated stress values with 6x18 grid model and k=0,3333 10^9 139
Table 4.16. Calculated stress values with 6x18 grid model and k=0,16667 10^9 139

Table 4.17. Calculated stress values with 6x18 grid model and k=0,3333 10^8 140
Table 4.18. Calculated stress values with 26x26 grid model and k=0,3333 10^9 144
Table 4.19. Calculated stress values with 26x26 grid model and k=0,16667 10^9 145
Table 4.20. Calculated stress values with 26x26 grid model and k=0,3333 10^8 145

CHAPTER 1
INTRODUCTION

The swelling potential of geological formation rich in anhydrite can be one of the major problems during tunnel construction. These materials may experience severe expansive phenomena when they are crossed by an excavation. Heave displacements usually manifest at tunnel floor level, affecting the functionality of the tunnel. The interpretation of swelling pressures in sulphated formations is not a straightforward task. Within this context, this thesis focuses on the action of swelling pressures on the Lilla tunnel circular lining and tries to reproduce its structural response.

1.1 Introduction

Lilla tunnel is an exceptional and reference case of damage induced by expansions involving sulphated formations. Vertical ground movement reached values closed to 1 m and maximum stresses measured on the rigid support were so high that rarely mentioned in literature. Rock massif excavated in Lilla tunnel, located in the route of a high-speed railway in the province of Tarragona (Spain), is a modern tertiary deposit characterized by anhydrite clay sediments from the Ebro basin.

First heave was detected in September/October 2002 in the tunnel flat slabs immediately after its construction. These expansions were quickly followed by damage of longitudinal drainage systems, and eventually by local failures of flat slabs. Geotechnical investigations and monitoring campaign were performed to gain knowledge of the mechanisms underlying the swelling mechanism and to study the extent of the expansive phenomena. In addition, test section with flat slabs and curved invert were installed and later, circular cross sections were constructed inside the original tunnel and subjected to wetting tests.

The entire tunnel was transformed in a heavily reinforced concrete cylinder, cast in place inside the original horseshoe-shaped section. The reinforced Lilla tunnel was instrumented in order to achieve a good understanding of the swelling pressure evolution at the rock/lining interface and the straining in the reinforcement bars. Monitoring data covering the period 2005-2011 made it possible to evaluate the response of the lining.

1.2 Objectives of the thesis

The aim of the thesis is to develop a numerical formulation and describe the modelling assumptions for the prediction of the Lilla tunnel circular lining behaviour when affected by extreme swelling pressures. Calculations will be compared to records of stresses in the steel reinforcement. To reach this target, the objectives of the thesis are:

- Develop numerical models with different calculation programs (Plaxis, Kratos) to simulate the rock mass expansion phenomena around the Lilla tunnel circular lining
- Validate the models developed with field observations.
- Assess and compile monitoring data.
- Determine reliable criteria to reproduce swelling pressure exerted by the anydritic claystone against the circular support of the tunnel.
- Study the behaviour of the circular lining dealing with rock expansions in two dimensional (plane strain) and three dimensional numerical analyses.
- Study the effect of rock stiffness and soil-lining interaction.
- Compare measured stresses in the circular lining with available stress measurements in the reinforcement of the Lilla tunnel.

CHAPTER 2

CASE HISTORY: THE LILLA TUNNEL

This Chapter describes the swelling phenomena in literature and the study itself of the expansive mechanism in sulphated claystones. Later, geological and tectonic conditions in the excavation area of Lilla tunnel are described and criteria for design and excavation of the original cross-section is presented. The Chapter focuses on the expansive phenomena affecting the tunnel during construction and the efficiency of the different test cross sections. Finally, the alternative selected for the support of the tunnel is described and its performance during six years of monitoring is presented. Special attention is given to Pressure and stresses–time records measured at seven cross-sections covering the period 2005—2011.

2.1 Background

The presence of swelling behaviour of clay-sulphate rocks has traditionally had deleterious effects on excavations, particularly on tunnels. The swelling manifests itself by heave of the tunnel floor, destruction of the lining or even uplift of the entire tunnel and the ground surface above. Such extreme expansive phenomena have been often associated to the transformation of the sulphate mineral anhydrite into gypsum because of water inflow in anhydrite-containing layers after tunnel excavation.

The phenomenon of the heave of a tunnel floor, or of damage to the invert arch, has been well-known since the beginnings of railroad tunnelling in the middle of the 19th century. Throughout recent history a considerable proportion of tunnels have experienced severe heave problems.

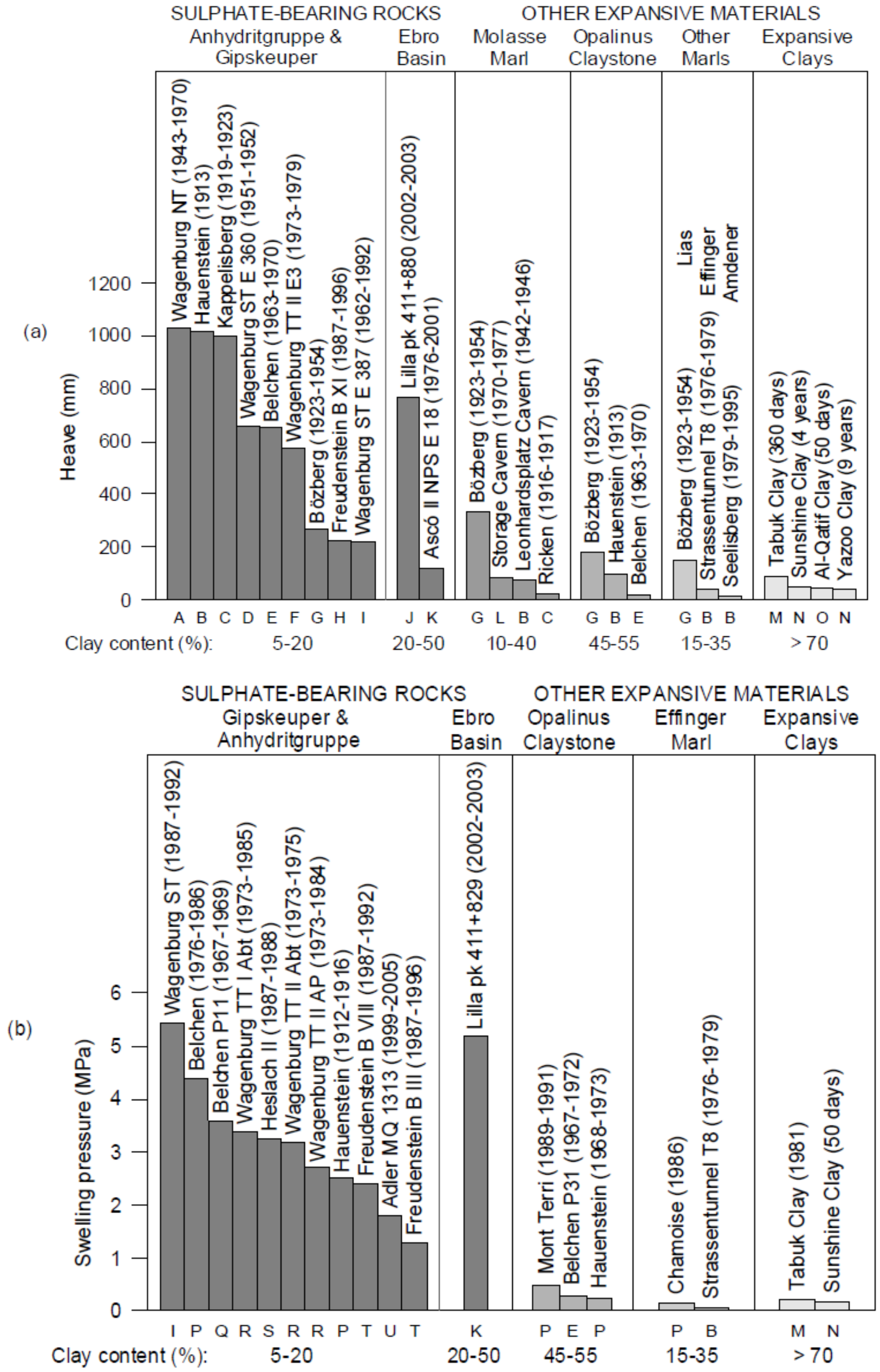

Figure 2.1. Field observations of extreme expansive phenomena in tunnels, caverns, deep excavations and foundations in swelling rocks and soils: (a) Heave (b) Swelling pressure Berdugo (2007)

In Figure 2.1 several field observations of extreme expansive phenomena in different underground works are presented. Geological formations where swelling related difficulties can occur are widespread; rock types exhibiting such swelling behaviour are certain types of claystone and anhydrite-bearing rocks, which can be commonly found in northern Switzerland (Jurassic claystones and Tertiary marlstones), southern Germany (Triassic Gypsum Keuper) and in eastern France (Jurassic claystones). Tunnelling in such materials is notoriously difficult. In Spain the most prominent example is the Lilla tunnel, where swelling occurred in Tertiary clay-sulphate rocks (Alonso and Olivella 2008; Ramon 2014).

Historically Tertiary, anhydrite clay sediments which characterize the Ebro Basin had not been affected by expansive phenomena of the intensity found in Lilla before. Both tunnel floor heaving (which reached values close to 1 m) and pressures against tunnel lining (around 6 MPa) take values rarely mentioned in literature. Therefore, the Lilla Tunnel is a reference case for tunnels construction in Spain, especially in the Central and Eastern Iberian Peninsula where anhydrite and gypsum formations are frequent.

Figure 2.1 facilitates a first assessment of the magnitude of the swelling phenomena dividing between sulphate-bearing rocks and other expansive materials. Under similar conditions of construction and operation of tunnels heave and swelling pressures, sulphate-bearing rocks could show heaves and pressures up to one order of magnitude greater than in other expansive clayey materials. The intensity of the swelling phenomena is significantly higher in sulphate-bearing formations when compared with clay or marl rocks. From the available data on heave and swelling pressure it emerges that in sulphated rocks heave, which is concentrated on tunnel floors, reaches values of 1 metres and pressures exceeds 5MPa.

2.2 Swelling mechanism of anhydritic-gypsiferous claystones

As mentioned before, the Lilla Tunnel, located in the province of Tarragona (Spain) and excavated in Tertiary anhydritic claystone, has experienced severe heave phenomena immediately after construction. Principles of the swelling mechanism are analysed to give a better understanding of the excavated claystone observed behaviour.

Many tunnelling projects of the present and the future have to deal with the swelling capability of anhydrite. The prediction of the mechanical interaction between the swelling rock and the tunnel is often difficult. Swelling behaviour of clay-sulphate rocks is controlled by coupled hydraulic, chemical and mechanical processes that can hardly reflected by a general law. A fundamental reason for our present inability to predict the swelling behaviour of clay-sulphate rocks is the lack of a comprehensive understanding of the processes involved (Anagnostou et al. 2010).

Swelling of rocks and soils can occur due to a single mechanism or due to multiple different mechanisms combined. Which mechanism is relevant, depends on several factors, most of all on the mineralogical composition of the rock. (Pimentel, 2015). According to classical interpretations, it has been postulated than the swelling phenomena may be caused by physical and chemical mechanisms. The physical mechanisms are driven by pore water pressure and the expansion of the clay matrix (short term “physical clay swelling”), while the other ones are always associated with chemical reactions (long term “chemical sulphate swelling”) (Berdugo, 2007).

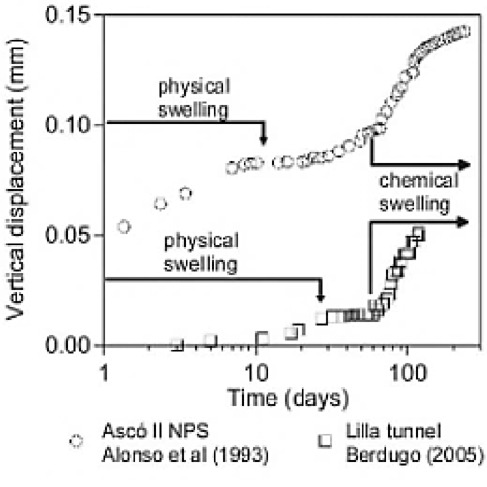

Figure 2.2. Classic interpretation of swelling in sulphate argillaceous rocks (Alonso et al., 2007)

The mineralogical composition of the undisturbed Lilla sulphated rock is dominated by a host clay matrix while the crystalline fraction is substantially characterized by anhydrite with percentages of gypsum. The argillaceous matrix is constituted by phyllosilicates (illite and paligorskite), by minerals rich in magnesium and calcium (dolomite) and, to a lesser extent, by quartz.

Table 2.1. Mineralogy and geotechnical indices of undisturbed Lilla Claystone (Alonso et al., 2013)

Minerals: relative content	
Quartz: %	2 - 7
Dolomite: %	11 - 13
Anhydrite: %	13 - 28
Gypsum: %	0 - 7
Clay (illite and paligorskite): %	51 - 67
Physical and Mechanical indices	
Specific unit weight	2,82 - 2,9
Water content: %	0,5 – 4,5
Total density: Mg/m3	2,40 – 2,86
Unconfined compressive strength: MPa	17 - 170

Rocks containing clay minerals and anhydrite exhibit the property of volume increase caused by water absorption. Swelling in anhydrite is of a chemical nature and depends on the transformation of anhydrite into gypsum, a reaction that is represented as:

$$C_aSO_4 + 2H_2O \rightarrow C_aSO_4 \cdot 2H_2O \qquad \text{Eq. 2.1}$$

The addition of two water molecules from outside the system (open system) imply, at a molecular level, a theoretical volume increase of 61%, which is responsible for the observed heave. This volume increase can be calculated from balancing molar volumes of anhydrite and gypsum. It must be noted that the volume increase of the total (clay and sulphate) rock is smaller, because only a part of the rock consists of sulphate minerals (Butsher et al., 2016). Anhydrite is a mineral whose chemical composition is anhydrous calcium sulphate which, in the presence of water, can be transformed into gypsum. The reaction involves a solution and a crystallization process (Rauh et al., 2006), which has a significant increase in volume. In underground excavations this could lead to an increase of the pressure exerted by the ground on the support.

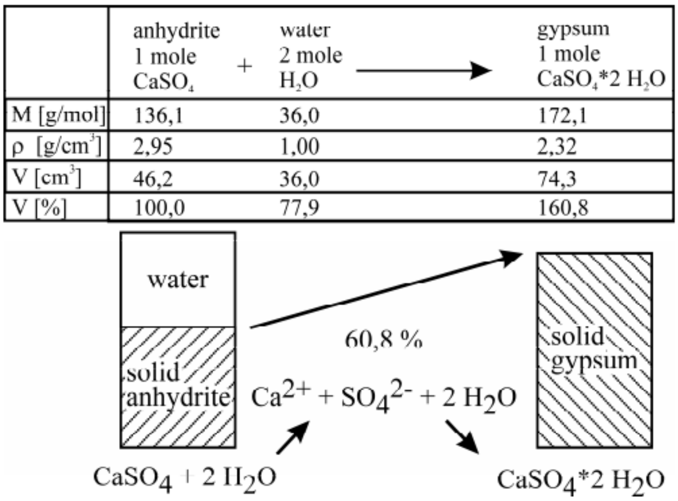

	anhydrite 1 mole $CaSO_4$	+ water 2 mole H_2O	→ gypsum 1 mole $CaSO_4 * 2\,H_2O$
M [g/mol]	136,1	36,0	172,1
ρ [g/cm³]	2,95	1,00	2,32
V [cm³]	46,2	36,0	74,3
V [%]	100,0	77,9	160,8

Figure 2.3. Chemical and physical basics of the anhydrite-gypsum conversion (M=molar mass, =density, V=volume) (modified after Amstad & Kovari 2001)

The classical theory, defended by authors such as Einfalt (1979), Einfalt & Götz (1976), Steiner (1993), Amstad & Kovari (2001) among others, is based on the analysis of the transformation anhydrite-gypsum as an irreversible chemical reaction dependent on temperature, pressure and foreign ions, which is accompanied by a volume increase from 60% to 63%.

According to Berdugo's studies (2007), the classic anhydrite theory also postulates that swelling could never be detected in undisturbed massive anhydrite not affected by microfractures. Anhydrite requires a large surface of exchange with water to be hydrated. In this context Rauh et al., (2006) suggested that the swelling potential of pure anhydrite depends on the size of the mineral grains of the anhydrite (crystallinity), with increasing size of the crystals the swelling potential decreases. Other authors (Madsen & Nüesch, 1991; Madsen et al., 1995; Einstein 1996) observed that a certain clay content is necessary for the anhydrite dissolution and subsequent crystallization of gypsum to develop considerable swelling.

Moreover, the studies of Madsen and Nüesch (1991) clearly show that the swelling potential of clay-sulfate rocks depends on the clay content of the anhydritic rock: the one that produces the largest swelling parameters is about 5%-15%. (Figure 2.4). At clay contents exceeding the 15%, the swelling potential decreases again.

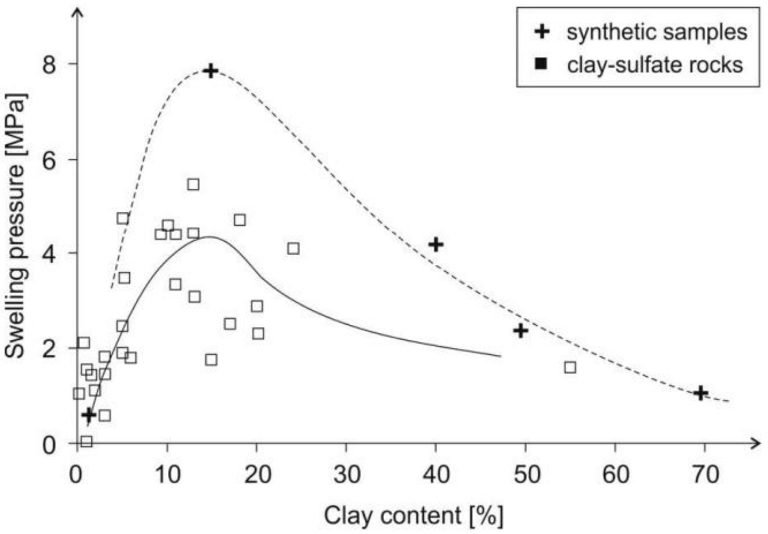

Figure 2.4. Swelling stress vs clay content (after Hauber et al.2005, with data from Madsen and Nüesch 1991)

To sum up, according to the classical interpretation, the hydration and consequent expansion of clay minerals (physical swelling) and the transformation of anhydrite into gypsum (chemical swelling) fully explain the theory of the expansive phenomena in anhydritic-gypsiferous clayey rocks.

Even though the occurrence of such swelling phenomena is undoubtable when dealing with expansive clay minerals, the controversial aspect is related to the direct transformation of anhydrite into gypsum generating a volumetric increase.

A second interpretation, supported by Orti (1977), Madsen et al., (1995), Pina et al. (2000), Pimentel (2003), Berdugo (2007) argues that the transformation of anhydrite into gypsum is highly time-consuming isovolumetric process, in which anhydrite dissolves as fast as secondary gypsum precipitates. The excess in hydrated calcium sulphate (62% in volume) could be either transported in aqueous solution or it could precipitate partially in the form of gypsum in open discontinuities of the host clayey rock (Berdugo et al., 2009).

Murray's observations (1964) suggest the existence of a diagenetic cycle in gypsum and anhydrite. In such minerals the deposition of gypsum is followed, during burial, by the replacement of gypsum (primary gypsum) by anhydrite. In such way, the anhydrite rocks recrystallise from gypsum rocks through diagenesis. During uplift and erosion of overlying strata, once the anhydrite rock has returned to the surface, it is slowly replaced by gypsum (secondary gypsum).

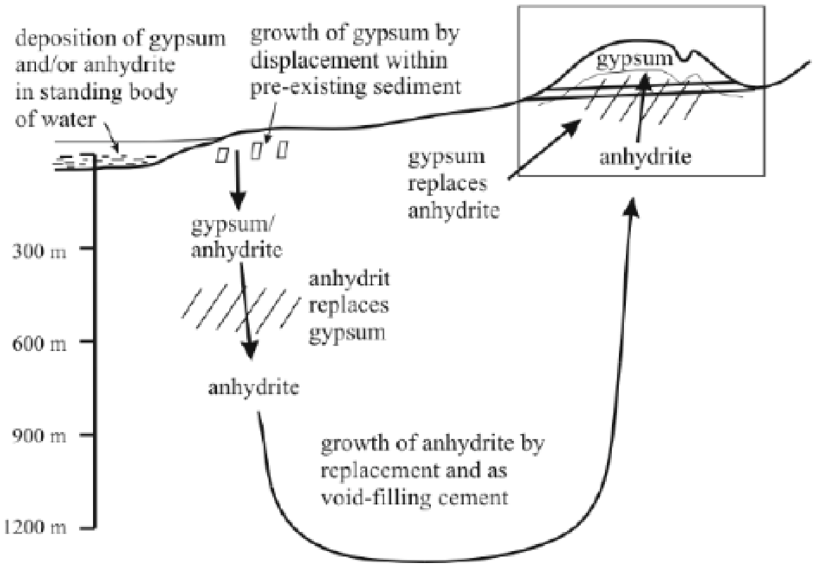
deposition of gypsum and/or anhydrite in standing body of water
growth of gypsum by displacement within pre-existing sediment
gypsum
anhydrite
gypsum replaces anhydrite
gypsum/ anhydrite
anhydrit replaces gypsum
anhydrite
growth of anhydrite by replacement and as void-filling cement
300 m
600 m
900 m
1200 m

Figure 2.5. Schematic diagram illustrating gypsum-anhydrite-gypsum cycle (according to Murray 1964)

On the other hand, observations by Pina et al. (2000) reveal that anhydrite cannot generate volumetric changes when exposed to water rich in sulphates, since the gypsum generates a film that protects anhydrite from water action. Therefore, such theory considers that the increase of volume is caused by the precipitation of gypsum mineral in fissures.

In this context, modern knowledge on the phenomenology of the swelling behaviour is not in in agreement the classical theory on long-term “chemical swelling” of anhydritic gypsiferous claystones, which nowadays does not seem realistic.

It is self-evident that swelling understanding is the key to the current research questions related to sulphated claystone. The mechanism involves geological, mineralogical, chemical, hydrological and mechanical processes. However, the rock degradation due to tensional changes and the wetting and drying processes seem to be the triggering factors (Ramon, 2014). Presently it is believed that the origin of the observed swelling on sulphated clay rock is directly linked with the precipitation of the gypsum crystals in the discontinuities or joint opening in the claystone due to supersaturation of groundwater.

It has been observed in Lilla Tunnel that gypsum crystal precipitation is detected in structural discontinuities of the sulphated claystone. It is essential that claystone allows water to be in contact with the anhydrite mineral to create supersaturated conditions for the gypsum crystals to precipitate. Therefore, presence of water is a requirement for the gypsum precipitation. In a naturally impervious claystone it is reasonable to state that water has two possibilities to enter the rock: either through the discontinuities caused by the excavation of the tunnel or through the new ones created by the expansion (crystal growth).

According to Berdugo (2007), supersaturation of groundwater can be induced by both evaporation of sulphate solutions and dissolution of anhydrite in the presence of gypsum. The first mechanism, the evaporation of water at the rock–tunnel atmosphere interface due to the gradient of relative humidity, was explored by Alonso & Olivella (2008). The evaporation towards the tunnel boundary (Lilla Tunnel floor) in the exposed surfaces of the rock was believed to be the fundamental explanation for the heave observed at Lilla (Ramon, 2014). The second mechanism, which was modelled by Oldecop & Alonso (2012) and Ramon & Alonso (2013), represents the supersaturation condition achievement because anhydrite is more soluble than gypsum at typical groundwater temperatures.

Alonso (2011) and Ramon (2014) presented a conceptual model of swelling based on the geochemical process of gypsum crystal growth in fissures from supersaturated water in argillaceous rock (Figure 2.6). Water in contact with anhydrite crystals dissolves anhydrite creating a supersaturated solution capable of precipitating gypsum.

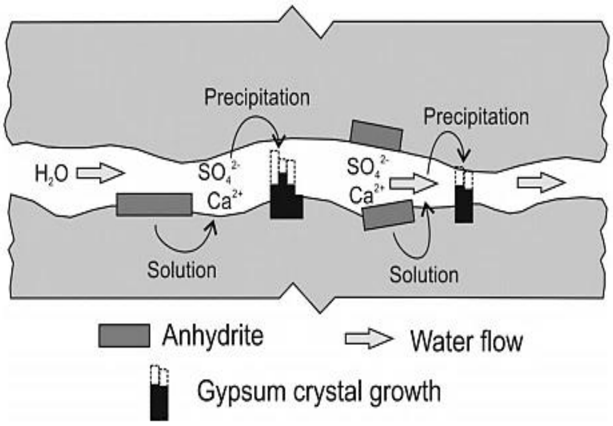

Figure 2.6. Conceptual model for swelling by crystal growth (gypsum precipitation) (from Alonso 2011; Ramon 2014)

2.3 Lilla tunnel

The Lilla tunnel belongs to the Madrid-Barcelona-French border high-speed railway (see Figure 2.7), and it is located near Montblanc city, in the province of Tarragona (Catalonia). With its 2034 m of longitude, Lilla tunnel is the longest of the three tunnels of the high-speed railway excavated in the Ebro Basin (Tertiary moderately soft gypsiferous-anhydritic claystones, Berdugo et al., 2009).

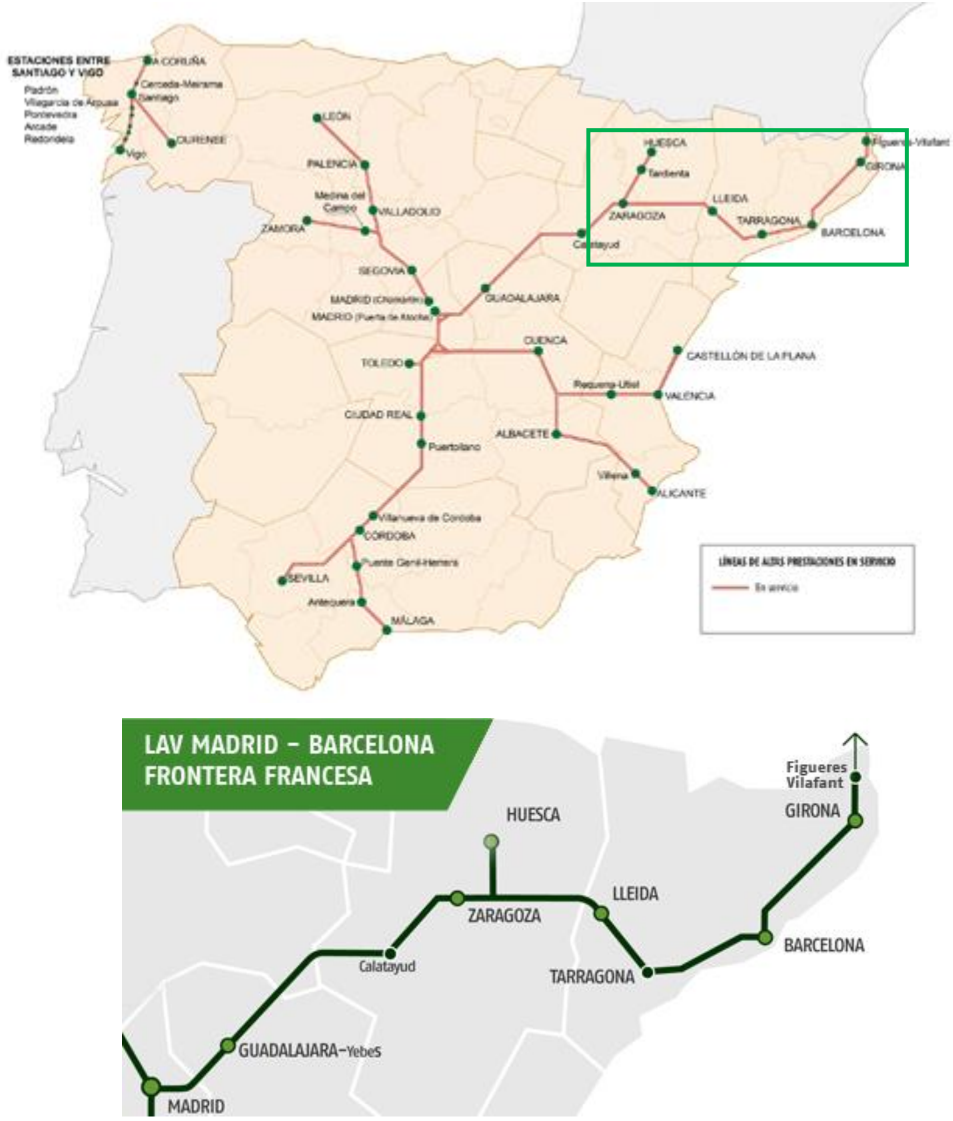
ESTACIONES ENTRE SANTIAGO Y VIGO
Padrón
Vilagarcía de Arousa
Pontevedra
Arcade
Redondela
A CORUÑA
Cerceda-Meirama
Santiago
OURENSE
Vigo
LEÓN
PALENCIA
Medina del Campo
VALLADOLID
ZAMORA
SEGOVIA
MADRID (Chamartín)
MADRID (Puerta de Atocha)
GUADALAJARA
Calatayud
HUESCA
Tardienta
ZARAGOZA
LLEIDA
TARRAGONA
BARCELONA
GIRONA
Figueres-Vilafant
TOLEDO
CUENCA
CASTELLÓN DE LA PLANA
Requena-Utiel
VALENCIA
CIUDAD REAL
Puertollano
ALBACETE
Villena
ALICANTE
Villanueva de Córdoba
CÓRDOBA
Puente Genil-Herrera
SEVILLA
Antequera
MÁLAGA
LÍNEAS DE ALTAS PRESTACIONES EN SERVICIO
En servicio
LAV MADRID – BARCELONA FRONTERA FRANCESA
HUESCA
Figueres Vilafant
GIRONA
LLEIDA
ZARAGOZA
BARCELONA
Calatayud
TARRAGONA
GUADALAJARA-Yebes
MADRID

Figure 2.7. High-speed railway Madrid-Barcelona-French border (Adif Alta Velocidad, 2006)

These three tunnels (Lilla, Camp Magré and Puig Cabrer tunnels), located at close distance to one another, were affected by expansive phenomena during construction. Although swelling occurred also in Camp Magré (954 m.) and Puig Cabrer (607 m) tunnels, it was the Lilla tunnel the one that experienced the most damaging heave and the highest swelling pressure, which exceeded 6 Mpa in some points (Ramon, 2014). Swelling phenomena in the Lilla tunnel were detected for the first time in September 2002, just after its construction. The expansions caused mainly failures of the tunnel floor flat slabs while there was no observable swelling sign in the abutments and the crown (Alonso et al.,2013).

To determine the plausible causes of the observed expansive phenomena and gain knowledge of the expansive mechanism, instrumentation was installed in the tunnel. Numerous field and laboratory tests were undertaken to measure swelling pressure (values and depth that could be reached) and evaluate the efficiency of the resisting support.

2.3.1 Geology

The Lilla tunnel is located on the eastern side of the Tertiary Lower Ebro Basin, which is one of the main Tertiary Basins of the Iberian Peninsula (Figure 2.8). 47 million years ago the Ebro Basin was an extensive bay which opened into the Atlantic and was limited to the east with the reliefs of the Catalan Coastal Range. Towards the late Eocene, some 37 million years ago, it passed from being connected to the open sea to a practically alluvial plain. In the early Oligocene the Ebro Basin was a depression subjected to an endorheic continental regime, which received the contributions of the rivers and streams that deposited their alluvium. In the central areas of the basin, relatively far from the fronts of the mountain chains, swamps and lacustrine areas developed where marl, carbonates and gypsum were deposited.

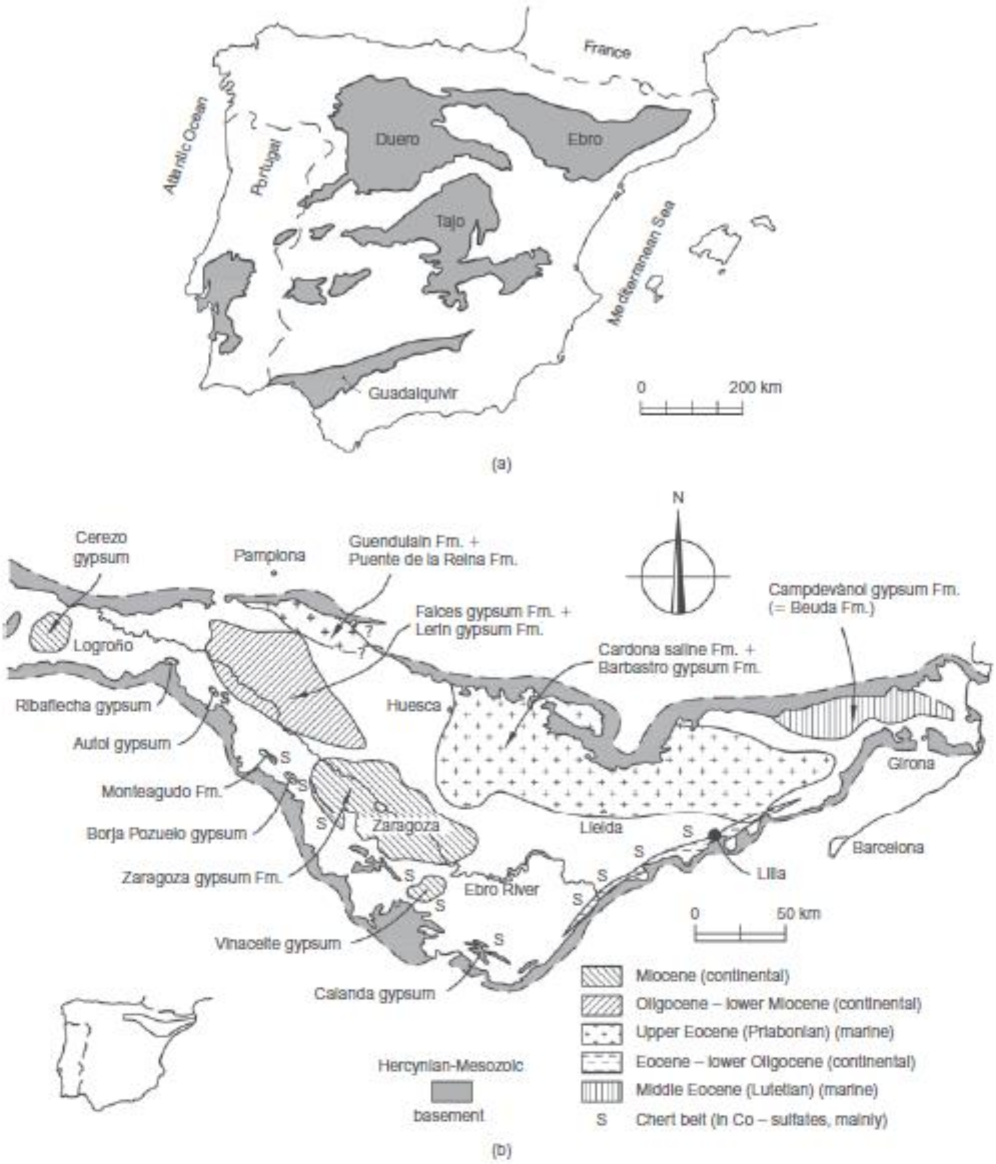
France
Atlantic Ocean
Portugal
Duero
Ebro
Tajo
Mediterranean Sea
Guadalquivir
0
200 km
(a)
N
Cerezo gypsum
Pamplona
Guendulain Fm. + Puente de la Reina Fm.
Campdevànol gypsum Fm. (= Beuda Fm.)
Falces gypsum Fm. + Lerin gypsum Fm.
Logroño
Cardona saline Fm. + Barbastro gypsum Fm.
Ribafiecha gypsum
Huesca
Autol gypsum
Girona
Monteagudo Fm.
Borja Pozuelo gypsum
Zaragoza
Lleida
Barcelona
Lilla
Zaragoza gypsum Fm.
Ebro River
0
50 km
Vinaceite gypsum
Calanda gypsum
S
Miocene (continental)
Oligocene – lower Miocene (continental)
Upper Eocene (Priabonian) (marine)
Eocene – lower Oligocene (continental)
Middle Eocene (Lutetian) (marine)
S Chert belt (in Co – sulfates, mainly)
Hercynian-Mesozoic basement
(b)

Figure 2.8. (a) Main Tertiary basins in Iberian Peninsula (modified after Salvany, 1989); (b) distribution of evaporite formations in Tertiary Ebro Basin (Ortı et al., 1989) and location of Lilla tunnel. (Alonso et al.,2013)

The Lilla tunnel runs through a relief composed by hills and valleys near Montblanc (Tarragona, Spain), following a north–south direction with a maximum gradient of 2.5%. The tunnel crosses mainly Early Eocene argillaceous rocks containing anhydrite and a complex system of cross-shaped moderately dipping fibrous gypsum veins.

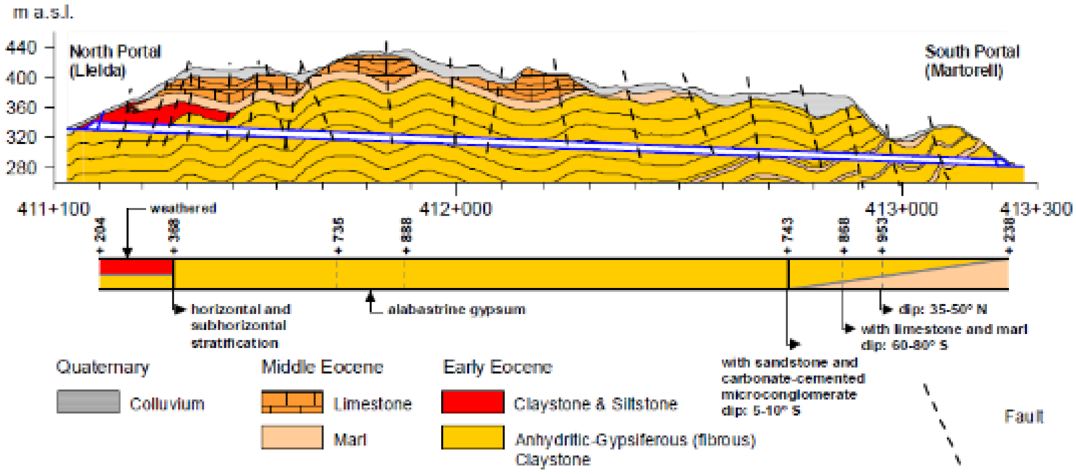
m a.s.l.
440
400
360
320
280
North Portal (Lleida)
South Portal (Martorell)
411+100
412+000
413+000
413+300
weathered
+ 204
+ 368
+ 736
+ 888
+ 743
+ 868
+ 953
+ 238
horizontal and subhorizontal stratification
alabastrine gypsum
dip: 35-50° N
with limestone and marl dip: 60-80° S
with sandstone and carbonate-cemented microconglomerate dip: 5-10° S
Quaternary
Middle Eocene
Early Eocene
Colluvium
Limestone
Marl
Claystone & Siltstone
Anhydritic-Gypsiferous (fibrous) Claystone
Fault

Figure 2.9. Geological longitudinal section of Lilla tunnel.

The excavated material consists basically of a horizontally-oriented monotonic series of gypsum-bearing brown argillaceous rocks (see Figure 2.9). Several studies carried out by Alonso, Ramon and Berdugo have provided the understanding of the mineralogy of the Lilla claystone. As mentioned previously, the mineralogical characterization of the material is made up of two main components: the host argillaceous matrix, and the sulphated crystalline fraction, constituted of anhydrite and gypsum.

Gypsum is mainly present as millimetric and centimetric fibrous veins, as well as small nodules and flakes (Figure 2.10 a). Locally, grey alabastrine gypsum occurs in sub horizontal strips in the host rock. An important aspect is the existence of a persistent system of open low-angle slickenside surfaces (see Figure 2.10 b). They are related to strong tectonic folds (Alonso & Olivella, 2008).

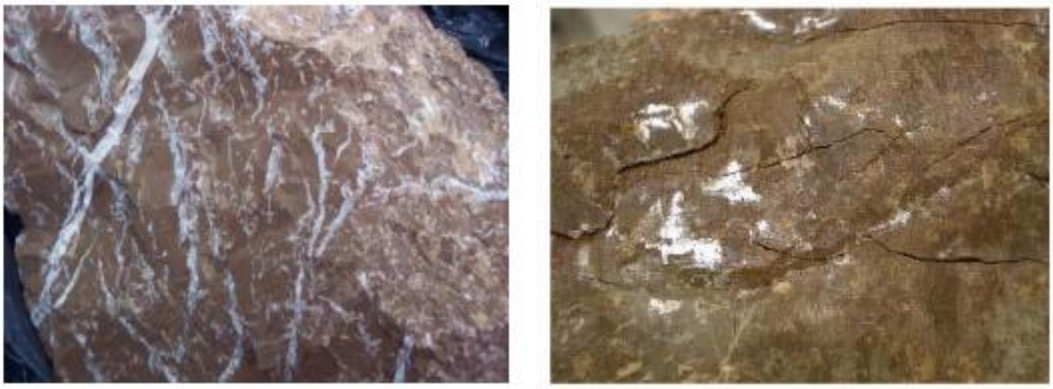

Figure 2.10. Details of Lilla claystone: (a) cross-shaped fibrous gypsum veins into the clayey matrix, (b) slickenside surfaces.

2.3.2 Design and construction of the original section

The Lilla tunnel has a length of 2034 m and the overburden varies between 32 m and 110 m. The original cross-section was initially of 117.3 m2 and had a horseshoe shape with radius 6.76 m (Figure 2.11). It is being called original horseshoe cross-section because it was later transformed into a circular one due to extreme floor heave, which reached displacements of more than 60 cm in some cross sections.

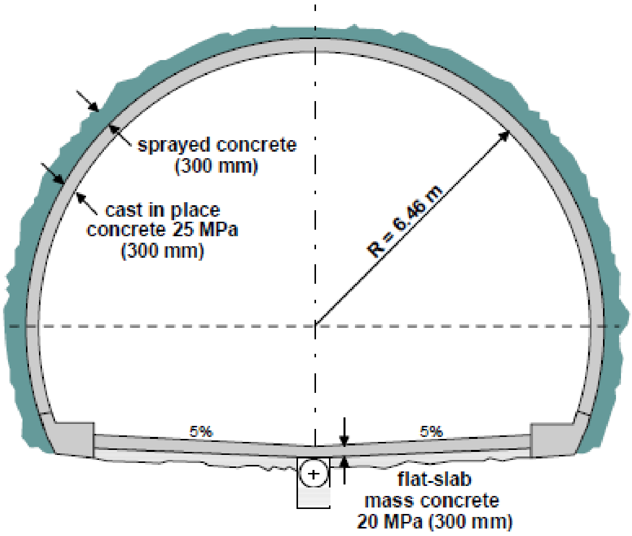

Figure 2.11. Original cross section of Lilla tunnel (Berdugo, 2007)

Table 2.2. General features of construction (Berdugo,2007)

Location	Catalonia, Northeast Spain
Geology	Anhydritic-gypsiferous claystone
Length	2034 m (1 tube)
Overburden	110 m (max)
Design	Convergence-confinement method
Excavated cross-section	Horseshoes 117.3 m^3 (R=6,76 m)
Excavated method	Drill+blast (head & bench) from the two portals
Construction period	2001-2002

The tunnel was excavated following the traditional drill and blast method from both portals simultaneously, dividing the section into head and bench. (see Figure 2.12 a and b). The resisting support was designed according to the convergence-confinement method (Panet, 1995).

According to the construction methodology of the new Austrian tunnelling method (NATM), sprayed concrete was applied systematically with a thickness of 300mm along the entire length of the tunnel, and additionally steel arch ribs (HEB 160) and rock bolts were used when the quality of the rock was low.

The final lining consisted of 300 mm thick cast-in-place unreinforced concrete of 25Mpa. The bench was excavated only after the break-head was achieved in February 2002, as is indicated in Figure 2.12 c. Once the bench was excavated throughout the full length of the tunnel, a 300 mm thick flat slab of unreinforced concrete (characteristic unconfined strength, fck = 20 MPa) was built on the floor. Therefore, the rock was exposed to the action of environmental agents and construction works for an extended period of time.

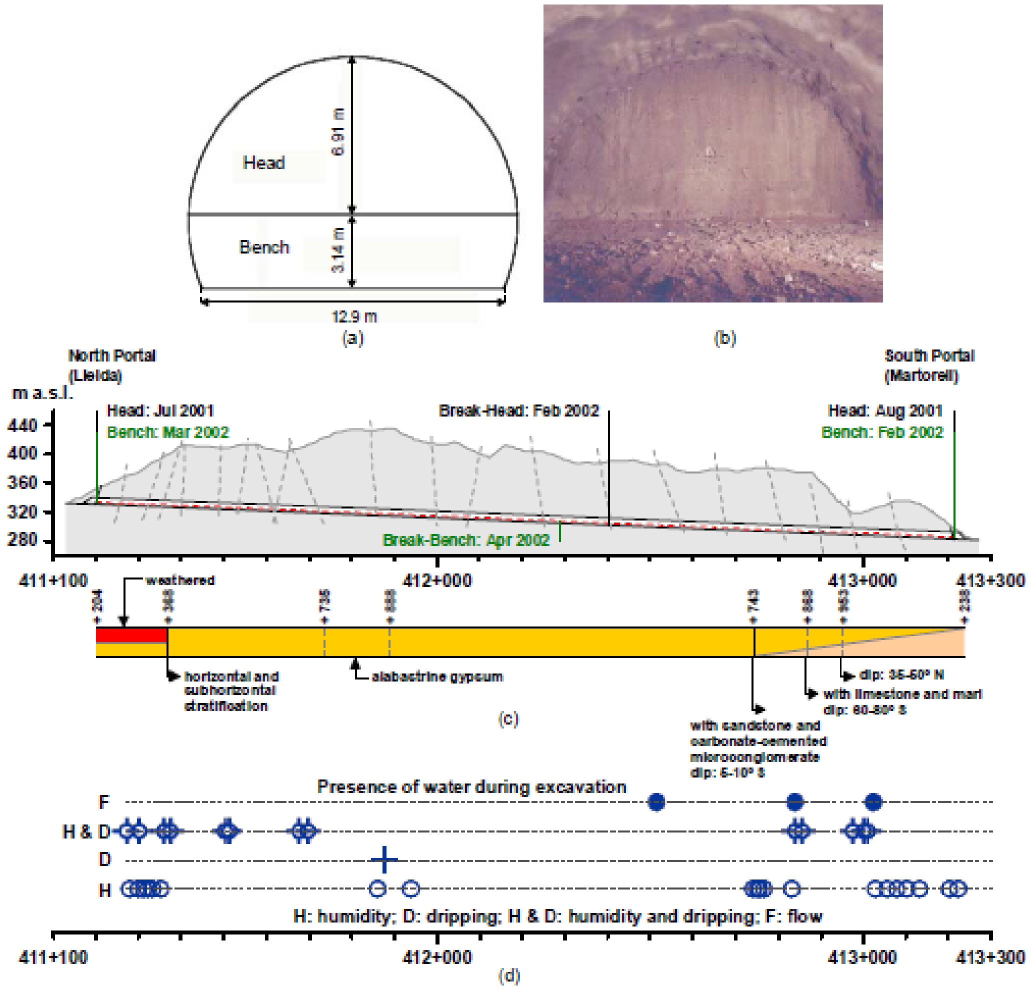
Head
6.91 m
Bench
3.14 m
12.9 m
(a)
(b)
North Portal
(Lleida)
South Portal
(Martorell)
m a.s.l.
440
400
360
320
280
Head: Jul 2001
Bench: Mar 2002
Break-Head: Feb 2002
Head: Aug 2001
Bench: Feb 2002
Break-Bench: Apr 2002
411+100
412+000
413+000
413+300
weathered
+204
+368
+735
+888
+743
+868
+953
+238
horizontal and subhorizontal stratification
alabastrine gypsum
dip: 35-60° N
with limestone and marl
dip: 60-80° S
with sandstone and carbonate-cemented microconglomerate
dip: 5-10° S
(c)
Presence of water during excavation
F
H & D
D
H
H: humidity; D: dripping; H & D: humidity and dripping; F: flow
411+100
412+000
413+000
413+300
(d)

Figure 2.12. Excavation stages in Lilla tunnel: (a) schematic representation of head and bench, (b) head section in station 412+474, (c) key dates during excavation, (d) presence of water during excavation (Berdugo,2007)

The initial flat-slab was constructed only in a short stretch of 158.8 m between stations 411+203.5 and 411+362.3. Figure 2.13 illustrates the excavation process of both the head and the bench from both the Southern and Northern portals. The excavation of the head was completed in eight months, proceeding from both portals from July 2001 to February 2002, while the bench excavation lasted from February 2002 to April 2002. It is noteworthy to remark that the foundation material was protected by the flat slab only in a short stretch, therefore exposed to environmental conditions for the rest of the tunnelling process. Moreover, it is important to emphasize that the design did not consider any precautions regarding the possible swelling of the clay rock.

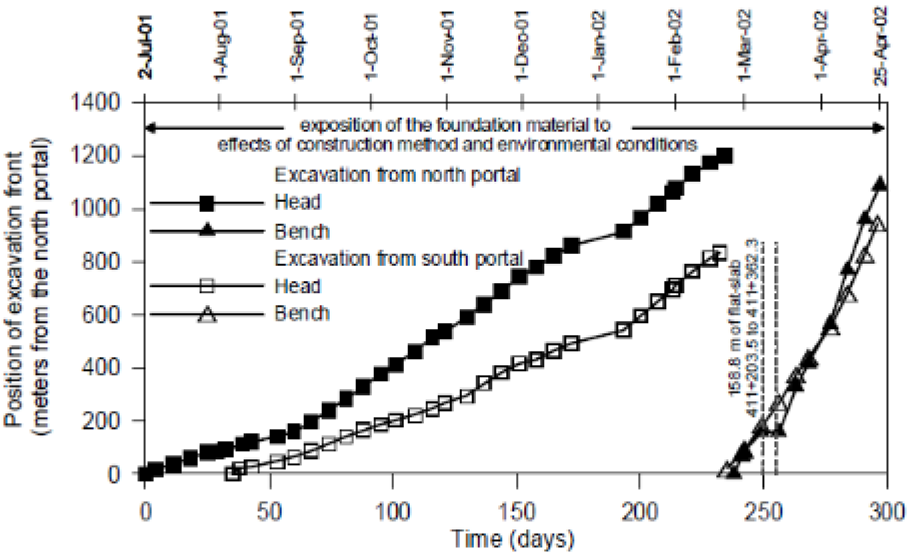

Figure 2.13. Evolution of the excavation process in Lilla tunnel (Berdugo, 2007)

Due to the low permeability of the rock, only areas close to the portals were waterproofed by means of a PVC sheet and a geotextile placed between the support and the lining. In the rest of the tunnel the longitudinal drainage system was composed of a 500 mm PVC collector, located 1.4 m below the floor.

For most of the time, the excavation was carried out in dry conditions. A relevant flow of water was reported only near the South portal due to minimum overburden, change in stratification and some failures connecting colluviums and the excavation (Berdugo, 2007). These details are clearly illustrated in Figure 2.12 d.

2.3.3 Expansive phenomena in the Lilla tunnel

The first expansions were detected in the flat-slab in September 2002, just after the tunnel was built and before the construction of the tunnel lining. Heave displacements occurred at floor level in stations 411+598, 411+685 and 412+540. The heave was followed by damage of the longitudinal drainage system and by local failures of flat slabs.

Figure 2.14 summarizes the conditions in the tunnel just one month after the expansive phenomena were detected for the first time. When floor heave occurred, the longitudinal drainage system was already installed. Even tough partial drainage of the foundation material could be expected, some isolated strong floor heave can damage the drainage tube, generating local water accumulation.

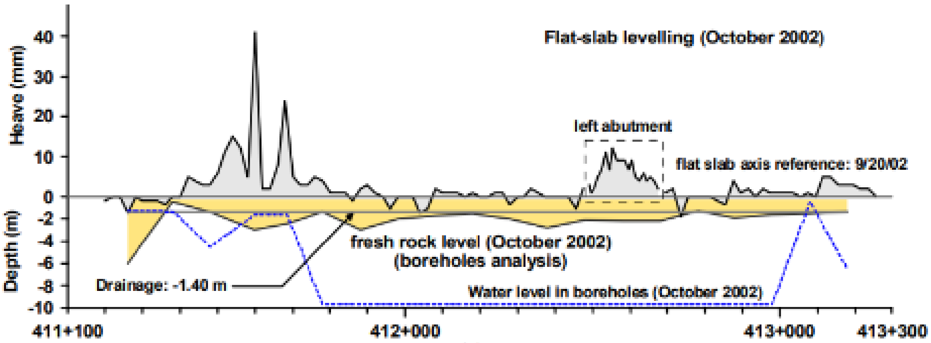

Figure 2.14. Groundwater level and distribution of heave affecting the flat-slab in October 2002 (Berdugo, 2007)

Heave of the floor slab evolved rapidly, and it soon became clear that the adopted resisting cross-section was unable to cope with the observed swelling phenomena. An alternative cross section was required. Studies aimed at clarifying the most probable causes of the expansions, the evolution of the swelling and the technical alternatives to reinforce the initial cross-section were conducted.

A comprehensive set of laboratory tests and in situ measurements were performed to obtain a good understanding of the mechanisms of the swelling phenomena and to study the extent of the expansions. Firstly, tests sections with flat-slab and invert-arch were constructed; then, instrumented circular cross-sections with both resisting and yielding support were built and subjected to flooding test.

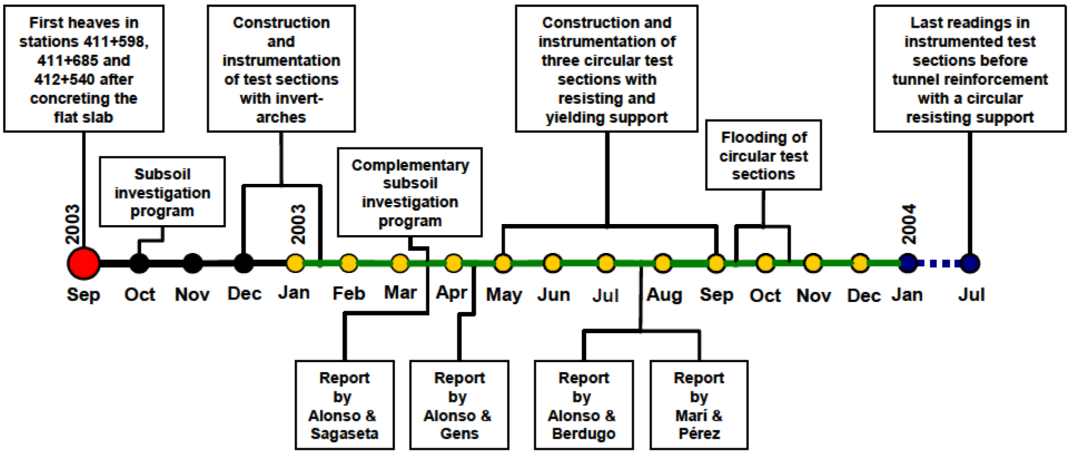
First heaves in stations 411+598, 411+685 and 412+540 after concreting the flat slab
Construction and instrumentation of test sections with invert-arches
Construction and instrumentation of three circular test sections with resisting and yielding support
Last readings in instrumented test sections before tunnel reinforcement with a circular resisting support
Subsoil investigation program
Complementary subsoil investigation program
Flooding of circular test sections
2003
2003
2004
Sep
Oct
Nov
Dec
Jan
Feb
Mar
Apr
May
Jun
Jul
Aug
Sep
Oct
Nov
Dec
Jan
Jul
Report by Alonso & Sagaseta
Report by Alonso & Gens
Report by Alonso & Berdugo
Report by Marí & Pérez

Figure 2.15. Summary of field activities to study the expansive phenomena in Lilla tunnel Berdugo (2007)

Undisturbed core specimens of the foundation material were recovered from boreholes drilled in the Lilla tunnel floor. Based on such borings, the depth of the damaged rock was estimated. Large diameter continuous cores were extracted from the “active zone”, which corresponds to depths at which swelling develops. The argillaceous rock specimens extracted from the active zone were very different from the ones belonging to the stable zone. (Figure 2.16).

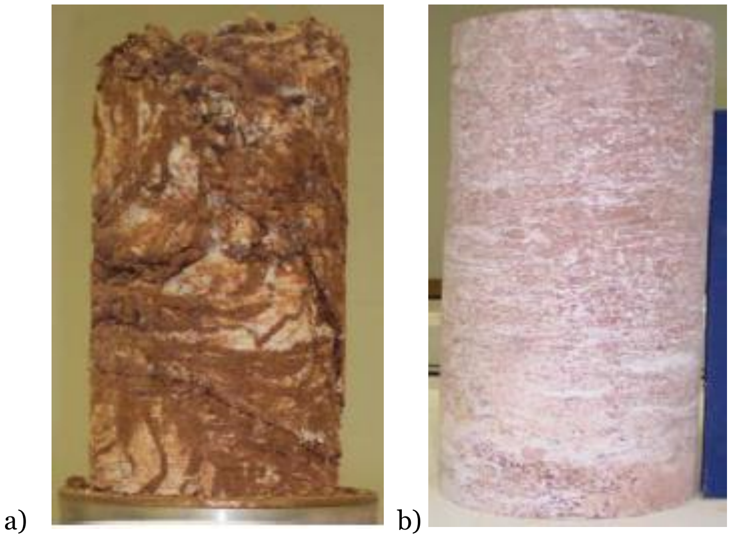

Figure 2.16. Core specimens of chainage 411+600. (a) Active zone, depth 2.8 – 3.0 m (Tarragó, 2006). (b) Stable zone, depth 6.9 – 7.2 m. (Berdugo, 2007)

In October 2002, March 2003 and December 2003 laboratory tests were undertaken to achieve continuous profiles of geotechnical properties of the samples, including the mineralogical composition of the solid phase. Sliding micrometers lectures, as well as laboratory tests on undisturbed samples, permitted to evaluate the extent of the active zone in the foundation material. A precise information of the extent of the upper active zone was provided by strain record measures in December 2003. According to Alonso, Berdugo, & Ramon (2013) the active zone has a thickness of 5.5 m and it can be easily identified because of its geotechnical and mineralogical characterization, which is different from the unchanged composition of the stable zone rock. Another aspect associated to active zone identification was the increase of water content and the evolution of total density. Degradation of foundation rock material in this zone is clearly illustrated by changes in water content regarding both time and depth. Water content is a measure of rock degradations and increase of sulphate content with water content could be expected. As shown in Figure 2.17, water content increased in a 6 months period from values typical of the undisturbed formation (2–4%) to values in the range 5–10%. Such water content increasing trend with time is accompanied by a decrease in total density.

Another remarkable aspect that can be observed in Figure 2.17 is the variation of gypsum content with depth. Within the stable zone, the percentage of gypsum varies from low to very low. However, approaching the active zone the gypsum content increases progressively from low values to 15– 18% in the upper part. On the other hand, anhydrite, which maintains a high concentration (25–50%) throughout the depth, seems to decrease a little its concentrations in the active zone. The plot suggests that, within the active zone, gypsum content has increased at the expense of anhydrite.

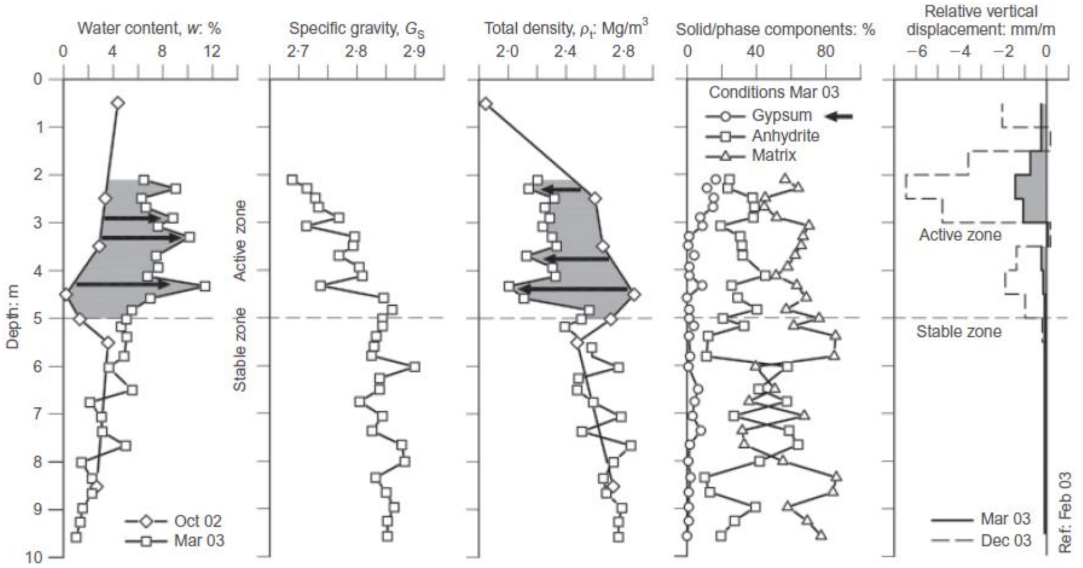

Figure 2.17. Geotechnical and mineralogical characterisation of rock at chainage 411+600 (invert arch), and vertical displacements measured by sliding micrometer installed in the axis. (Alonso, E. E. et al.,2013)

In all the vertical profiles, the occurrence of neo-formation gypsum needles on slickenside surfaces was found in the active zone (Figure 2.18a). Another significant aspect was the existence of neo-formation gypsiferous aggregations in relatively confined discontinuities of samples extracted from deeper depths compared to the active zone (Figure 2.18b). A probable explanation could be related with a sort of "wedge effect" capable of moving parts of the rock mass as a rigid body, phenomenon that would occur simultaneously at the swelling mechanisms in the active zone (Alonso & Olivella, 2008).

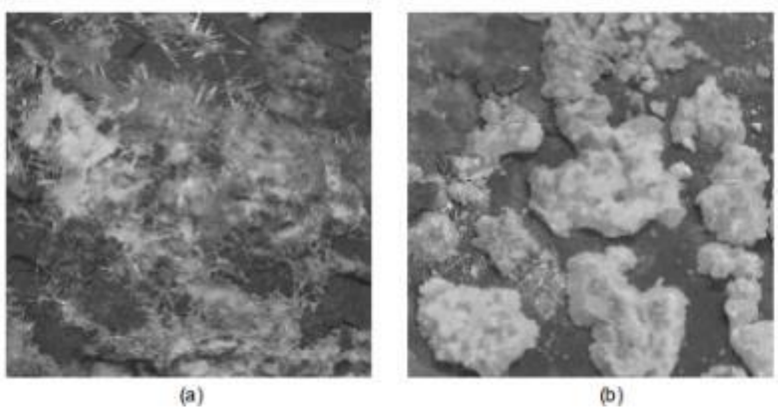

Figure 2.18. (a) Gypsum needles on an open slickenside surface located into the active zone, (b) gypsiferous aggregations in a confined discontinuity located in the lower part of the active zone (Alonso & Olivella, 2008)

2.3.4 Performance of flat-slab floor

Extreme expansive phenomena were detected in a generalized way in cross sections characterized by flat-slabs. Floor heaves damaged and interrupted to the central longitudinal drainage system at various chainages and caused local failures of the concrete slabs. Figure 2.19 provides a first straightforward evidence of the magnitude of the swelling phenomenon.

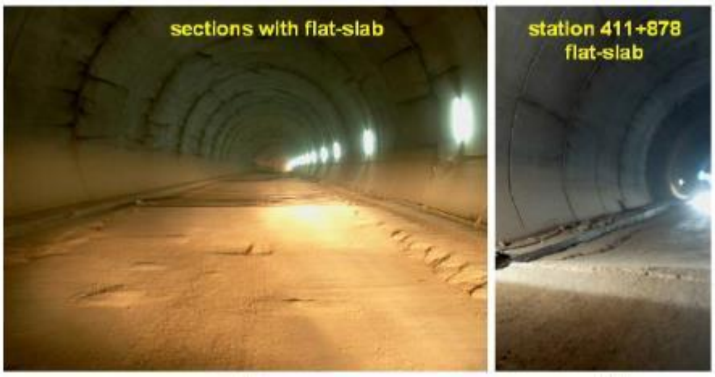

Figure 2.19. Distortion, heave and failure of flat-slabs in photos taken in March 2003. (Berdugo, 2007)

In March 2003 the first truly damaging heave was detected at chainage 411+880. It was six months after the initial expansive mechanism observation and two weeks after a moderate rain event. Photographs taken in March, May and September 2003 are presented in Figure 2.20, showing the progression in time of the floor heave. Note the severe level of the expansion in the subsoil. According to Alonso et al., (2013) the intense heave was due to the uncontrolled presence of water on the tunnel floor.

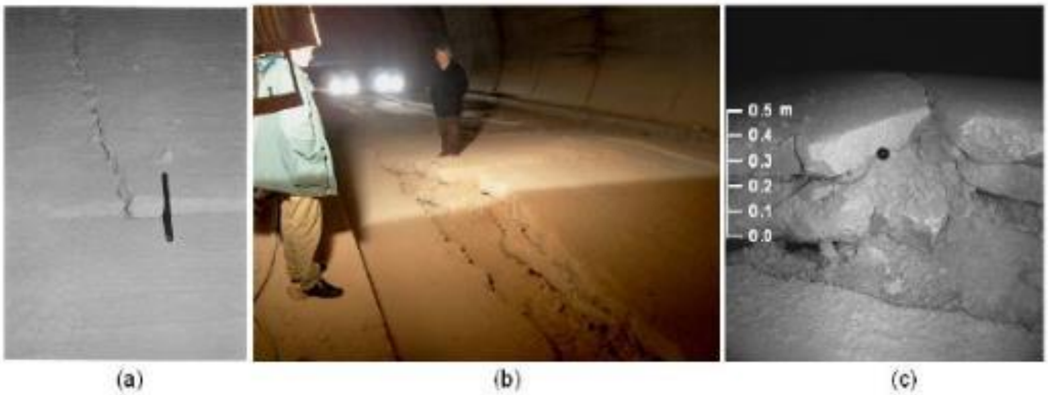

Figure 2.20. Evolution of the heave and failure of the flat-slab in station 411+880: (a) March 2003, (b) May 2003, (c) September 2003 (Berdugo, 2007)

Figure 2.21 is presented to make some remarkable consideration and to get an overall understanding of the Lilla tunnel heave mechanism between October 2002 to December 2003. The heave magnitude along the tunnel is showed with respect to the flat slab axis, which was taken as a reference the 20th of September 2002. Almost all the measurements refer to the tunnel floor but there are a few that are taken in the left abutment (approximately between stations 412+ 500 and 412 + 700).

While between chainages 411 + 556 and 411 + 860 no measurements are shown because a curved invert was cast in place in those sections, the heaviest vertical displacements occurred in a 300 m long zone close to the northern portal. As mentioned previously, the first strong expansive events were detected in station 411+880, which corresponds to a chainage where the lining ended. It seems that the heave intensity decreased towards the southern portal. A 400 m long stretch, next to the south portal, did not exhibit any swelling. A comparison with Figure 2.14 should be done to get knowledge of the magnitude and the temporal evolution of the swelling phenomenon: the maximum measured heaved passed from around 40mm in October 2002 to almost 700mm a year later. According to Alonso, Berdugo & Ramon (2013) the maximum displacement recorded was among the highest reported in tunnels built in Gipskeuper formations in Central Europe.

The evolution of the floor heave in the monitored sections near to the northern portal is close to 2 mm/day with no indication of slowing. This is presented in Figure 2.22, which indicates approximately constant mean rates, varying between 1.2 and 2 mm/day in critical stations (411+420, 411+880 and 411+900) (Berdugo,2007). In December 2003, heave between 513 and 763 mm were reached. February to December long lasting sliding micrometer measurements allowed the identification of a 4-meter thickness active zone in the foundation material below the flat-slab. Such active zone remained basically unchanged during the monitoring program. This conclusion was drawn based on the sliding micrometers readings between stations 412+150 and 412+500, which indicate that the boundary of the active zone has a certain regularity. On the other hand, boreholes drilled previously in October 2002 showed that the fresh rock level was far to be regular. In Figure 2.23 fresh rock depth and active zone depth at the end of the monitoring program (December 2003) are compared to the circumference that completes the tunnel vault. The first assessment that facilitates the figure is that there may exist a relation between the tunnel diameter and the extension of the active zone. As a matter of fact, one of the arguments favouring the installation of a circular section was that an entire excavation would remove the active zone and consequently dodge the swelling issue.

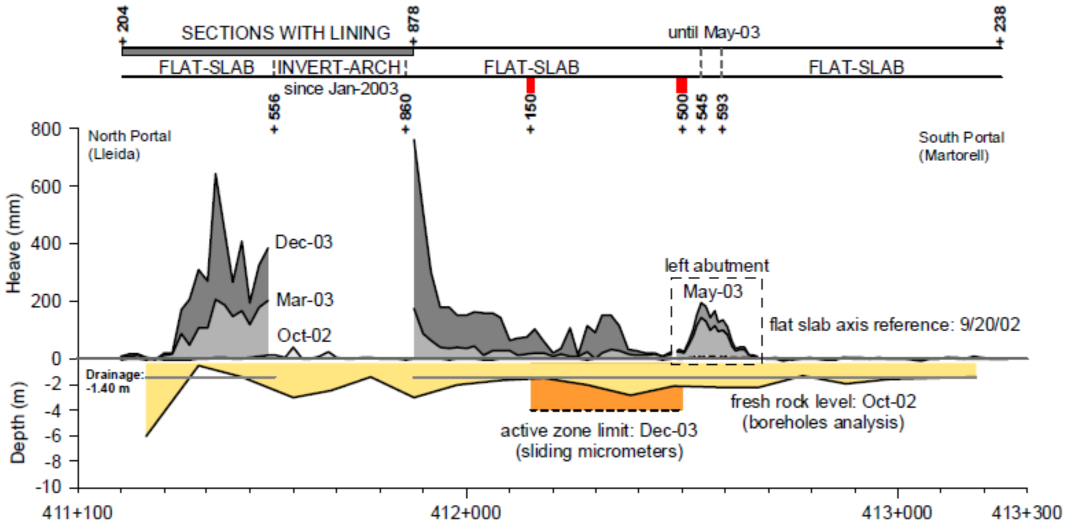

Figure 2.21. Heave of the flat-slab between October 2002 and December 2003 and their connection with conditions of the rock in October 2002 and the depth of the active zone (Berdugo,2007)

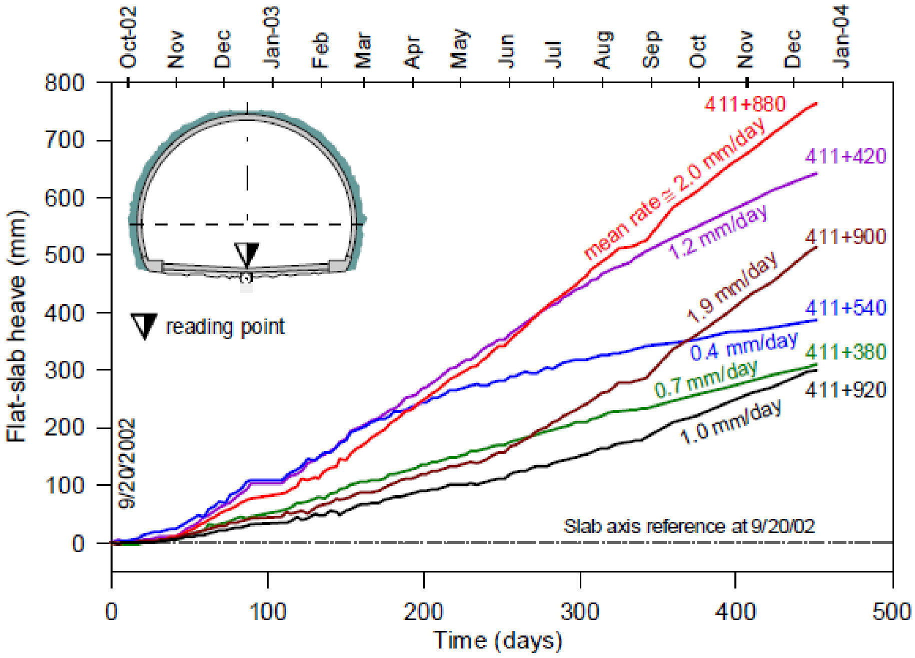

Figure 2.22. Evolution of floor heave between September 2002 and December 2003 in critical sections with flat-slab (Berdugo, 2007)

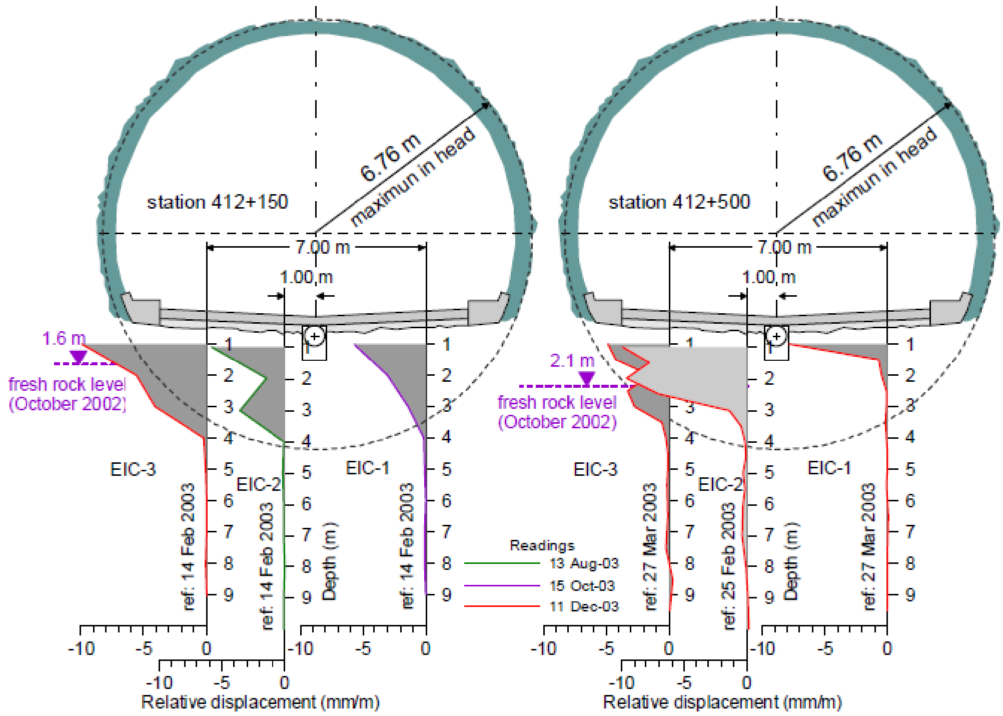

Figure 2.23. Relationship between the depth of the active zone below test sections with flat-slab and the maximum radius of excavation (Berdugo, 2007)

2.3.5 Performance of the curved invert

A curved invert was designed to adopt some preventive actions to resist swelling pressure of 0.5 MPa. Such value was obtained from results of swelling pressure tests carried out on undisturbed samples recovered from boreholes drilled at 2.50-meter depth below the floor slab at chainage 411+480 (very active swelling zone) in October 2002. The invert-arch cross section adopted was built in January 2003 after the demolition of the previous flat slab between stations 411 + 556 and 411 + 860. It was cast in place in two stretches of different invert thickness: the first 194 m long stretch (from chainage 411 + 556 to 411 + 750) was 400 mm thick while the following 110m (between points 411 + 750 and 411 + 860) was 600mm thick (Figure 2.24). The design is characterized by two longitudinal concrete massifs, aimed at support the abutments.

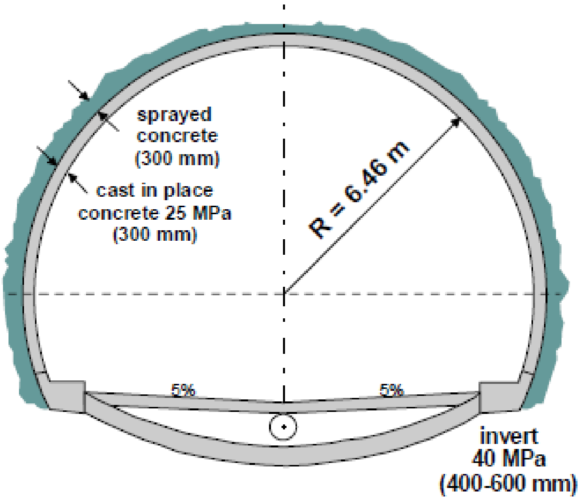

Figure 2.24. Design of the cross-section with invert-arch (Berdugo, 2007)

Vertical displacement rates reduced more than one order of magnitude compared to the flat slab section, but they did not present any stabilization trend of slowing in almost a year (Figure 2.25). At critical station 411+663 the mean heave rate was 0.1 mm/day and, 10 months after the construction of the curved invert, a 27 mm heave was reached.

In general, the effectivity of the invert-arches was quite satisfactory in terms of heave reduction at floor level; nevertheless, once they were installed, high radial pressures against the curved invert were measured.

Figure 2.26 shows the longitudinal and transverse variation of pressure, at the end of the measuring period (December 2003), recorded in the test sections. The maximum recorded pressure is close to 5 MPa, but the distribution along the tunnel as well as in cross-sections is very irregular. At a given cross-section measured pressures in the abutment rock-concrete contact are higher than the values measured in the central position. Floor heave of the corresponding cross-sections is also given.

Vertical displacements below the invert-arch in station 411+600 (invert thickness of 400 mm) were obtained by means of sliding micrometers. After ten months recording period, from February to December 2003, it was evident that the phenomenon already affecting the flat slab was repeating: expansions were concentrated within a zone of finite extension that remained basically invariable. This situation is illustrated in Figure 2.27, in which the thickness of the active zone varies from 4 meters to almost 6 meters under the invert at the tunnel axis. From a comparison with the situation presented in Figure 2.23 it seems that the construction of the invert has extended the initial active zone, which now is not confined inside the circular section. (Alonso et al., 2013).

The conclusion to the invert-arch design and installation was that, on one hand, the expansive phenomenon appeared to be diminished and on the other hand, it possibly caused an enlargement of the active zone. However, despite the improvement produced in the sections with invert-arch, the swelling continued to be intolerable for a high-speed railway. In addition, the measured radial pressure reached maximum values that could affect the stability of the tunnel.

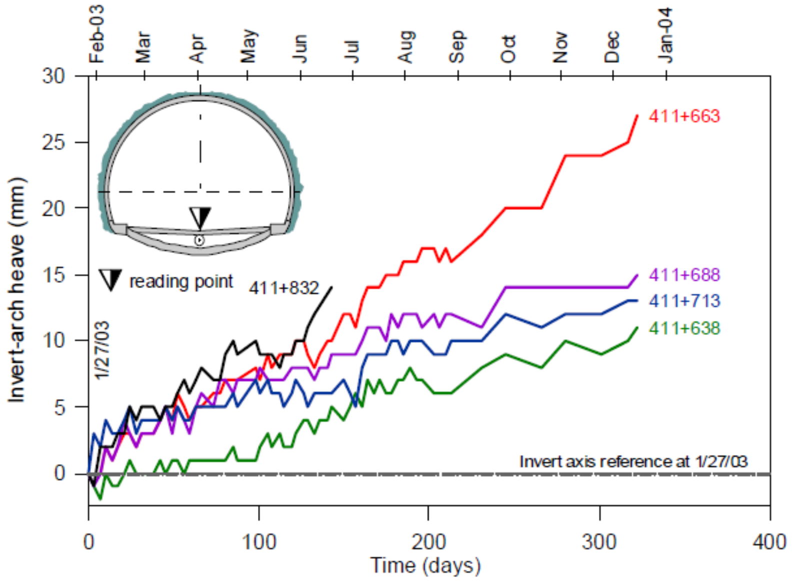

Figure 2.25. Evolution of floor heave between January and December 2003 in test sections with invert-arch (Berdugo, 2007)

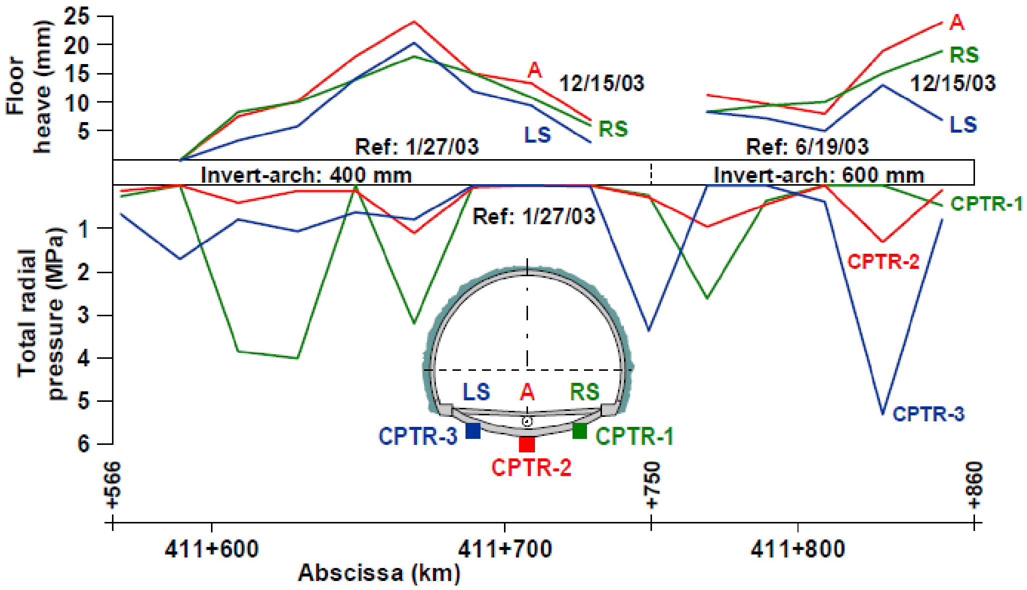

Figure 2.26. Distribution of the floor heave and the total radial pressures in test sections with invert-arch in December 2003 (Berdugo, 2007)

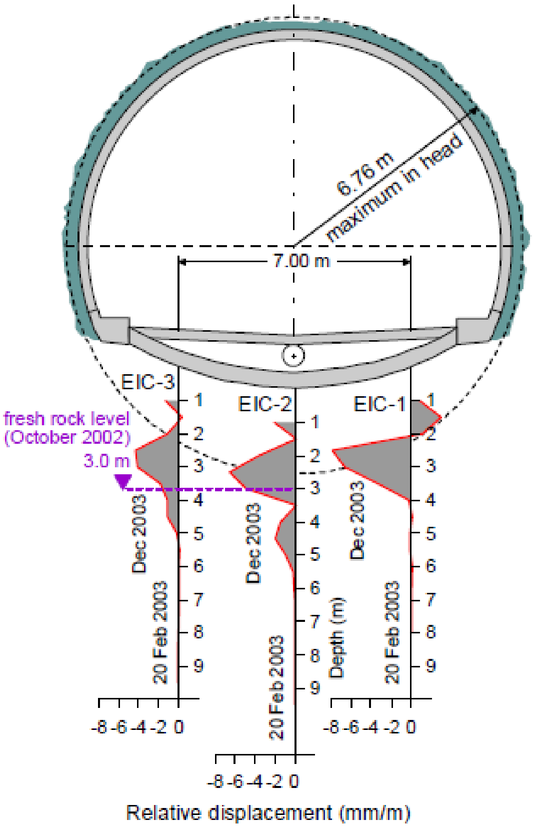
6.76 m
maximum in head
7.00 m
EIC-3
EIC-2
EIC-1
fresh rock level
(October 2002)
3.0 m
1
2
3
4
5
6
7
8
9
Dec 2003
20 Feb 2003
Depth (m)
-8 -6 -4 -2 0
Relative displacement (mm/m)

Figure 2.27. Sliding micrometer readings below test section 411 + 600 with invert arch of 400 mm; strains recorded February–December 2003 (Berdugo, 2007)

2.3.6 Performance of circular test sections

Aiming at the elimination of the existing active zone and the study of the consequences associated with an additional excavation and an alternative stiffness, circular test sections were built between May and August 2003. Three circular sections were built between stations 412 + 543 and 412 + 593 (Figure 2.28). The tunnel floor had to be excavated to complete the circular geometry. Each one of the sections was intended to test a design criterion. Specifically, the first section was designed according to the principle of resisting support (Figure 2.29a) and the other two according to the principle of yielding support, using slots in the contact between the vault and the invert (Figure 2.29b), and a polyurethane foam at the rock-invert interface (Figure 2.29c). The resisting support was installed between stations 412+543 and 412+565 and consisted in a rigid concrete lining reacting against the excavated rock. The first yielding support, which was composed by a set of springs allowing for the shortening of the tunnel lining under the circumferential load imposed by ground swelling, was built from chainage 412+571 to 412+581, and the second yielding support was a 40 cm thick foam layer located below the invert that was cast in place in chainages 412+583 to 412+593.

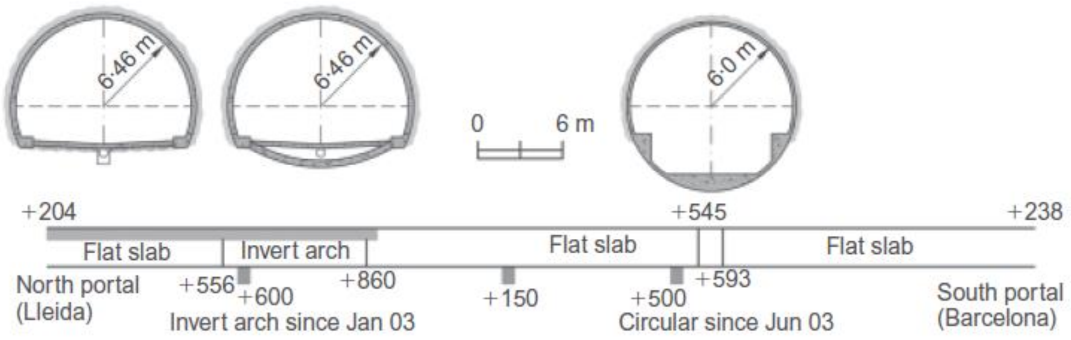

Figure 2.28. Initial cross sections and testing sections in the longitudinal section of Lilla tunnel

The excavation of the circular geometry reached as maximum a depth of 4 m under the original horizontal slab. It was argued that the construction of the circular section would have led to the removal of a substantial proportion of the active zone which developed under the original flat slab floor. Hence, in addition to the circular cross-section structural advantages, the swelling activity would be reduced. In all three sections the circular excavation was performed carefully to minimise further rock damage.

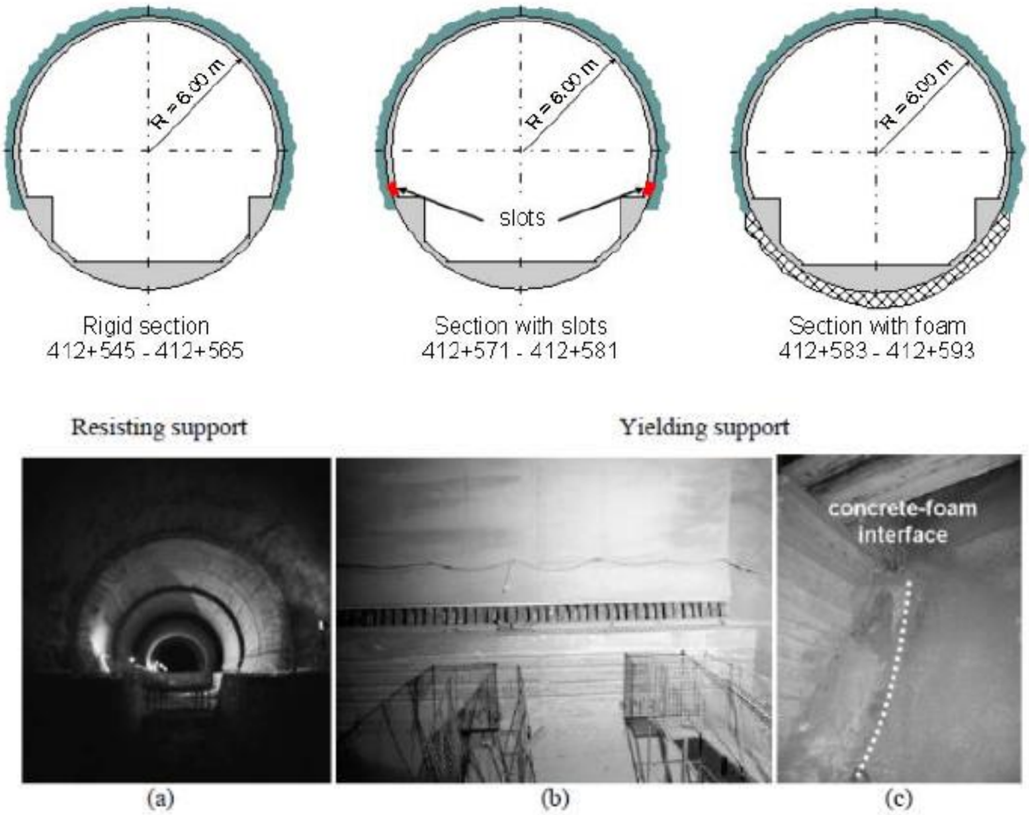
R = 6.00 m
R = 6.00 m
R = 6.00 m
slots
Rigid section
412+545 - 412+565
Section with slots
412+571 - 412+581
Section with foam
412+583 - 412+593
Resisting support
Yielding support
concrete-foam interface
(a)
(b)
(c)

Figure 2.29. Distribution and typical characteristics of circular test sections with resisting and yielding supports (Berdugo, 2007)

It was known that the most critical situation would be found when rock under the invert was wet. Hence, extreme wet conditions of the foundation material were forced by means of flooding the invert using natural groundwater from the tunnel area. To do so, vertical holes were drilled through the concrete lining allowing the direct access of water when the tunnel floor was inundated through tubes of 110mm as diameter. The performance of the three sections was monitored with the installation of pressure cells and sliding micrometers. Moreover, a geotextile strip was installed along the longitudinal axis of the holes to provide a regular distribution of water below the invert.

The flooding was initiated on September 2003. A free water level was simulated and maintained for 30 days. Figure 2.31 also shows the flooding in the total radial pressure measurements together with the instrumentation which was installed in three tested cross sections. Such circular test sections (411+ 552, 412 + 574, 412 + 590) were instrumented using pressure cells in both the invert and the vault, while two sliding micrometers of 12 m long were installed at foundation level. Because no significant movement in the vault was capture, the focus of the thesis will be on the five pressure cells at the concrete-rock interface (or concrete-foam in one of the yielding support designs). Figure 2.31a illustrates the performance of the three circular tests sections with resisting support, slots and foam, respectively. The pressure cells measurements detected a linear increase of total pressure. It is noteworthy that in all the test sections expansions began before the artificial flooding stage, which apparently did not have any influence on the rate of pressure increase. Records on the yielding support, especially in the exhibited reduced swelling pressures against inverts proving their expected benefits.

Extensometer measurements indicated that a new active zone was effectively generated after the circular section excavation. Extensometers under the foam section could not be monitored, however. It was possible to identify the depth of the active zone between 4 and 6 m, a thickness like the one found in the flat and curved invert sections. Figure 2.33 illustrates the calculated swelling strains measured at varying depths within the active layer below the resisting and the yielding supports. Initially strains increase fast and later they progressively slow down, although no limit for swelling strains was achieved. Note that the evolution of the swelling strains is higher in the sections with yielding support systems.

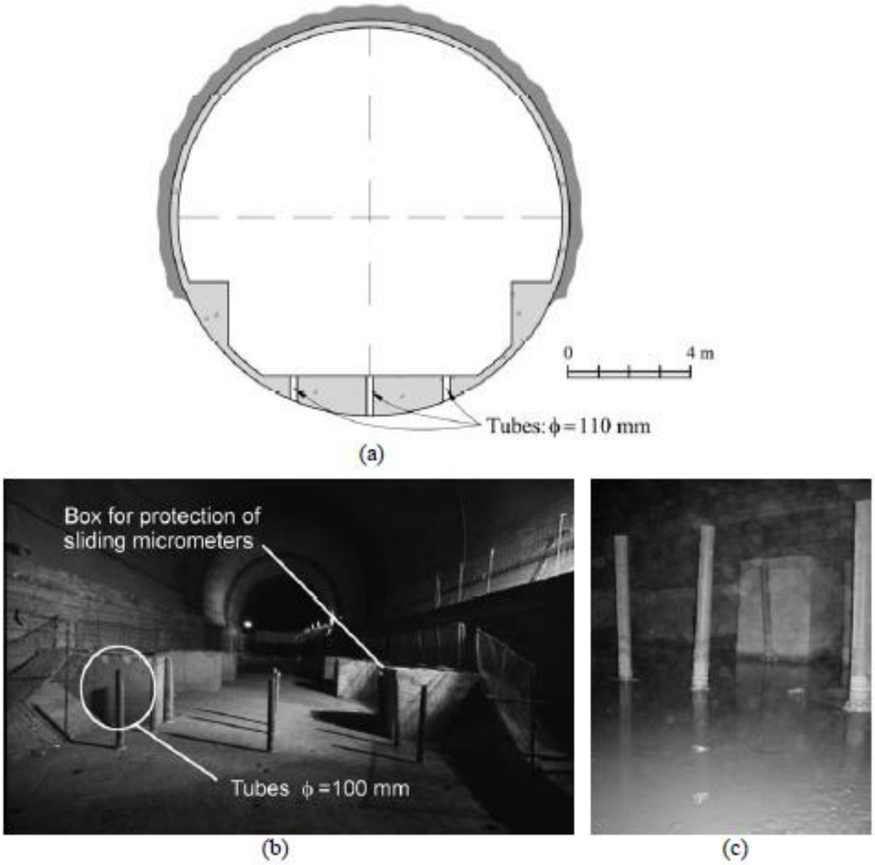

(a)

(b) (c)

Figure 2.30. Details of the system for the flooding in circular sections with resisting and yielding supports: (a) design of cross-section and boreholes to allow wetting the rock; (b) test section before the start of the test; (c) flooded test section (Ramon, 2014)

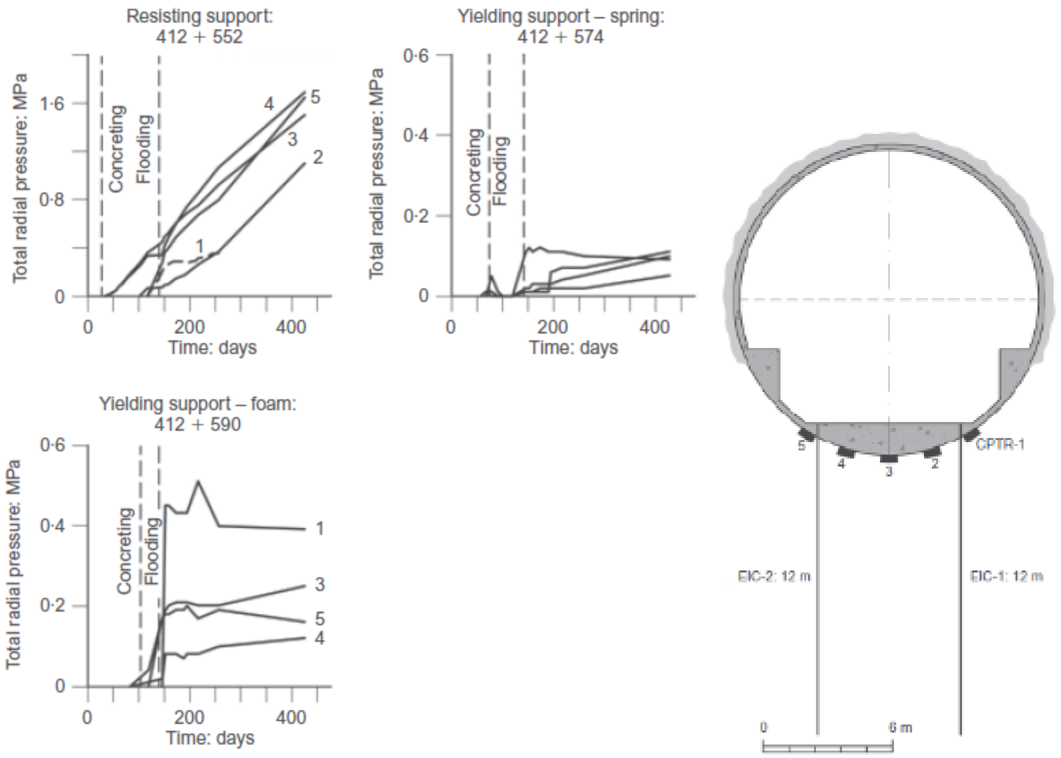

Figure 2.31. Total radial pressure against inverts and instrumentation of a test section (Alonso et al.,2013)

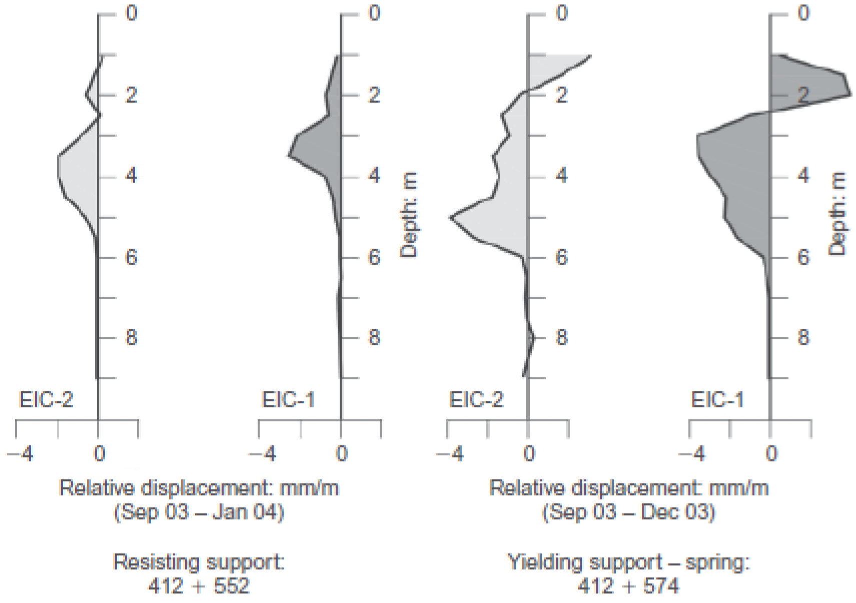

Figure 2.32. Sliding micrometers' readings (Alonso et al.,2013)

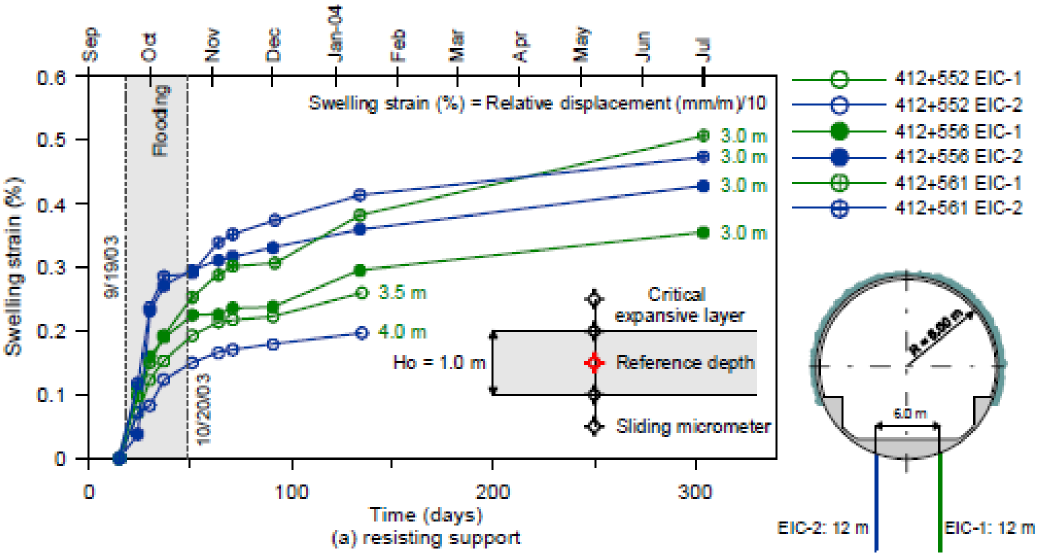

(a) resisting support

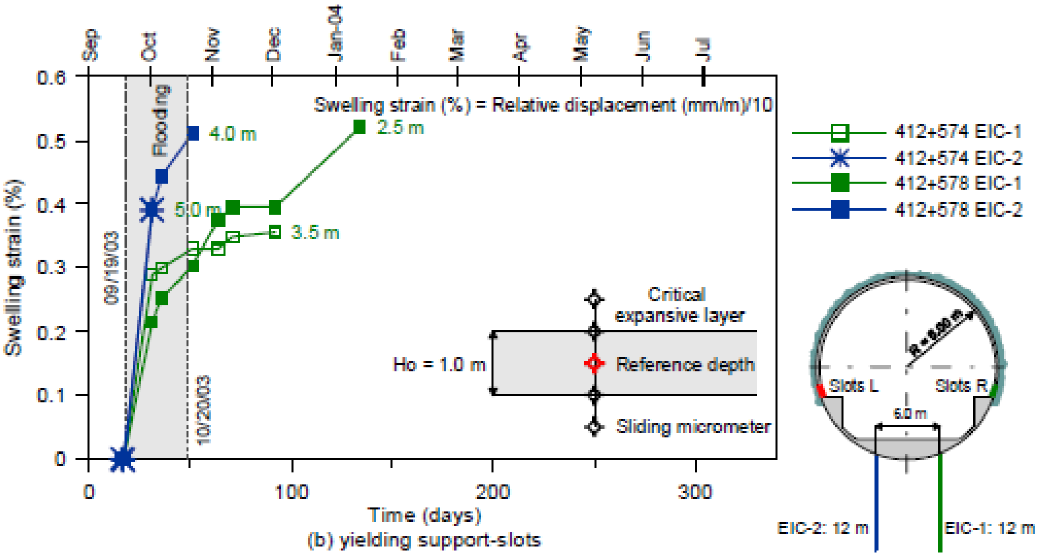

(b) yielding support-slots

Figure 2.33. Evolution of calculated swelling strains in critical expansive layers below circular test sections: (a) below the resisting support, (b) below the yielding support-slots (Berdugo, 2007)

2.3.7 Tunnel reinforcement

The final circular cross-section of the Lilla tunnel was eventually designed and reinforced according to the principles of resisting support. Despite having measured greater radial pressures, the active zone extension with a rigid support was smaller and the long-term swelling forecastable. Moreover, due to the unclear performance of the yielding support with time, it was considered more appropriate and conservative to make use of a resisting lining with design swelling pressure of 4,5 MPa (Alonso, Berdugo, & Ramon, 2013). Therefore, a reinforced circular cross-section was adopted and cast in place inside the original horseshoe section along the entire tunnel. The problem was that by then the tunnel was partially built. As a matter of fact, the original flat-slab had already been installed along an important stretch of the tunnel, as well as stretches with curved invert and circular sections. Therefore, the construction stages consisted in first demolition of the initial floor, the anchor of the abutments and consequently the excavation of the circular cross section. The detail of the reinforced Lilla tunnel circular section is illustrated in Figure 2.34. Concrete with a characteristic strength of 80 MPa and steel B500S reinforcement and confinement bars were used. The new circular resisting support reinforcement was built between July 2004 and October 2005.

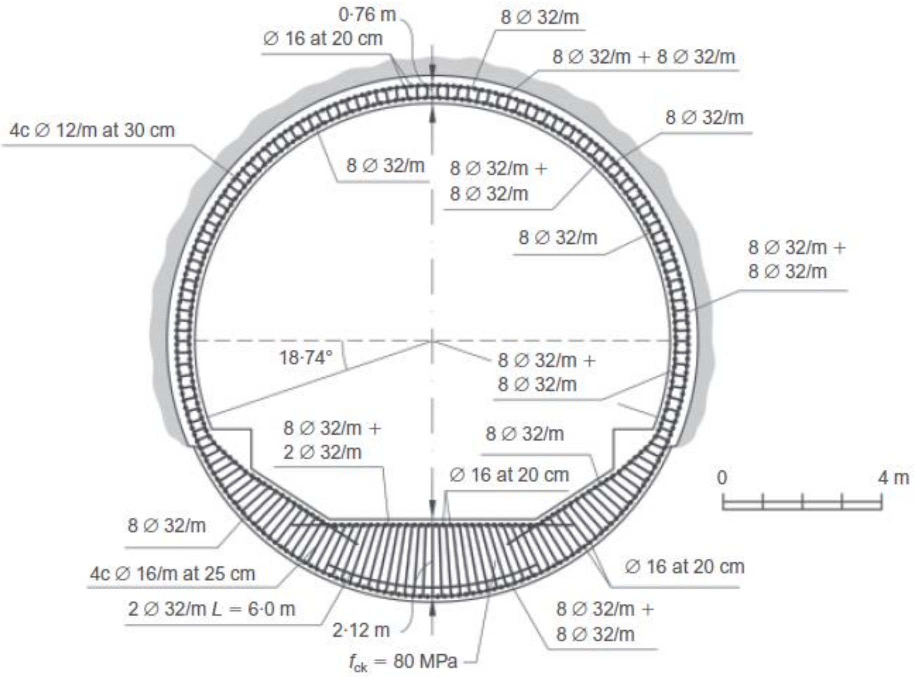
0·76 m
Ø 16 at 20 cm
8 Ø 32/m
8 Ø 32/m + 8 Ø 32/m
4c Ø 12/m at 30 cm
8 Ø 32/m
8 Ø 32/m
8 Ø 32/m +
8 Ø 32/m
8 Ø 32/m
8 Ø 32/m +
8 Ø 32/m
18·74°
8 Ø 32/m +
8 Ø 32/m
8 Ø 32/m +
2 Ø 32/m
8 Ø 32/m
Ø 16 at 20 cm
0
4 m
8 Ø 32/m
4c Ø 16/m at 25 cm
Ø 16 at 20 cm
2 Ø 32/m L = 6·0 m
2·12 m
8 Ø 32/m +
8 Ø 32/m
f_ck = 80 MPa

Figure 2.34. Resisting support adopted for the reinforcement of Lilla tunnel (ADIF, 2006; Alonso et al.,2013)

2.3.8 Performance of the reinforced tunnel

The reinforced tunnel was instrumented to measure the evolution of total radial pressures at the rock-lining interface and the straining of the steel reinforcement. Pressures were calculated in both the invert and the vault with radial and hoop pressure cells. Moreover, vibrating wire extensometers and mobile extensometers were installed at the invert. Details of the instrumentation used in the tunnel are presented in Figure 2.35 and Figure 2.36. Twenty-one cross-sections were instrumented along the tunnel. Instrumentation results are now discussed with more details. Note that the long term expansive phenomena observed in the Lilla tunnel is analysed in the present work referring to the studies and articles of Alonso, Berdugo, & Ramon (2013).

As expected, maximum radial pressures, which were measured by total pressure cells from 2005 to 2011, were recorded in cells installed at the invert. Figure 2.37 illustrates the distribution of the swelling pressure along the longitudinal section of the Lilla tunnel: cross-sections next to the northern portal (approximatively from chainage 411 + 240 to chainage 412 + 700) present significant swelling values while the southern part of the tunnel is characterized by almost no pressure. The performance of the reinforced tunnel is provided by pressure-time records, measured in the period 2005 - 2011, that are here presented for seven cross-sections from Figure 2.38 to Figure 2.44. Furthermore, stresses recorded in the reinforcement bars are given as well as the instrument distribution in the section.

Several radial pressure devices installed in the invert detected a sudden increase of pressure between April and May 2005. This behaviour was most likely related to the concreting of the vault, which was performed once the entire circular tunnel invert had been built. The vault concreting implied the closing of the circular reinforced section. Hence, a structural link between the frames was build, offering high resistance to swelling and thus increasing the pressures recorded. A second sudden increase in pressure was evident from the October 2006 measuring campaign. However, no relation between swelling pressure and structural behaviour could be established, since the tunnel reinforcement construction works concluded in June 2005. The reactivation of pressure seemed to be related to heavy rainfalls which occurred in September and October 2006. In some stations, pressure values tent to stabilize after the first few years increasing trend. Nevertheless, some other records show a long-lasting increase of pressure with time during the monitoring period. For instance, pressures in two loading cells at chainage 411 + 826 increase at a rate of 70 kPa/month (Alonso, Berdugo, & Ramon, 2013). Basically, the monitoring of the tunnel during construction and consequent operation has shown that there is a variability of the recorded intensity of swelling radial pressure. To sum up the observed behaviour, the maximum recorded swelling pressures recorded during tunnel operation are close to 5 - 6 MPa in most of the sections. However, higher values of radial pressure, up to 6-7 MPa, were measured at the invert of some sections.

According to Alonso, Berdugo, and Ramon, the most significant result is the extreme variability of recorded radial pressures in a given section. That is the case of sections at chainages 411 + 348, 411 + 468 and 411 + 707, whose pressure records are plotted in Figure 2.45. Measured distributions of radial pressure in the three sections indicated in December 201 The interesting result was that, while one pressure cell may had registered a quite high value (more than 5 MPa), the remaining cells in the same section, closely located, recorded very low values or even no pressures. Even admitting recording errors and recognising that a continuous pressure distribution cannot be provided by six loading cells, it is evident that ground response is fundamentally different from the loading assumptions that were made at the moment of the reinforced cross-section design. The explanation of a such heterogeneous behaviour would presumably rely on the variability on both the transversal and the longitudinal direction (Alonso, Berdugo, & Ramon, 2013). This observation is the key starting point for the present work analysis.

The implications of the abovementioned pressure distribution are positive and not surprisingly the massive reinforced concrete tube seems to resist well the three-dimensional distribution of “point loads” on the outer boundary. In support of this argument, measured stresses in the reinforcement bars in seven cross-sections are presented (see Figure 2.38b, Figure 2.39b, Figure 2.40b, Figure 2.41b, Figure 2.42b, Figure 2.43d-f, Figure 2.44e-g). In the case of invert reinforcement, the plots refer either to a reinforcement located close to the outer circular boundary or to a horizontal reinforcement close to the upper boundary of the invert. Measurements show that almost all bars, both close to the outer and inner boundary, are subjected to compressions. Compressive stresses take rather small values, the maximum ones are rarely bigger than 13 – 14 MPa. If strain compatibility is accepted for the reinforcement bars-concrete interface, then stresses in the concrete do not reach 2 MPa, which is a very low value.

It is concluded that the heavily reinforced high strength concrete circular lining works in compression despite the extremely high swelling pressures recorded in some positions. The structure can transform the highly heterogeneous swelling pressure distribution into a ring of small compressive stresses. The steel reinforcement is also under compressive stresses at virtually all measuring points. The magnitude of the stresses is small, very far from yielding conditions.

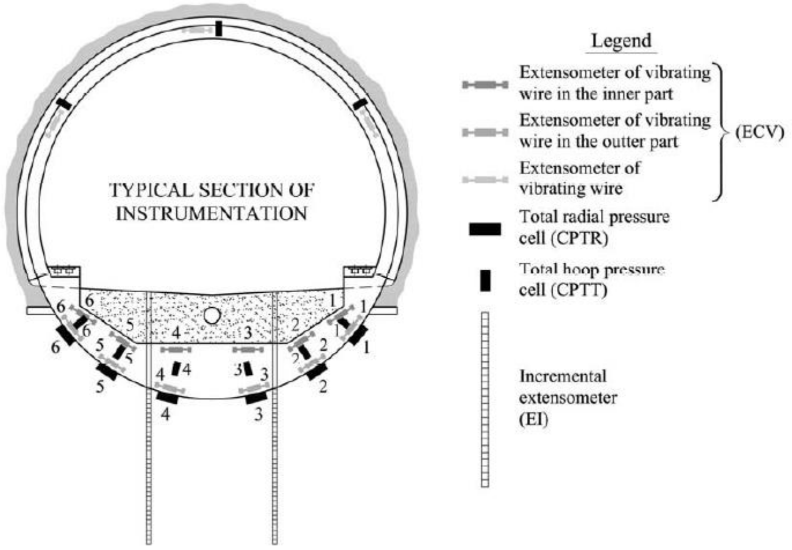
TYPICAL SECTION OF INSTRUMENTATION
Legend
Extensometer of vibrating wire in the inner part
Extensometer of vibrating wire in the outter part
Extensometer of vibrating wire
(ECV)
Total radial pressure cell (CPTR)
Total hoop pressure cell (CPTT)
Incremental extensometer (EI)
1
2
3
4
5
6

Figure 2.35. Typical instrumented section of reinforced tunnel with instruments in vault and invert (Ramon, 2014)

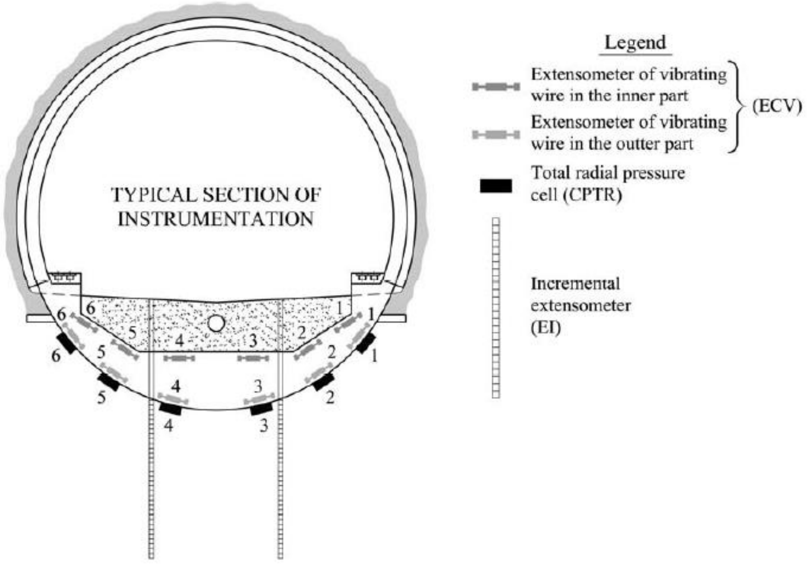
TYPICAL SECTION OF INSTRUMENTATION
Legend
Extensometer of vibrating wire in the inner part
Extensometer of vibrating wire in the outter part
(ECV)
Total radial pressure cell (CPTR)
Incremental extensometer (EI)
1
2
3
4
5
6

Figure 2.36. Typical instrumented section of reinforced tunnel with instruments installed only in invert (Ramon, 2014)

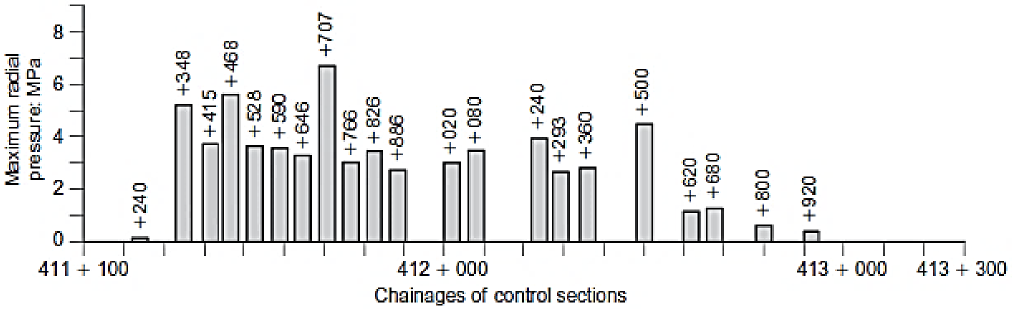

Figure 2.37. Maximum radial pressures recorded from January 2005 to December 2011 (Alonso et al.,2013)

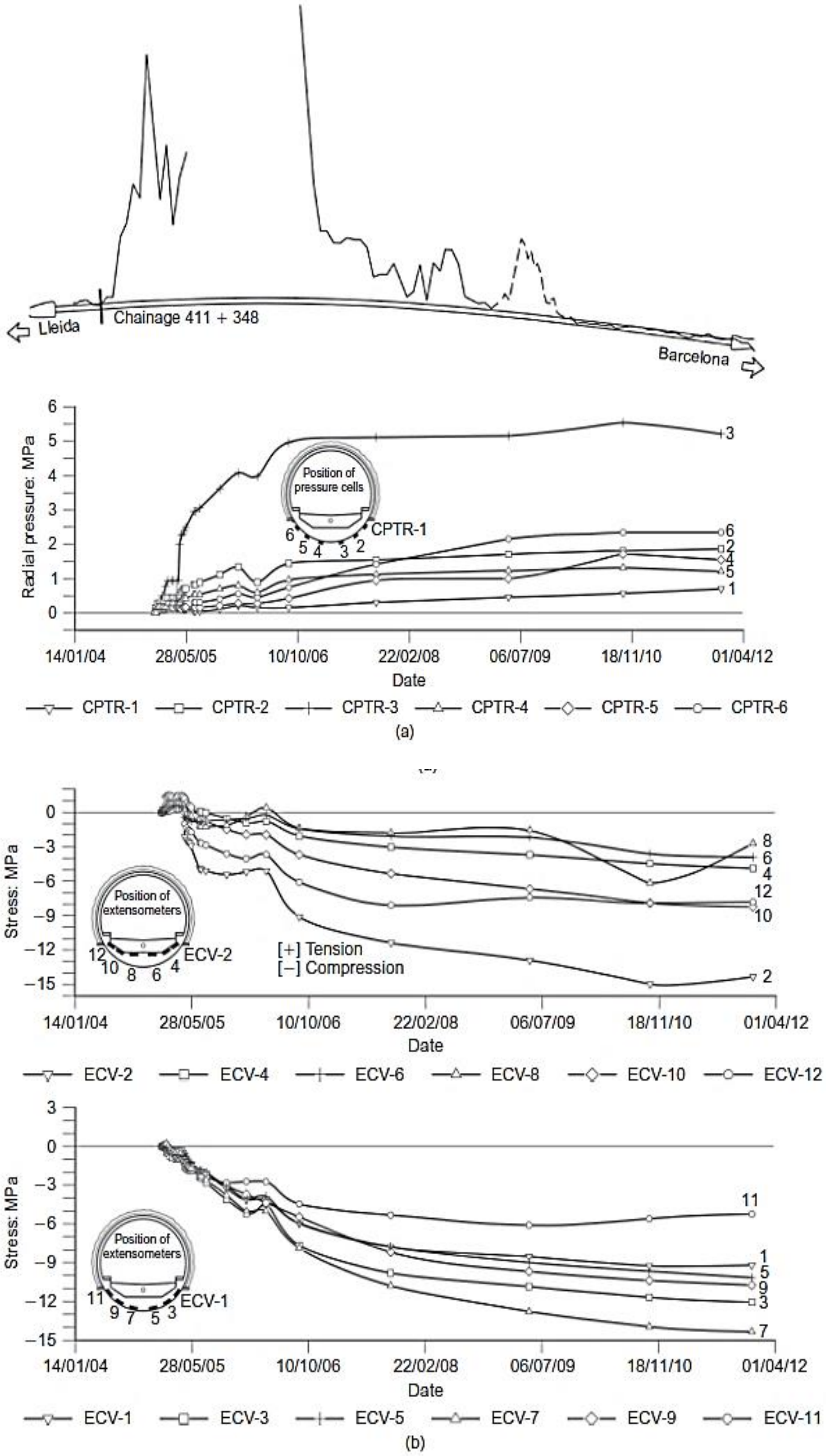

Figure 2.38. Monitoring results for reinforced Lilla tunnel, chainage 411 + 348: (a) pressure cells; (b) stresses in reinforcement. (Alonso et al.,2013)

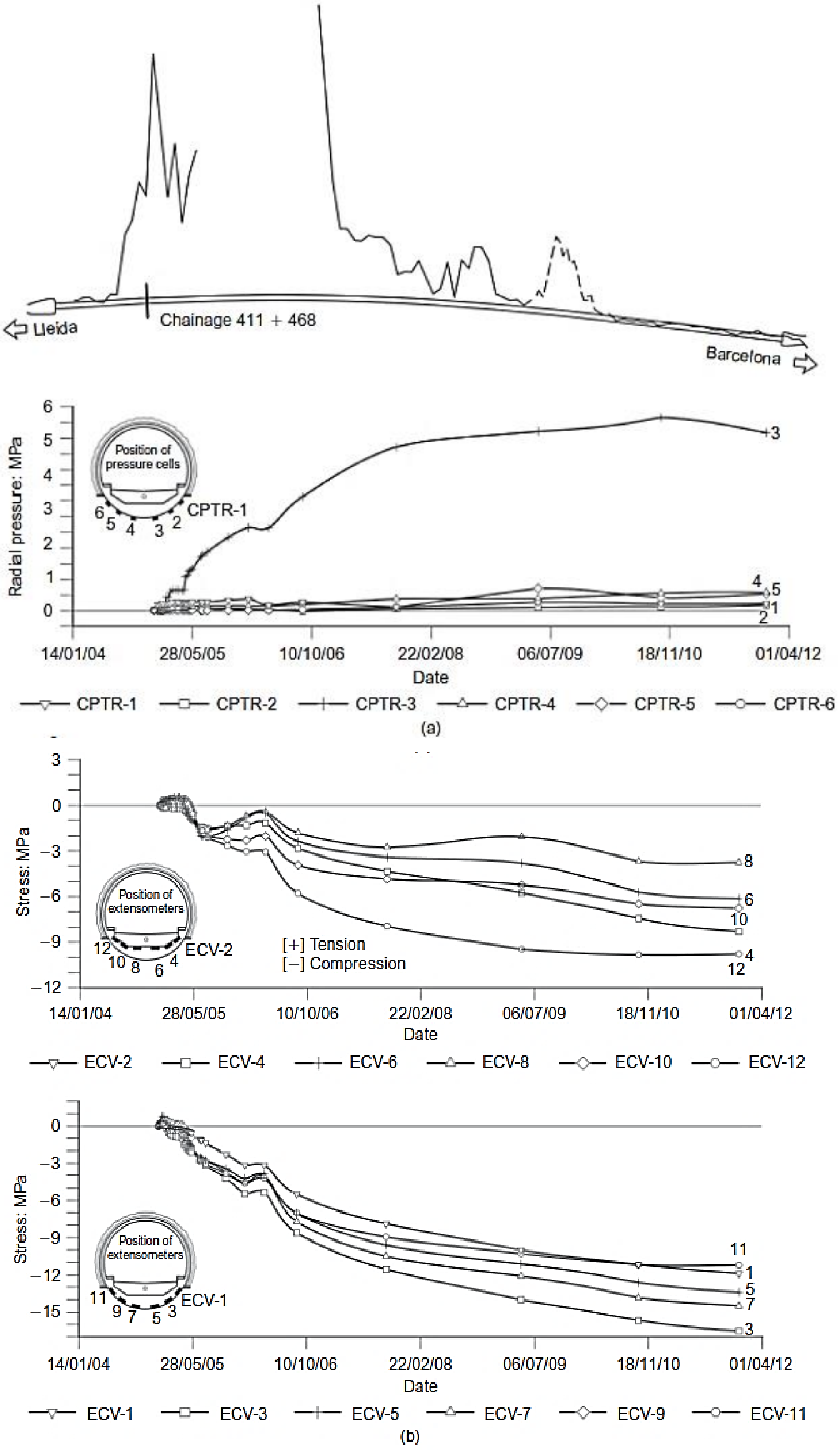

Figure 2.39. Monitoring results for reinforced Lilla tunnel, chainage 411 + 468:(a) pressure cells; (b) stresses in reinforcement. (Alonso et al.,2013)

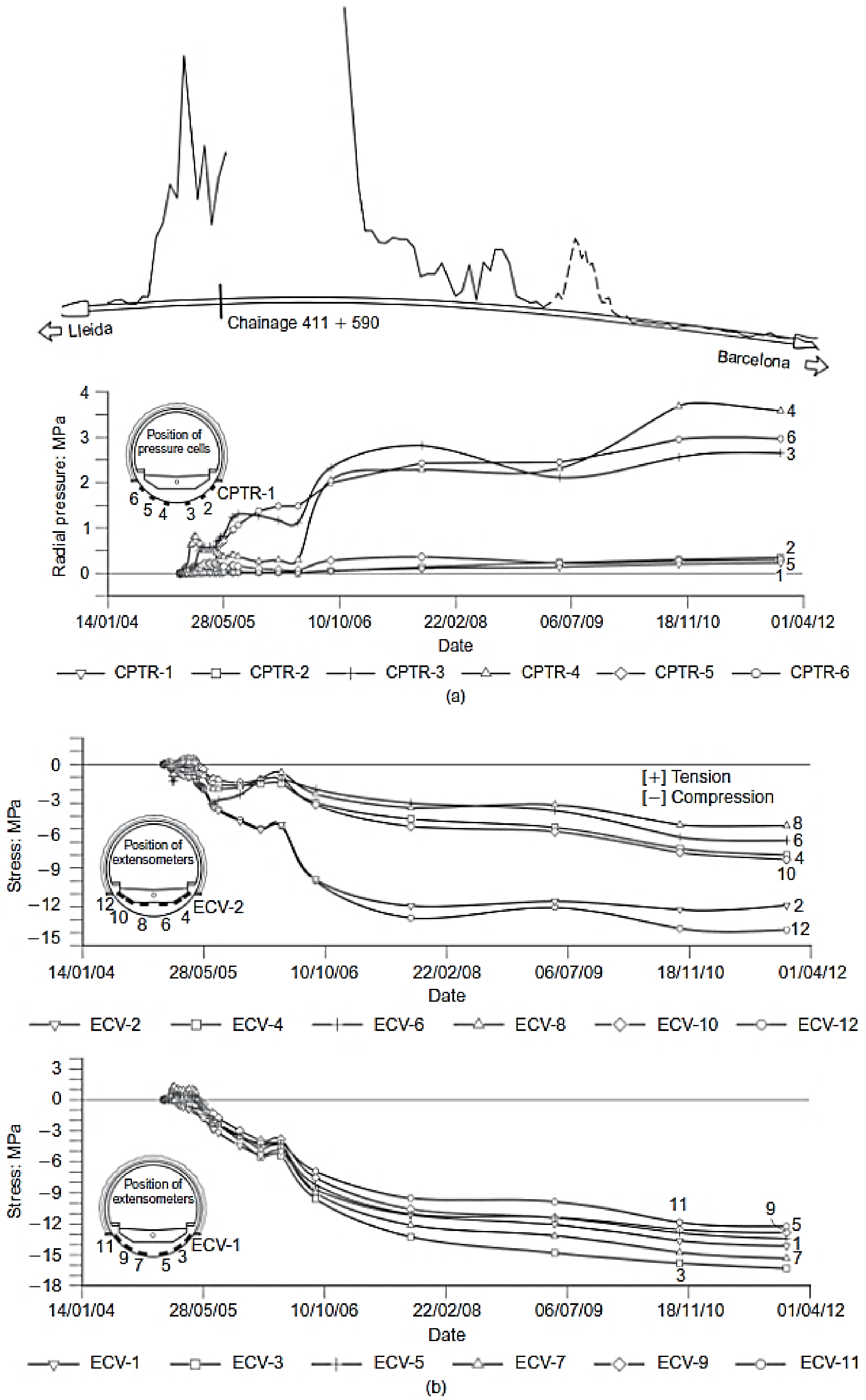

Figure 2.40. Monitoring results for reinforced Lilla tunnel, chainage 411 + 590: (a) pressure cells; (b) stresses in reinforcement. (Alonso et al.,2013)

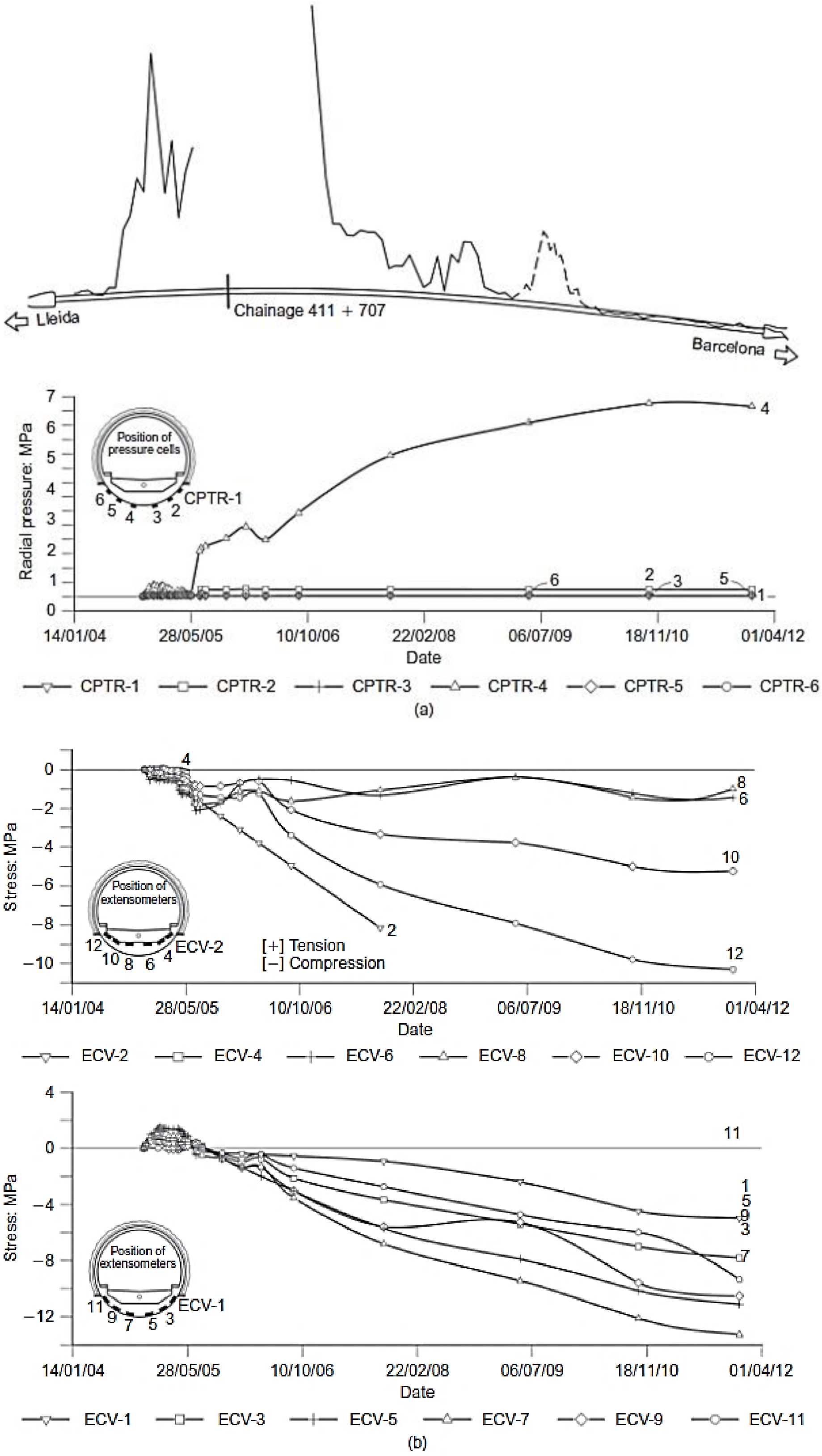

Figure 2.41. Monitoring results for reinforced Lilla tunnel, chainage 411 + 707: (a) pressure cells; (b) stresses in reinforcement. (Alonso et al.,2013)

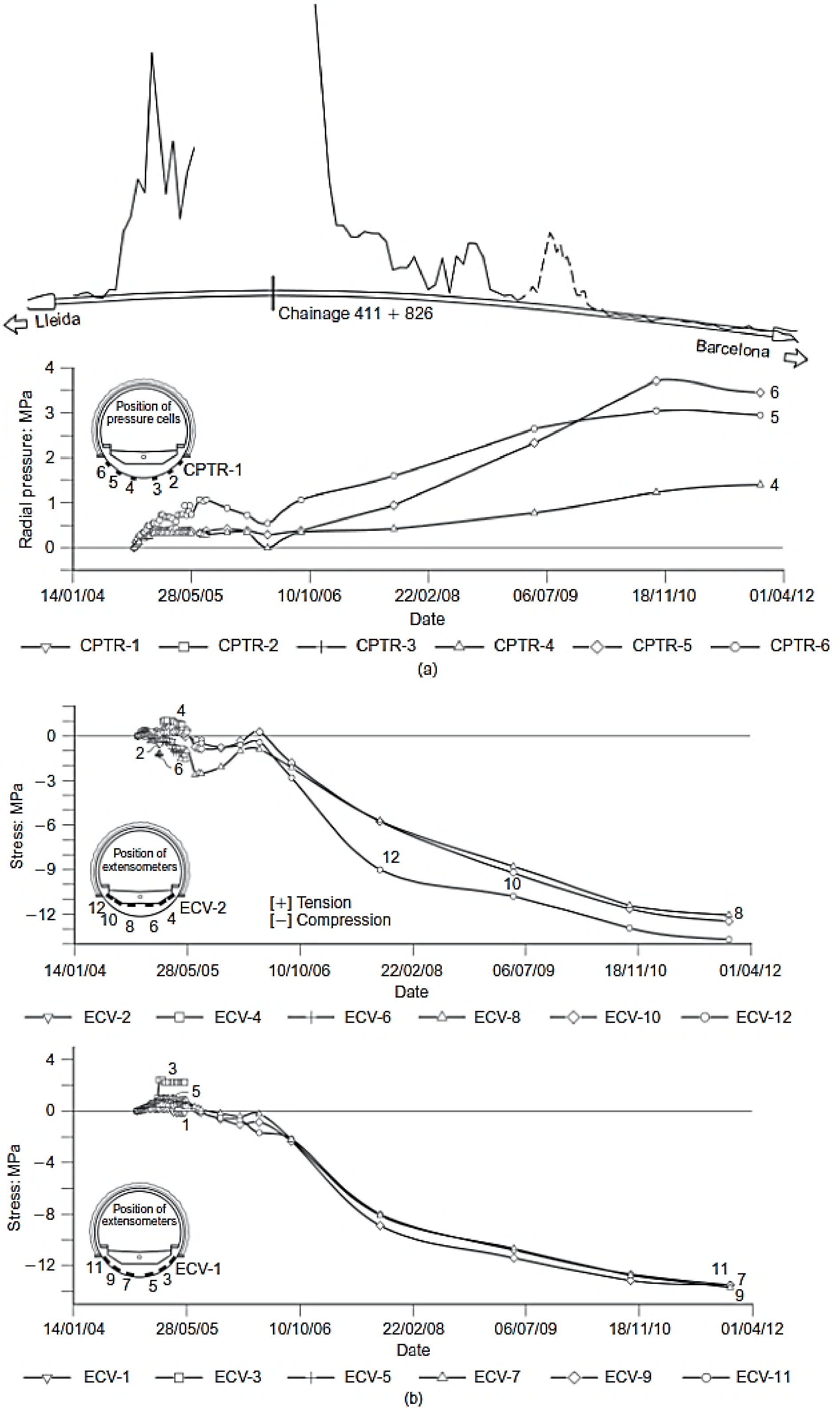

Figure 2.42. Monitoring results for reinforced Lilla tunnel, chainage 411 + 826: (a) pressure cells; (b) stresses in reinforcement. (Alonso et al.,2013)

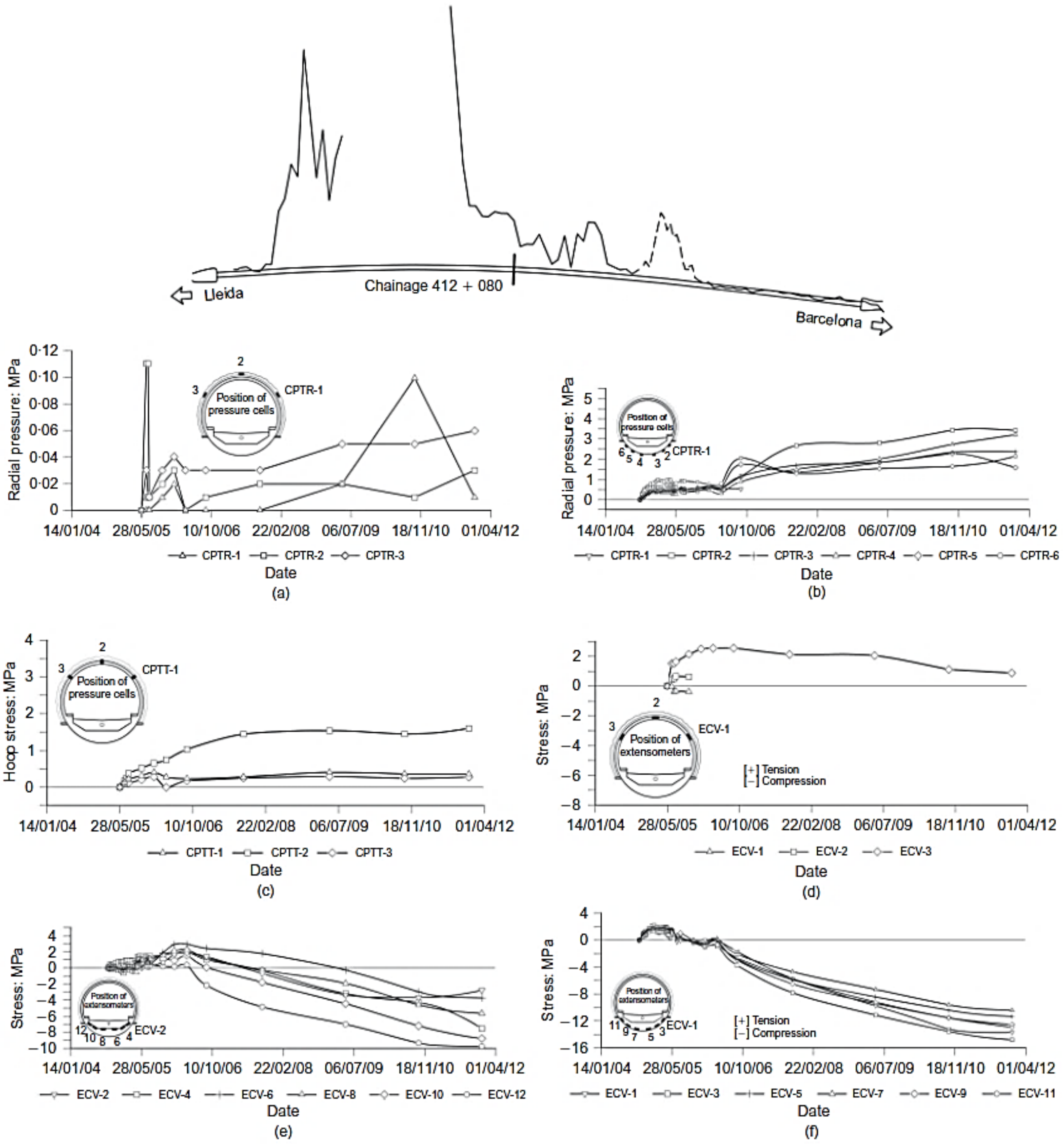

Figure 2.43. Monitoring results for reinforced Lilla tunnel, chainage 412 + 080: (a) radial pressures against vault; (b) radial pressures against invert; (c) hoop stresses in vault; (d) stresses in vault reinforcement; (e), (f) stresses in invert reinforcement. (Alonso et al.,2013)

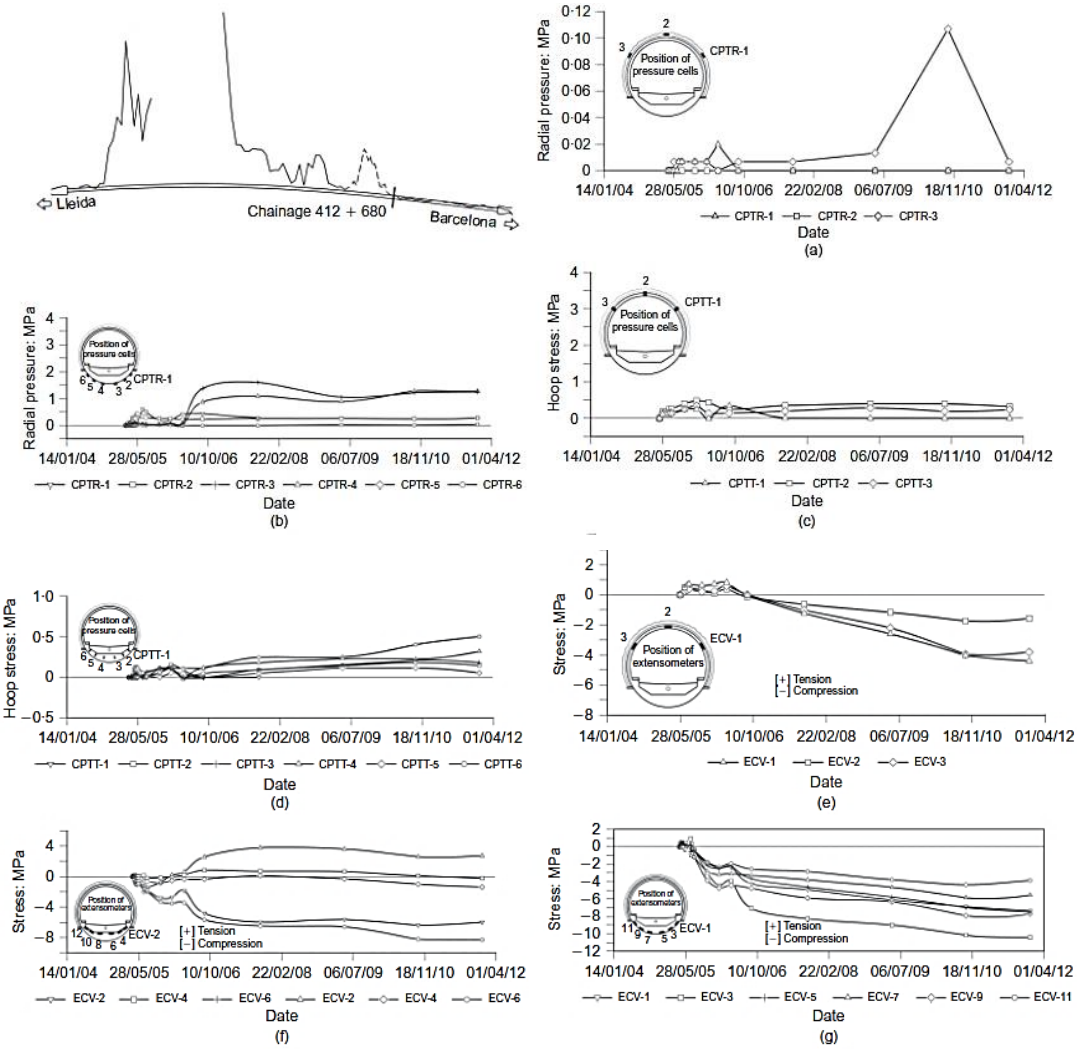

Figure 2.44. Monitoring results for reinforced Lilla tunnel, chainage 412 + 680: (a) radial pressures against vault; (b) radial pressures against invert; (c) hoop stresses in vault; (d) hoop stresses in invert; (e) stresses in vault reinforcement; (f), (g) stresses in invert reinforcement. (Alonso et al.,2013)

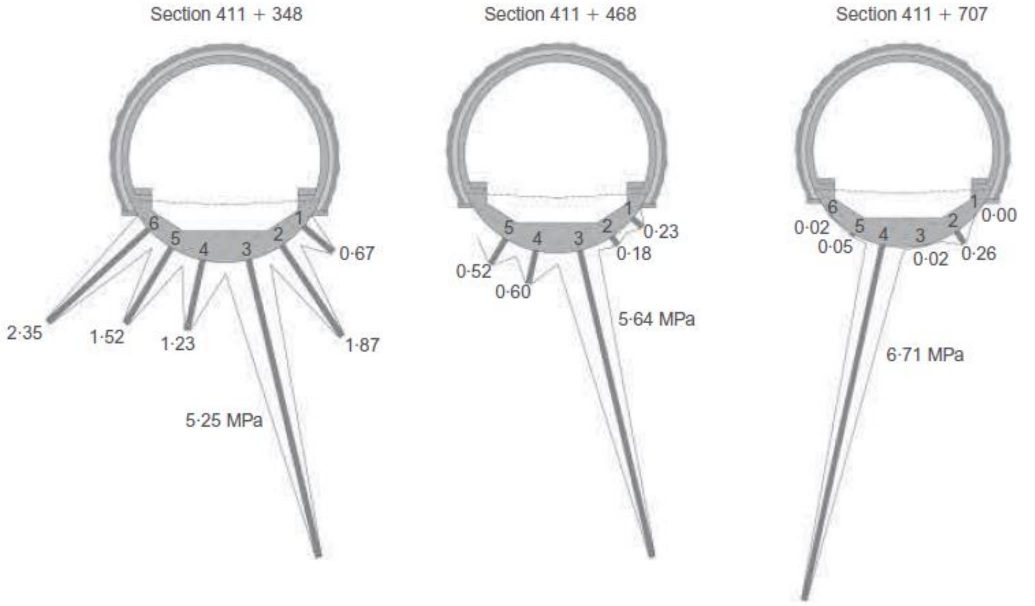
Section 411 + 348
Section 411 + 468
Section 411 + 707
1
2
3
4
5
6
0·67
1·87
5·25 MPa
1·23
1·52
2·35
0·23
0·18
5·64 MPa
0·60
0·52
0·00
0·26
0·02
6·71 MPa
0·05
0·02

Figure 2.45. Measured distributions of radial pressure in the three sections indicated in December 2011 (Alonso et al.,2013)

CHAPTER 3

2D FINITE ELEMENT METHOD ANALYSIS

This chapter describes the two-dimensional formulation developed to reproduce the Lilla tunnel circular lining behaviour and the recorded swelling pressure extreme variability acting on the tunnel invert. The analyses have been performed with the two-dimensional version of the finite element code Plaxis. Many loading distributions have been modelled in the attempt to clarify the swelling pressure trend and the interaction anhydritic rock-circular lining. Reference is made specifically to three benchmark cross sections. Comparisons between estimated stresses from simulations and measured stresses in the reinforcement are used to validate the model.

3.1 Geotechnical model

The geotechnical domain used for all simulations and analysis carried out with PLAXIS, is shown in Figure 3.1. The tunnel centreline is located at a depth of 84 m below the ground surface. It has been considered an average tunnel cover value of the analysed cross sections. As mentioned previously, plane strain conditions have been assumed. This hypothesis can be supported by the suggestion that the length of the tunnel is such that allows for considering the out of plane strains to be equal to zero for reasons of simplicity (Milioritsas, 2015). Therefore, only a vertical cross section perpendicular to the tunnel centreline has been considered for the analyses. No symmetry has been assumed with respect to the vertical plane along the axis of the excavation because of the non-symmetric distribution of swelling pressure.

The rock thickness below the tunnel centreline extends 40m, depth beyond which the boundaries are deemed not to affect significantly the results of the numerical analyses. The boundary conditions adopted for the tunnel analysis of the present thesis are illustrated in Figure 3.1. The bottom boundary has total fixities restraining both horizontal and vertical displacement, whereas the vertical boundaries are free to move in the vertical direction (horizontal displacement is restrained). No fixities were introduced to the upper horizontal boundary of the mesh. The model width is of 100 m. The finite element mesh comprised of 1192 triangular elements (see Figure 3.2).

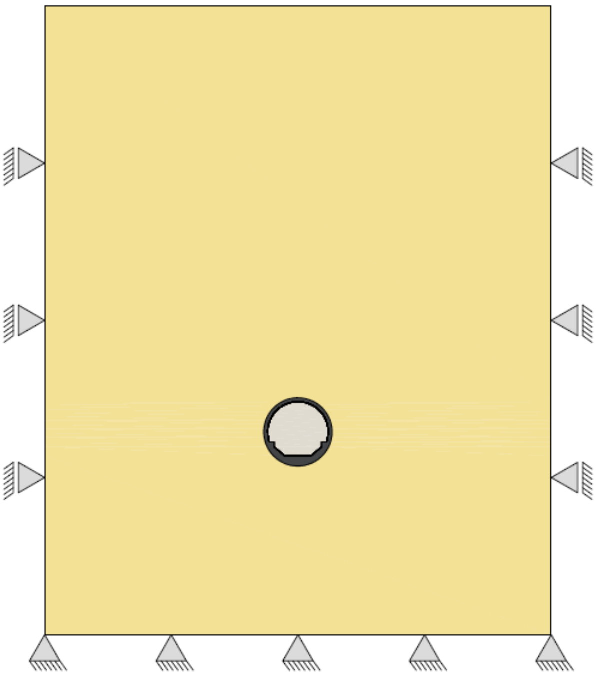

Figure 3.1. Geometry and boundary conditions of the analysis domain

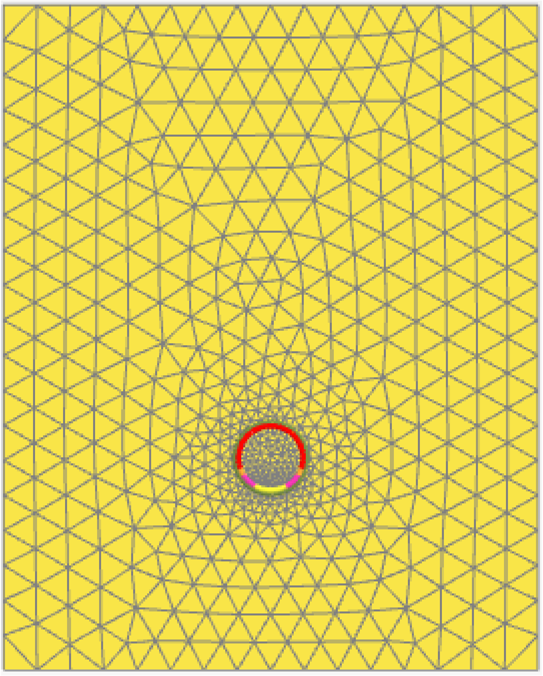

Figure 3.2. Finite element mesh

3.1.1 Soil

For the soil stratigraphy, the borehole tool is used in PLAXIS. Top and bottom height of the different layers can be given, and material properties assigned. The response of the anhydritic rock has been modelled with a Mohr-Coulomb model, which was considered to perform in the best simplest way the material condition. The influence of different constitutive models was not examined, as the present analysis is focused on the lining behaviour and different soil models are not of specific importance. The water level was set at the lower boundary of the domain. Groundwater level was not considered to be representative for the prediction of the expansive behaviour of the rock in this study. Therefore, the excavation is realised under undrained conditions. The claystone matrix parameters are listed in Table 3.1. Soil properties.

Table 3.1. Soil properties

		value	unit
Properties	Solid unit weight	28,5	kN/m^3
	Water content	0,02	
	Porosity	0,06	
	Specific gravity	2,85	

Void ratio	0,064	
Saturated unit weight	27,4	kN/m3
Unsaturated unit weight	27,3	kN/m3

The values indicated in Table 3.1 were selected from the geotechnical characterization results of the rock of Figure 2.17. Geotechnical and mineralogical characterisation of rock at chainage 411+600 (invert arch), and vertical displacements measured by sliding micrometer installed in the axis. (Alonso, E. E. et al.,2013) The specific gravity (Gs) and the water content (w) values were chosen as representative to approximate the rock behaviour in the stable zone, w and Gs are equal to 2.85 and 2% respectively. With these chosen values, the other parameters are calculated consistently. Solid unit weight value was taken from the parameters for the analysis of Lilla tunnel in Ramon's modelling (Ramon, A. et al., 2017). It corresponds to the density of the inert materials in the author's paper.

3.1.2 Mohr-Coulomb model

The Linear Elastic Perfectly Plastic (Mohr Coulomb) model is a simple model and is used to get a first approximation of the soil behaviour. It is a linear elastic perfectly plastic model; thus, no hardening or softening will occur. Hooke's law of isotropic elasticity is the basis for the elastic part and the perfectly plastic one is based on the Mohr-Coulomb failure criterion. Irreversible strains develop with plastic behaviour while, based on the elastic theory, the strains will be reversible during unloading. The boundary between this elastic and plastic behaviour is given by the yield function which is a function of the stress and strain. Since it is a perfectly plastic model, this yield function is fixed and only defined by its model parameters. This means that straining will not affect the yield function. Stress states within the yield function are characterized by elastic and reversible behaviour, whereas plastic behaviour will occur for stress states outside the yield function. The Mohr-Coulomb requires six input parameters, which are:

- E Young's modulus
- ν Poisson's ratio
- c Cohesion
- ϕ Friction angle
- ψ Dilatancy angle
- σ_t Tension cut-off and tensile strength

Mohr–Coulomb strength parameters (cohesion and friction angle) for the rock mass have been calculated with a software program named RocLab. Based upon the generalized Hook & Brown failure criterion the program RocLab performs rapidly the calculations and the empirical equations of the criterion (Bejarbaneh et al., 2015). In addition, RocLab calculates Mohr-Coulomb equivalent stress parameters. The best-fit MohrCoulomb strength envelope is determined over a stress range that the user can define based on the application (i.e. tunnelling or slope stability).

To compute the Generalised Hoek–Brown strength parameters of a rock mass in RocLab software four input parameters are required:

- σ_{ci} = uniaxial compressive strength of the intact rock
- mi = intact rock parameter
- GSI = Geological Strength Index (0–100).
- D = rock mass disturbance factor (0–1).

The uniaxial compressive strength of the rock was estimated from the physical and mechanical indices of the Lilla claystone presents in the Alonso et al. analysis (2013). The average value in the article unconfined compressive strength range was chosen.

Concerning the intact rock parameter, RocLab allows the user to determine a suitable value of *mi* by selecting one of the proposed values. Ranges of values for different rock type and mineralogical composition are given in the program. The prevalent mineral component of Lilla rock is clay, therefore the RocLab default mi parameter for claystone was chosen (*mi* = 4). As for the Geological strength index, a value of 46 was considered appropriate to represent the blocky slickenside claystone. The excavation was carried out to result in a minimal disturbance to the surrounding rocks. Hence, the disturbance factor was taken as zero. The Generalised Hoek–Brown strength parameters are resumed in Table 3.2.

Table 3.2. Generalised Hoek–Brown strength parameters

		value	unit
Properties	uniaxial compressive strength	93	MPa
	mi	4	
	Geological Strength Index	46	
	rock mass disturbance factor	0	

The Mohr-Coulomb cohesion and friction angles parameters are determined from the aforementioned range of values and are defined based on a tunnelling application, which require a further information: the values of the rock unit weight (27,3 kN/m3) and the tunnel depth (81 m). The values provided by Roclab are respectively 44,05° for the friction angle and 875 kPa for the cohesion. Eventually, a lower value of cohesion was adopted to account for disturbance around the tunnel. The dilatancy angle of Lilla claystone is zero. The entered value for the tensile strength is zero. The Young's modulus and Poisson's ratio values are considered to be valid the parameters showed in the paper *Hydro-chemo-mechanical modelling of tunnels in sulphated rocks* (Ramon et al., 2017).

Table 3.3. Mohr-Coulomb parameters

		value	unit
Properties	Young's modulus	1000	MPa
	Poisson's ratio	0,02	
	Cohesion	300	kPa
	Friction angle	44,05	°
	Dilatancy angle	0	°
	Tension cut-off and tensile strength	0	kN/m^2

3.2 Tunnel geometry and lining properties

Modelling the tunnel is done through the tunnel designer tool in PLAXIS. In this tool a circle representing the tunnel of internal radius of 6m is created from the composition of arcs as input. The subdivision of the tunnel cross-section into different arcs is explained by the need of having different lining discretization, which at the same time represent the different thickness of the resisting support and a tool to impose loads on segments (see Figure 3.3. Definition of tunnel subdivisions).

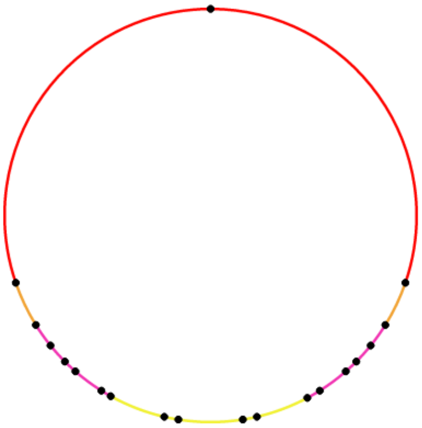

Figure 3.3. Definition of tunnel subdivisions

A tunnel shape consists of a tunnel cross-sections, composed by arc and lines, optionally supplied by linings (plate), interface, loads etc. (PLAXIS 2D, 2017). Plates are structural objects used to model slender structures in the ground with a significant flexural rigidity and a normal stiffness. Hence, plates are used to simulate the influence of linings. Each of the arcs of the tunnel subdivision is a plate. The plate material type is elastic and isotropic. Such elastic behaviour in plain strain conditions is defined by the axial stiffness EA and the flexural rigidity EI. They both are stiffnesses per unit width in the out-of-plane direction. Moreover, a plate has in general two main properties: the equivalent thickness d (in the unit of length), which is automatically calculated from the stiffnesses, and the plate specific weight w (force per unit length per unit width in the out-of-plane direction). It is evident from Figure 2.34 that Lilla tunnel resisting support has different thickness. With this regard, different stiffnesses have been specified for the tunnel cross-section subdivisions. Figure 3.4 shows the comparison between the virtual tunnel ring inserted in the model and the real correspondent thickness of the support. The entered parameters for the different plates are illustrated in Table 3.4.

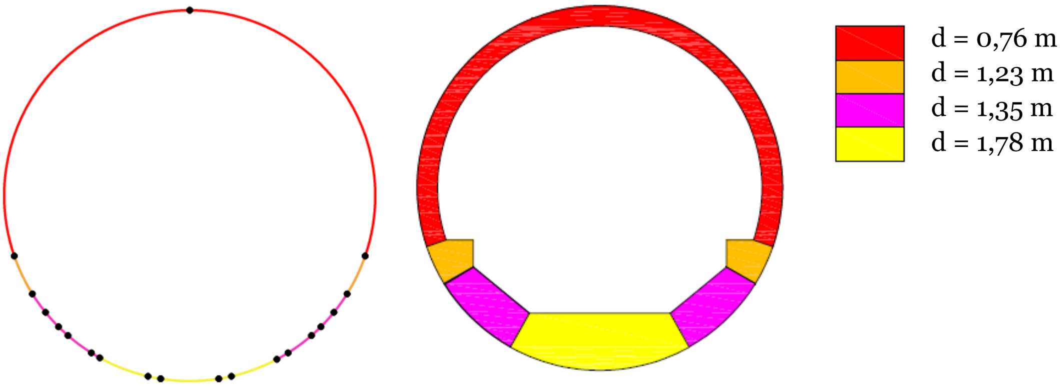

Figure 3.4. Comparison between model and real lining (*d* is the thickness of the lining segment measured in m)

The axial stiffness and the flexural rigidity have been deducted from the Young's modulus of the high strength concrete selected for the circular resisting support of the Lilla tunnel. Approximate values for the modulus of elasticity are given in the Eurocode 2 (EN 1992-1-1, 2004). For a characteristic strength of concrete fck of 80 MPa, the correspondent modulus of elasticity is 42 GPa. Moreover, it is noted that the cross-sectional area (*A*) of the lining per meter out of plane, for plane strain conditions, is equal to its thickness. The introduction of specific weight of the material is done through entering a force per unit length per unit width. For relatively massive structures, the weight of the plate is obtained by multiplying the unit weight of the plate material by the thickness of the plate. (PLAXIS 2D, 2017). The unit weight of concrete has been considered as 25 kN/m^3. Table 3.4 shows the input values that have been used for each plate.

Table 3.4. Plates parameters

Properties	value				unit
d	0,76	1,23	1,35	1,78	m
EA axial stiffness	31,9 10^6	51,6 10^6	56,7 10^6	75,1 10^6	kN/m
EI flexural rigidity	1,54 10^6	6,51 10^6	8,6 10^6	19,9 10^6	kNm^2/m

	w	19	30,75	33,75	44,66	kN/m^2
	Poisson's ratio	0,15	0,15	0,15	0,15	

From the tunnel ring, negative interfaces are created. The interfaces are elements to be added to the plates for a proper modelling of soil-structure interaction. A negative interface is assigned to each line defining the shape of the tunnel (see Figure 3.5). Note that the interface is negative because it appears at the external side of the geometry line to enable the interaction between the plate lining and the surrounding soil. According to PLAXIS Reference Manual, for real soil-structure interaction the interface is weaker and more flexible than the surrounding soil.

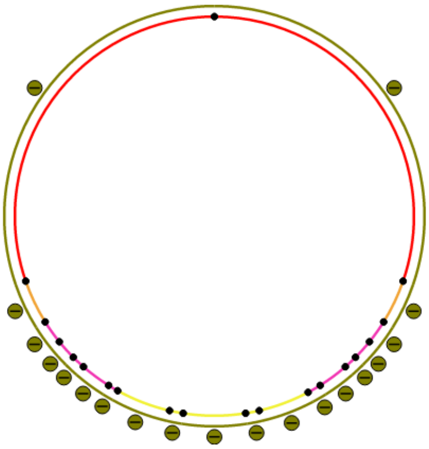

Figure 3.5. Definition of tunnel subdivision with negative interfaces

3.3 Calculation phases

The modelling technique of the several aspects of the tunnel construction process and the consequent swelling loading application is based on a stage construction calculation. The calculation procedure comprises five steps:

1) The K_0 procedure, in which the initial stress field is generated. The initial stresses in a soil body are influenced by the weight of the material and the history of the formation. This stress state is usually characterized by an initial vertical effective stress. The initial horizontal effective stress is related to the initial vertical effective stress by the coefficient of lateral earth pressure K_0. The value of K_0 specified was taken according to Ramon's article (Ramon et al., 2017). A value $K_0=2$ was adopted in view of the intense tectonism in the area. Note once again that water is not considered in this simulation. The general phreatic level should remain at the model base (see Figure 3.6).

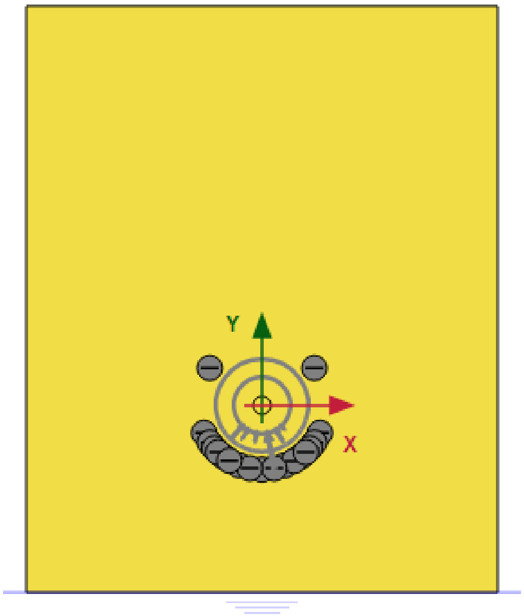

Figure 3.6. K0 procedure phase

2) The excavation phase, in which the soil cluster inside the tunnel is deactivated. The most popular method to simulate installation procedures would seem to be the so called Converge confinement method, often referred to as the β-method. The stress relaxation of the ground due to the delayed installation of the shotcrete lining and the load sharing between ground and lining are addressed by this method. Starting from the initial geostatic stresses the stress reduction method comprises two calculation phases. In the first calculation phase the tunnel and the initial ground pressure p_0, which is acting on the inside of the tunnel, is reduced to β p_0, with $0 < \beta < 1$. β is the load reduction factor. In the second calculation phase the lining is installed and the remaining load β p_0 is divided over the lining and the ground. To sum up, the idea is that the initial stresses p_0 acting around the location where the tunnel is to be constructed are divided into a part (1- β) p_0 that is applied to the unsupported tunnel and a part β p_0 that is applied to the supported tunnel. To apply this in PLAXIS one can use the staged construction option with a reduced ultimate level of **Σ**Mstage. Applying a determined value for **Σ**Mstage correspond to a β value of 1-**Σ**Mstage. However, in this thesis the excavation is simulated in a single step. The **Σ**Mstage correspondent to the tunnel excavation is set to 1. This is due to the aim of the present work: the focus of the analysis is the understanding of the claystone swelling behaviour in terms of pressure against the lining. It is noteworthy to remark that the last distribution of radial pressure acting on the circular cross sections was captured in December 2011, 8 years after the tunnel construction. With this regard, it is

acceptable to consider the tunnel as a continuous and existent excavation. As a matter of fact, the conventional tunnelling method (NATM) does not affect the interaction between ground and lining 8 years after its construction (see Figure 3.7).

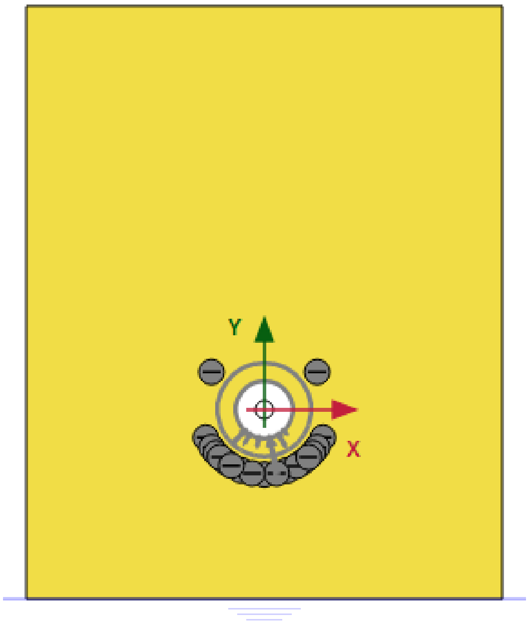

Figure 3.7. Excavation phase

3) The lining application phase, which consist in both the tunnel lining plate and the negative interface activation. Note that the soil cluster inside the tunnel is deactivated and the tunnel plate get coloured (see Figure 3.8).

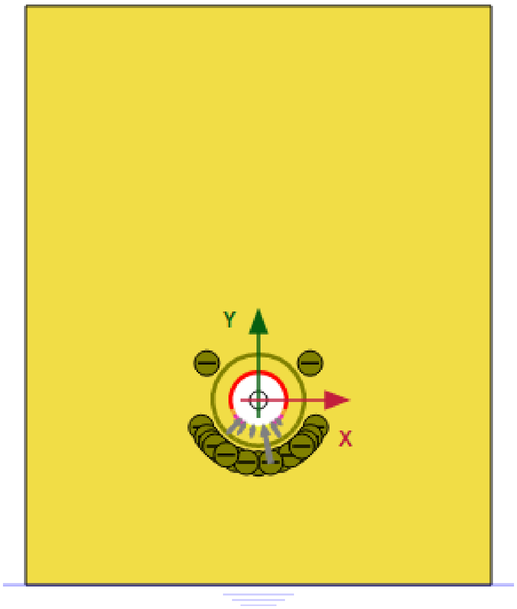

Figure 3.8. Tunnel construction phase

4) The swelling pressure imposition phase. Within the circumstances explained in the previous chapter, this thesis tries to reproduce the heterogeneous swelling pressure distribution recorded in the six loading cells installed in the invert at different cross sections along the Lilla tunnel. In PLAXIS, this step is simply reached by activating the loads. More specifics on this step are given in the following paragraphs.

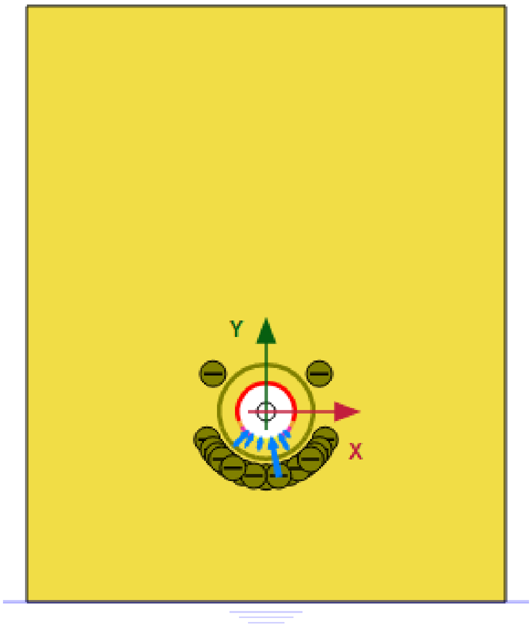

Figure 3.9. Swelling pressure application phase

3.4 Swelling pressure distribution

As mentioned previously, the recorded pressure extreme variability and the ground behaviour modelling is the focus of the present work. The key point is that six loading cells measurements cannot provide a continuous or reliable distribution of radial pressures acting on the invert. Hence, starting from the pressure records measured in sections at chainages 411 + 348, 411 + 468 and 411 + 707, various possible distribution and combination of load are considered to get better knowledge of the material response in general, and its interaction against the circular lining, especially between the pressure cells measurements, where we have no information by now. To prove the reality of the modelled behaviour, comparison will be made with the measured stress in reinforcement. Ramon and Alonso studies already proved that the high-strength concrete circular lining works in compression, despite the extremely high swelling pressures recorded in some positions. The circular lining can transform the heterogeneous swelling pressure distribution into a ring of compressive stresses. Furthermore, also the steel reinforcement is under compressive stresses at all measuring points (Alonso et al., 2013). Five different swelling pressure distributions are analysed, each one tested on the three sections (sections at chainages 411 + 348, 411 + 468 and 411 + 707) where the most discontinuous distribution was captured by the instrumentation in December 2011.

Each of the five above mentioned possible distributions of swelling pressures is implemented in PLAXIS as an external load acting on the invert of the tunnel lining. The loads' action is activated in the fourth step of the staged calculation, once the tunnel excavation is done and the lining cast in place. As a result of the four phases calculation bending moment, axial force and shear develop in the ring lining. It is noteworthy to emphasize that for the purpose of the present work, just axial forces and bending moments will be taken into consideration in the sectional analysis. Longitudinal reinforcement bars will be considered without influence of shear effect. The internal forces are calculated in stress points of the plate element (PLAXIS 2D, 2017). Stress points (or Gauss points) are the points involved in the numerical integration performed by the software. The key point of the formulation is that axial forces and bending moments calculated by PLAXIS in stress points of the circular lining plate element are assumed to act in equivalent rectangular cross sections, virtually situated in points having the same position of the reinforcement bar measuring device. The six stress points considered for the calculations and consistent with the extensometers position are illustrated in Figure 3.10. Hence, bending moment and axial force computed by the program would provide the stress state of the reinforcement bars of a generic rectangular cross-section, which can be compared to the monitored results for the reinforced Lilla tunnel. The situation is graphically explained in Figure 3.10. In particular, the measured stresses in the vault reinforcement of the three mentioned cross sections which will be used as benchmarks are illustrated in Figure 3.12, Figure 3.13 and Figure 3.14. They provide a graphical summary of the plots in Figure 2.38, Figure 2.39 and Figure 2.41. Concerning the concrete stress comparison, cross sections at chainages 411 + 348, 411 + 468 and 411 + 707 were not instrumented with pressure cells measuring hoop stresses in concrete. For that reason, values of field concrete stresses will be calculated multiplying the higher steel stress in the same section by the ratio of the rigidity moduli of steel and concrete. These comparisons would lead to the conclusion that either or not the imposed swelling pressure reproduce the field data.

Through a sectional analysis, stresses in the longitudinal reinforcement (longitudinal direction of the tunnel) bars are obtained from the coupling of the internal forces M and N. Several hypotheses are considered for the analysis:

- concrete and steel behaviours are linear elastic according to Hooke's law
- the contribution of tensioned concrete is neglected
- compatibility of deformations is accepted for interfaces between concrete and steel

- a plane cross section remains plane and perpendicular to the neutral axis after deformations

Referring to Figure 3.11, the following relationship holds:

$$\varepsilon(y) = \ {}^{1}\!/_{r}\,(y - y_n) \qquad \text{Eq. 3.1}$$

Where y is a generic ordinate value, considering a system where the y-axis is zero in the upper fibre and it increases going down the section height, and ${}^{1}\!/_{r}$ the radius of curvature.

The parameter y_n is the neutral axis value, which is an unknow of the problem. Its value is different for every cross section, as it depends on the internal forces acting on that section. The neutral axis resolution formula will be found later in the study with the development of the mathematical expressions. The constitutive equations are:

$$\sigma_s = E_s\varepsilon_s = \ E_s\ {}^{1}\!/_{r}\,(y - y_n)$$

$$\begin{cases} \sigma_c = E_c\varepsilon_c = E_c\ {}^{1}\!/_{r}\,(y - y_n) & \varepsilon_c \geq 0 \\ \sigma_c = 0 & \varepsilon_c < 0 \end{cases} \qquad \text{Eq. 3.2}$$

Stresses in concrete and steel are denoted as σ_c and σ_s respectively and the correspondent Young's moduli are E_c, which takes the value of 42 GPa, and E_s, that is 210 GPa. Parameters referring to the section are the height h and the width b while d and d' are the effectives depths from the top of the reinforced concrete section to the centroid of the lower and upper steel reinforcement, respectively. Steel areas is expressed by A_s (lower reinforcement area) and $A_{s'}$(upper reinforcement area). All numerical values are illustrated in Table 3.5. N and M symbols refer to axial force and bending moment, whose values vary depending on the six stress points and three reference cross sections considered. Their values will be showed together with the results of the analyses. By mathematical equations, the equilibrium in the horizontal axis is given by:

$$\int_0^{y_n} E_c\ {}^{1}\!/_{r}\,(y - y_n)\,b(y)dy + E_s\,{}^{1}\!/_{r}\,(d - y_n)A_s + E_s\,{}^{1}\!/_{r}\,(d' - y_n)A_{s'} = N \qquad \text{Eq. 3.3}$$

Whereas the rotational equilibrium around the neutral axis is:

$$\begin{aligned} &\int_0^{y_n} E_c\ {}^{1}\!/_{r}\,(y - y_n)^2\,b(y)dy + E_s\,{}^{1}\!/_{r}\,(d - y_n)^2A_s + E_s\,{}^{1}\!/_{r}\,(d' - y_n)^2A_{s'} \\ &\qquad = \mathrm{M} - N(y_{sup} - y_n) \end{aligned} \qquad \text{Eq. 3.4}$$

Where y_{sup} is the effective depth from the top of the section to the centroid of the concrete area, which in the case of rectangular cross section it corresponds to ${}^{h}\!/_{5}$. Its value will vary depending on the height of the section considered. Dividing the Eq. 3.3 by E_c and putting ${}^{1}\!/_{r}$ out of the integral, the relation becomes:

$$1/_{r}\int_{0}^{y_n}(y-y_n)\,b(y)dy+{}^{E_s}/_{E_c}\,1/_{r}\,(d-y_n)A_s+{}^{E_s}/_{E_c}\,1/_{r}\,(d'-y_n)A_{s'}={}^{\mathrm{N}}/_{E_c}\qquad\text{Eq. 3.6}$$

Where $n={}^{E_s}/_{E_c}=5$ is so called modular ratio, the integral term is the static moment of the compressed area with respect to the neutral axis ($S_{cy_n}=\int_0^{y_n}(y-y_n)\,b(y)dy$) and the other two terms are respectively the static moments of the steel areas with respect to the neutral axis ($S_{sy_n}=(d-y_n)A_s$ and $S_{s'y_n}=(d'-y_n)A_{s'}$) multiplied by the factors n and $1/_{r}$. The same reasoning path can be carried out for Eq 3.4 and the correspondent inertia moment are found. Inertia moment of compressed area with respect to normal axis is $I_{cy_n}=\int_0^{y_n}(y-y_n)^2\,b(y)dy$, while inertia moments of lower and upper steel areas are $I_{sy_n}=(d-y_n)^2A_s$and $I_{s'y_n}=(d'-y_n)^2A_{s'}$ The final system of equations results is:

$$\begin{cases}1/_{r}\;[S_{cy_n}+n\,(S_{sy_n}+\;S_{s'y_n})]={}^{\mathrm{N}}/_{E_c} & \text{Eq. 3.7}\\ 1/_{r}\;[I_{cy_n}+n\,(I_{sy_n}+\;I_{s'y_n})]={}^{\mathrm{M}-N(y_{sup}-y_n)}/_{E_c} & \text{Eq. 3.8}\end{cases}$$

If $S_{y_n}=S_{cy_n}+n\,(S_{sy_n}+\;S_{s'y_n})$ and $I_{y_n}=I_{cy_n}+n\,(I_{sy_n}+\;I_{s'y_n})$ then the following simple relationships hold:

$$\begin{cases}1/_{r}\,S_{y_n}\,E_c=N & \text{Eq. 3.9}\\ 1/_{r}\,I_{y_n}\,E_c=\mathrm{M}-N(y_{sup}-y_n) & \text{Eq. 3.10}\end{cases}$$

The system results in a single implicit equation which is represented by:

$$^{I_{y_n}}/_{S_{y_n}}=e+\;y_{\mathrm{sup}}+\;y_n\qquad\text{Eq. 3.11}$$

In the case of rectangular cross section, Eq. 3.10 becomes:

$$\frac{bh^3/_3+nA_s\cdot[(d-y_n)^2+\beta(d'-y_n)^2]}{-by_n{}^2/_2+A_s\cdot[(d-y_n)+\beta(d'-y_n)]}=e+\;{}^{h}/_{2}+\;y_n\qquad\text{Eq. 3.12}$$

Note that $\boldsymbol{\beta}$ is the ratio ${}^{A_{s'}}/_{A_s}$. In the present work analysis, the upper and lower reinforcement bars are the same so that the value of $\boldsymbol{\beta}$ is equal to one. The e represents the eccentricity it is the ratio ${}^{\mathrm{M}}/_{\mathrm{N}}$. Finally, the stresses in the reinforcement steel bars and in the concrete can be estimated with:

$$\begin{cases}\sigma_c={}^{\mathrm{M}-N(y_n-y_{\mathrm{sup}})}/_{I_{y_n}}\,(y_{\mathrm{sup}}-y_n) & \text{Eq. 3.13}\\ \sigma_s={}^{\mathrm{M}-N(y_n-y_{\mathrm{sup}})}/_{I_{y_n}}\,(d-y_n) & \text{Eq. 3.14}\\ \sigma_{s'}={}^{\mathrm{M}-N(y_n-y_{\mathrm{sup}})}/_{I_{y_n}}\,(d'-y_n) & \text{Eq. 3.15}\end{cases}$$

The comparison between calculated stresses and field data will be assesed in the following paragraphs, especifically for every different load ditribution considered.

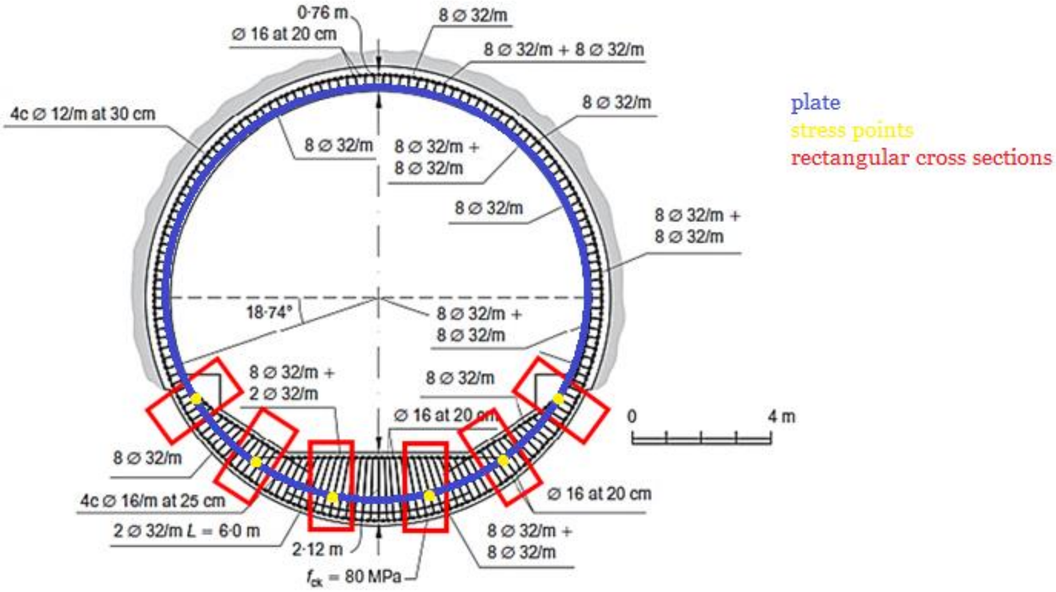
0·76 m
∅ 16 at 20 cm
8 ∅ 32/m
8 ∅ 32/m + 8 ∅ 32/m
4c ∅ 12/m at 30 cm
8 ∅ 32/m
8 ∅ 32/m
8 ∅ 32/m +
8 ∅ 32/m
8 ∅ 32/m
8 ∅ 32/m +
8 ∅ 32/m
18·74°
8 ∅ 32/m +
8 ∅ 32/m
8 ∅ 32/m +
2 ∅ 32/m
8 ∅ 32/m
∅ 16 at 20 cm
0
4 m
8 ∅ 32/m
∅ 16 at 20 cm
4c ∅ 16/m at 25 cm
2 ∅ 32/m L = 6·0 m
2·12 m
8 ∅ 32/m +
8 ∅ 32/m
f_ck = 80 MPa
plate
stress points
rectangular cross sections

Figure 3.10. Internal forces acting on stress points in the plate are imposed on rectangular cross-section in the same positions

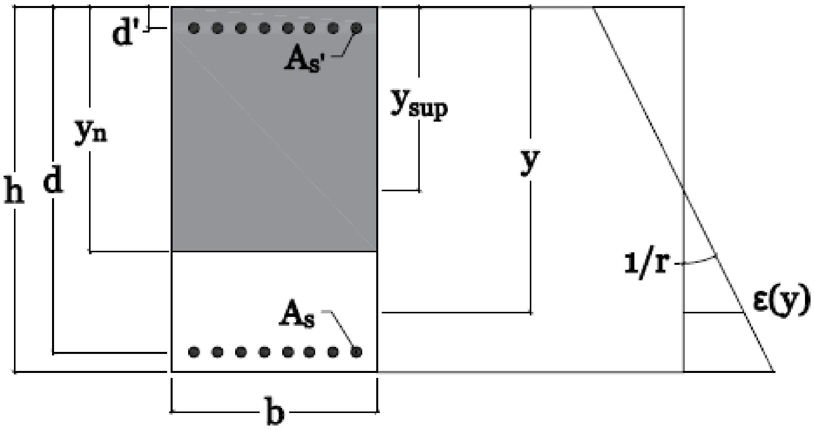
d'
As'
ysup
yn
h
d
y
1/r
ε(y)
As
b

Figure 3.11. Rectangular cross-section properties

Concerning the cross-section dimensional values, three different height values have been considered corresponding to the different lining invert thickness. In Table 3.5 general cross-sections dimensional properties are presented. Note that, considering a one-meter width section, both the upper and the lower reinforcements are composed by eight bars of 32mm as diameter. All six sections have been considered to have the same quantity of reinforcement bars.

Table 3.5. Cross-sections dimensional values

		value			unit
Properties	h	1,23	1,35	1,78	m
	b	1	1	1	m
	d	1,18	1,35	1,73	m
	d’	0,05	0,05	0,05	m
	A_s	0,0064	0,0064	0,0064	m^2
	$A_{s'}$	0,0064	0,0064	0,0064	m^2

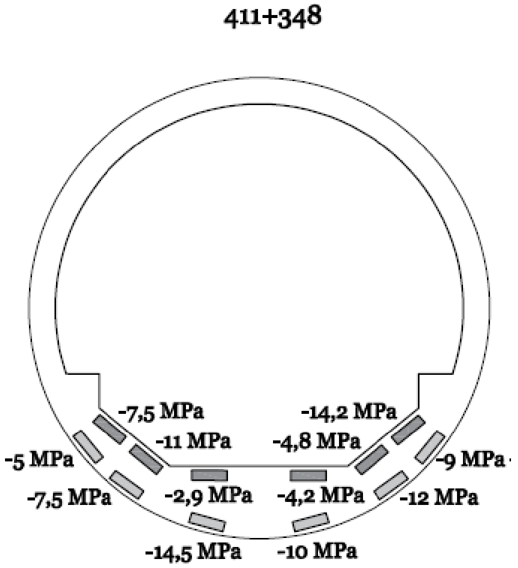
411+348
-7,5 MPa
-14,2 MPa
-11 MPa
-4,8 MPa
-5 MPa
-9 MPa
-7,5 MPa
-2,9 MPa
-4,2 MPa
-12 MPa
-14,5 MPa
-10 MPa

Figure 3.12. Measured stresses in invert reinforcement at chainage 411+348

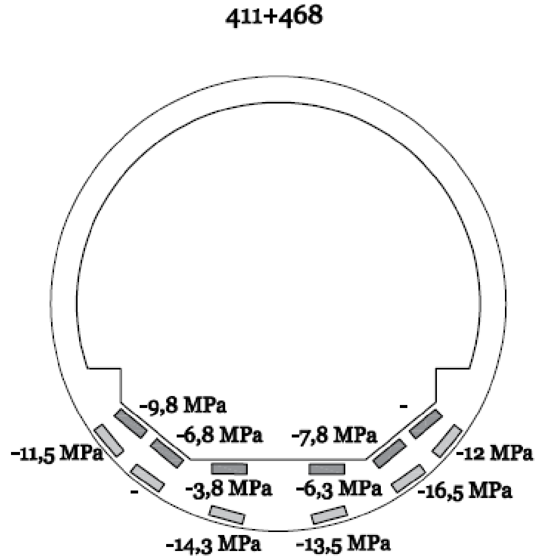
411+468
-9,8 MPa
-
-6,8 MPa
-7,8 MPa
-11,5 MPa
-12 MPa
-
-3,8 MPa
-6,3 MPa
-16,5 MPa
-14,3 MPa
-13,5 MPa

Figure 3.13. Measured stresses in invert reinforcement at chainage 411+468

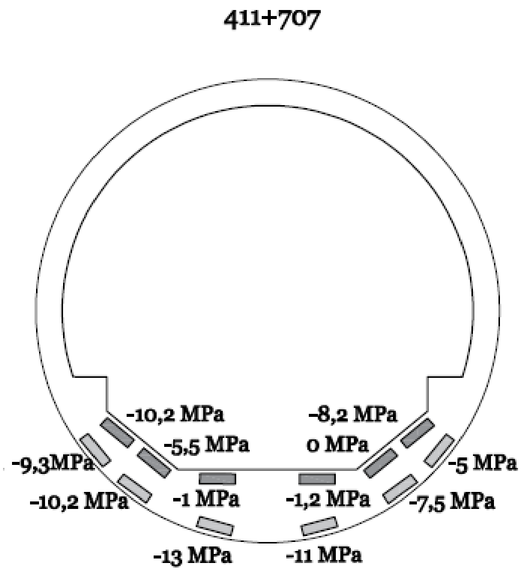

Figure 3.14. Measured stresses in invert reinforcement at chainage 411+707

3.4.1 Case a

The distribution of loadings acting perpendicularly to the circumference of the tunnel lining has been extrapolated from the obtained pressures mentioned in Alonso et al., (2013), where the authors plotted the radial pressure against the invert of the Lilla tunnel. Starting from the most emblematic distribution of pressure measured in three sections, represented in Figure 2.45, the purpose of the first case is to model a heterogeneous but continuous distribution of swelling pressure. The aforementioned distribution is a linear interpolation of the six loading cells measurements. The three different distributions correspondents to the cross-sections at chainages 411 + 348, 411 + 468 and 411 + 707 are illustrated in Figure 3.15, Figure 3.16 and Figure 3.17.

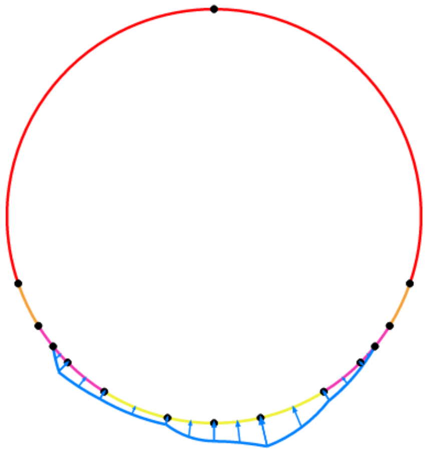

Figure 3.15. Continuous heterogeneous distribution of section at chainage 411 + 348

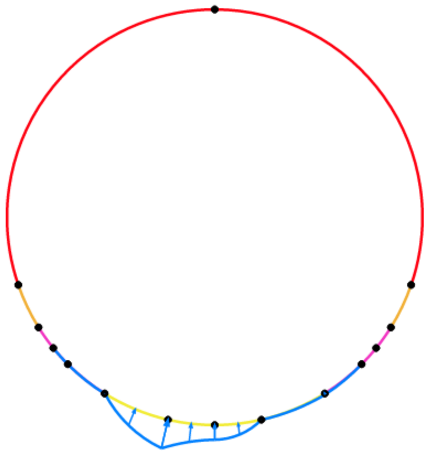

Figure 3.16. Continuous heterogeneous distribution of section at chainage 411 + 468

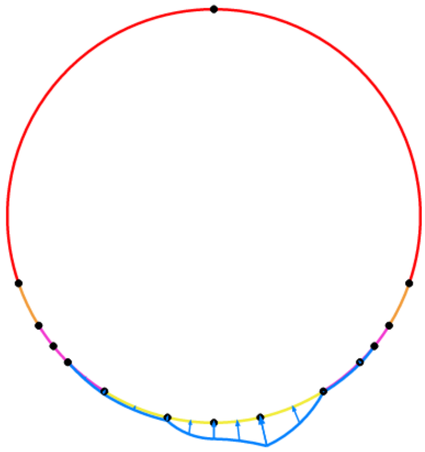

Figure 3.17. Continuous heterogeneous distribution of section at chainage 411 + 707

3.4.2 Results

The construction phases analysed previously, ending with the activation of the loads corresponding to the expansive behaviour of the Lilla claystone, lead to some internal lining forces over the circular plate. The considered plate internal forces in the plane strain model are axial forces N and bending moments M. Stress analysis of unit width rectangular cross-sections, virtually corresponding to lining points, is studied to evaluate the comparison between calculated and measured values in the steel. Upper reinforcement bars values should be compared to extensometer of vibrating wire in the upper part measurement, whereas lower reinforcement stresses should be compared with the lower part devices readings. Location and enumeration of the instrumentation is showed in Figure 2.36. Every stress point composing the plate discretization is subjected to a couple of N and M. Starting from values in selected points, stresses in the bars are evaluated. In the following tables, the calculated stresses in the concrete (σ_c) and in the upper (σ_s) and lower ($\sigma_{s'}$) steel bars are illustrated compared to the measured values. Stresses are calculated for the 6 instrumentations position in the cross-sections at stations 411 + 348, 411 + 468 and 411 + 707.

Table 3.6. Stresses in the reinforcement at position ECV 12-11-10-9. Chainage 411+348

ECV 12-11 **411+348**	M [KNm/m]	-1361,94	
	N [kN/m]	-11213,8	
		model	field
	σ_C [MPa]	-7,68	-1,4
	σ_S [MPa]	-21,15	-5
	$\sigma_{S'}$ [MPa]	-58,13	-7,5

ECV 10-9 **411 + 348**	M [KNm/m]	1640,56	
	N [kN/m]	-11348,4	
		model	field
	σ_C [MPa]	-12,84	-2,2
	σ_S [MPa]	-17,84	-7,5
	$\sigma_{S'}$ [MPa]	-62,39	-11

Table 3.7. Stresses in the reinforcement at position ECV 8-7-6-5. Chainage 411+348

ECV 8-7 **411+348**	M [KNm/m]	1640,56	
	N [kN/m]	-11348,4	
		model	field
	σ_C [MPa]	-8,94	-2,9
	σ_S [MPa]	-17,38	-14,5
	$\sigma_{S'}$ [MPa]	-43,9	-2,9

ECV 6-5 **411 + 348**	M [KNm/m]	13435,83	
	N [kN/m]	-10267,2	
		model	field
	σ_C [MPa]	-48,9	-2
	σ_S [MPa]	581,2	-10
	$\sigma_{S'}$ [MPa]	-220,9	-4,2

Table 3.8. Stresses in the reinforcement at position ECV 4-3-2-1. Chainage 411+348

ECV 4-3 **411+348**	M [KNm/m]	4826,983	
	N [kN/m]	-11099,1	
		model	field
	σ_C [MPa]	-13,52	-2,4
	σ_S [MPa]	59,9	-12
	$\sigma_{S'}$ [MPa]	-115,8	-4,8

ECV 2-1 **411 + 348**	M [KNm/m]	-82,531	
	N [kN/m]	-11368,1	
		model	field
	σ_C [MPa]	-8,28	-2,84
	σ_S [MPa]	-41,31	-9
	$\sigma_{S'}$ [MPa]	-39,07	-14,2

Table 3.9. Stresses in the reinforcement at position ECV 12-11-10-9. Chainage 411+468

ECV 12-11 **411+468**	M [KNm/m]	-2986,2	
	N [kN/m]	-7999,06	
		model	field
	σ_C [MPa]	-15,25	-2,3
	σ_S [MPa]	22,2	-11,5
	$\sigma_{S'}$ [MPa]	-72,46	-9,8

ECV 10-9 **411+468**	M [KNm/m]	-1347,9	
	N [kN/m]	-8360,7	
		model	field
	σ_C [MPa]	-9,86	-2,9
	σ_S [MPa]	-47,86	-14,5
	$\sigma_{S'}$ [MPa]	-11,26	-6,3

Table 3.10. Stresses in the reinforcement at position ECV 8-7-6-5. Chainage 411+468

ECV 8-7 411+468	M [KNm/m]	5106,75	
	N [kN/m]	-8098,71	
		model	field
	σ_C [MPa]	-15,71	-2,84
	σ_S [MPa]	-74,2	-14,2
	$\sigma_{S'}$ [MPa]	54,66	-3,8

ECV 6-5 411+468	M [KNm/m]	13400,74	
	N [kN/m]	-7308,99	
		model	field
	σ_C [MPa]	-50,07	-2,7
	σ_S [MPa]	-221,3	-13,5
	$\sigma_{S'}$ [MPa]	759,8	-6,3

Table 3.11. Stresses in the reinforcement at position ECV 4-32-1. Chainage 411+468

ECV 4-3 411+468	M [KNm/m]	4169,88	
	N [kN/m]	-8257,76	
		model	field
	σ_C [MPa]	-21,6	-3,3
	σ_S [MPa]	78,97	-16,5
	$\sigma_{S'}$ [MPa]	-100,9	-7,8

ECV 2-1 411+468	M [KNm/m]	907,6	
	N [kN/m]	-8419,54	
		model	field
	σ_C [MPa]	-8,61	-2,4
	σ_S [MPa]	-42,8	-12
	$\sigma_{S'}$ [MPa]	-17,44	-

Table 3.12. Stresses in the reinforcement at position ECV 12-11-10-9. Chainage 411+707

ECV 12-11 411+707	M [KNm/m]	501,5	
	N [kN/m]	-8780	
		model	field
	σ_C [MPa]	-7,6	-2,1
	σ_S [MPa]	-37,8	-5
	$\sigma_{S'}$ [MPa]	-24,2	-10,2

ECV 10-9 411+707	M [KNm/m]	5097	
	N [kN/m]	-8507	
		model	field
	σ_C [MPa]	-27,4	-2,1
	σ_S [MPa]	-125,9	-10,2
	$\sigma_{S'}$ [MPa]	144,8	-5,5

Table 3.13. Stresses in the reinforcement at position ECV 8-7-6-5. Chainage 411+707

ECV 8-7 411+707	M [KNm/m]	15567	
	N [kN/m]	-7336	
		model	field
	σ_C [MPa]	-58,4	-2,6
	σ_S [MPa]	-257	-13
	$\sigma_{S'}$ [MPa]	957	-1

ECV 6-5 411+707	M [KNm/m]	4326	
	N [kN/m]	-8611	
		model	field
	σ_C [MPa]	-12,94	-2,2
	σ_S [MPa]	-62,2	-11
	$\sigma_{S'}$ [MPa]	22,3	-1,2

Table 3.14. Stresses in the reinforcement at position ECV 4-3-2-1. Chainage 411+707

ECV 4-3 **411+707**	M [KNm/m]	-2443	
	N [kN/m]	-8920	
		model	field
	σ_C [MPa]	-13,52	-1,5
	σ_S [MPa]	2,1	-7,5
	$\sigma_{S'}$ [MPa]	-64,9	0

ECV 2-1 **411+707**	M [KNm/m]	-3650,8	
	N [kN/m]	-8421	
		model	field
	σ_C [MPa]	-18,6	-1,64
	σ_S [MPa]	44,6	-5
	$\sigma_{S'}$ [MPa]	-87,6	-8,2

These tables provide interesting information on the lining behaviour. First, note that axial forces are positive when they generate tensile stresses. As expected the resulting internal axial forces in the tunnel are all of compression type.

A remarkable result is that the calculated stresses are frequently one order of magnitude larger than the measured ones, sometimes two orders. The situation is clearly illustrated in Figure 3.18, Figure 3.19 and Figure 3.20, which represent graphically the tables results. The highest values of stresses have been found in the central extensometers positions of all cross sections. It is evident that a continuous distribution of swelling pressure, obtained by interpolation of the real measured punctual values of pressure, cause a combination of internal lining forces very high.

Moreover, from the model calculation it results that not all the reinforcement steel bars work in compression, as they do in reality. While the excessive magnitude of the stresses values derives directly from the high internal forces combination and could be reasonably solved with the application of a lower distribution of pressure, the presence of tensions is not that straightforward to avoid. It is believed that lower or upper reinforcement bars work in tension whenever the couple axial force N and bending moment M generates a high eccentricity value.

From the first case analysis it is reasonable to conclude that between the pressure cell devices, where no field information is available, the swelling pressures do not follow the pattern assumed in the analysis, i.e. they do not linearly increase, or decrease respectively, from one measured punctual value to another.

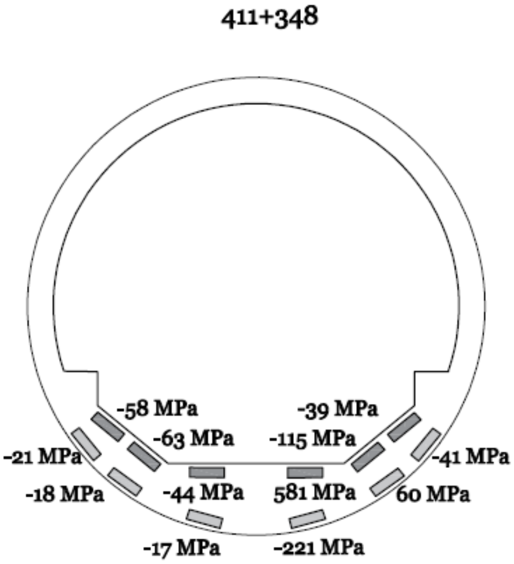
411+348
-58 MPa
-39 MPa
-63 MPa
-115 MPa
-21 MPa
-41 MPa
-18 MPa
-44 MPa
581 MPa
60 MPa
-17 MPa
-221 MPa

Figure 3.18. Calculated stresses in reinforcement bars at chainage 411+348 with case a swelling distribution

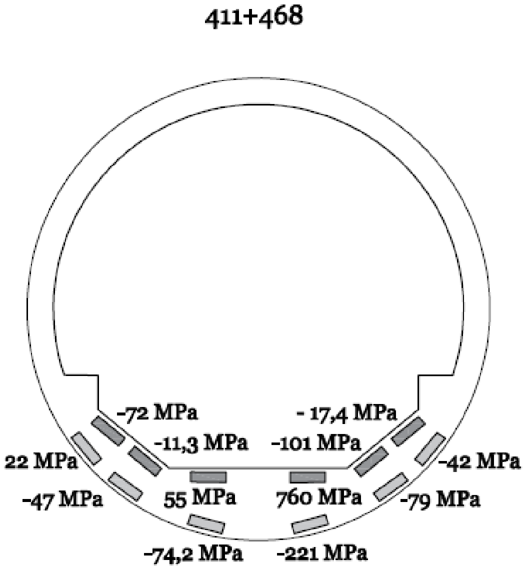
411+468
-72 MPa
- 17,4 MPa
-11,3 MPa
-101 MPa
22 MPa
-42 MPa
-47 MPa
55 MPa
760 MPa
-79 MPa
-74,2 MPa
-221 MPa

Figure 3.19. Calculated stresses in reinforcement bars at chainage 411+468 with case a swelling distribution

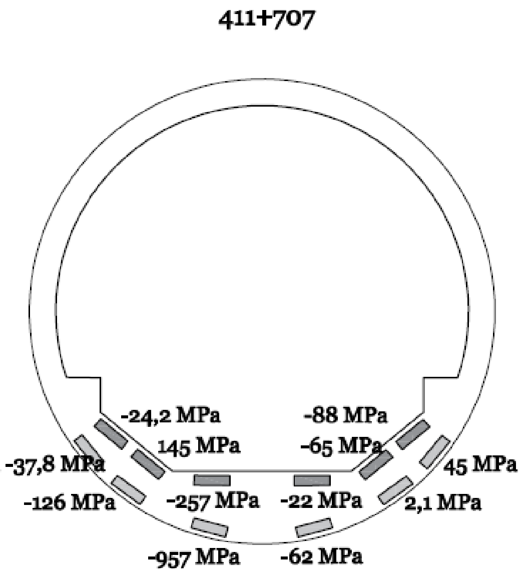

Figure 3.20. Calculated stresses in reinforcement bars at chainage 411+707 with case a swelling distribution

3.4.3 Case b

The second loading configuration case is an attempt to better capture the rock behaviour in the invert of the Lilla tunnel, specifically in the pressure cell device area and, at the same time, reducing the magnitude of the internal forces generated in the plate. Once again, the reference values of radial pressure are the ones of Figure 2.45. In this section the measured values are considered to be uniformly distributed in a 40 cm long arc around the pressure cell device position. This new configuration of loads is imposed to cross-sections at chainages 411 + 348, 411 + 468 and 411 + 707. The graphical representation of the three swelling distributions is shown in Figure 3.21, Figure 3.22 and Figure 3.23.

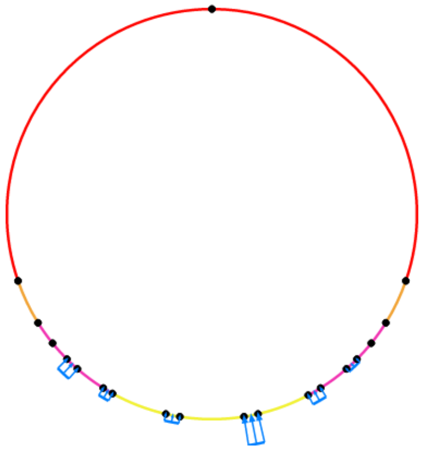

Figure 3.21. Uniform distributions extended 40 cm in section at chainage 411 + 348

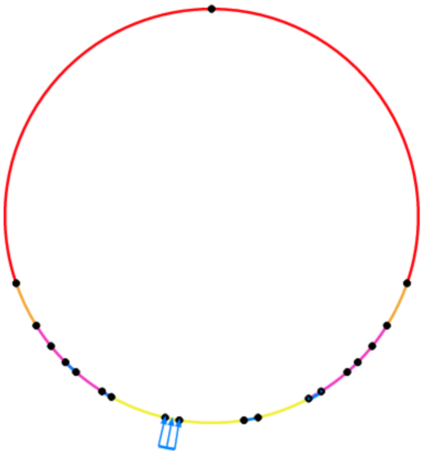

Figure 3.22. Uniform distributions extended 40 cm in section at chainage 411 + 468

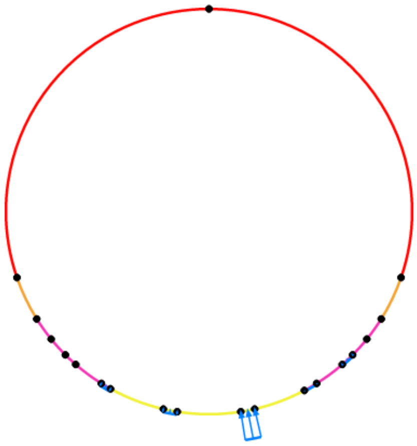

Figure 3.23. Uniform distributions extended 40 cm in section at chainage 411 + 707

3.4.4 Results

In this second case the steps of the analysis end with activation of the 40 cm extended uniform pressure distributions representing the swelling behaviour of the Lilla claystone against the lining. The simulation procedure and the calculation do not vary from the continuous heterogeneous swelling distribution case described before. From axial forces and bending moments values, a sectional analysis is conducted to get knowledge of the steel and concrete stresses. Upper steel bars values are compared to upper part vibrating extensometer readings, while lower steel reinforcement stresses with lower part instrument measurements. Note that compressive stresses are negatives. In the following tables, the calculated stresses in the concrete (σ_c) and in the upper (σ_s) and lower ($\sigma_{s'}$) steel bars are presented compared to the extensometer readings. Stresses are calculated for the 6 devices position in the cross-sections at stations 411 + 348, 411 + 468 and 411 + 707.

Table 3.15. Stresses in the reinforcement at position ECV 12-11-10-9. Chainage 411+348

ECV 12-11 **411+348**	M [KNm/m]	440,641	
	N [kN/m]	-2074,33	
		model	field
	σ_C [MPa]	-0,174	-1,5
	σ_S [MPa]	-13,32	-5
	$\sigma_{S'}$ [MPa]	-1,35	-7,5

ECV 10-9 **411 + 348**	M [KNm/m]	626,44	
	N [kN/m]	-2337,8	
		model	field
	σ_C [MPa]	-3,49	-2,2
	σ_S [MPa]	-16,81	-7,5
	$\sigma_{S'}$ [MPa]	0,33	-11

Table 3.16. Stresses in the reinforcement at position ECV 8-7-6-5. Chainage 411+348

ECV 8-7 **411+348**	M [KNm/m]	1136,14	
	N [kN/m]	-2400,56	
		model	field
	σ_C [MPa]	-3,415	-2,9
	σ_S [MPa]	-16,45	-14,5
	$\sigma_{S'}$ [MPa]	4,69	-2,9

ECV 6-5 **411 + 348**	M [KNm/m]	2671,78	
	N [kN/m]	-2075,9	
		model	field
	σ_C [MPa]	-9,71	-2
	σ_S [MPa]	-43,88	-10
	$\sigma_{S'}$ [MPa]	113,6	-4,2

Table 3.17. Stresses in the reinforcement at position ECV 4-3-2-1. Chainage 411+348

ECV 4-3 **411+348**	M [KNm/m]	1412,61	
	N [kN/m]	-2066,2	
		model	field
	σ_C [MPa]	-7,78	-2,4
	σ_S [MPa]	-35,43	-12
	$\sigma_{S'}$ [MPa]	51,78	-4,8

ECV 2-1 **411 + 348**	M [KNm/m]	377,06	
	N [kN/m]	-2007,13	
		model	field
	σ_C [MPa]	-2,52	-2,84
	σ_S [MPa]	-12,22	-9
	$\sigma_{S'}$ [MPa]	-1,97	-14,2

Table 3.18. Stresses in the reinforcement at position ECV 8-7-6-5. Chainage 411+468

ECV 12-11 **411+468**	M [KNm/m]	-275,67	
	N [kN/m]	-535,86	
		model	field
	σ_C [MPa]	1,08	-2,3
	σ_S [MPa]	7,51	-11,5
	$\sigma_{S'}$ [MPa]	-15,41	-9,8

ECV 10-9 **411+468**	M [KNm/m]	-250,62	
	N [kN/m]	-604,28	
		model	field
	σ_C [MPa]	-1,01	-1,36
	σ_S [MPa]	3,9	-
	$\sigma_{S'}$ [MPa]	-14,72	-6,8

Table 3.19. Stresses in the reinforcement at position ECV 8-7-6-5. Chainage 411+468

ECV 8-7 **411+468**	M [KNm/m]	250,55		**ECV 6-5** **411+468**	M [KNm/m]	1793,18	
	N [kN/m]	-658,37			N [kN/m]	-447,52	
		model	field			model	field
	σ_C [MPa]	-1,05	-2,86		σ_C [MPa]	3,99	-2,9
	σ_S [MPa]	-15,1	-14,3		σ_S [MPa]	-54	-14,5
	$\sigma_{S'}$ [MPa]	2,86	-3,8		$\sigma_{S'}$ [MPa]	143,2	-6,3

Table 3.20. Stresses in the reinforcement at position ECV 4-3-2-1. Chainage 411+468

ECV 4-3 **411+468**	M [KNm/m]	109,43		**ECV 2-1** **411+468**	M [KNm/m]	-136,01	
	N [kN/m]	-628,4			N [kN/m]	-599,95	
		model	field			model	field
	σ_C [MPa]	-0,67	-3,3		σ_C [MPa]	-0,71	-2,4
	σ_S [MPa]	-3,77	-16,5		σ_S [MPa]	-1,28	-12
	$\sigma_{S'}$ [MPa]	-2,44	-7,8		$\sigma_{S'}$ [MPa]	-10,39	-

Table 3.21. Stresses in the reinforcement at position ECV 12-11-10-9. Chainage 411+707

ECV 12-11 **411+707**	M [KNm/m]	356,905		**ECV 10-9** **411+707**	M [KNm/m]	1266,9	
	N [kN/m]	-1377,79			N [kN/m]	-1362,11	
		model	field			model	field
	σ_C [MPa]	-2,02	-2,04		σ_C [MPa]	-27,4	-2,04
	σ_S [MPa]	-9,73	-5		σ_S [MPa]	-32,37	-10,2
	$\sigma_{S'}$ [MPa]	0,015	-10,2		$\sigma_{S'}$ [MPa]	71,15	-5,5

Table 3.22. Stresses in the reinforcement at position ECV 8-7-6-5. Chainage 411+707

ECV 8-7 **411+707**	M [KNm/m]	3535,03		**ECV 6-5** **411+707**	M [KNm/m]	1100	
	N [kN/m]	-1045,57			N [kN/m]	-1340	
		model	field			model	field
	σ_C [MPa]	-2,89	-2,6		σ_C [MPa]	-0,264	-2,2
	σ_S [MPa]	-57	-13		σ_S [MPa]	-16,93	-11
	$\sigma_{S'}$ [MPa]	259	-1		$\sigma_{S'}$ [MPa]	23,18	-1,2

Table 3.23. Stresses in the reinforcement at position ECV 4-3-2-1. Chainage 411+707

ECV 4-3 **411+707**	M [KNm/m]	-245,788	
	N [kN/m]	-1312,01	
		model	field
	σ_C [MPa]	-0,47	-1,5
	σ_S [MPa]	1,3	-7,5
	$\sigma_{S'}$ [MPa]	-7,9	0

ECV 2-1 **411+707**	M [KNm/m]	-594,237	
	N [kN/m]	-1202,47	
		model	field
	σ_C [MPa]	-0,62	-1,64
	σ_S [MPa]	10,63	-5
	$\sigma_{S'}$ [MPa]	-14,35	-8,2

From the previous tables, it can be stated that the results of the second case swelling distribution seem not to show any improvement in terms of tensile stresses appearance. As a matter of fact, all the three cross sections are still characterized by a tensile behaviour at some points. In the model, tensile stresses appear mostly on upper steel bars. A probable explanation lies on the sign of the bending moment. According to PLAXIS's convention, positive bending moments cause low fibres to undergo compression while negative moments induce tensile states in the upper fibres. The calculated stresses with case b swelling distribution are lower than with the case a distribution. Nevertheless, stress values showed in Figure 3.24, Figure 3.25 and Figure 3.26 are far from the measured ones, as represented in Figure 3.12, Figure 3.13 and Figure 3.14. Most of the difference focuses in the records of the central position extensometers.

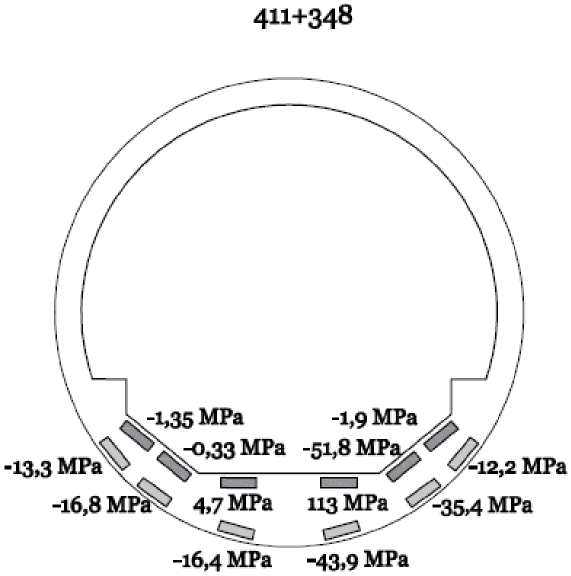

Figure 3.24. Calculated stresses in reinforcement bars at chainage 411+348 with case b swelling distribution

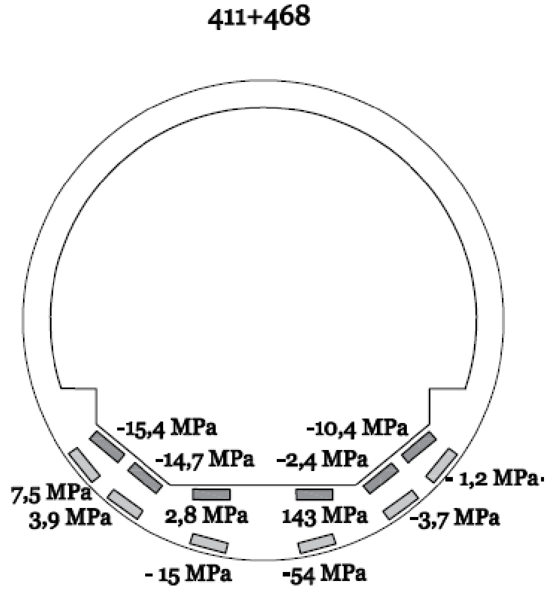
411+468
-15,4 MPa
-10,4 MPa
-14,7 MPa
-2,4 MPa
- 1,2 MPa
7,5 MPa
3,9 MPa
2,8 MPa
143 MPa
-3,7 MPa
- 15 MPa
-54 MPa

Figure 3.25. Calculated stresses in reinforcement bars at chainage 411+468 with case b swelling distribution

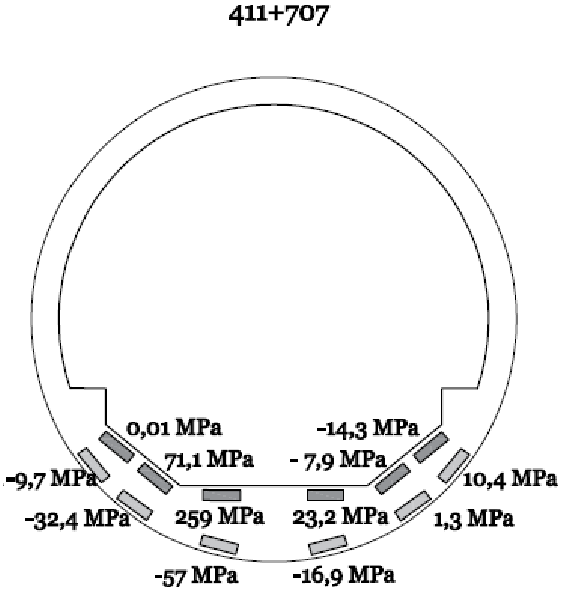
411+707
0,01 MPa
-14,3 MPa
71,1 MPa
- 7,9 MPa
-9,7 MPa
10,4 MPa
-32,4 MPa
259 MPa
23,2 MPa
1,3 MPa
-57 MPa
-16,9 MPa

Figure 3.26. Calculated stresses in reinforcement bars at chainage 411+707 with case b swelling distribution

3.4.5 Case c

The third loading configuration case is similar to the second one: six swelling pressure distributions are imposed on 30 cm long areas around the measurement points. The load magnitude in the distinct positions coincide with the radial pressure captured in December 2011 (see Figure 2.45). The purpose of shortening the extension of the arc with respect to the previous case, from 40 cm to 30 cm, is to further decrease the values of axial forces and bending moments developed in the plate. Thus, stresses in the concrete and steel decrease consequently. Figure 3.27, Figure 3.28 and Figure 3.29 show the six loading distributions in cross-sections at chainages 411 + 348, 411 + 468 and 411 + 707.

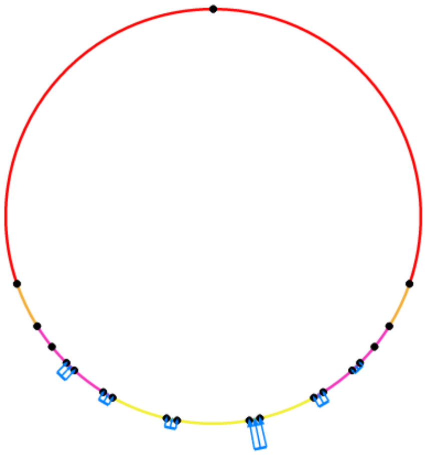

Figure 3.27. Uniform distributions extended 30 cm in section at chainage 411 + 348

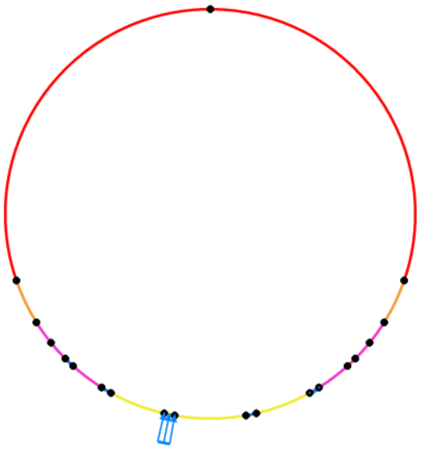

Figure 3.28. Uniform distributions extended 30 cm in section at chainage 411 + 468

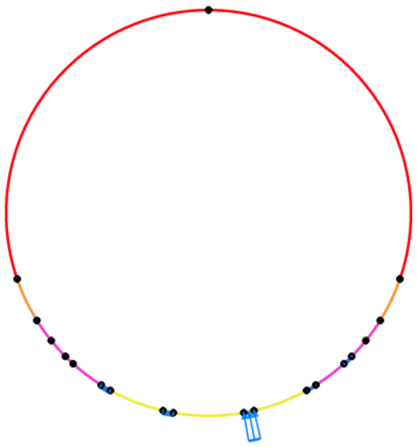

Figure 3.29. Uniform distributions extended 30 cm in section at chainage 411 + 707

3.4.6 Results

This third case analysis has the aim of examining the consequences of the application of a 30 cm extended uniform pressure distribution. The calculation procedure does not vary from former cases and neither the sectional analysis. Ground behaviour is here modelled as six small uniform distributions. Moreover, the 30 cm extension might be representative as comparable to the dimension of a pressure cell, which could vary between 200 and 300mm. Similar to the previous cases, concrete and steel stresses are determined in the six devices positions for the benchmark cross sections. Tables and plots showing the results are represented below.

Table 3.24. Stresses in the reinforcement at position ECV 12-11-10-9. Chainage 411+348

ECV 12-11 **411+348**	M [KNm/m]	347,52	
	N [kN/m]	-883,58	
		model	field
	σ_C [MPa]	-1,78	-1,5
	σ_S [MPa]	-8,38	-5
	$\sigma_{S'}$ [MPa]	3,15	-7,5

ECV 10-9 **411 + 348**	M [KNm/m]	415,69	
	N [kN/m]	-963,8	
		model	field
	σ_C [MPa]	-0,67	-2,2
	σ_S [MPa]	-9,98	-7,5
	$\sigma_{S'}$ [MPa]	5,03	-11

Table 3.25. Stresses in the reinforcement at position ECV 8-7-6-5. Chainage 411+348

ECV 8-7 **411+348**	M [KNm/m]	540,83	
	N [kN/m]	-1045,69	
		model	field
	σ_C [MPa]	-1,67	-2,9
	σ_S [MPa]	-7,76	-14,5
	$\sigma_{S'}$ [MPa]	3,09	-2,9

ECV 6-5 **411 + 348**	M [KNm/m]	1256,36	
	N [kN/m]	-911,06	
		model	field
	σ_C [MPa]	-4,6	-2
	σ_S [MPa]	-20,7	-10
	$\sigma_{S'}$ [MPa]	57,2	-4,2

Table 3.26. Stresses in the reinforcement at position ECV 4-3-2-1. Chainage 411+348

ECV 4-3 **411+348**	M [KNm/m]	577,61		**ECV 2-1** **411 + 348**	M [KNm/m]	11,73	
	N [kN/m]	-922,57			N [kN/m]	-913,07	
		model	field			model	field
	σ_C [MPa]	-3,13	-2,4		σ_C [MPa]	-0,68	-2,84
	σ_S [MPa]	-14,34	-12		σ_S [MPa]	-3,38	-9
	$\sigma_{S'}$ [MPa]	17,96	-4,8		$\sigma_{S'}$ [MPa]	-3,07	-14,2

Table 3.27. Stresses in the reinforcement at position ECV 12-11-10-9. Chainage 411+468

ECV 12-11 **411+468**	M [KNm/m]	-203,16		**ECV 10-9** **411+468**	M [KNm/m]	-112,22	
	N [kN/m]	-425,71			N [kN/m]	-475,81	
		model	field			model	field
	σ_C [MPa]	-0,81	-2,3		σ_C [MPa]	-0,6	-1,36
	σ_S [MPa]	4,89	-11,5		σ_S [MPa]	-0,54	-
	$\sigma_{S'}$ [MPa]	-11,5	-9,8		$\sigma_{S'}$ [MPa]	-8,72	-6,8

Table 3.28. Stresses in the reinforcement at position ECV 8-7-6-5. Chainage 411+468

ECV 8-7 **411+468**	M [KNm/m]	194,62		**ECV 6-5** **411+468**	M [KNm/m]	1374,98	
	N [kN/m]	-504,8			N [kN/m]	-341,86	
		model	field			model	field
	σ_C [MPa]	-0,81	-2,86		σ_C [MPa]	-3,13	-2,9
	σ_S [MPa]	-11,8	-14,3		σ_S [MPa]	-42,31	-14,5
	$\sigma_{S'}$ [MPa]	2,34	-3,8		$\sigma_{S'}$ [MPa]	112,1	-6,3

Table 3.29. Stresses in the reinforcement at position ECV 4-3-2-1. Chainage 411+468

ECV 4-3 **411+468**	M [KNm/m]	241,19		**ECV 2-1** **411+468**	M [KNm/m]	-45,81	
	N [kN/m]	-471,73			N [kN/m]	-463,04	
		model	field			model	field
	σ_C [MPa]	-0,95	-3,3		σ_C [MPa]	-0,41	-2,4
	σ_S [MPa]	-13,59	-16,5		σ_S [MPa]	-2,97	-12
	$\sigma_{S'}$ [MPa]	6,52	-7,8		$\sigma_{S'}$ [MPa]	-6,03	-

Table 3.30. Stresses in the reinforcement at position ECV 12-11-10-9. Chainage 411+707

ECV 12-11 **411+707**	M [KNm/m]	280,17	
	N [kN/m]	-934,424	
		model	field
	σ_C [MPa]	-1,53	-2,04
	σ_S [MPa]	-7,2	-9,3
	$\sigma_{S'}$ [MPa]	0,66	-10,2

ECV 10-9 **411+707**	M [KNm/m]	1034,4	
	N [kN/m]	-599,23	
		model	field
	σ_C [MPa]	-1,6	-2,04
	σ_S [MPa]	-25,9	-10,2
	$\sigma_{S'}$ [MPa]	89,6	-5,5

Table 3.31. Stresses in the reinforcement at position ECV 8-7-6-5. Chainage 411+707

ECV 8-7 **411+707**	M [KNm/m]	2638,51	
	N [kN/m]	-716,424	
		model	field
	σ_C [MPa]	-2,89	-2,6
	σ_S [MPa]	-42,3	-13
	$\sigma_{S'}$ [MPa]	197,9	-1

ECV 6-5 **411+707**	M [KNm/m]	637,383	
	N [kN/m]	-996,07	
		model	field
	σ_C [MPa]	-0,26	-2,2
	σ_S [MPa]	-9,26	-11
	$\sigma_{S'}$ [MPa]	7,12	-1,2

Table 3.32. Stresses in the reinforcement at position ECV 4-3-2-1. Chainage 411+707

ECV 4-3 **411+707**	M [KNm/m]	-216,03	
	N [kN/m]	-976,96	
		model	field
	σ_C [MPa]	-0,47	-1,5
	σ_S [MPa]	-0,51	-7,5
	$\sigma_{S'}$ [MPa]	-6,4	0

ECV 2-1 **411 + 707**	M [KNm/m]	-462,23	
	N [kN/m]	-889,74	
		model	field
	σ_C [MPa]	-0,62	-1,64
	σ_S [MPa]	12,57	-5
	$\sigma_{S'}$ [MPa]	-25,87	-8,2

Comparing Figure 3.30, Figure 3.31, Figure 3.32 with Figure 3.24, Figure 3.25, Figure 3.26 it is evident a stress magnitude reduction, certainly due to the loading distribution extension decrease. Not surprisingly central extensometers values are the highest and are still very high with respect to the ones plotted in Figure 3.12, Figure 3.13 and Figure 3.14. On the other hand, there are other positions in which calculated stress values are smaller than the measured in Lilla tunnel. Furthermore, tensile stresses still seem to appear in all sections.

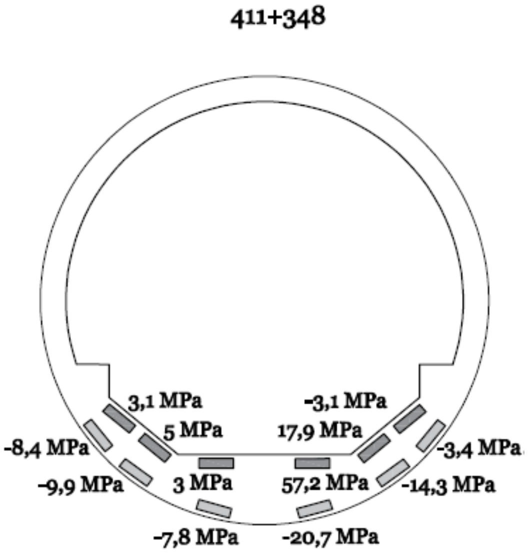
411+348
3,1 MPa
-3,1 MPa
5 MPa
17,9 MPa
-8,4 MPa
-3,4 MPa
-9,9 MPa
3 MPa
57,2 MPa
-14,3 MPa
-7,8 MPa
-20,7 MPa

Figure 3.30. Calculated stresses in reinforcement bars at chainage 411+348 with case c swelling distribution

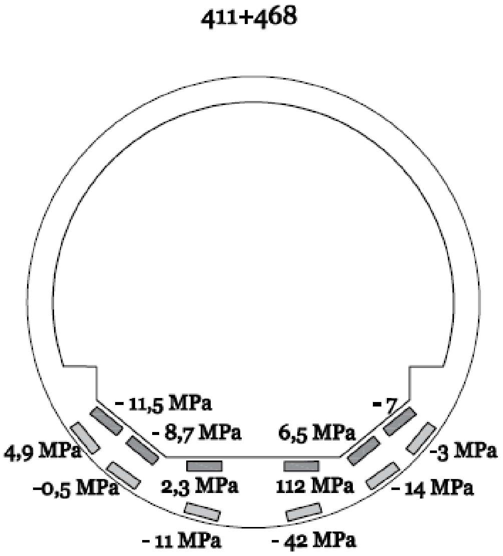
411+468
- 11,5 MPa
- 7
- 8,7 MPa
6,5 MPa
4,9 MPa
-3 MPa
-0,5 MPa
2,3 MPa
112 MPa
- 14 MPa
- 11 MPa
- 42 MPa

Figure 3.31. Calculated stresses in reinforcement bars at chainage 411+468 with case c swelling distribution

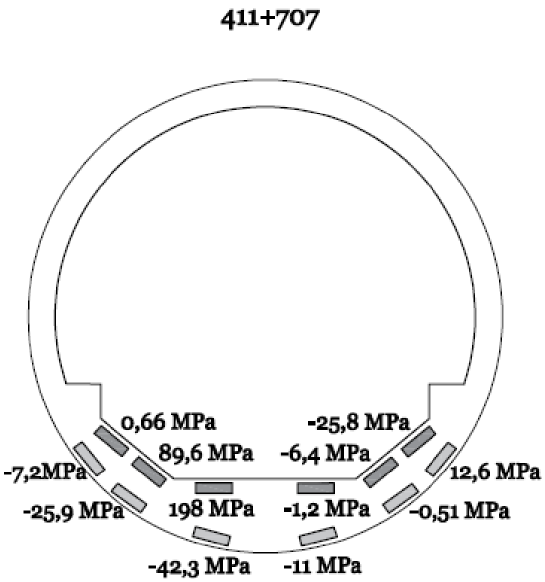

Figure 3.32. Calculated stresses in reinforcement bars at chainage 411+707 with case c swelling distribution

3.4.7 Case d

The fourth case is a further attempt to reduce the swelling pressure distribution extension. As a matter of fact, the loading acting on the invert is applied in six 20 cm long arcs. The idea behind the decrease of the loading extension is to reproduce the real behaviour. Even tough for sake of simplicity radial measured pressures are represented as punctual forces, the pressure cell devices do not have a negligible dimension. The purpose of these paragraphs is also to understand how the device dimension could affect and distort the measured ground behaviour with respect to the model one. Reference values, pressure cell device positions and analysed cross-sections do not change from previous cases. The graphical representation of the three swelling distributions is shown in Figure 3.33, Figure 3.34 and Figure 3.35.

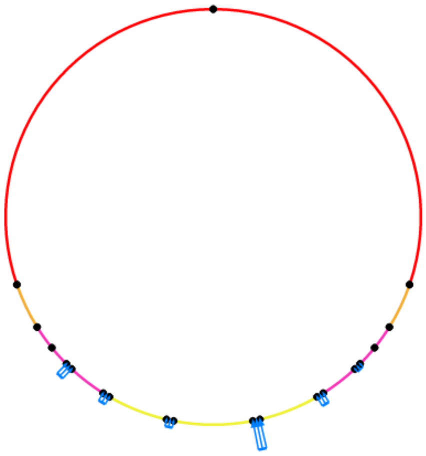

Figure 3.33. Uniform distributions extended 20 cm in section at chainage 411 + 348

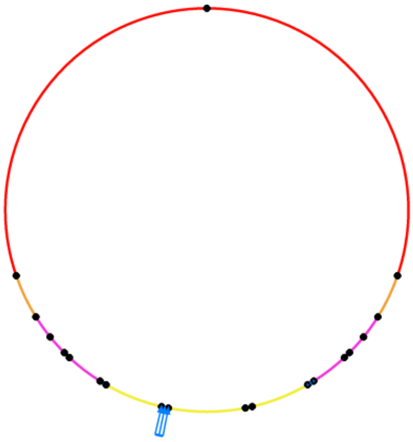

Figure 3.34. Uniform distributions extended 20 cm in section at chainage 411 + 468

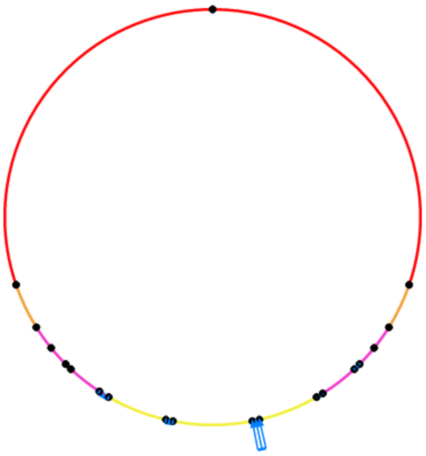

Figure 3.35. Uniform distributions extended 20 cm in section at chainage 411 + 707

3.4.8 Results

Not differently from the previous cases, results for case d analysis are presented in the form of both graphs and cross section schematization.

Table 3.33. Stresses in the reinforcement at position ECV 12-11-10-9. Chainage 411+348

ECV 12-11 **411+348**	M [KNm/m]	254,39		**ECV 10-9** **411 + 348**	M [KNm/m]	265,35	
	N [kN/m]	-620,97			N [kN/m]	-701,38	
		model	field			model	field
	σ_C [MPa]	-1,07	-1,5		σ_C [MPa]	-0,54	-2,2
	σ_S [MPa]	-6,46	-5		σ_S [MPa]	-7,72	-7,5
	$\sigma_{S'}$ [MPa]	1,89	-7,5		$\sigma_{S'}$ [MPa]	2,94	-11

Table 3.34. Stresses in the reinforcement at position ECV 8-7-6-5. Chainage 411+348

ECV 8-7 **411+348**	M [KNm/m]	398,66	
	N [kN/m]	-782,57	
		model	field
	σ_C [MPa]	-1,04	-2,9
	σ_S [MPa]	-7,25	-14,5
	$\sigma_{S'}$ [MPa]	2,8	-2,9

ECV 6-5 **411 + 348**	M [KNm/m]	1035,02	
	N [kN/m]	-648,63	
		model	field
	σ_C [MPa]	-2,49	-2
	σ_S [MPa]	-14,7	-10
	$\sigma_{S'}$ [MPa]	50,28	-4,2

Table 3.35. Stresses in the reinforcement at position ECV 4-3-2-1. Chainage 411+348

ECV 4-3 **411+348**	M [KNm/m]	327,27	
	N [kN/m]	-660,14	
		model	field
	σ_C [MPa]	-1,31	-2,4
	σ_S [MPa]	-18,45	-12
	$\sigma_{S'}$ [MPa]	8,24	-4,8

ECV 2-1 **411 + 348**	M [KNm/m]	78,73	
	N [kN/m]	-650,64	
		model	field
	σ_C [MPa]	-0,6	-2,84
	σ_S [MPa]	-8,99	-9
	$\sigma_{S'}$ [MPa]	-3,71	-14,2

Table 3.36. Stresses in the reinforcement at position ECV 12-11-10-9. Chainage 411+468

ECV 12-11 **411+468**	M [KNm/m]	-135,84	
	N [kN/m]	-286,4	
		model	field
	σ_C [MPa]	-0,54	-2,3
	σ_S [MPa]	3,08	-11,5
	$\sigma_{S'}$ [MPa]	-7,73	-9,8

ECV 10-9 **411+468**	M [KNm/m]	-69,81	
	N [kN/m]	-322,18	
		model	field
	σ_C [MPa]	-0,37	-1,36
	σ_S [MPa]	-0,79	-
	$\sigma_{S'}$ [MPa]	-5,47	-6,8

Table 3.37. Stresses in the reinforcement at position ECV 8-7-6-5. Chainage 411+348

ECV 8-7 **411+468**	M [KNm/m]	172,35	
	N [kN/m]	-339,38	
		model	field
	σ_C [MPa]	-0,44	-2,86
	σ_S [MPa]	-6,38	-14,3
	$\sigma_{S'}$ [MPa]	1,61	-3,8

ECV 6-5 **411+468**	M [KNm/m]	920,15	
	N [kN/m]	-233,07	
		model	field
	σ_C [MPa]	-2,09	-2,9
	σ_S [MPa]	-27,8	-14,5
	$\sigma_{S'}$ [MPa]	74,22	-6,3

Table 3.38. Stresses in the reinforcement at position ECV 4-3-2-1. Chainage 411+348

ECV 4-3 **411+468**	M [KNm/m]	148,07	
	N [kN/m]	-317,53	
		model	field
	σ_C [MPa]	-0,59	-3,3
	σ_S [MPa]	-8,45	-16,5
	$\sigma_{S'}$ [MPa]	3,23	-7,8

ECV 2-1 **411+468**	M [KNm/m]	-39,76	
	N [kN/m]	-307,32	
		model	field
	σ_C [MPa]	-0,29	-2,4
	σ_S [MPa]	-1,66	-12
	$\sigma_{S'}$ [MPa]	-4,43	-

Table 3.39. Stresses in the reinforcement at position ECV 12-11-10-9. Chainage 411+707

ECV 12-11 **411+707**	M [KNm/m]	201,62	
	N [kN/m]	-624,245	
		model	field
	σ_C [MPa]	-0,32	-2,04
	σ_S [MPa]	-5,05	-9,3
	$\sigma_{S'}$ [MPa]	0,77	-10,2

ECV 10-9 **411+707**	M [KNm/m]	655,798	
	N [kN/m]	-599,23	
		model	field
	σ_C [MPa]	-1,6	-2,04
	σ_S [MPa]	-16,76	-10,2
	$\sigma_{S'}$ [MPa]	42,96	-5,5

Table 3.40. Stresses in the reinforcement at position ECV 8-7-6-5. Chainage 411+707

ECV 8-7 **411+707**	M [KNm/m]	1722,87	
	N [kN/m]	-444,44	
		model	field
	σ_C [MPa]	-2,89	-2,6
	σ_S [MPa]	-27,58	-13
	$\sigma_{S'}$ [MPa]	130,8	-1

ECV 6-5 **411+707**	M [KNm/m]	321,69	
	N [kN/m]	-636,577	
		model	field
	σ_C [MPa]	-0,26	-2,2
	σ_S [MPa]	-4,6	-11
	$\sigma_{S'}$ [MPa]	1,69	-1,2

Table 3.41. Stresses in the reinforcement at position ECV 4-3-2-1. Chainage 411+707

ECV 4-3 **411+707**	M [KNm/m]	-186,724	
	N [kN/m]	-597,142	
		model	field
	σ_C [MPa]	-0,47	-1,5
	σ_S [MPa]	0,61	-7,5
	$\sigma_{S'}$ [MPa]	-4,72	0

ECV 2-1 **411 + 707**	M [KNm/m]	-299,984	
	N [kN/m]	-543,01	
		model	field
	σ_C [MPa]	-0,62	-1,64
	σ_S [MPa]	7,1	-5
	$\sigma_{S'}$ [MPa]	-7,3	-8,2

Analysing the tables, it can be concluded that case d swelling distribution lead to a stress state configuration in the three examined cross sections similar to the previous model analysis. Stresses magnitude has reduced but tensile states still appear. For instance, at chainage 411+468 half of the calculated stresses have a positive value. In all the sections tensile stresses develop in the upper bars of the central part and they reach the highest values.

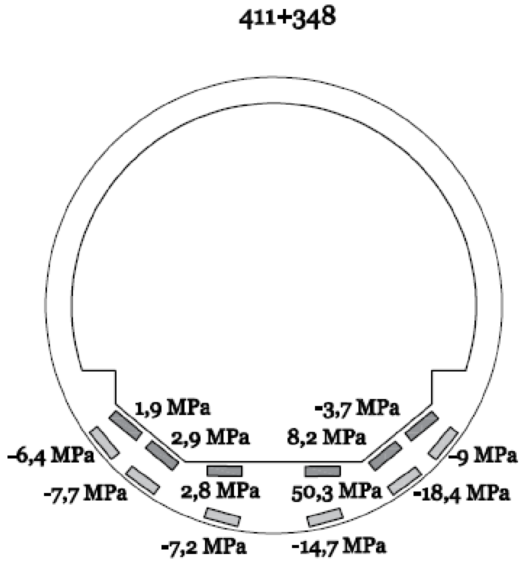
411+348
1,9 MPa
-3,7 MPa
2,9 MPa
8,2 MPa
-6,4 MPa
-9 MPa
-7,7 MPa
2,8 MPa
50,3 MPa
-18,4 MPa
-7,2 MPa
-14,7 MPa

Figure 3.36. Calculated stresses in reinforcement bars at chainage 411+348 with case d swelling distribution

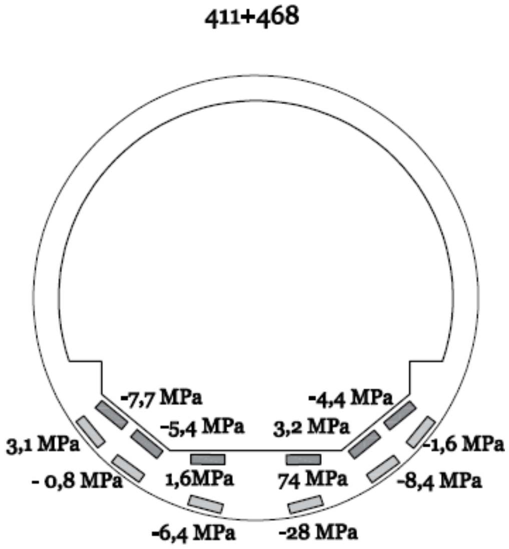
411+468
-7,7 MPa
-4,4 MPa
-5,4 MPa
3,2 MPa
3,1 MPa
-1,6 MPa
- 0,8 MPa
1,6MPa
74 MPa
-8,4 MPa
-6,4 MPa
-28 MPa

Figure 3.37. Calculated stresses in reinforcement bars at chainage 411+468 with case d swelling distribution

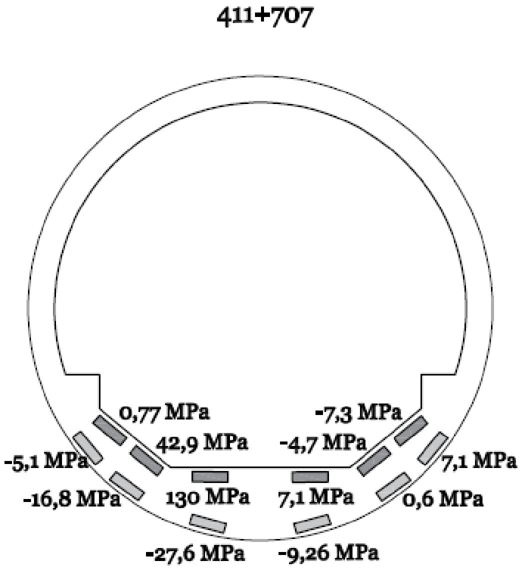
411+707
0,77 MPa
-7,3 MPa
42,9 MPa
-4,7 MPa
-5,1 MPa
7,1 MPa
-16,8 MPa
130 MPa
7,1 MPa
0,6 MPa
-27,6 MPa
-9,26 MPa

Figure 3.38. Calculated stresses in reinforcement bars at chainage 411+707 with case d swelling distribution

3.4.9 Case e

The fifth and last case represents the loading distribution with the smallest swelling pressure extension. This is the case of 10 cm long arcs in the invert, corresponding to the smallest dimension of the loaded arc. The transition from 40 cm to 10 cm distribution is graphically evident from the figures along the cases paragraphs. The following figures illustrate the loading at cross-sections at chainages 411 + 348, 411 + 468 and 411 + 707. (see Figure 3.39, Figure 3.40 and Figure 3.41).

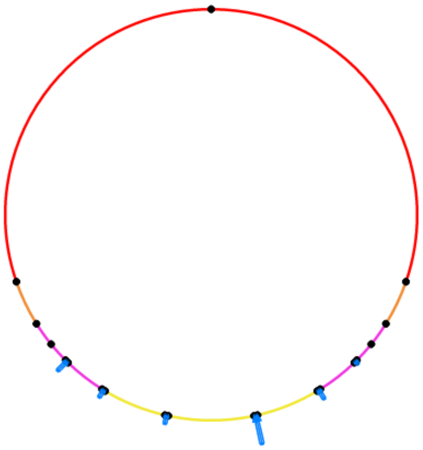

Figure 3.39. Uniform distributions extended 10 cm in section at chainage 411 + 348

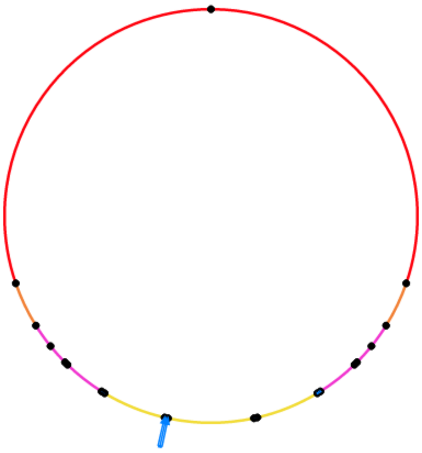

Figure 3.40. Uniform distributions extended 10 cm in section at chainage 411 + 468

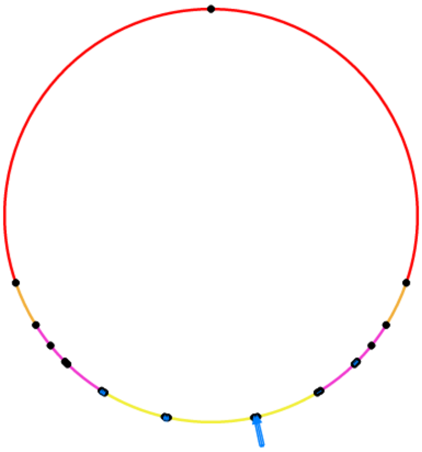

Figure 3.41. Uniform distributions extended 10 cm in section at chainage 411 + 707

3.4.10 Results

Last case results are showed below. In the following tables, calculated stresses in the upper (σ_s) and lower ($\sigma_{s'}$) steel bars and in concrete (σ_c) are presented in comparison to in situ measurements. Not varying from previous analysis, the focus will be on the six instruments position in the invert of cross-sections at stations 411 + 348, 411 + 468 and 411 + 707.

Table 3.42. Stresses in the reinforcement at position ECV 12-11-10-9. Chainage 411+348

ECV 12-11 **411+348**	M [KNm/m]	134,87	
	N [kN/m]	-358,37	
		model	field
	σ_C [MPa]	-0,68	-1,5
	σ_S [MPa]	-1,01	-5
	$\sigma_{S'}$ [MPa]	3,26	-7,5

ECV 10-9 **411 + 348**	M [KNm/m]	126,64	
	N [kN/m]	-401,244	
		model	field
	σ_C [MPa]	-0,66	-2,2
	σ_S [MPa]	-0,43	-11
	$\sigma_{S'}$ [MPa]	3,19	-7,5

Table 3.43. Stresses in the reinforcement at position ECV 8-7-6-5. Chainage 411+348

ECV 8-7	**411+348**	M [KNm/m]	149,23	
		N [kN/m]	-449,16	
			model	field
		σ_C [MPa]	-0,49	-2,9
		σ_S [MPa]	0	-14,5
		$\sigma_{S'}$ [MPa]	2,43	-2,9

ECV 6-5	**411 + 348**	M [KNm/m]	553,78	
		N [kN/m]	-386,40	
			model	field
		σ_C [MPa]	-2,04	-2
		σ_S [MPa]	-26,14	-10
		$\sigma_{S'}$ [MPa]	9,13	-4,2

Table 3.44. Stresses in the reinforcement at position ECV 4-3-2-1. Chainage 411+348

ECV 4-3	**411+348**	M [KNm/m]	300,66	
		N [kN/m]	-385,418	
			model	field
		σ_C [MPa]	-1,69	-2,4
		σ_S [MPa]	-13,57	-12
		$\sigma_{S'}$ [MPa]	7,63	-4,8

ECV 2-1	**411 + 348**	M [KNm/m]	92,205	
		N [kN/m]	-378,429	
			model	field
		σ_C [MPa]	-0,53	-0,44
		σ_S [MPa]	-0,08	-9
		$\sigma_{S'}$ [MPa]	-2,59	-14,2

Table 3.45. Stresses in the reinforcement at position ECV 12-11-10-9. Chainage 411+468

ECV 12-11	**411+468**	M [KNm/m]	-67,71	
		N [kN/m]	-144,89	
			model	field
		σ_C [MPa]	-0,27	-2,3
		σ_S [MPa]	1,48	-11,5
		$\sigma_{S'}$ [MPa]	-3,86	-9,8

ECV 10-9	**411+468**	M [KNm/m]	-36,7	
		N [kN/m]	-165,23	
			model	field
		σ_C [MPa]	-0,19	-1,36
		σ_S [MPa]	-0,37	-
		$\sigma_{S'}$ [MPa]	-2,83	-6,8

Table 3.46. Stresses in the reinforcement at position ECV 8-7-6-5. Chainage 411+468

ECV 8-7	**411+468**	M [KNm/m]	76,47	
		N [kN/m]	-179,49	
			model	field
		σ_C [MPa]	-0,31	-2,86
		σ_S [MPa]	-4,48	-14,3
		$\sigma_{S'}$ [MPa]	1,29	-3,8

ECV 6-5	**411+468**	M [KNm/m]	453,614	
		N [kN/m]	-126,12	
			model	field
		σ_C [MPa]	-0,59	-2,9
		σ_S [MPa]	-0,186	-14,5
		$\sigma_{S'}$ [MPa]	-8,63	-6,3

Table 3.47. Stresses in the reinforcement at position ECV 4-3-2-1. Chainage 411+468

ECV 4-3 411+468	M [KNm/m]	70,09		**ECV 2-1 411+468**	M [KNm/m]	-15,9	
	N [kN/m]	-162,05			N [kN/m]	-154,27	
		model	field			model	field
	σ_C [MPa]	-0,35	-3,3		σ_C [MPa]	-0,138	-2,4
	σ_S [MPa]	-1,88	-16,5		σ_S [MPa]	-0,34	-12
	$\sigma_{S'}$ [MPa]	0,85	-7,8		$\sigma_{S'}$ [MPa]	-0,74	-

Table 3.48. Stresses in the reinforcement at position ECV 12-11-10-9. Chainage 411+707

ECV 12-11 411+707	M [KNm/m]	58,384		**ECV 10-9 411+707**	M [KNm/m]	272,0,25	
	N [kN/m]	-214,019			N [kN/m]	-196,013	
		model	field			model	field
	σ_C [MPa]	-0,32	-2,04		σ_C [MPa]	-1,603	-2,04
	σ_S [MPa]	-1,55	-9,3		σ_S [MPa]	-6,89	-10,2
	$\sigma_{S'}$ [MPa]	0,04	-10,2		$\sigma_{S'}$ [MPa]	21,07	-5,5

Table 3.49. Stresses in the reinforcement at position ECV 8-7-6-5. Chainage 411+707

ECV 8-7 411+707	M [KNm/m]	778,476		**ECV 6-5 411+707**	M [KNm/m]	79,801	
	N [kN/m]	-135,619			N [kN/m]	-235,214	
		model	field			model	field
	σ_C [MPa]	-2,89	-2,6		σ_C [MPa]	-0,26	-1,9
	σ_S [MPa]	-12,24	-13		σ_S [MPa]	-1,28	-9,5
	$\sigma_{S'}$ [MPa]	63,67	-1		$\sigma_{S'}$ [MPa]	0,014	-1,2

Table 3.50. Stresses in the reinforcement at position ECV 4-3-2-1. Chainage 411+707

ECV 4-3 411+707	M [KNm/m]	-92,308		**ECV 2-1 411 + 707**	M [KNm/m]	-118,135	
	N [kN/m]	-233,91			N [kN/m]	-218,124	
		model	field			model	field
	σ_C [MPa]	-0,46	-1,5		σ_C [MPa]	0,62	-1,64
	σ_S [MPa]	0,84	-7,5		σ_S [MPa]	2,67	-5
	$\sigma_{S'}$ [MPa]	-2,23	0		$\sigma_{S'}$ [MPa]	-2,88	-8,2

For case e model, results presented in Figure 3.42, Figure 3.43 and Figure 3.44 are acquired. As expected, with 10 meters distribution extension stress values are the lowest ever calculated. The overall response of the lining seems to lead to a stress state that not exceed 14 MPa, but still there are some very high calculated values. It can be said that mostly the magnitude of the response might be comparable to the measured one. Nevertheless, tensile stresses have not disappeared.

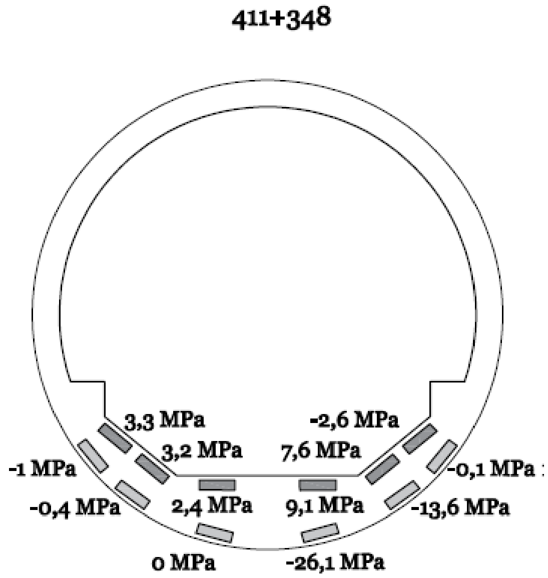
411+348
3,3 MPa
-2,6 MPa
3,2 MPa
7,6 MPa
-1 MPa
-0,1 MPa
-0,4 MPa
2,4 MPa
9,1 MPa
-13,6 MPa
0 MPa
-26,1 MPa

Figure 3.42. Calculated stresses in reinforcement bars at chainage 411+348 with case e swelling distribution

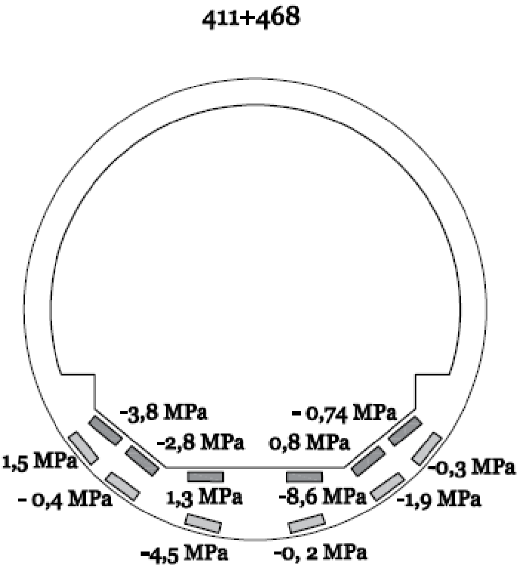
411+468
-3,8 MPa
- 0,74 MPa
-2,8 MPa
0,8 MPa
1,5 MPa
-0,3 MPa
- 0,4 MPa
1,3 MPa
-8,6 MPa
-1,9 MPa
-4,5 MPa
-0, 2 MPa

Figure 3.43. Calculated stresses in reinforcement bars at chainage 411+468 with case e swelling distribution

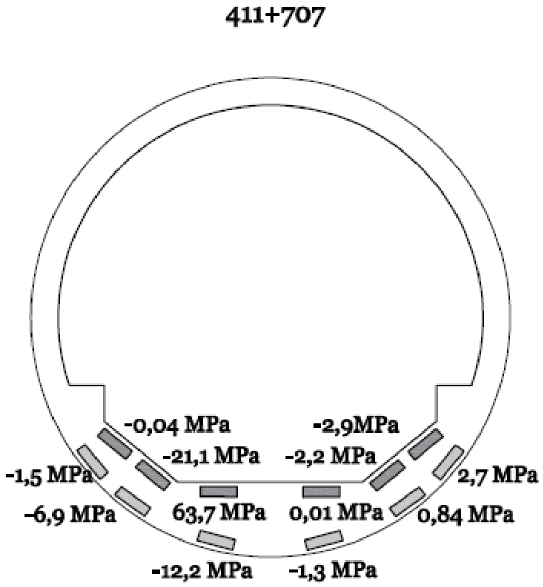

Figure 3.44. Calculated stresses in reinforcement bars at chainage 411+707 with case e swelling distribution

3.5 Conclusions

The different cases analysis intended to provide a valuable model for the evolution of swelling pressures against the lining and the ground behaviour in terms of expansive mechanism. The long-term monitoring of the reinforced Lilla tunnel and its interpretation was the starting point of the modelling. Specifically, the monitoring results permitted to evaluate stresses developed in the resisting structure which are used in the present work as comparison term to verify the reliability of the model.

Based on the results and the discussions, it seems that the stresses measured in reinforcement bars cannot be explained only by the considered distribution of swelling pressures against the lining. It could be stated that the two-dimensional (plane strain) hypothesis that was adopted for the latter analysis appear not to be completely correct. Even tough numerical analysis of geotechnical problems is generally worked out using the plane strain condition, far from the advancing front (Segato & Scarpelli, 2006), it is clear that the response of the Lilla tunnel circular lining cannot be interpreted by a two-dimensional formulation.

The modelled heterogeneous distribution of swelling pressure eventually leads to steel bar stresses values very different from the extensometer captured records. With the different cases analysis eventually, the magnitude of the stresses is managed to be reduced but the tensile stresses development cannot be solved. Therefore, it is evident that, with the two-dimensional finite element analysis present in Chapter 3, the heavy reinforcement of concrete circular lining does not entirely work in compression as it was measured. The model does not appear to be suitable for the assessment of the Lilla tunnel lining behaviour.

Furthermore, other remarkable results are the magnitude variability of the stresses and their order of magnitude. In many few cases the pattern of the monitored results in terms of reinforcement stresses has been reproduced. From the measured response of the Lilla tunnel, upper and lower bars stresses seem not to follow a predictable distribution, neither varying from one device position to another in the same invert nor in different cross-sections along the tunnel. Inner part extensometers may measure stress values greater than outer part extensometers in one position, while in the other positions register bigger values in the outer part extensometers. The alternation of the stress values magnitude is found both in different instrumentation positions in the same cross section and in the same instrumentation position at different cross sections. This behaviour is not reproduced by the stresses calculated from the set of internal forces generated with the PLAXIS analysis. Hence, the apparently random alternation of compression stress magnitudes appears not to be captured entirely with the analysis. Regarding the orders of magnitude, the measured stresses have rather low values, they stay in a range between 0 and 14 MPa. On the other hand, calculated stresses vary in much wider ranges, depending on the imposed distribution. With the first three analysis (case a, case b and case c) the stress values are completely overestimated. Even tough with the last two models it was possible to adjust the overall order of magnitude, discrepancies between the model and the monitoring data were still found.

It is concluded that the Lilla tunnel lining response is fundamentally different from the modelling assumptions made in the present Chapter. The explanation lies in the fact that variability in the longitudinal direction was not considered as the structure was calculated under two-dimensional, plane-strain conditions and. Indeed, the response of Lilla tunnel is characterised by a strong variability in both transversal (different measurements in a given cross-section) and longitudinal direction (different cross-sections). This heterogeneous response may be attributed to the irregular distribution of anhydrite concentration, details of natural rock fracturing and local phenomena (water infiltration). Hence, the expected longitudinal variability should be considered when comparing field data with the response of the numerical analysis.

CHAPTER 4
3D FINITE ELEMENT METHOD ANALYSIS

Tunnel linings present a significant 3D response when they are subjected to localized swelling loads or to expansive phenomena that produce different deformations. The subject of this chapter is the lining response mobilized in such conditions, determining the structural behaviour of the support in terms of stresses. A complete set of numerical analyses is carried out on a 3D numerical model that accurately reproduces the Lilla tunnel circular section. Numerical results show the lining three-dimensional structural response when subjected to localized loads, representing the swelling pressures measured from 2005 to 2011 in the Lilla tunnel.

4.1 First model definition

It has been pointed out the necessity of accurately comprehend the three-dimensional effects governing the structural response of the Lilla tunnel lining when analysing its behaviour under swelling loads. According to Chapter 3 analysis and discussion, the consideration of the variability in the longitudinal direction is crucial for the estimation of the lining behaviour. For this reason, a three-dimensional model has been developed in Chapter 4 to reproduce the high strength concrete circular lining. Alonso's studies (Alonso, Berdugo & Ramon, 2013) showed that the implications of accounting for the variability in the longitudinal direction are positive because the massive reinforced concrete tube is well prepared to resist a three-dimensional heterogeneous distribution of 'point loads' on its outer boundary.

The present chapter analyses and describes the structural mechanisms and phenomena involved in the transfer of forces between a cylinder representing the tunnel and the adjacent expansive soil, clearly determining the influence of the most relevant parameters in the structural response of the lining. For such purpose, a 3D numerical model is developed in order to reproduce the structural response of the tunnel support, especially the variable stress state in the concrete cylinder. The structural response of the Lilla tunnel circular section is analysed under localized swelling loads for different scenarios of ground stiffness. The detailed analysis of the numerical results provides significant conclusions about the three-dimensional response of the structure in terms of compression stress levels in the tunnel lining.

The three-dimensional finite element soil-tunnel interaction is addressed by the use of program Kratos as solver program with the GiD interface (pre and post processor). The determination of the three-dimensional response of Lilla tunnel lining under localized swelling loads is tackled through the numerical analysis of a concrete cylindrical tube. The distribution of punctual loads, equivalent to the measured swelling pressure, has been applied on the central part of the cylinder invert, on a grid extended 12,5 m below the invert. The results in terms of stresses will be compared to those measured.

The tunnel structure is modelled as a 52,5 m long cylinder in a three-dimensional space. The longitudinal axis is represented by the z-axis (see Figure 4.1). In the longitudinal direction, the cylinder is composed by two lateral stretches of 20 meters and a central one of 12,5 m as it is illustrated in Figure 4.2. The circular cross-section is the one represented in Figure 2.34.

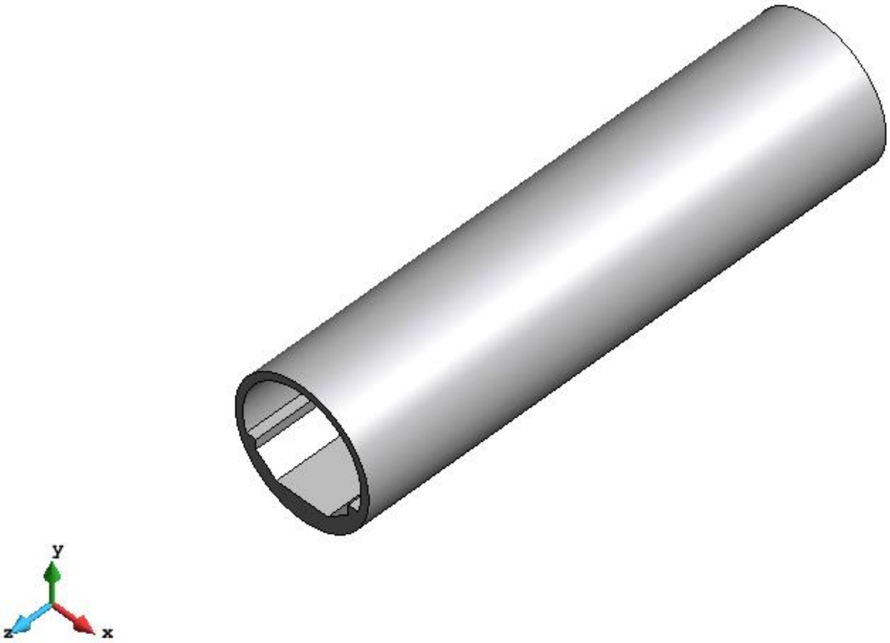

Figure 4.1. Tunnel cylindrical structure

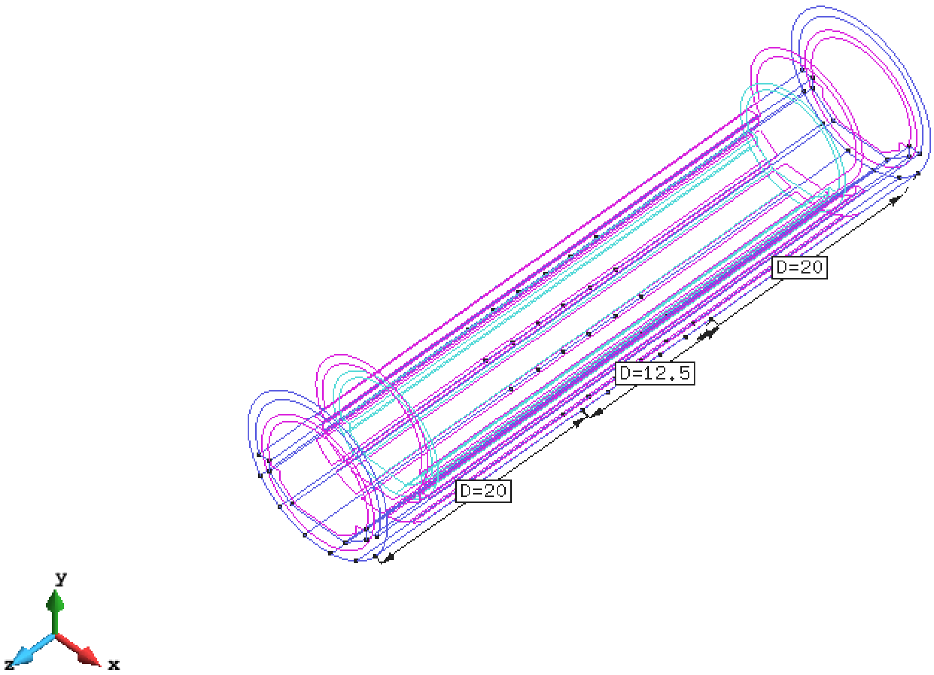

Figure 4.2. Geometrical model of the tunnel

In the present structural analysis, the cylinder is made of concrete. The mechanical properties assigned to the high strength concrete structure are equivalent to the ones used in the plane strain analysis, they are presented in the table below.

Table 4.1. Concrete's properties

		value	unit
Properties	Young's modulus	42	MPa
	density	2550	kg/m^3
	Poisson's ratio	0,15	

In the modelling process, various assumptions were incorporated. Regarding the boundary conditions, the two external surfaces are left free to move in the y-direction while the displacement in the x-direction and z-direction is restrained.

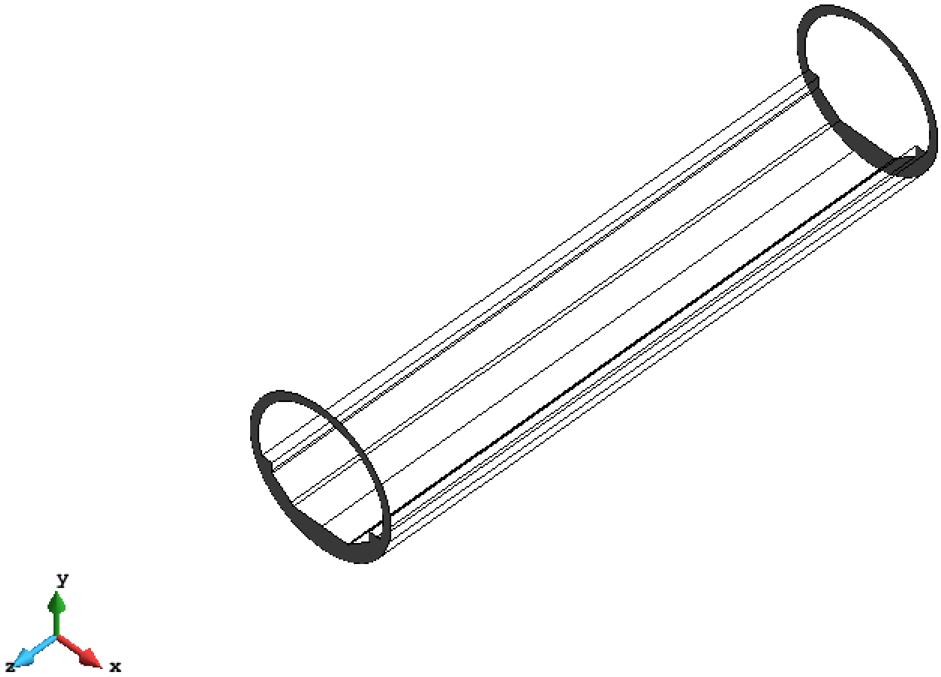

Figure 4.3. Boundary conditions

The three-dimensional response of the lining is provided by the structural interaction of the support and the ground; therefore, it is directly conditioned by the configuration a spring stiffness coefficient. The interaction between soil and the tunnel lining is presented via the spring stiffness in this model. According to Alonso and Sagaseta (2003), the spring stiffness coefficient k, for soil-circular tunnel interaction, is directly related with the elastic shear modulus of the rock massif, G, through the relationship:

$$k = \frac{\Delta p}{s} = \frac{2G}{r} \qquad \text{Eq. 4.1}$$

Where Δp is the applied unit radial pressure, s the corresponding displacement and r the radius of the tunnel. Eq. 4.1 is valid when a uniform pressure p acts on the ground in the internal part of the circular tunnel. If distributed loads are applied to a sector of the perimeter, the lining stiffness will help to distribute the loads all over the perimeter, and this will make the equation sufficiently valid.

To study the effect of the rigidity of the rock massif, different values of the modulus of shear have been considered. The spring coefficient is consequently calculated through Eq. 4.1, considering the radius of the tunnel equal to 6 meters. In Table 4.2 are presented the different combination of shear modulus and spring coefficient used for the analyses.

Table 4.2. Values of shear modulus and spring coefficient considered

Shear modulus G [MPa]	Spring coefficient [N/m^3]
1000	$0,3333\ 10^{9}$
500	$0,16666\ 10^{9}$
100	$0,3333\ 10^{6}$

Hence, three cases will be carried out varying k value in every analysis. The spring coefficient value has been assigned to the exterior surface of the tunnel, the one in contact with lining and soil (see Figure 4.4). Referring to a cross-section plane, springs have been considered to act in horizontal (x-axis) and vertical (y-axis) direction with the same value of k (the one calculated with Eq. 4.1); longitudinal direction (z-axis) has not been deemed relevant concerning the spring coefficient contribution.

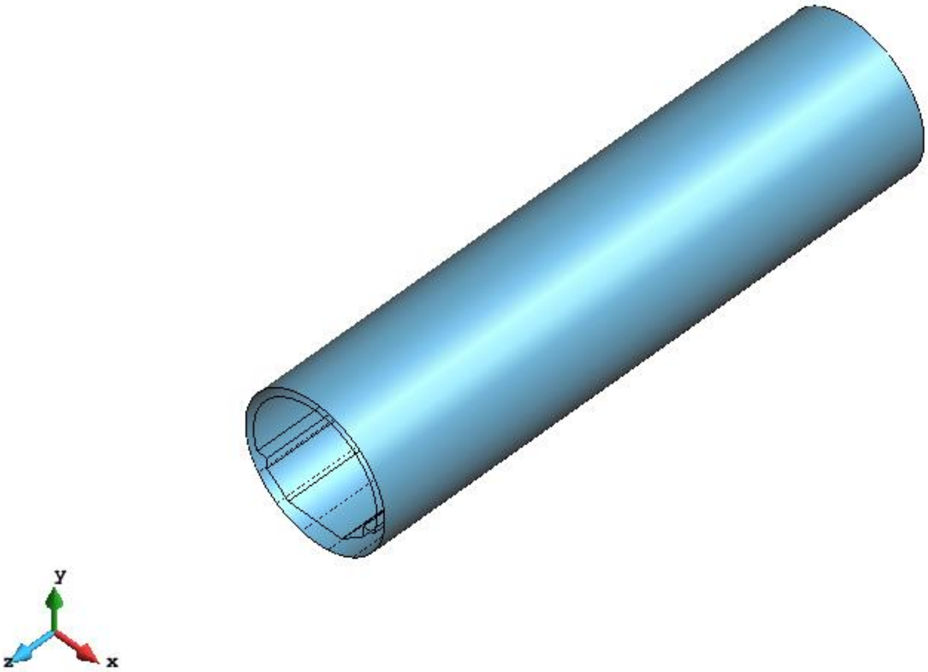

Figure 4.4. Spring stiffness condition

4.2 Swelling loads definition

From the previous chapter, it is concluded that a significant three-dimensional response of the lining should be expected when certain ground scenarios can cause localized loads over certain tunnel sections, i.e. swelling phenomena. Therefore, an important aspect to consider is the pressure that the ground exerts on the lining. In this regard, the readings of the total pressure cells, measured in the period 2005-2011 and plotted in Figs 2.38-2.44, indicated that, although almost all of them remained below the value of 3 MPa, there were other cases in which such pressure value was widely exceeded. Radial pressure records measured in the 36 installed cells under the counter-vault are presented in Figure 4.5 in the form of a histogram. It can be seen that most of the readings give small values (below 1,5 MPa). However, three of them measure values above 5 MPa, with a maximum of 6,71 MPa.

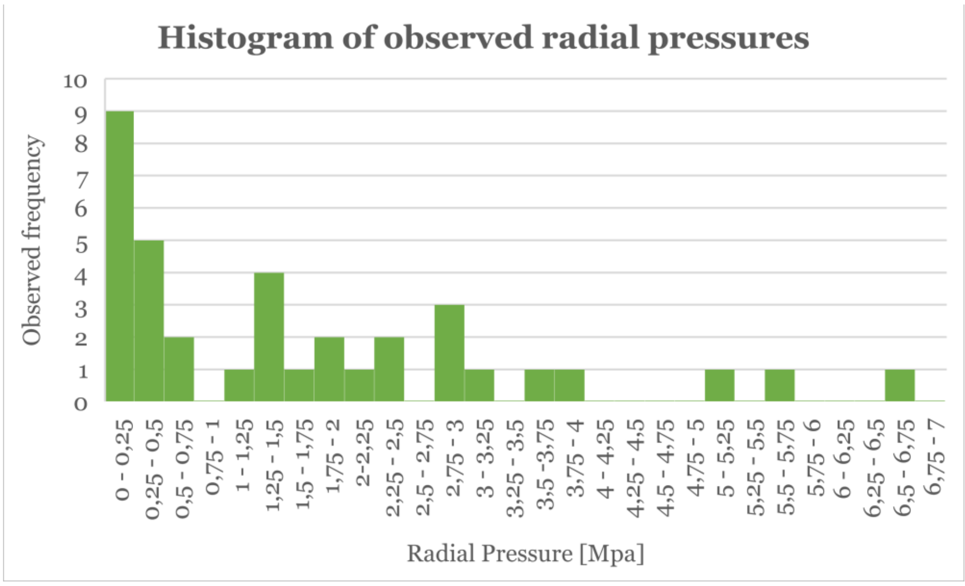

462

Figure 4.5. Histogram of observed radial pressures

As mentioned previously in the work, the distribution of values is erratic and does not follow a clear pattern: the maximum values measured coexist in a same section in only one of the cells, with low values in the others, as it is evident from Figure 2.45.

A first attempt to reproduce the distribution of the swelling pressure was done in chapter 3 but no significative results was found. In this context, a second step to go further in the investigation of the real swelling distribution is to assess the degree of uncertainty of the available data. Plotting the frequency of occurrences of the observed data in intervals of pressure in bars yields the histogram of Figure 4.5. The height, and more usefully, the area, of each bar are proportional to the number of occurrences in that interval. It is evident that pressure records between 0 and 0,25 MPa were the most frequent. If relative frequencies, which corresponds to the ratio of the observed frequencies (the ordinates of Figure 4.5) by the total number of events (36 in the study), is divided by the interval length a probability density function would result. In assigning the probabilities plotted in Figure 4.5 to a mathematical model (the probability density function), the observed frequencies have been smoothed to facilitate their description and use (Benjamin and Cornell, 1970). Thus, while the histogram is a representation of the observed empirical data, the probability density function describes the probability law of mathematical variables. The probability density function modelling the histogram of Figure 4.5 is plotted in light blue colour in Figure 4.6. Such "PDF", probability density function, seem not to have a mathematical expression easy to identify. Therefore, a distribution with a known and simple expression has been modelled to approximate the probability density function. This distribution has the shape of an exponential function and it is illustrated in green in Figure 4.6. The chosen exponential function has the following expression:

$$f(x) = A + Bexp^{(-\alpha x)} \qquad \text{Eq. 4.2}$$

The exponential function has been found imposing the conditions reported below:

$$\begin{cases} f(x) = 1 & x = 0 \\ f(x) = 0{,}2 & x = 2 \\ f(x) = 0{,}02 & x = 6 \end{cases} \qquad \text{Eq. 4.3}$$

Hence, the resulting mathematical expression is:

$$f(x) = 0{,}0173 + 0{,}9827exp^{(-0{,}8412x)} \qquad \text{Eq. 4.4}$$

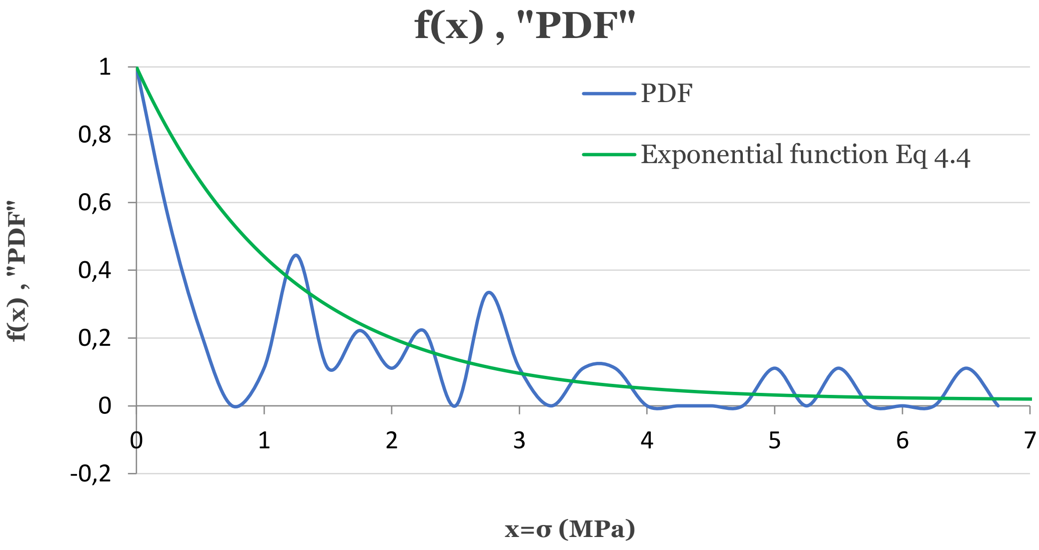

Figure 4.6. Probability density function and exponential distribution

To reproduce the swelling pressure pattern exerted against the curved invert of the Lilla tunnel, the idea is to create a fictitious distribution of swelling pressures, whose probability density function coincide to the one of the measured data (see Figure 4.6). Within this framework, the creation of the loading distribution is done through a random number generator. In the present study the random number generation has been carried out with the *rand* function of Matlab program. In Appendix B, details of the code are presented. The code includes the generation of random numbers and the consequent evaluation of random values of swelling pressure. By the generation of a sequence of numbers that cannot be predicted better than by a random chance, the truly randomness of the resulting distribution is ensured. From a set of random numbers in between 0 and 1, the corresponding values of probability density function have been calculated. For instance, if 0,5 is the random number chosen it means that function $f(x)$ of Eq. 4.4 value is 0,5. The equation then need to be inverted to find the value of the x (swelling pressure) (see Appendix B for more details).

It has been chosen a set of 36 numbers, which eventually leads to a grid of 36 (6x6) punctual forces defining the swelling distribution. This grid of loads is extended for 12,5 meters in the longitudinal direction below the curved invert of the tunnel. This loading condition is assumed to model, in the most realistic way, the measured radial pressure exerting by the soil on the lining.

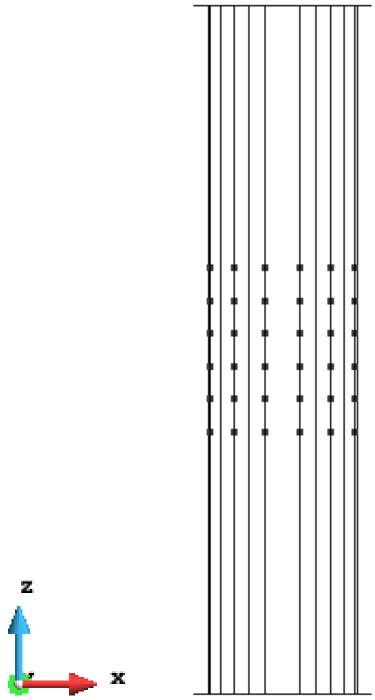

Figure 4.7. Grid of 36 swelling loads from x-z plane

Every loading point is distant from the others, in both longitudinal and transversal direction, 2,5 meters. A punctual force directed to in the radial direction is applied to every point and it is calculated through the exponential function using a random number. The set of 36 random numbers used for the analysis is presented below:

Table 4.3. Set of random numbers

Random numbers

0,669	0,5996	0,8322	0,108	0,8487	0,5078
0,5002	0,056	0,6174	0,517	0,9168	0,5856
0,218	0,0563	0,0196	0,1432	0,987	0,7629
0,5716	0,1525	0,8639	0,5594	0,5051	0,083
0,1222	0,5201	0,0977	0,4406	0,2714	0,6616
0,6712	0,4352	0,9081	0,7667	0,1008	0,517

Once these random numbers are inserted in the exponential function expression, 36 values of the function are obtained. Then, inverting the mathematical expression of the function (details of the Matlab code are provided in Appendix B), the 36 values of swelling pressures are easily randomly calculated. As the exponential function is not defined for values lower then 0,02, due to the conditions with which it has been found, a maximum value of pressure equal to 6 MPa is associated with numbers less than 0,02. In Eq. 4.3 the set of calculated pressure is presented.

Table 4.4. Set of swelling pressures in MPa

Swelling Pressures [MPa]

0,4732	2,3824	2,875	3,2162	2,1473	0,7497
0,3732	0,2531	0,0681	1,1434	1,6662	2,4498
0,9952	0,7757	6	1,6853	2,4443	0,2137
3,2271	0,0258	0,3304	0,2916	2,5357	0,5985
1,8475	3,3331	0,2657	1,0489	0,1908	1,3059
0,1309	1,017	0,1917	0,1345	0,6848	0,8344

Table 4.4 presents the punctual values that the swelling pressure distribution assumes in every point of the grid of Figure 4.7. For practical purposes, as the forces act on points, they should be expressed in Newtons (N). Pressure cells, which are intended to measure contact earth pressures on the surface of the concrete lining, on average have a diameter of 250mm. Multiplying the swelling pressure values in MegaPascals (MPa) by the area of a pressure cell, swelling loads in Newton are obtained and presented in the following table.

Table 4.5. Set of swelling forces in N

Swelling Forces [N]

23229	116946	141127	157873	105408	36799
18320	12425	3344,1	56127	81788	120252
48850	38075	294524	82727	119985	10492
158412	1265,9	16221	14314	124473	29376
90687	163611	13043	51487	9367,2	64104
6424,9	49920	9408,1	6600,4	33615	40957

These values represent the forces acting on every point of the grid. Therefore, these forces point to the centre of tunnel, as they come from values of radial pressure against the invert. Swelling forces modular values should be decomposed in their components in the vertical (y-axis) and horizontal (x-axis) direction to be inserted in the software for the finite element structural analysis. The x and y components of the forces can be calculated following the angles plotted in Figure 4.8. Components in the x direction are found multiplying the values of the forces by the *cosin* of the upper angle (respectively from right hand side, 35°, 57° and 79°) while y components multiplying by the *sin* of the same angle. Finally, the resulting values of the 36 punctual loads with both their vertical and horizontal components are presented in Table 4.6 and Table 4.7.

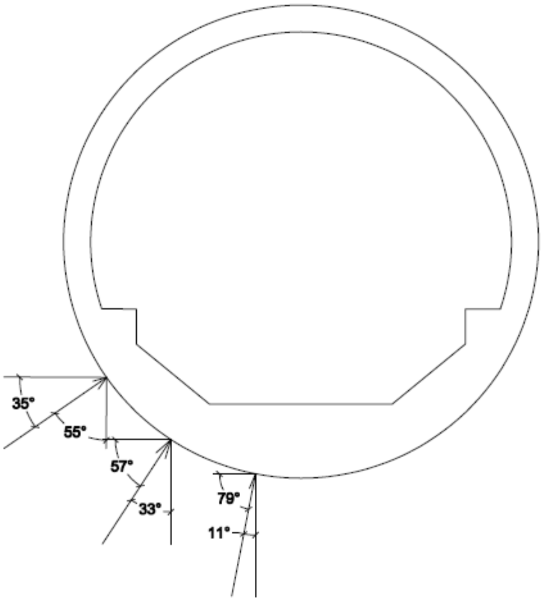

Figure 4.8. Forces components with respect to the perpendicular to the lining

Table 4.6. Set of swelling forces x component in N

Swelling Forces x component [N]					
19028	63694	26928	30124	57409	30144
15007	6766,9	638,09	10710	44545	98505
40016	20737	56198	15785	65348	8594,6
129763	689,45	3095,1	2731,2	67793	24064
74286	89109	2488,6	9824,2	5101,7	52511
5262,9	27188	1795,2	1259,4	18308	33550

Table 4.7. Set of swelling forces y component in N

Swelling Forces y component [N]					
13323	98079	138534	154972	88402	21107
10508	10420	3282,7	55096	68593	68974
28019	31933	289113	81207	100628	6018
90861	1061,7	15923	14051	104391	16850
52016	137216	12803	50541	7856	36769
3685,2	41866	9235,3	6479,1	28192	23492

The graphic representation of the grid of loads is illustrated in the following pictures. Figure 4.9 describes the cross-sectional view. Every cross section has six loads, which correspond to the six pressure cells placed at different chainages in Lilla tunnel. The distance between the loads in longitudinal direction is 2,5 meters while in the transversal it varies between 2m and 2,5m. For that reason, the total length of the grid is 12,5 m (see Figure 4.10). For a more comprehensive three-dimensional illustration, Figure 4.10Figure 4.11 and Figure 4.11. Global view of the swelling forces grid show the grid of swelling forces acting on the cylindrical tunnel.

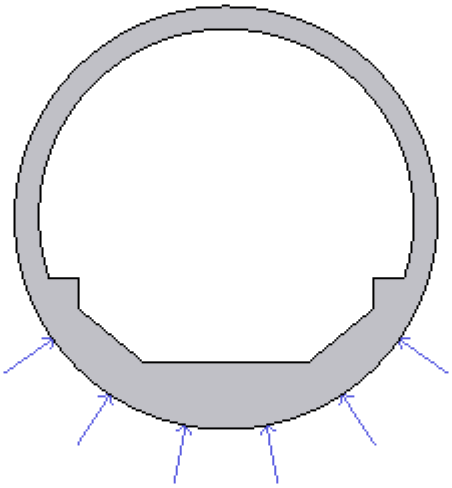

Figure 4.9. x-y plane view

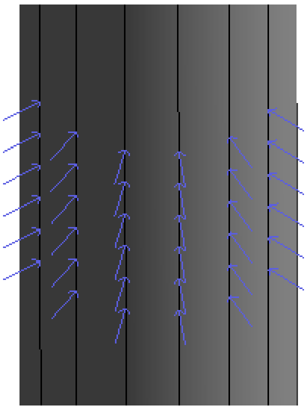

Figure 4.10. Grid of swelling forces in the x-z plane

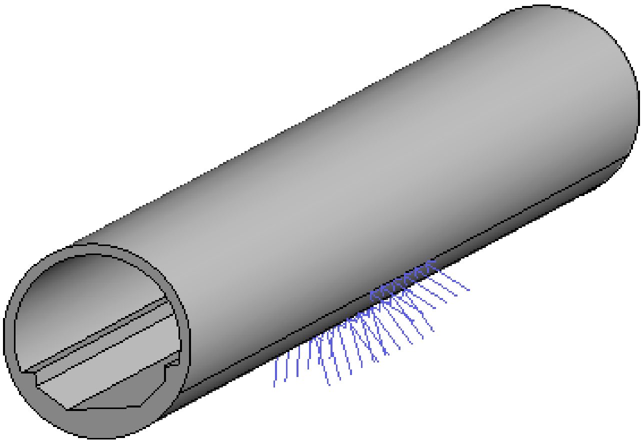

Figure 4.11. Global view of the swelling forces grid

4.3 Methodology

Chapter 4 modelling aims at the rectification of all discrepancies between Chapter 3 model and the monitoring data, converting the Lilla tunnel into a cylindrical heavily reinforced structure and applying a distribution of point loads to the invert boundary equivalent to the swelling pressure.

To prove if the model is suitable for reproducing the instrumented lining behaviour, once again reference will be made with the monitoring results covering the period 2005-2011. Relevant results in terms of stresses in the steel reinforcement of the Lilla tunnel invert will be used to demonstrate if the three-dimensional analysis adjusts the observed behaviour. Hoop stresses at every 12 extensometer positions, measured at seven cross sections and extrapolated from Figure 2.38, Figure 2.39, Figure 2.40, Figure 2.41, Figure 2.42, Figure 2.43 and Figure 2.44 are presented below.

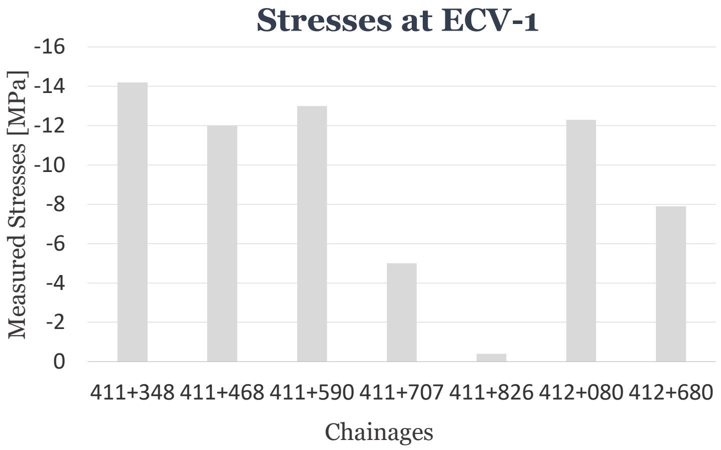

Figure 4.12. Measured hoop stresses at ECV-1 at different cross sections

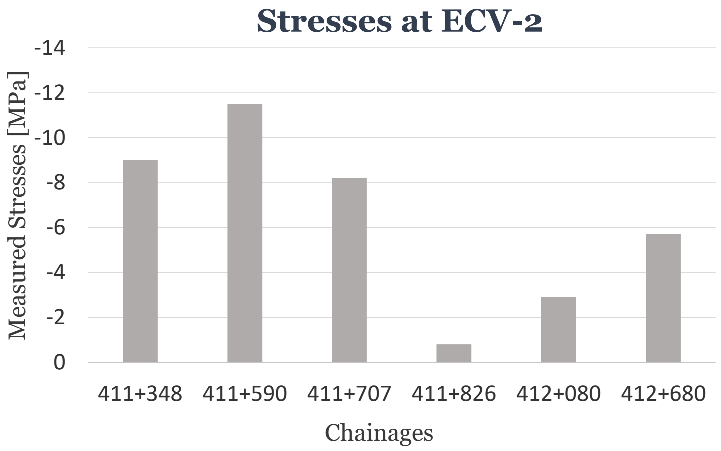

Figure 4.13. Measured hoop stresses at ECV-2 at different cross sections

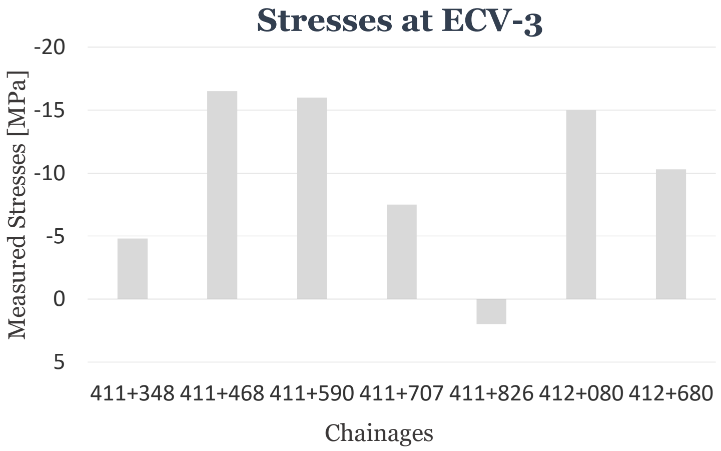

Figure 4.14. Measured hoop stresses at ECV-3 at different cross sections

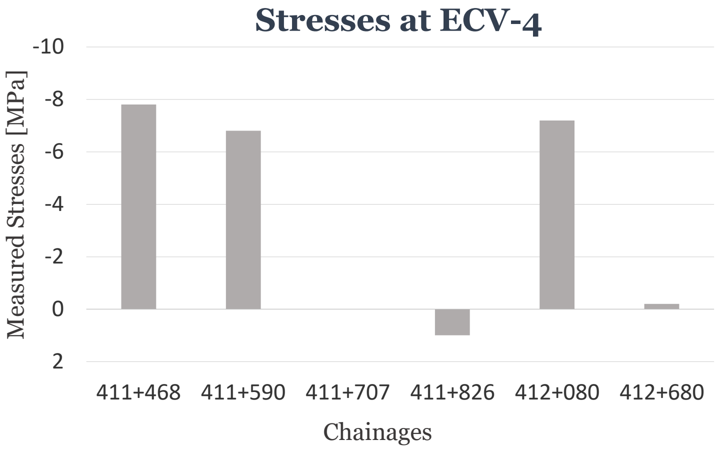

Figure 4.15. Measured hoop stresses at ECV-4 at different cross sections

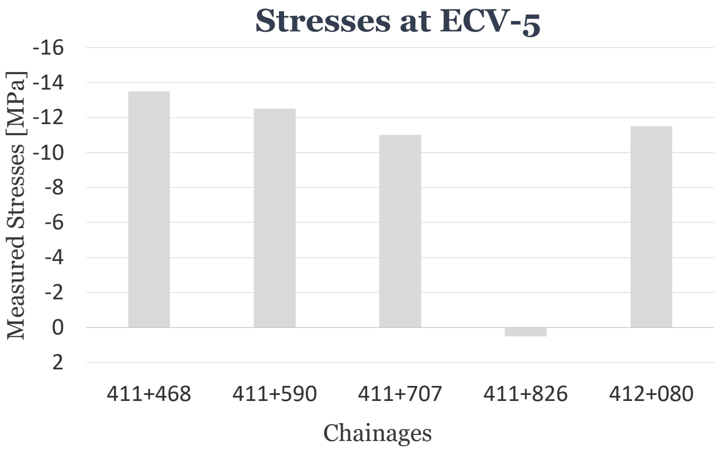

Figure 4.16. Measured hoop stresses at ECV-5 at different cross sections

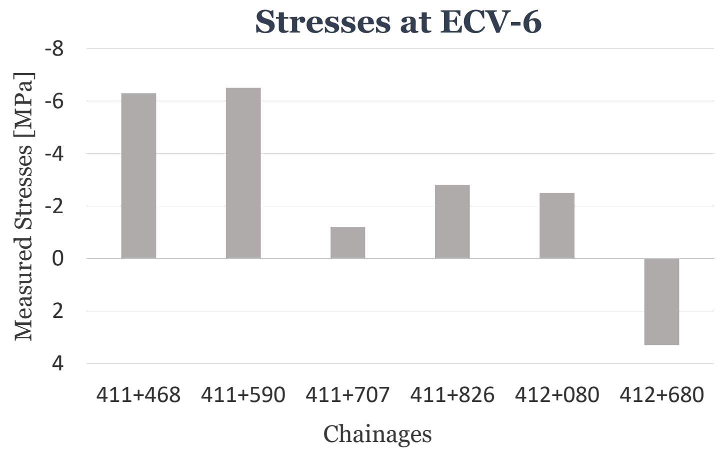

Figure 4.17. Measured hoop stresses at ECV-6 at different cross sections

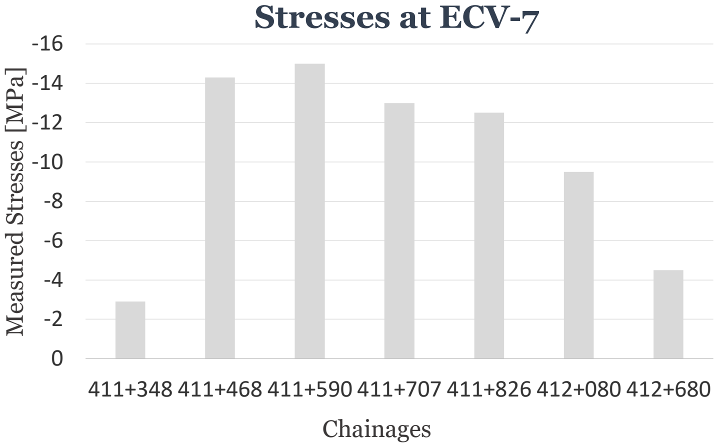

Figure 4.18. Measured hoop stresses at ECV-7 at different cross sections

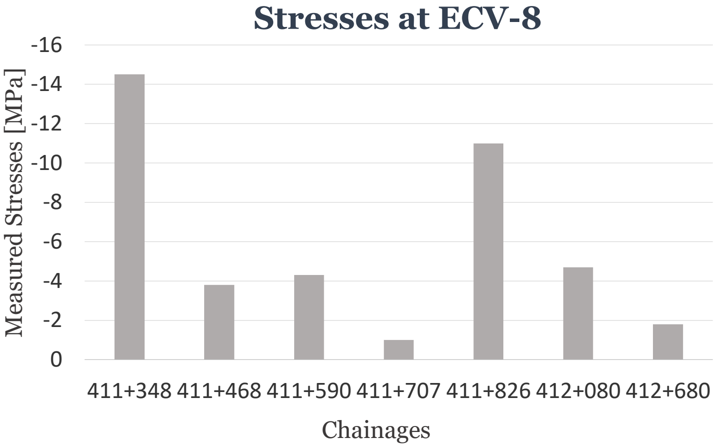

Figure 4.19. Measured hoop stresses at ECV-8 at different cross sections

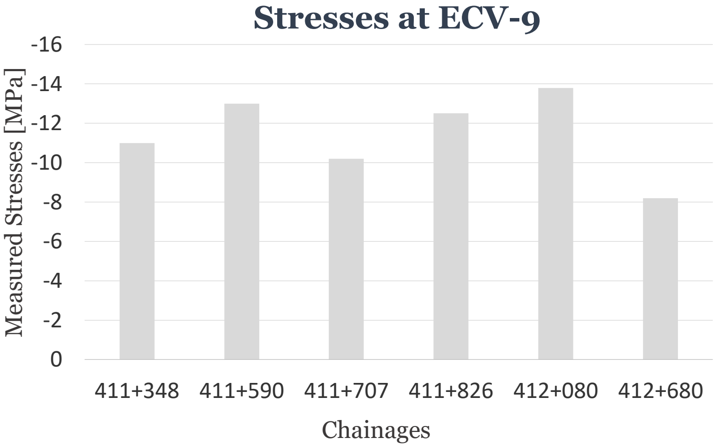

Figure 4.20. Measured hoop stresses at ECV-9 at different cross sections

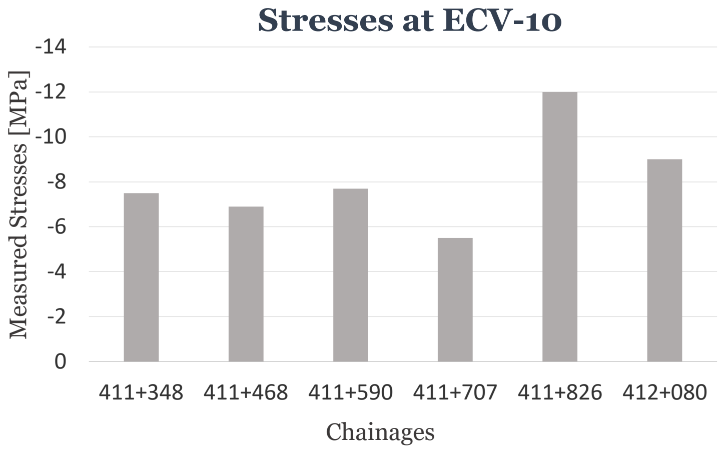

Figure 4.21. Measured hoop stresses at ECV-10 at different cross sections

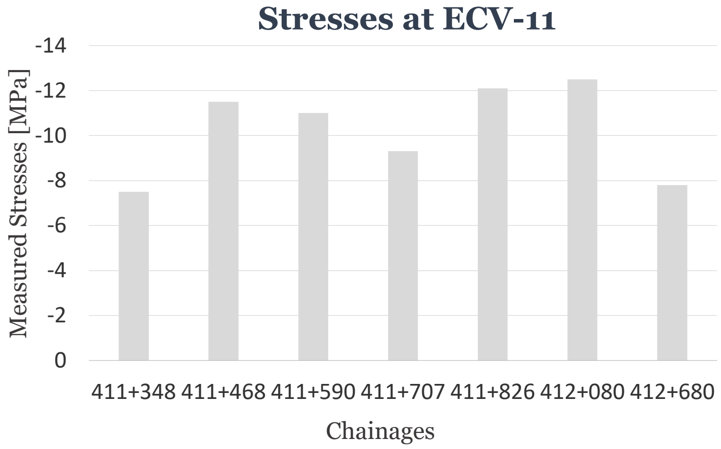

Figure 4.22. Measured hoop stresses at ECV-11 at different cross sections

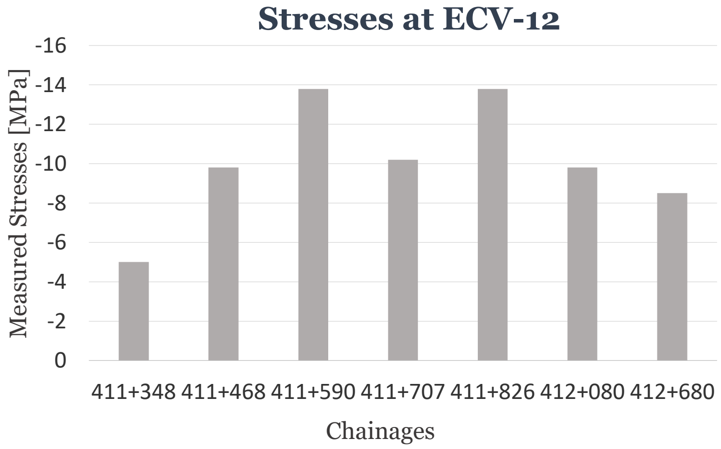

Figure 4.23. Measured hoop stresses at ECV-12 at different cross sections

Figures 4.12-4.23 represent the stress values at every position of the extensometers and at each one of the seven instrumented cross sections along the tunnel. For every device position, stresses mean value and standard deviation are calculated to indicate if measured readings tent to be close to the mean or spread out. Stress values mean values and deviations are reported in the tables below.

Table 4.8. Hoop stress values in MPa at ECV – 1-2-3-4

ECV - 1		**ECV - 2**		**ECV - 3**		**ECV - 4**	
411+348	-14,2	411+348	-9	411+348	-4,8	411+348	-12
411+468	-12	411+590	-11,5	411+468	-16,5	411+468	-7,8
411+590	-13	411+707	-8,2	411+590	-16	411+590	-6,8
411+707	-5	411+826	-0,8	411+707	-7,5	411+707	0
411+826	-0,4	412+080	-2,9	411+826	2	411+826	1
412+080	-12,3	412+680	-5,7	412+080	-15	412+080	-7,2
412+680	-7,9	mean	-6,35	412+680	-10,3	412+680	-0,2
mean	-9,257	SD	4,0024	mean	-9,729	mean	-4,714
SD	5,0603			SD	6,8327	SD	4,9731

Table 4.9. Hoop stress values in MPa at ECV – 5-6-7-8

ECV - 5		**ECV - 6**		**ECV - 7**		**ECV - 8**	
411+348	-4,2	411+348	-10	411+348	-2,9	411+348	-14,5
411+468	-13,5	411+468	-6,3	411+468	-14,3	411+468	-3,8
411+590	-12,5	411+590	-6,5	411+590	-15	411+590	-4,3
411+707	-11	411+707	-1,2	411+707	-13	411+707	-1
411+826	0,5	411+826	-2,8	411+826	-12,5	411+826	-11
412+080	-11,5	412+080	-2,5	412+080	-9,5	412+080	-4,7
mean	-8,7	412+680	3,3	412+680	-4,5	412+680	-1,8
SD	5,5767	mean	-3,714	mean	-10,24	mean	-5,871
		SD	4,3164	SD	4,8173	SD	4,9866

Table 4.10. Hoop stress values in MPa at ECV – 9-10-11-12

ECV - 9		**ECV - 10**		**ECV - 11**		**ECV - 12**	
411+348	-11	411+348	-7,5	411+348	-7,5	411+348	-5
411+590	-13	411+468	-6,9	411+468	-11,5	411+468	-9,8
411+707	-10,2	411+590	-7,7	411+590	-11	411+590	-13,8
411+826	-12,5	411+707	-5,5	411+707	-9,3	411+707	-10,2
412+080	-13,8	411+826	-12	411+826	-12,1	411+826	-13,8
412+680	-8,2	412+080	-9	412+080	-12,5	412+080	-9,8
mean	-11,45	mean	-8,1	412+680	-7,8	412+680	-8,5
SD	1,8866	SD	2,0306	mean	-10,24	mean	-10,13
				SD	2,0444	SD	3,0587

Mean stress values are taken as target values for comparison with the analysis results. They are showed in Figure 4.24 in a cross-sectional view to give a visual representation.

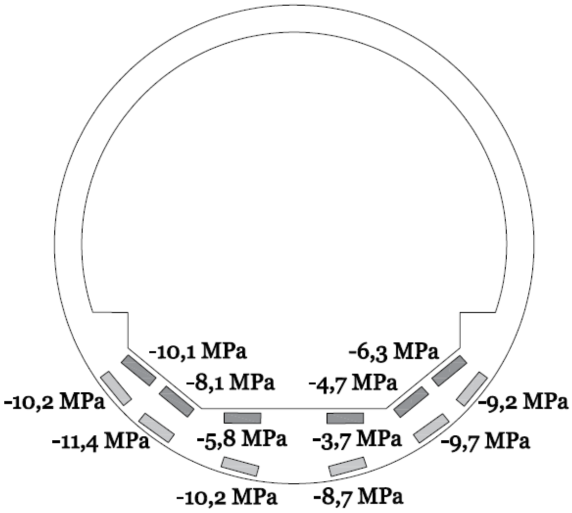

Figure 4.24. Measured mean hoop stresses values

If the model would have been analysed as an axisymmetric one in cylindrical coordinates, then, hoop stresses could have been evaluated immediately. However, this is not the case. Chapter 4 model has been developed with a three-dimensional formulation in the cartesian reference system. Thus, hoop stresses cannot be obtained directly from the solver program. In order to evaluate circumferential stresses (=hoop stresses), a representative cross section in the middle of the tunnel longitudinal direction becomes the focus of the study, as if it was cut and extrapolated from the cylinder. Therefore, the central cross-section can be analysed in two dimensions so that a plane stress transformation can be performed to achieve the knowledge of hoop stresses.

Acknowledging that the whole problem is of a three-dimensional type and that the stress state in every element is characterized by all the components of the Cauchy stress tensor, it is here assumed that an element in the central cross section of the tunnel can be investigated under two-dimensional conditions. Thus, the faces of such element are subjected only to stresses in the x-y plane, i.e. σ_{xx}, σ_{yy} and τ_{xy} (see Figure 4.25a).

In this context, the stress transformation in two dimensions, to pass from cartesian stresses to hoop ones, is a problem of finding stresses along a given normal direction, which for the present work coincides with the circumferential. The purpose of the stress transformation is to find normal stresses in terms of rotated coordinate system, namely stresses acting in the normal direction inclined by a θ angle (see Figure 4.25b). Therefore, if normal directions are orientated as the circumferential ones, then normal stresses correspond to hoop stresses. Figure 4.25 (a) illustrates the actual situation while Figure 4.25 (b) represents a generic element inclined by an angle of θ with respect to the horizontal direction.

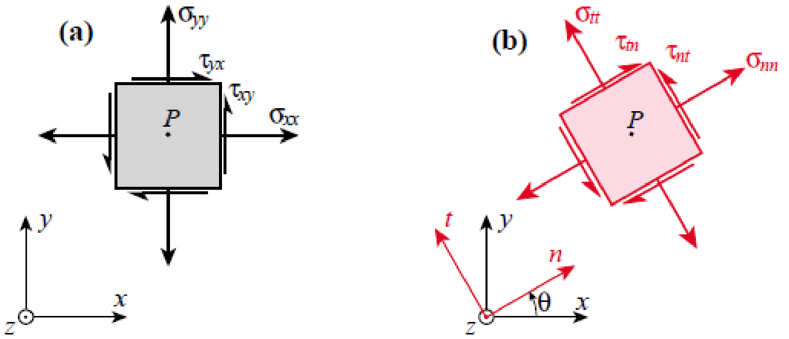

Figure 4.25. Global axes x,y (a). Local axes n,t rotated by θ with respect to x,y

The transformation equations may be written as:

$$\sigma_{nn} = \frac{\sigma_{xx}+\sigma_{yy}}{2} + \frac{\sigma_{xx}-\sigma_{yy}}{2} cos(2\theta) + \tau_{xy} sen(2\theta)$$
$$\sigma_{tt} = \frac{\sigma_{xx}+\sigma_{yy}}{2} - \frac{\sigma_{xx}-\sigma_{yy}}{2} cos(2\theta) - \tau_{xy} sen(2\theta) \qquad \text{Eq. 4.5}$$
$$\tau_{nt} = -\frac{\sigma_{xx}-\sigma_{yy}}{2} sen(2\theta) + \tau_{xy} cos(2\theta)$$

Imaging of virtually rotate a generic element in the device position, the element passes from the situation plotted in Figure 4.25a to the one in Figure 4.25b. If the rotation is carried out in such a way that the rotated element has a normal coinciding with the circumferential direction in that point, only normal stresses are of interest for the model interpretation to be compared to real hoop stresses.

The θ angle varies depending on the position of the extensometers. Referring to the extensometers enumeration provided in Figure 2.38-Figure 2.44, elements in ECV-1 and ECV-2 position should be rotated with an angle of 51° in the counter clockwise sense with respect to the horizontal direction (x-axis), elements in ECV-3 and ECV-4 with a 36° angle in the same direction and elements in ECV-5 with a 15° angle. ECV-6 and ECV-8 extensometers elements do not need any rotation because the horizontal direction already corresponds to the circumferential in that points. Thus, horizontal stresses are equivalent to the circumferential ones in those two positions. Extensometers elements in right hand side of the cross-section should be rotated with the same angle of the ones in the left but in clockwise sense. For instance, for elements in ECV-11 and ECV-12 position the rotation would be of -51°. With the same path of reasoning rotation angles can be evaluated easily for all elements position.

Eventually, normal stresses acting on the rotated different elements can be esteemed as circumferential stresses and compared to the Lilla tunnel reinforcement bars monitoring results dating 2011.

It is noteworthy to remind that the explained methodology and procedure refer to the analysis of the cylindrical concrete tube, while available monitoring data is related to the invert steel reinforcement. Therefore, concrete stresses should be switch to steel stresses. Compatibility of deformation is accepted for the interface between concrete and steel reinforcement so that stresses in concrete and in bars differ by a factor depending on the respective elasticity moduli. If high strength concrete is assumed to have 42 GPa as Young's modulus and steel 210 GPa, then steel stresses are five times bigger than concrete ones.

4.4 Results and discussion

In this section the results acquired with the 6x6 grid model are discussed. They can be firstly appreciated in a form of a table, to get a first comprehension of the stress magnitude order. Results are differentiated in accordance with the different spring coefficient value assigned to the soil-lining interaction. Calculated stresses for every extensometer position in the central cross section of the cylindrical tunnel are reported above.

Table 4.11. Calculated stress values with 6x6 grid model and k=0,3333 10^9

	G=1000 Mpa k=0,3333 e9				
	σ_x [kPa]	σ_y [kPa]	τ_{xy} [kPa]	σ_n concr [kPa]	σ_n steel [kPa]
ECV - 1	-12	-20,3	-1,6	-18,6	**-92,9**
ECV - 2	-7,6	-8,8	-10,6	-18,7	**-93,5**
ECV - 3	-10	-14,6	-4,7	-16,1	**-80,3**
ECV - 4	-28	-19,4	-9,8	-34,3	**-171,7**
ECV - 5	-35	-12,2	-7,3	-37,1	**-185,6**
ECV - 6	-36			-36,0	**-180,0**
ECV - 7	-50	-14	12	-53,6	**-267,9**
ECV - 8	-33			-33,0	**-165,0**
ECV - 9	-17	-16	6	-22,4	**-111,8**
ECV - 10	-64	-26	34	-83,2	**-416,0**
ECV - 11	-27	-22	19	-42,6	**-212,8**
ECV - 12	-28	0	-9	-2,3	**-11,4**

Table 4.12. Calculated stress with 6x6 grid model and k=0,16667 10^9

	G=500 Mpa k=0,16666 e9				
	σ_x [kPa]	σ_y [kPa]	τ_{xy} [kPa]	σ_n concr [kPa]	σ_n steel [kPa]
ECV - 1	-16	-22	-2,7	-22,3	**-111,3**
ECV - 2	-11	-11	-12,5	-23,2	**-116,1**
ECV - 3	-12	-3,9	-26	-33,9	**-169,6**
ECV - 4	-45	-21	-14	-50,0	**-250,1**
ECV - 5	-36	-16	-7,3	-38,3	**-191,6**
ECV - 6	-48			-48,0	**-240,0**
ECV - 7	-53	-18	12	-56,7	**-283,3**
ECV - 8	-46			-46,0	**-230,0**
ECV - 9	-23	-20	6,6	-28,2	**-141,2**
ECV - 10	-62	-30	36	-85,2	**-425,9**
ECV - 11	-34	-40	36	-72,8	**-364,2**
ECV - 12	-34	-1,6	10,7	-24,9	**-124,5**

Table 4.13. Calculated stress values with 6x6 grid model and k=0,3333 10^8

	G=100 Mpa k=0,3333 e8				
	σ_x [kPa]	σ_y [kPa]	τ_{xy} [kPa]	σ_n concr [kPa]	σ_n steel [kPa]
ECV - 1	-5,4	-18	-1,3	-14,3	**-71,4**
ECV - 2	-31	-2	-21	-34,0	**-170,1**
ECV - 3	-9,4	-22	-7	-20,4	**-102,1**
ECV - 4	-77	-23	-29	-85,9	**-429,6**
ECV - 5	-16	-20	-5	-18,8	**-93,8**
ECV - 6	-88			-88,0	**-440,0**
ECV - 7	-35	-23	10	-39,2	**-196,0**
ECV - 8	-86			-86,0	**-430,0**
ECV - 9	-23	-19	1,5	-23,0	**-115,2**
ECV - 10	-118	-33	50	-136,2	**-680,9**
ECV - 11	-43	-43	38	-80,2	**-400,8**
ECV - 12	-59	-10	20	-49,0	**-244,8**

Table 4.11, Table 4.12 and Table 4.13 show the stresses in an element (virtually located in the extensometer position). Horizontal, vertical and shear stresses information (σ_x, σ_y and τ_{xy}) are extrapolated from the software while normal stresses in a rotated element in the extensometer position are calculated following the aforementioned Eq. 4.5.

The most evident result is surely the order of magnitude of the calculated values. Calculated results are expressed in terms of kPa while measured stresses vary between 0 and 15 MPa. Mean values of calculated steel normal stresses in Table 4.11, Table 4.12 and Table 4.13 are respectively -166kPa, -220 kPa and -281kPa while standard deviations are 105 kPa, 100 kPa and 191 kPa. These values are very far from the recorded data. Maximum calculated stress reaches almost 0,7 MPa only in one extensometer position and for the case of the lowest value of structural interaction between soil and lining.

It can be expected that stresses get greater with the decrease of the shear modulus of elasticity and consequently of the rigidity. This is explained by the fact that a lower value of the spring coefficient leads to a looser connection between rock and circular lining so that the structure is likely to show more deformation dealing with swelling forces. Nevertheless, with no one of the three different values of spring coefficient considered, the results adjust the monitoring data.

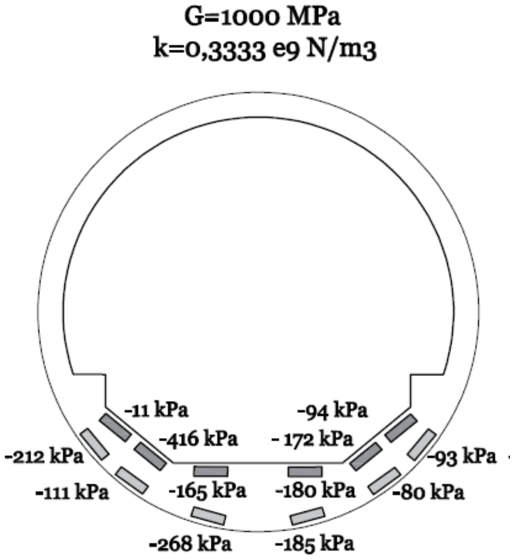
G=1000 MPa
k=0,3333 e9 N/m3
-11 kPa
-94 kPa
-416 kPa
- 172 kPa
-212 kPa
-93 kPa
-111 kPa
-165 kPa
-180 kPa
-80 kPa
-268 kPa
-185 kPa

Figure 4.26. Calculated hoop stresses with 6x6 grid model and k=0,3333 10^9

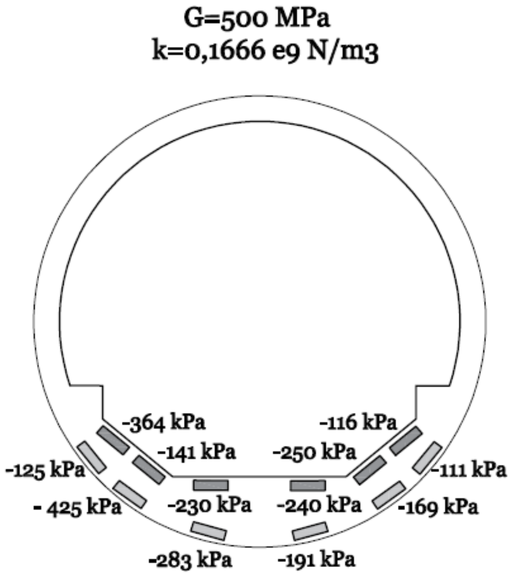
G=500 MPa
k=0,1666 e9 N/m3
-364 kPa
-116 kPa
-141 kPa
-250 kPa
-125 kPa
-111 kPa
- 425 kPa
-230 kPa
-240 kPa
-169 kPa
-283 kPa
-191 kPa

Figure 4.27. Calculated hoop stresses with 6x6 grid model and k=0,16667 10^9

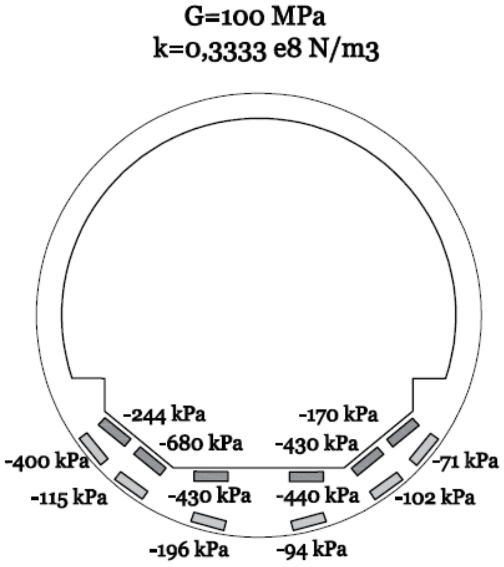

Figure 4.28. Calculated hoop stresses with 6x6 grid model and k=0,3333 10^8

Comparing Figure 4.26, Figure 4.27 and Figure 4.28 the expected behaviour of increasing stress trend with decreasing G value is not that evident. Even though hoop stress mean value gets greater (greater in the sense that more negative) with the loss of rigidity, not all extensometer positions show a stress increase with the different analyses. Therefore, it can be stated that the overall stress hoop values on average tend to decrease but despite this, there are some cases that deviate and do not show any increasing trend.

By comparison of Figure 4.26, Figure 4.27 and Figure 4.28 with Figure 4.24 it is obvious that calculated hoop stresses are very far from the measured one, regardless of the soil-structure interaction rigidity.

Figure 4.29 summarizes the results of the first model calculation. It represents the comparison of the calculated and the measured hoop stress values. The orange column refers to measured mean stress values, which derived from the instrumentation readings of the Lilla tunnel steel straining covering the period 2005-2011. Blue columns indicate calculated values. The difference of magnitude is undisputed, blue columns barely can be identified next to the orange ones.

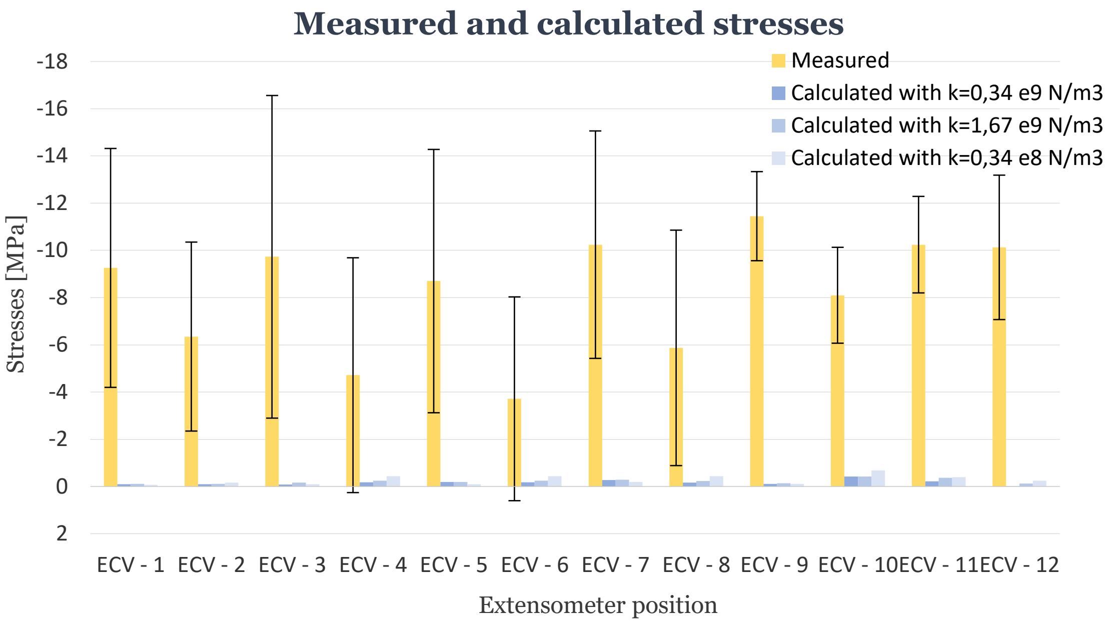

Figure 4.29. Comparison between measured and calculated stresses with the 6x6 grid model

The observed magnitude of the analyses values suggests that the model swelling loads were not able to reproduce the expected lining behaviour. This probably denotes that adopting a system of 36 punctual forces, 2,5 meters distant from each other, acting on a 12,5-meter-long section of the cylinder invert is not a realistic formulation to model the Lilla circular lining response.

It could be said that the issues with this first model analysis could be either the fact the grid of load is not dense enough or that the loading extension in the longitudinal direction is not representative. Or both. To support the first statement, it is unlikely that the rock massif action against the lining concentrates on points distant 2,5 meters so that a major quantity of loads is most certainly needed. In favour of the second statement instead, it could be stated that a 12,5 meters long loaded area is not enough to argue that the response of a central cross section is not influenced by forces beyond that value.

4.5 Second model definition

In order to account for a more extended loaded area, a second model has been developed. Geometry and mechanical properties have not changed respect to the first model, except for the dimension of the grid of loads.

The Lilla tunnel remains modelled as a cylindrical tube with a distribution of swelling punctual loads acting on the invert. The cylinder longitude (in the z direction) still is 52,5 m but this time, the central loaded stretch of 12,5 m has been tripled to 37,5 m. Unloaded stretches of 7,5 meters separate loaded area from the two extreme sections. Structural interaction between rock and support is once again reproduced by the spring coefficient calculated with Eq. 4.1. Different values will be considered referring to different rock shear moduli.

4.6 Swelling loads definition

To model the swelling pressure acting on the invert of the Lilla tunnel, the intention to create a fictitious distribution of swelling pressures with a determined probability density function is still valid. Second model grid of loads is extended 37,5 meters along the central part of the tunnel invert. The correspondent grid is of 108 punctual forces (6x18) and it is represented by the former set of loads triplicated. The loads still are distant 2,5 meters from one another (see Figure 4.30).

The choice not to generate another sequence of random numbers to calculate the 108 new loads but to use the former set is due to first, the purpose of the second analysis and secondly, the computational convenience of utilizing the existent distribution and repeating it. As the aim of the more extended loaded area model is to evaluate whether or not the effects of the loads are negligible on the lateral stretches of the tunnel invert, the repetition of the previous set of loads have been considered to best option to both fulfil the probability assumptions and the time-consuming computational aspect.

The used grid is showed in Figure 4.30. Every punctual load is directed to the centre of the tunnel in the upward direction. Figure 4.30. Grid of 108 swelling loads from x-z planeThe values of the modular forces acting on every point of the grid are represented in Table 4.14.

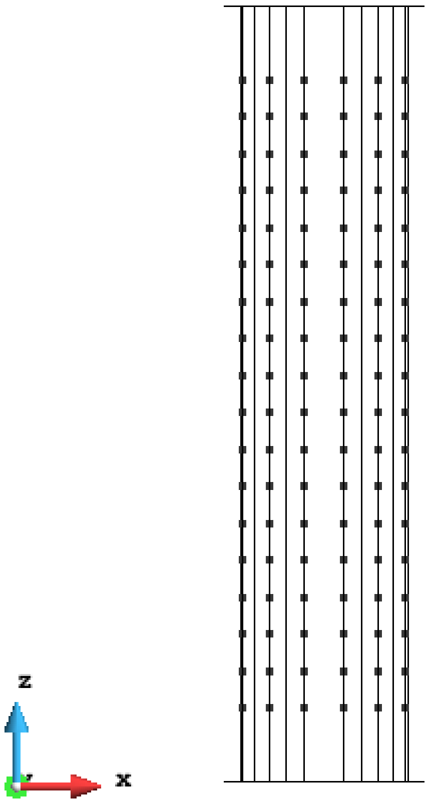

Figure 4.30. Grid of 108 swelling loads from x-z plane

Table 4.14. Set of 108 swelling forces in N

Swelling Forces [N]					
23229	116946	141127	157873	105408	36799
18320	12425	3344,1	56127	81788	120252
48850	38075	294524	82727	119985	10492
158412	1265,9	16221	14314	124473	29376
90687	163611	13043	51487	9367,2	64104
6424,9	49920	9408,1	6600,4	33615	40957
23229	116946	141127	157873	105408	36799
18320	12425	3344,1	56127	81788	120252
48850	38075	294524	82727	119985	10492
158412	1265,9	16221	14314	124473	29376
90687	163611	13043	51487	9367,2	64104
6424,9	49920	9408,1	6600,4	33615	40957
23229	116946	141127	157873	105408	36799
18320	12425	3344,1	56127	81788	120252
48850	38075	294524	82727	119985	10492
158412	1265,9	16221	14314	124473	29376
90687	163611	13043	51487	9367,2	64104
6424,9	49920	9408,1	6600,4	33615	40957

4.7 Results and discussion

Observations and comments respect the monitoring results of the reinforced Lilla tunnel and the method to calculate hoop stresses refer to the Methodology subchapter of the first analysis. No changes have been made regarding recorded data, plane stress transformation and respectively explanations.

To prove if the added loads are negligible regarding the behaviour of the central cross section of the tunnel, the comparison will be made to both the first model results and the captured tunnel response. In the following tables, results regarding the stress state of elements ubicated in the all extensometers position in the central cross section of the tunnel cylinder are presented, together with the circumferential stress values in the same points. Three tables represent the three different case of rock rigidity that reflected on three different spring coefficient values.

Table 4.15. Calculated stress values with 6x18 grid model and k=0,3333 10^9

	G=1000 Mpa k=0,3333 e9				
	σ_x [kPa]	σ_y [kPa]	τ_{xy} [kPa]	σ_n concr [kPa]	σ_n steel [kPa]
ECV - 1	-0,6	-6	-7	-10,71	**-53,54**
ECV - 2	-2,7	-7,3	-1,3	-6,7	**-33,7**
ECV - 3	-30	-27	-17	-45,1	**-225,7**
ECV - 4	-14	-3,7	-8	-18,0	**-90,2**
ECV - 5	-2	-15	-1,1	-3,4	**-17,1**
ECV - 6	-48			-48,0	**-240,0**
ECV - 7	-28	-17	7,1	-30,8	**-154,1**
ECV - 8	-30			-30,0	**-150,0**
ECV - 9	-9,7	-14	0,49	-11,7	**-58,3**
ECV - 10	-59	-21	26	-70,6	**-353,0**
ECV - 11	-25	-31	27	-55,0	**-275,2**
ECV - 12	-33	6	4	-13,4	**-66,8**

Table 4.16. Calculated stress values with 6x18 grid model and k=0,16667 10^9

	G=500 Mpa k=0,16666 e9				
	σ_x [kPa]	σ_y [kPa]	τ_{xy} [kPa]	σ_n concr [kPa]	σ_n steel [kPa]
ECV - 1	-2,9	-32	-2,7	-23,1	**-115,6**
ECV - 2	6,8	-9	-0,1	-2,8	**-14,2**
ECV - 3	-34	-28	-17	-48,1	**-240,5**
ECV - 4	-20	-11	0,74	-16,2	**-80,9**
ECV - 5	-4,3	-15	-0,4	-5,2	**-26,1**

ECV - 6	-73			-73,0	**-365,0**
ECV - 7	-33	-18	-6,6	-28,7	**-143,5**
ECV - 8	-43			-43,0	**-215,0**
ECV - 9	-16	-13	13	-27,3	**-136,6**
ECV - 10	-69	-19	14	-65,0	**-325,2**
ECV - 11	-31	-37	32	-65,9	**-329,6**
ECV - 12	-30	7	0,5	-8,1	**-40,7**

Table 4.17. Calculated stress values with 6x18 grid model and k=0,3333 10^8

	G=100 Mpa k=0,3333 e8				
	σ_x [kPa]	σ_y [kPa]	τ_{xy} [kPa]	σ_n concr [kPa]	σ_n steel [kPa]
ECV - 1	-7,8	-35	-13	-36,94	**-184,7**
ECV - 2	-6	-6	-6	-11,9	**-59,3**
ECV - 3	-36	-26	-13	-44,9	**-224,5**
ECV - 4	-34	-6	3,7	-20,8	**-104,0**
ECV - 5	-11	-15	2	-10,3	**-51,3**
ECV - 6	-90			-90,0	**-450,0**
ECV - 7	-19	-19	5	-21,5	**-107,5**
ECV - 8	-62			-62,0	**-310,0**
ECV - 9	-16	-10	-5	-9,2	**-45,9**
ECV - 10	-88	-27	35	-100,2	**-501,1**
ECV - 11	-48	6	17	-32,0	**-160,1**
ECV - 12	-38	-38	34	-71,3	**-356,3**

The first remarkable result of the second analysis is the stresses magnitude. Calculated stress values remain in the kPa order of magnitude. Even tough stresses do increase along the analyses, passing from the greatest value of shear modulus to the lowest, calculations are still very low and far from the monitoring data. Mean values of steel normal stresses in Table 4.15, Table 4.16 and Table 4.17 are -143 kPa, - 169 kPa and -212kPa respectively.

Figure 4.31, Figure 4.32 and Figure 4.33 give a more comprehensive illustration of the calculated response of the reinforcement bars with the extended grid of punctual forces. Values varies in the ranges of some hundreds of kPa with no sign of increase with respect to the first analysis. As a matter of fact, comparing these figures with Figure 4.26, Figure 4.27 and Figure 4.28 it can be stated that the stress results are overall characterized similar values. In addition, focusing on the mean value comparison it seems that 6x18 grid analyses lead to even smaller values. In can be concluded that both first and second analysis lead to values that appear not to be realistic for the interpretation of the Lilla tunnel circular lining.

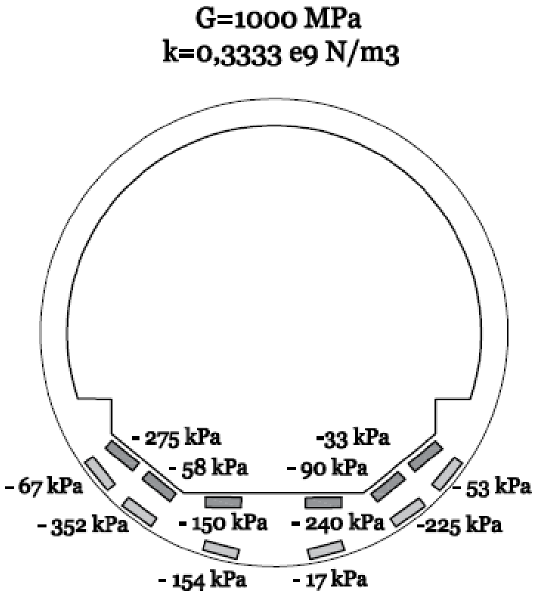
G=1000 MPa
k=0,3333 e9 N/m3
- 275 kPa
-33 kPa
- 58 kPa
- 90 kPa
- 67 kPa
- 53 kPa
- 352 kPa
- 150 kPa
- 240 kPa
-225 kPa
- 154 kPa
- 17 kPa

Figure 4.31. Calculated hoop stresses with 6x18 grid model and k=0,3333 10^9

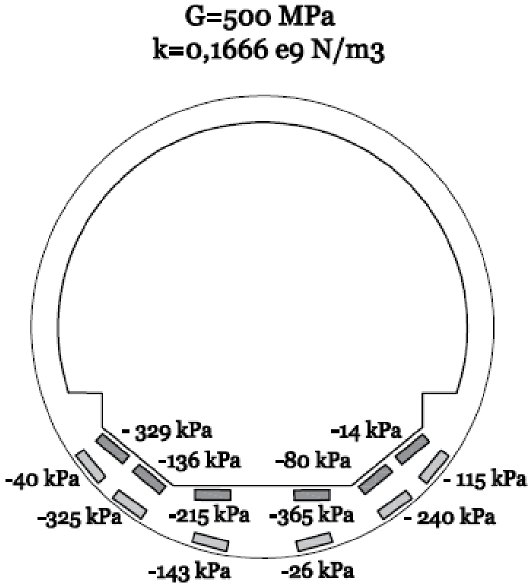
G=500 MPa
k=0,1666 e9 N/m3
- 329 kPa
-14 kPa
-136 kPa
-80 kPa
-40 kPa
- 115 kPa
-325 kPa
-215 kPa
-365 kPa
- 240 kPa
-143 kPa
-26 kPa

Figure 4.32. Calculated hoop stresses with 6x18 grid model and k=0,16667 10^9

The last figure summarizes the purpose of the second analysis. Figure 4.34 provides a clear and interesting information of the response of the tunnel when subject to a grid of punctual loads extended for almost the whole longitudinal dimension of the invert. Light blue columns refer to first analysis results while yellow ones are the 6x18 grid model results. All values but one are lower than -0,5 MPa. Therefore, it is evident that the model cannot match the recorded values.

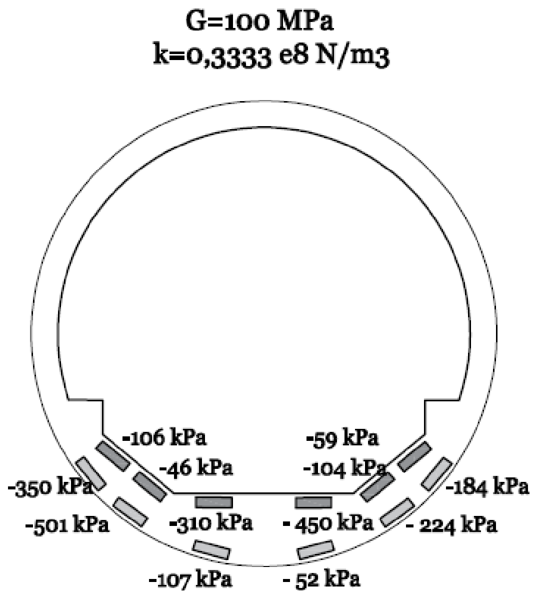
G=100 MPa
k=0,3333 e8 N/m3
-106 kPa
-46 kPa
-59 kPa
-104 kPa
-350 kPa
-184 kPa
-501 kPa
-310 kPa
- 450 kPa
- 224 kPa
-107 kPa
- 52 kPa

Figure 4.33. Calculated hoop stresses with 6x18 grid model and k=0,3333 10^8

Moreover, it is noteworthy to emphasize that stresses calculated with the extended loaded area not differ very much from the first model results. Surprisingly they appear to get smaller values at some measurement point. Hence, it can be stated that forces beyond the 12,5 meters extended area not influence the response of the central cross section of the tunnel. They are negligible regarding the purpose of calculation of stresses in the middle of the structure.

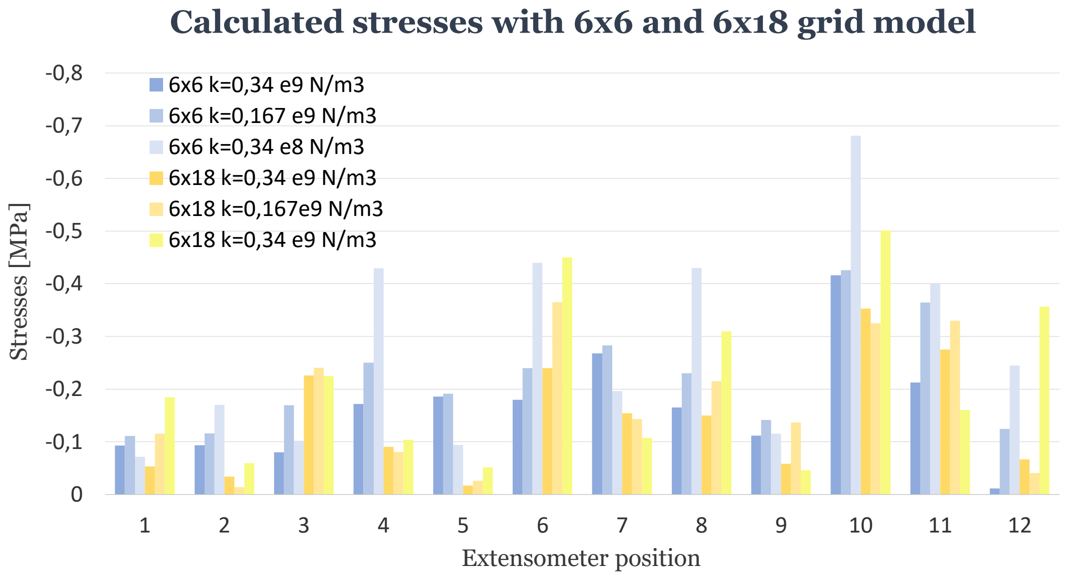

Figure 4.34. Comparison between calculated stress with 6x6 grid model and 18x6 grid model

4.8 Third model definition

In view of the results and discussion of the first two analyses, it can be stated that a denser loading distribution is needed to model Lilla claystone behaviour against the circular lining. As already mentioned in previous subchapters, to rectify discrepancies between the model and the monitoring data it is most likely to be required a grid of punctual loads whose gap between points is rather smaller than the used one. Therefore, to convert the model into a more realistic interpretation of the Lilla tunnel swelling phenomena a system of 676 punctual loads is adopted. Thus, every force is distant 0,5 meters to the nearby ones.

Going back to the first model definition, once again the design of the three-dimensional concrete cylindrical tube is addressed by a finite element structural analysis. Swelling loads are localized on 12,5 meters extended area. For the geometry and mechanical properties reference is made to first model. The structure in its invert part is composed by two lateral stretches of 20 meters and a central one of 12,5 m as it is illustrated in Figure 4.2. Mechanical properties are the ones illustrated in Table 4.1. Moreover, interaction between ground and circular lining is modelled by the springs, whose coefficient is calculated with Eq. 4.1. Different elastic coefficients will be considered depending on shear moduli different values.

4.9 Swelling loads definition

Swelling behaviour of the Lilla claystone exerting on the invert of the tunnel is reproduced by a dense distribution of random punctual loads whose probability density function coincides with the one of Figure 4.6. Third model grid of loads cover 12,5 meters of the invert, in correspondence with the central cross section of the tunnel. Every point of the grid is 0,5 meters away from the subsequent, resulting in a combination of 676 forces (26x26) acting on the cylinder. The procedure to calculate the 676 random numbers and each one of the swelling loads has already been made clear in the first analysis subchapter Swelling loads definition (see Figure 4.35).

The set of 676 random number through which the swelling loads have been calculated, the swelling forces themselves expressed in MPa and N, with their components in the cartesian direction are illustrated in Appendix C.

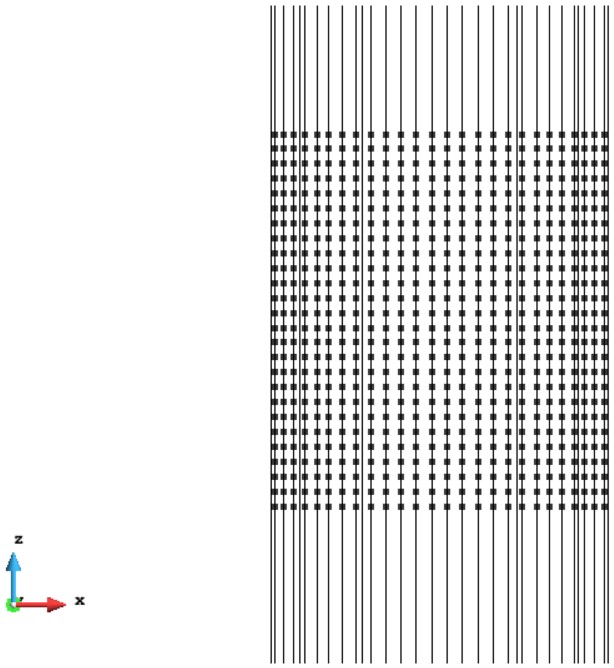

Figure 4.35. Grid of 676 loads from x-z plane

4.10 Results and discussion

And now, results of the 26x26 grid model analyses are presented. They are showed in terms of cartesian and hoop stresses in all the extensometer position elements. Horizontal, vertical and shear stresses are an immediate output of the structural analysis performed while hoop stresses estimation has been carried out following the Eq. 4.5 and the explanation of the previous subchapter of Methodology.

Table 4.18. Calculated stress values with 26x26 grid model and k=0,3333 10^9

	G=1000 Mpa k=0,3333 e9				
	σ_x [MPa]	σ_y [MPa]	τ_{xy} [MPa]	σ_n concr [MPa]	σ_n steel [MPa]
ECV - 1	-0,31	-1,30	-0,73	-1,62	**-8,11**
ECV - 2	-0,72	-0,38	-0,21	-0,73	**-3,63**
ECV - 3	-1,53	0,56	-0,67	-1,44	**-7,22**
ECV - 4	-1,14	-2,69	0,50	-1,20	**-5,99**
ECV - 5	-1,70	-0,10	0,26	-1,46	**-7,32**
ECV - 6	-1,21			-1,21	**-6,05**
ECV - 7	-2,38	-0,27	-0,37	-2,05	**-10,27**
ECV - 8	-0,96			-0,96	**-4,79**
ECV - 9	-1,60	-0,68	0,77	-2,01	**-10,07**
ECV - 10	-0,74	-0,28	0,64	-1,18	**-5,92**
ECV - 11	-0,30	-1,00	0,62	-1,32	**-6,62**
ECV - 12	-0,82	-0,42	0,53	-1,09	**-5,46**

Table 4.19. Calculated stress values with 26x26 grid model and k=0,16667 10^9

	G=500 Mpa k=0,16666 e9				
	σ_x [MPa]	σ_y [MPa]	τ_{xy} [MPa]	σ_n concr [MPa]	σ_n steel [MPa]
ECV - 1	-0,86	-1,40	-0,27	-1,45	**-7,24**
ECV - 2	-0,32	-0,93	-0,88	-1,55	**-7,74**
ECV - 3	-1,81	-0,77	-0,88	-2,29	**-11,44**
ECV - 4	-1,17	-0,36	-0,51	-1,38	**-6,88**
ECV - 5	-2,22	-0,35	-0,36	-2,27	**-11,37**
ECV - 6	-1,23			-1,23	**-6,15**
ECV - 7	-2,97	-0,35	0,05	-2,82	**-14,10**
ECV - 8	-0,96			-0,96	**-4,81**
ECV - 9	-1,95	-0,93	1,00	-2,55	**-12,75**
ECV - 10	-0,69	-0,35	0,44	-0,99	**-4,97**
ECV - 11	-0,97	-0,62	0,81	-1,55	**-7,73**
ECV - 12	-0,26	-1,49	0,29	-1,28	**-6,42**

Table 4.20. Calculated stress values with 26x26 grid model and k=0,3333 10^8

	G=100 Mpa k=0,3333 e8				
	σ_x [MPa]	σ_y [MPa]	τ_{xy} [MPa]	σ_n concr [MPa]	σ_n steel [MPa]
ECV - 1	-0,63	-2,12	-1,25	-2,75	**-13,76**
ECV - 2	-1,06	-0,51	-0,20	-0,92	**-4,60**
ECV - 3	-2,38	-1,32	-1,51	-3,45	**-17,25**
ECV - 4	-0,97	-0,32	-0,43	-1,15	**-5,77**
ECV - 5	-3,55	-0,10	-0,65	-3,64	**-18,22**
ECV - 6	-0,95			-0,95	**-4,76**
ECV - 7	-4,40	-0,46	0,28	-4,28	**-21,38**
ECV - 8	-0,49			-0,49	**-2,45**
ECV - 9	-2,68	-1,50	1,60	-3,79	**-18,97**
ECV - 10	-0,83	-0,25	0,26	-0,87	**-4,36**
ECV - 11	-0,27	-2,28	1,29	-2,75	**-13,73**
ECV - 12	-1,20	-0,57	0,36	-1,17	**-5,84**

Results obtained with the 676 swelling forces are plotted in Table 4.18, Table 4.19 and Table 4.20. The first remarkable result, compared to the earlier cases, is the magnitude order of the stresses. All the stresses stay in a range between some few MPa and about 20 MPa. For the first time in Chapter 4 analyses, Lilla tunnel monitoring data order of magnitude has been reproduced correctly. The three tables correspond to the different values of rigidity assigned to the soil-lining interaction. The various value of spring coefficient affectation to the lining response could be better appreciated making reference to Figure 4.36, Figure 4.37 and Figure 4.38. They graphically show the values of hoop stresses at every of the 12 positions analysed during the present work. The benchmark situation is the one of Figure 4.24.

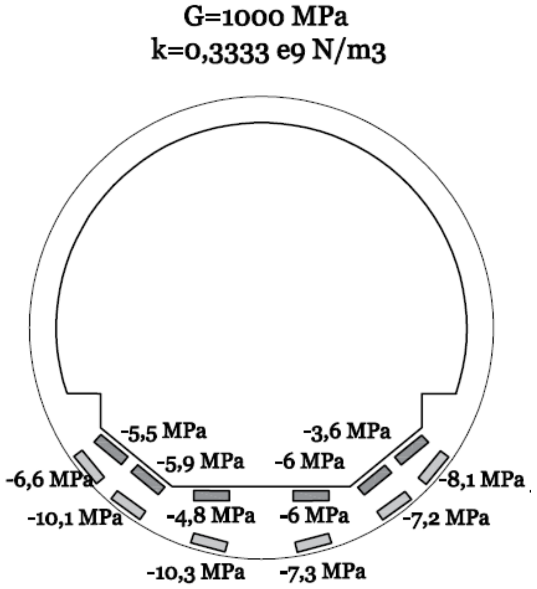
G=1000 MPa
k=0,3333 e9 N/m3
-5,5 MPa
-3,6 MPa
-5,9 MPa
-6 MPa
-6,6 MPa
-8,1 MPa
-10,1 MPa
-4,8 MPa
-6 MPa
-7,2 MPa
-10,3 MPa
-7,3 MPa

Figure 4.36. Calculated hoop stresses with 26x26 grid model and k=0,3333 10^9

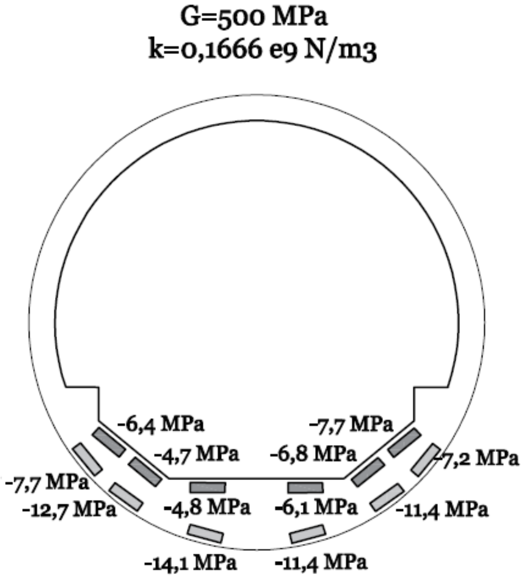
G=500 MPa
k=0,1666 e9 N/m3
-6,4 MPa
-7,7 MPa
-4,7 MPa
-6,8 MPa
-7,2 MPa
-7,7 MPa
-12,7 MPa
-4,8 MPa
-6,1 MPa
-11,4 MPa
-14,1 MPa
-11,4 MPa

Figure 4.37. Calculated hoop stresses with 26x26 grid model and k=0,16667 10^9

The overall tendency is the expected one, that is stress values get greater with the decrease of elastic shear modulus. However, it could be noted that not all values of stresses increase with the same factor during the three analyses. Moreover, there are some points which present smaller values with greater rigidity. This behaviour is locally restricted to some points and it can be explained by the different interaction of the combination of loads with the variation of the elastic coefficient. Nevertheless, the mentioned phenomena could barely be appreciated.

It could be stated that the average tendency of the tunnel circular lining behaviour is to develop higher stresses when the rock is characterized by a lower rigidity. This statement is supported by the appreciation of the mean values of calculated hoop stresses, which are -6,8 MPa, -8,5 MPa and -10,9 MPa respectively for the three different spring coefficient cases.

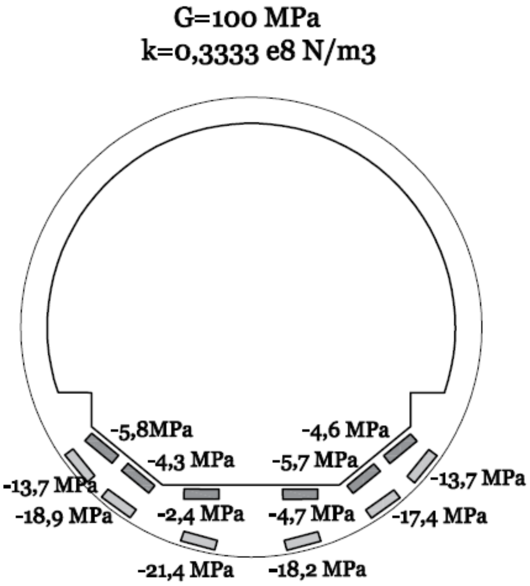

Figure 4.38. Calculated hoop stresses with 26x26 grid model and k=0,3333 10^8

Figure 4.39 plots in a very effective way the summary of the third analysis. Measured hoop stresses deriving from the instrumentation campaign of Lilla tunnel circular lining are compared to the calculated ones with the 26x26 grid model. Measured values are represented in orange columns for every extensometer position. The black bar is the standard deviation with respect to the mean value, derived from the study of monitoring results performed and discussed in early in the Chapter. Blue columns instead, describe the circular support behaviour under the imposed system of loads, varying with increasing value of rock shear modulus.

It is clear from Figure 4.39 that measured hoop stresses are overall well estimated through the last 26x26 grid model. In most of the instrumented positions the calculated stresses are situated in the deviation range, regardless of the spring coefficient value considered. It is true tough, that the lowest rigidity case overestimates the data in some points. Furthermore, it seems recordings from extensometers situated in the left part of the section (ECV-9, ECV-10, ECV-11, ECV-12) have a small dispersion with respect to the mean value compared to the other devices, in such a way that it is more complex for estimated value to adjust the real ones. Nevertheless, the results show to fit the overall response of the tunnel support.

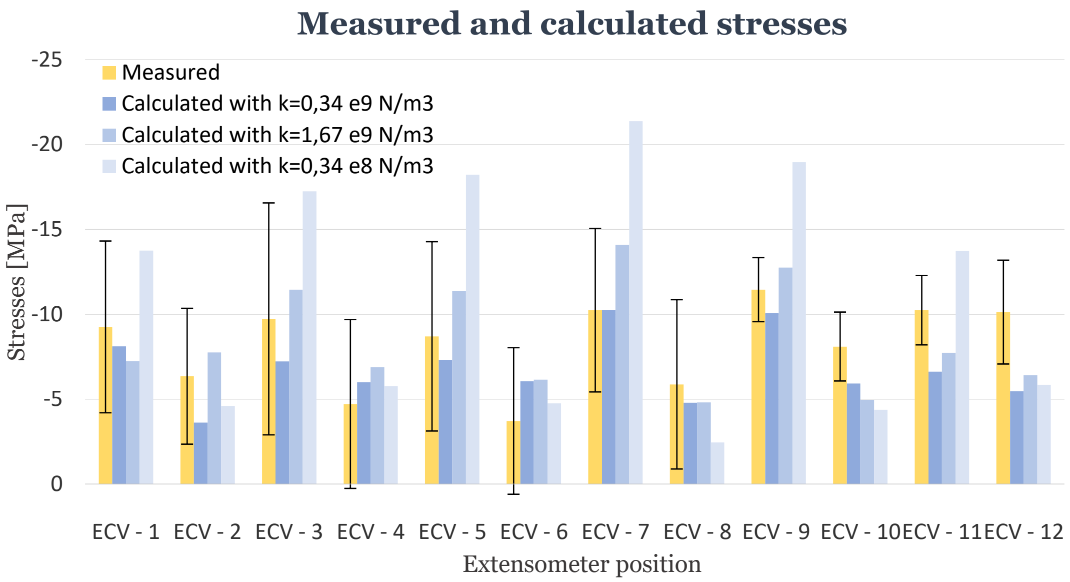

Figure 4.39. Comparison between measured and calculated stresses with the 26x26 grid model

It can be stated that the 26x26 grid model has been deemed capable of reproducing the Lilla tunnel circular lining behaviour. It appears that the situation that better capture the instrumented response is the intermediate rigidity case. Moreover, the sensitivity analysis on the interaction soil-lining has played a significant role in the accuracy of the predicted hoop stresses. In light of the studies of the effect of the different interaction values and of the rock massif rigidity it can be argued that G=500 MPa could be a reasonable value to be attributed to Lilla claystone shear modulus.

To conclude, the third analysis proved that adopting a distribution of loads compared to swelling punctual forces, heading the centre of the tunnel and spaced 0,5 meters, is realistic. Magnitude of calculated stresses coincide with the long-term monitoring data of the reinforced Lilla tunnel and compressive response of the structure is reproduced. Therefore, the third model appears to be suitable to provide a valuable interpretation of the swelling pressure action against the circular lining invert.

CHAPTER 5
CONCLUSIONS AND FUTURE RESEARCH

5.1 Conclusions

Both the two dimensional and the three-dimensional analyses provided interesting information regarding the action of swelling pressures against the lining and the rock behaviour in terms of expansive phenomena. Field information and long-monitoring records were chosen as reference to test modelling predictions. Particularly, available data permitted to achieve knowledge of the stresses developed in the Lilla tunnel circular lining, which in the thesis have been compared to the ones measured in the steel reinforcement to verify the reliability of the model.

From the Chapter 3 analyses, it seems that discrepancies between the modelling assumptions and the monitoring data were found. No one of the five cases analysed appear to be suitable for the assessment of the Lilla tunnel circular lining response. The modelled heterogeneous distributions of swelling pressure led to reinforcement bar stresses significantly smaller from the extensometer readings. Monitoring data showed that steel stresses values stay in a range between 0 and 14 MPa while calculated stresses vary in much wider ranges, depending on the considered loading combination. Moreover, model calculations suggested that the heavy reinforced circular lining would develop tensile stresses, in contrast with the instrumented response. It is evident that the Lilla tunnel circular lining response is fundamentally different from the modelling assumptions adopted in the Chapter 3. The two-dimensional plane strain hypothesis did not provide a reliable interpretation of the tunnel behaviour. The response of the tunnel is characterised by a marked variability in both transversal (different measurements in a given cross-section) and longitudinal direction (different cross-sections), which cannot be captured under a two-dimensional formulation. Hence, the expected longitudinal variability should be considered when comparing field data with the interpretation of the numerical analysis.

Chapter 4 describes three-dimensional formulations seeking to reproduce the structural response of the tunnel support, especially the variable stress state in the high-strength concrete. The structural behaviour of the Lilla tunnel is analysed under various combinations of localized swelling loads for different scenarios of rock-lining interaction. Such combinations derive from the statistic distribution of the measured stresses. The interpretation of numerical results provided significant conclusions about the three-dimensional response of the structure in terms of compression stress states in the circular lining.

For the 6x6 grid model case, the most evident result is the order of magnitude of the calculated stresses. Model predictions lead to stress values of some hundreds of kPa while measured stresses vary between 0 and 15 MPa. Even tough calculated stresses increased with the reduction of the rock rigidity, no value of spring coefficients permitted the results to adjust the monitoring data. It was concluded that adopting a system of 36 punctual forces, 2,5 meters distant from each other was not a realistic model to reproduce the Lilla circular lining response.

The 6x18 grid model case was elaborated to question the loading extension in the longitudinal direction. Results showed that stresses calculated with the extended loaded were not so far from first model calculations. Therefore, forces beyond the 12,5 meters extended loaded area appeared not to influence the response of the central cross section of the tunnel and can be neglected regarding the purposes of the work.

Last model, 26x26 grid one, replied to the request of a denser grid of loads. Properly, it was truly unlikely that rock massif effects against the lining concentrated on points very 2,5 meters. Model predictions showed that stresses magnitude order varied between some few MPa and about 20 MPa. It seemed that Lilla tunnel monitoring data order of magnitude and compression state were reproduced correctly. Generally, the tunnel tendency was to develop higher stresses when characterized by a lower rigidity. Nevertheless, calculated stresses were overall situated in the standard deviation range, regardless of the spring coefficient value considered. It can be stated that the 26x26 grid model was able to model the Lilla tunnel circular lining behaviour. Swelling loads should be applied at 0,5 m to one another in order to reproduce the instrumented data.

In conclusion, the results show a clear difference between the three-dimensional and the two-dimensional analysis, stressing the importance of considering the effects of a 3D complex geometry and the variability in the third dimension. Moreover, Chapter 4 third analysis proved that adopting a distribution of swelling loads distant 0,5 meters led to realistic results. Calculated stresses magnitude coincided with the reinforced Lilla tunnel long-term monitoring data and the structure compressive response was well reproduced. Therefore, the 26x26 grid model was suitable to provide a reliable interpretation of the swelling pressures action on the circular lining invert.

To sum up, the two-dimensional analyses led to the conclusion that if variability in the longitudinal direction is not considered, the estimation of the lining behaviour under extreme swelling pressure turns out to be incorrect. Making use of three-dimensional analyses instead, the circular lining response is better captured, at least in terms of compressive behaviour of the structure. Different swelling loads combination analyses revealed that the truly reliable model is a 3D cylinder where swelling forces are applied every 0,5 m.

5.2 Future research

The Lilla tunnel circular lining response under swelling pressure action on the invert has been well reproduced, however recommendations will be made for researchers that would like to continue with this topic:

- The model developed for the simulation of rock mass expansion phenomena and for the reproduction of swelling pressure action against the circular lining does not incorporate the physico-chemical phenomena involved in the rock swelling. The precipitation of gypsum crystals in discontinuities due to evaporation of sulphated water may be included.
- The transition from calculated stresses in a generical cross section to hoop stresses may not be tackled by a plane stress transformation. Another approach would be to analyse the three values of principal stresses and principal directions in a point and then calculate the normal stress acting on a plane with determined normal.
- Stresses calculated in concrete have been multiplied by the ratio of the correspondent material rigidity to evaluate stresses in steel bars. Researches may find a more complex manner to pass from concrete to steel stresses.
- Spring coefficient values has been assigned to the rock-lining contact surface with the same modulus in the x and y direction. Future studies may develop a model with springs in the direction normal to the contact surface.

References

[1] Alonso E. & Olivella S. Modelling Tunnel Performance in Expansive Gypsum Claystone. The 12th International Conference of International Association for Computer Methods and Advances in Geomechanics (IACMAG) 1-6 October, 2008

[2] Alonso E., Berdugo I., Ramon A. Extreme expansive phenomena in anhydritic-gypsiferous claystone: the case of Lilla tunnel. (2013). Geotechnique 63, No. 7, 584–612

[3] Alonso E., Ramon A. Heave of a railway bridge induced by gypsum crystal growth: field observations. (2013) Geotechnique 63(9):707–719

[4] Alonso, E. E. & Sagaseta, C. (2003). Informe previo sobre los problemas derivados de la expansividad del terreno en los túneles de Lilla, Camp Magré y Puig Cabrer.Barcelona, Spain: Department of Geotechnical Engineering and Geosciences, UPC.

[5] Behnam Yazdani Bejarbaneh, Danial Jahed Armaghani, Mohd For Mohd Amin. Strength characterisation of shale using Mohr–Coulomb and Hoek–Brown criteria. Measurement. Volume 63, March 2015, Pages 269-281

[6] Benjamin J. and Cornell C. Probability, Statistics and Decision for Civil Engineers. McGraw-Hill, 1970.

[7] Berdugo I., Alonso E., Romero E.E., Gens A. Tunnelling and Swelling in Triassic Sulphate–Bearing Rocks. Part I. Case studies from Baden–Württemberg .

[8] Berdugo I., Alonso E., Romero. Swelling mechanisms in sulphate-bearing rocks. Eurock 2006: Multiphysics Coupling and Long-Term Behaviour in Rock Mechanics, pp.451-454

[9] Berdugo I., Guimarães L., Gens A. and Alonso E. HMC Analysis of a Tunnel in Swelling Rock” 2nd International Conference on Computational Methods in Tunnelling Ruhr University Bochum, 9-11 September 2009 Aedificatio Publishers, 477-484.

[10] Berdugo, I., Tunnelling in sulphate bearing rocks: Expansive phenomena. (2007). PhD Thesis, UPC, Barcelona, Spain.

[11] Brinkgreve R.B.J., Kumarswamy S., and Swolfs W.M. Plaxis 2017. Plaxis bv, Delft, 2017.

[12] Brinkgreve, R.B.J. and Swolfs, W.M. and Engin, E. PLAXIS 2D 2017 - Reference manual. PLAXIS bv, Delft, The Netherlands.

[13] Brinkgreve, R.B.J. and Swolfs, W.M. and Engin, E. PLAXIS 2D 2017 – Material models manual. PLAXIS bv, Delft, The Netherlands.

[14] Brinkgreve, R.B.J. and Swolfs, W.M. and Engin, E. PLAXIS 2D 2017 – Tutorial manual. PLAXIS bv, Delft, The Netherlands

[15] Deu A., Romero E.E. & Berdugo I. Laboratory experiments on swelling due to crystal growth in sulphate argillaceous rocks (2013)

[16] Milioritsas M., (2014). Geotechnical modelling of a deep tunnel excavation in the Boom Clay formation. Master of Science Thesis, Delft University of Technology.

[17] Murray R. Origin and diagenesis of gypsum and anhydrite. Journal of sedimentary petrology, Vol. 34, No. 3, PP. 512-523. (1964)

[18] Ramon A. Expansion mechanisms in sulphated rocks and soils. (2014). PhD Thesis, UPC, Barcelona, Spain.

[19] Ramon A., Alonso E. & Olivella S. Hydro-chemo-mechanical modelling of tunnels in sulfated rocks. (2017). Géotechnique 67, No. 11, 968–982

[20] Ramon A., Alonso E. Crystal growth and soil expansion: the role of interfacial pressure and pore structure. A: International Conference on Unsaturated Soils. "Unsaturated Soils: Research & Applications". Sydney: CRC Press,(2014) p. 875-881.

[21] Ramon, A. & Alonso, E. E. (2013). Heave of a railway bridge: modelling gypsum crystal growth. Géotechnique 63, No. 9, 720–732, http://dx.doi.org/10.1680/geot.12.P.035.

[22] Rauh F., Spaun G. and Thuro K. Assessment of the swelling potential of anhydrite in tunnelling projects. IAEG2006 Paper number 473. (2006)

[23] Rauh F., Thuro K. Investigations on the swelling behaviour of pure anhydrite. Proceedings of the 1st Canada-US rock mechanics symposium—rock mechanics meeting society's challenges and demands, pp 527–534. (2007)

[24] The European Union Per Regulation 305/2011, Directive 98/34/EC, Directive 2004/18/EC. EN 1992-1-1 Eurocode 2: Design of concrete structures - Part 1-1: General rules and rules for buildings.

APPENDIX A

Calculations for 411+348 cross section case a

411+707 h=1,35

h [m]	1,35	Es [Mpa]	210000
h/2 [m]	0,675	Ec [Mpa]	42000
d [m]	1,3	alpha	5
d' [m]	0,05	yn [m]	1,6965
As [m2]	0,0064	b [m]	1
beta	1	e+h/2 [m]	0,5535
M [KNm/m]	-1362	0,5536	
N	-11214	Iyn* [m3]	1,7197
e [m]	0,1215	σ_c [Kpa]	-7678
ysup	0,675	σ_s [Kpa]	-21150
		$\sigma_{s'}$ [Kpa]	-58130
	σ_c [Mpa]	-1,5	-7,678
11	σ_s [Mpa]	-5	-21,15
12	$\sigma_{s'}$ [Mpa]	-7,5	-58,13

411+707 h=1,35

h [m]	1,35	Es [Mpa]	210000
h/2 [m]	0,675	Ec [Mpa]	42000
d [m]	1,3	alpha	5
d' [m]	0,05	yn [m]	1,6281
As [m2]	0,0064	b [m]	1
beta	1	e+h/2 [m]	0,5304
M [KNm/m]	1640,6	0,5304	
N	-11348	Iyn* [m3]	1,522
e [m]	-0,145	σ_c [Kpa]	-12840
ysup	0,675	σ_s [Kpa]	-17840
		$\sigma_{s'}$ [Kpa]	-62390
	σ_c [Mpa]	-2,2	-12,84
9	σ_s [Mpa]	-7,5	-17,84
10	$\sigma_{s'}$ [Mpa]	-11	-62,39

411+707 h=1,7865

h [m]	1,7865	Es [Mpa]	210000
h/2 [m]	0,8933	Ec [Mpa]	42000
d [m]	1,7365	alpha	5
d' [m]	0,05	yn [m]	2,2838
As [m2]	0,0064	b [m]	1
beta	1	e+h/2 [m]	0,7487
M [KNm/m]	1640,6	0,7487	
N	-11348	Iyn* [m3]	4,1406
e [m]	-0,145	σ_c [Kpa]	-8945
ysup	0,8933	σ_s [Kpa]	-17380
		$\sigma_{s'}$ [Kpa]	-43940
	σ_c [Mpa]	-2,9	-8,945
7	σ_s [Mpa]	-14,5	-17,38
8	$\sigma_{s'}$ [Mpa]	-2,9	-43,94

411+707 h=1,7865

h [m]	1,7865	Es [Mpa]	210000
h/2 [m]	0,8933	Ec [Mpa]	42000
d [m]	1,7365	alpha	5
d' [m]	0,05	yn [m]	0,5144
As [m2]	0,0064	b [m]	1
beta	1	e+h/2 [m]	-0,415
M [KNm/m]	13436	-0,415	
N	-10267	Iyn* [m3]	0,1004
e [m]	-1,309	σ_c [Kpa]	-48930
ysup	0,8933	σ_s [Kpa]	581200
		$\sigma_{s'}$ [Kpa]	-2E+05
	σ_c [Mpa]	-2	-48,93
5	σ_s [Mpa]	-10	581,2
6	$\sigma_{s'}$ [Mpa]	-4,2	-220,9

411+707 h=1,35				411+707 h=1,35			
h [m]	1,35	Es [Mpa]	210000	h [m]	1,35	Es [Mpa]	210000
h/2 [m]	0,675	Ec [Mpa]	42000	h/2 [m]	0,675	Ec [Mpa]	42000
d [m]	1,3	alpha	5	d [m]	1,3	alpha	5
d' [m]	0,05	yn [m]	0,875	d' [m]	0,05	yn [m]	2,038
As [m2]	0,0064	b [m]	1	As [m2]	0,0064	b [m]	1
beta	1	e+h/2 [m]	0,2401	beta	1	e+h/2 [m]	0,6677
M [KNm/m]	4827	0,2406		M [KNm/m]	-82,53	0,6675	
N	-11099	Iyn* [m3]	0,251	N	-11368	Iyn* [m3]	2,9661
e [m]	-0,435	σ_c [Kpa]	-13520	e [m]	0,0073	σ_c [Kpa]	-8280
ysup	0,675	σ_s [Kpa]	59890	ysup	0,675	σ_s [Kpa]	-41310
		$\sigma_{s'}$ [Kpa]	-1E+05			$\sigma_{s'}$ [Kpa]	-39070
	σ_c [Mpa]	-2,4	-13,52		σ_c [Mpa]	-2,84	-8,28
3	σ_s [Mpa]	-12	59,89	1	σ_s [Mpa]	-9	-41,31
4	$\sigma_{s'}$ [Mpa]	-4,8	-115,8	2	$\sigma_{s'}$ [Mpa]	-14,2	-39,07

Calculations for 411+468 cross section case a

411+707 h=1,35				411+707 h=1,35			
h [m]	1,35	Es [Mpa]	210000	h [m]	1,35	Es [Mpa]	210000
h/2 [m]	0,675	Ec [Mpa]	42000	h/2 [m]	0,675	Ec [Mpa]	42000
d [m]	1,3	alpha	5	d [m]	1,3	alpha	5
d' [m]	0,05	yn [m]	1,00459	d' [m]	0,05	yn [m]	1,62807
As [m2]	0,00643	b [m]	1	As [m2]	0,00643	b [m]	1
beta	1	e+h/2 [m]	0,30168	beta	1	e+h/2 [m]	0,83622
M [KNm/m]	-2986,21	0,30078		M [KNm/m]	-1347,92	0,53042	
N	-7999,06	Iyn* [m3]	0,37006	N	-8360,71	Iyn* [m3]	1,52203
e [m]	0,37332	σ_c [Kpa]	-15250	e [m]	0,16122	σ_c [Kpa]	-9860
yg*	0,675	σ_s [Kpa]	22220	yg*	0,675	σ_s [Kpa]	-47860
		$\sigma_{s'}$ [Kpa]	-72460			$\sigma_{s'}$ [Kpa]	-11260
	σ_c [Mpa]	-1,5	-15,25		σ_c [Mpa]	-2,2	-9,86
11	σ_s [Mpa]	-5	22,22	9	σ_s [Mpa]	-11	-47,86
12	$\sigma_{s'}$ [Mpa]	-7,5	-72,46	10	$\sigma_{s'}$ [Mpa]	-7,5	-11,26

411+707 h=1,7865				411+707 h=1,7865			
h [m]	1,7865	Es [Mpa]	210000	h [m]	1,7865	Es [Mpa]	210000
h/2 [m]	0,89325	Ec [Mpa]	42000	h/2 [m]	0,89325	Ec [Mpa]	42000
d [m]	1,7365	alpha	5	d [m]	1,7365	alpha	5
d' [m]	0,05	yn [m]	2,28378	d' [m]	0,05	yn [m]	0,514428
As [m2]	0,00643	b [m]	1	As [m2]	0,00643	b [m]	1
beta	1	e+h/2 [m]	0,26269	beta	1	e+h/2 [m]	-0,94021
M [KNm/m]	5106,75	0,74868		M [KNm/m]	13400,7	-0,41533	
N	-8098,71	Iyn* [m3]	4,14062	N	-7308,99	Iyn* [m3]	0,100362
e [m]	-0,63056	σ_c [Kpa]	-15710	e [m]	-1,83346	σ_c [Kpa]	-50070
yg*	0,89325	σ_s [Kpa]	-74240	yg*	0,89325	σ_s [Kpa]	-221300
		$\sigma_{s'}$ [Kpa]	54660			$\sigma_{s'}$ [Kpa]	759800
	σ_c [Mpa]	-2,9	-15,71		σ_c [Mpa]	-2	-50,07
7	σ_s [Mpa]	-14,5	-74,24	5	σ_s [Mpa]	-10	-221,3
8	$\sigma_{s'}$ [Mpa]	-2,9	54,66	6	$\sigma_{s'}$ [Mpa]	-4,2	759,8

	411+707 h=1,35				411+707 h=1,35		
h [m]	1,35	Es [Mpa]	210000	h [m]	1,35	Es [Mpa]	210000
h/2 [m]	0,675	Ec [Mpa]	42000	h/2 [m]	0,675	Ec [Mpa]	42000
d [m]	1,3	alpha	5	d [m]	1,3	alpha	5
d' [m]	0,05	yn [m]	0,87496	d' [m]	0,05	yn [m]	2,037977
As [m2]	0,00643	b [m]	1	As [m2]	0,00643	b [m]	1
beta	1	e+h/2 [m]	0,17003	beta	1	e+h/2 [m]	0,78279
M [KNm/m]	4169,88	0,2406		M [KNm/m]	907,6	0,66754	
N	-8257,76	Iyn* [m3]	0,25098	N	-8419,54	Iyn* [m3]	2,966135
e [m]	-0,50497	σ_c [Kpa]	-21600	e [m]	-0,1078	σ_c [Kpa]	-8610
yg*	0,675	σ_s [Kpa]	78970	yg*	0,675	σ_s [Kpa]	-42800
		$\sigma_{s'}$ [Kpa]	-100900			$\sigma_{s'}$ [Kpa]	-17440
	σ_c [Mpa]	-2,4	-21,6		σ_c [Mpa]	-2,84	-8,61
3	σ_s [Mpa]	-12	78,97	1	σ_s [Mpa]	-9	-42,8
4	$\sigma_{s'}$ [Mpa]	-4,8	-100,9	2	$\sigma_{s'}$ [Mpa]	-14,2	-17,44

Calculations for 411+707 cross section case a

	411+707 h=1,35				411+707 h=1,35		
h [m]	1,35	Es [Mpa]	210000	h [m]	1,35	Es [Mpa]	210000
h/2 [m]	0,675	Ec [Mpa]	42000	h/2 [m]	0,675	Ec [Mpa]	42000
d [m]	1,3	alpha	5	d [m]	1,3	alpha	5
d' [m]	0,05	yn [m]	2,23284	d' [m]	0,05	yn [m]	3,88177
As [m2]	0,00643	b [m]	1	As [m2]	0,00643	b [m]	1
beta	1	e+h/2 [m]	0,73212	beta	1	e+h/2 [m]	1,27417
M [KNm/m]	-501,493	0,73191		M [KNm/m]	-5097,33	1,27418	
N	-8779,79	Iyn* [m3]	3,89195	N	-8507,26	Iyn* [m3]	20,1838
e [m]	0,05712	σ_c [Kpa]	-7678	e [m]	0,59917	σ_c [Kpa]	-27340
yg*	0,675	σ_s [Kpa]	-37850	yg*	0,675	σ_s [Kpa]	-125900
		$\sigma_{s'}$ [Kpa]	-24230			$\sigma_{s'}$ [Kpa]	144800
	σ_c [Mpa]	-2,04	-7,678		σ_c [Mpa]	-2,04	-27,34
11	σ_s [Mpa]	-5	-37,85	9	σ_s [Mpa]	-10,2	-125,9
12	$\sigma_{s'}$ [Mpa]	-10,2	-24,23	10	$\sigma_{s'}$ [Mpa]	-5,5	144,8

	411+707 h=1,7865				411+707 h=1,7865		
h [m]	1,7865	Es [Mpa]	210000	h [m]	1,7865	Es [Mpa]	210000
h/2 [m]	0,89325	Ec [Mpa]	42000	h/2 [m]	0,89325	Ec [Mpa]	42000
d [m]	1,7365	alpha	5	d [m]	1,7365	alpha	5
d' [m]	0,05	yn [m]	-3,35244	d' [m]	0,05	yn [m]	4,23897
As [m2]	0,00643	b [m]	1	As [m2]	0,00643	b [m]	1
beta	1	e+h/2 [m]	-1,228681	beta	1	e+h/2 [m]	1,3956
M [KNm/m]	15567,3	-1,22879		M [KNm/m]	-4325,92	1,39586	
N	-7336,36	Iyn* [m3]	-11,35424	N	-8611,44	Iyn* [m3]	26,1558
e [m]	-2,12193	σ_c [Kpa]	-58410	e [m]	0,50235	σ_c [Kpa]	-12940
yg*	0,89325	σ_s [Kpa]	-256000	yg*	0,89325	σ_s [Kpa]	-62200
		$\sigma_{s'}$ [Kpa]	957600			$\sigma_{s'}$ [Kpa]	22320
	σ_c [Mpa]	-2,6	-58,41		σ_c [Mpa]	-1,9	-12,94
7	σ_s [Mpa]	-13	-256	5	σ_s [Mpa]	-9,5	-62,2
8	$\sigma_{s'}$ [Mpa]	-1	957,6	6	$\sigma_{s'}$ [Mpa]	-1,2	22,32

411+707 h=1,35

h [m]	1,35	Es [Mpa]	210000
h/2 [m]	0,675	Ec [Mpa]	42000
d [m]	1,3	alpha	5
d' [m]	0,05	yn [m]	1,26173
As [m2]	0,00643	b [m]	1
beta	1	e+h/2 [m]	0,40113
M [KNm/m]	2443,02	0,40195	
N	-8920,43	Iyn* [m3]	0,7168
e [m]	-0,27387	σ_c [Kpa]	-13520
yg*	0,675	σ_s [Kpa]	2174
		$\sigma_{s'}$ [Kpa]	-64990
	σ_c [Mpa]	-2,1	-13,52
3	σ_s [Mpa]	-10,5	2,174
4	$\sigma_{s'}$ [Mpa]	0	-64,99

411+707 h=1,35

h [m]	1,35	Es [Mpa]	210000
h/2 [m]	0,675	Ec [Mpa]	42000
d [m]	1,3	alpha	5
d' [m]	0,05	yn [m]	0,87801
As [m2]	0,00643	b [m]	1
beta	1	e+h/2 [m]	0,24144
M [KNm/m]	3650,81	0,24214	
N	-8420,63	Iyn* [m3]	0,25341
e [m]	-0,43356	σ_c [Kpa]	-18560
yg*	0,675	σ_s [Kpa]	44870
		$\sigma_{s'}$ [Kpa]	-87620
	σ_c [Mpa]	-1,64	-18,56
1	σ_s [Mpa]	-8	44,87
2	$\sigma_{s'}$ [Mpa]	-8,2	-87,62

Calculations for 411+348 cross section case b

411+707 h=1,35

h [m]	1,35	Es [Mpa]	210000
h/2 [m]	0,675	Ec [Mpa]	42000
d [m]	1,3	alpha	5
d' [m]	0,05	yn [m]	1,00038
As [m2]	0,00643	b [m]	1
beta	1	e+h/2 [m]	0,46257
M [KNm/m]	440,641	0,29896	
N	-2074,3	Iyn* [m3]	0,36565
e [m]	-0,2124	σ_c [Kpa]	-174
yg*	0,675	σ_s [Kpa]	-13320
		$\sigma_{s'}$ [Kpa]	-1351
	σ_c [Mpa]	-1,5	-0,174
11	σ_s [Mpa]	-5	-13,32
12	$\sigma_{s'}$ [Mpa]	-7,5	-1,351

411+707 h=1,35

h [m]	1,35	Es [Mpa]	210000
h/2 [m]	0,675	Ec [Mpa]	42000
d [m]	1,3	alpha	5
d' [m]	0,05	yn [m]	1,1498
As [m2]	0,00643	b [m]	1
beta	1	e+h/2 [m]	0,40704
M [KNm/m]	626,438	0,35981	
N	-2337,8	Iyn* [m3]	0,54633
e [m]	-0,268	σ_c [Kpa]	-3490
yg*	0,675	σ_s [Kpa]	-16810
		$\sigma_{s'}$ [Kpa]	334,5
	σ_c [Mpa]	-2,2	-3,49
9	σ_s [Mpa]	-11	-16,81
10	$\sigma_{s'}$ [Mpa]	-7,5	0,3345

411+707 h=1,7865

h [m]	1,7865	Es [Mpa]	210000
h/2 [m]	0,89325	Ec [Mpa]	42000
d [m]	1,7365	alpha	5
d' [m]	0,05	yn [m]	1,73822
As [m2]	0,00643	b [m]	1
beta	1	e+h/2 [m]	0,41997
M [KNm/m]	1136,14	0,56108	
N	-2400,6	Iyn* [m3]	1,8423
e [m]	-0,4733	σ_c [Kpa]	-3415
yg*	0,89325	σ_s [Kpa]	-16450
		$\sigma_{s'}$ [Kpa]	4698
	σ_c [Mpa]	-2,9	-3,415
7	σ_s [Mpa]	-14,5	-16,45
8	$\sigma_{s'}$ [Mpa]	-2,9	4,698

411+707 h=1,7865

h [m]	1,7865	Es [Mpa]	210000
h/2 [m]	0,89325	Ec [Mpa]	42000
d [m]	1,7365	alpha	5
d' [m]	0,05	yn [m]	0,48686
As [m2]	0,00643	b [m]	1
beta	1	e+h/2 [m]	-0,3938
M [KNm/m]	2671,79	-0,5399	
N	-2075,9	Iyn* [m3]	0,09484
e [m]	-1,287	σ_c [Kpa]	-9710
yg*	0,89325	σ_s [Kpa]	-43880
		$\sigma_{s'}$ [Kpa]	113600
	σ_c [Mpa]	-2	-9,71
5	σ_s [Mpa]	-10	113,6
6	$\sigma_{s'}$ [Mpa]	-4,2	-43,88

411+707 h=1,35				411+707 h=1,35			
h [m]	1,35	Es [Mpa]	210000	h [m]	1,35	Es [Mpa]	210000
h/2 [m]	0,675	Ec [Mpa]	42000	h/2 [m]	0,675	Ec [Mpa]	42000
d [m]	1,3	alpha	5	d [m]	1,3	alpha	5
d' [m]	0,05	yn [m]	0,49981	d' [m]	0,05	yn [m]	1,34032
As [m2]	0,00643	b [m]	1	As [m2]	0,00643	b [m]	1
beta	1	e+h/2 [m]	-0,00868	beta	1	e+h/2 [m]	0,48714
M [KNm/m]	1412,61	-0,10499		M [KNm/m]	377,06	0,43045	
N	-2066,2	Iyn* [m3]	0,06873	N	-2007,13	Iyn* [m3]	0,85622
e [m]	-0,68368	σ_c [Kpa]	-7780	e [m]	-0,18786	σ_c [Kpa]	-2520
yg*	0,675	σ_s [Kpa]	-35430	yg*	0,675	σ_s [Kpa]	-12220
		$\sigma_{s'}$ [Kpa]	51780			$\sigma_{s'}$ [Kpa]	-1970
	σ_c [Mpa]	-2,4	-7,78		σ_c [Mpa]	-2,84	-2,52
3	σ_s [Mpa]	-12	-35,43	1	σ_s [Mpa]	-9	-12,22
4	$\sigma_{s'}$ [Mpa]	-4,8	51,78	2	$\sigma_{s'}$ [Mpa]	-14,2	-1,97

Calculations for 411+468 cross section case b

411+707 h=1,35				411+707 h=1,35			
h [m]	1,35	Es [Mpa]	210000	h [m]	1,35	Es [Mpa]	210000
h/2 [m]	0,675	Ec [Mpa]	42000	h/2 [m]	0,675	Ec [Mpa]	42000
d [m]	1,3	alpha	5	d [m]	1,3	alpha	5
d' [m]	0,05	yn [m]	1,12966	d' [m]	0,05	yn [m]	0,40072
As [m2]	0,00643	b [m]	1	As [m2]	0,00643	b [m]	1
beta	1	e+h/2 [m]	0,16056	beta	1	e+h/2 [m]	0,26026
M [KNm/m]	-275,67	0,35197		M [KNm/m]	-250,62	-0,42017	
N	-535,86	Iyn* [m3]	0,51896	N	-604,28	Iyn* [m3]	0,05142
e [m]	0,51444	σ_c [Kpa]	1080	e [m]	0,41474	σ_c [Kpa]	-1010
yg*	0,675	σ_s [Kpa]	7510	yg*	0,675	σ_s [Kpa]	3900
		$\sigma_{s'}$ [Kpa]	-15410			$\sigma_{s'}$ [Kpa]	-14720
	σ_c [Mpa]	-2,3	1,08		σ_c [Mpa]	-1,36	-1,01
11	σ_s [Mpa]	-11,5	7,51	9	σ_s [Mpa]	-	3,9
12	$\sigma_{s'}$ [Mpa]	-9,8	-15,41	10	$\sigma_{s'}$ [Mpa]	-6,8	-14,72

411+707 h=1,7865				411+707 h=1,7865			
h [m]	1,7865	Es [Mpa]	210000	h [m]	1,7865	Es [Mpa]	210000
h/2 [m]	0,89325	Ec [Mpa]	42000	h/2 [m]	0,89325	Ec [Mpa]	42000
d [m]	1,7365	alpha	5	d [m]	1,7365	alpha	5
d' [m]	0,05	yn [m]	14,4095	d' [m]	0,05	yn [m]	1,2842
As [m2]	0,00643	b [m]	1	As [m2]	0,00643	b [m]	1
beta	1	e+h/2 [m]	0,51269	beta	1	e+h/2 [m]	4,90018
M [KNm/m]	250,55	4,77025		M [KNm/m]	1793,18	0,388	
N	-658,37	Iyn* [m3]	1009,1	N	-447,52	Iyn* [m3]	0,76155
e [m]	-0,38056	σ_c [Kpa]	-1050	e [m]	-4,00693	σ_c [Kpa]	3990
yg*	0,89325	σ_s [Kpa]	-15100	yg*	0,89325	σ_s [Kpa]	-54000
		$\sigma_{s'}$ [Kpa]	2860			$\sigma_{s'}$ [Kpa]	143200
	σ_c [Mpa]	-2,86	-1,05		σ_c [Mpa]	-2,9	3,99
7	σ_s [Mpa]	-14,3	-15,1	5	σ_s [Mpa]	-14,5	-54
8	$\sigma_{s'}$ [Mpa]	-3,8	2,86	6	$\sigma_{s'}$ [Mpa]	-6,3	143,2

	411+707 h=1,35				411+707 h=1,35		
h [m]	1,35	Es [Mpa]	210000	h [m]	1,35	Es [Mpa]	210000
h/2 [m]	0,675	Ec [Mpa]	42000	h/2 [m]	0,675	Ec [Mpa]	42000
d [m]	1,3	alpha	5	d [m]	1,3	alpha	5
d' [m]	0,05	yn [m]	1,15607	d' [m]	0,05	yn [m]	0,68461
As [m2]	0,00643	b [m]	1	As [m2]	0,00643	b [m]	1
beta	1	e+h/2 [m]	0,50086	beta	1	e+h/2 [m]	0,9017
M [KNm/m]	109,43	0,36224		M [KNm/m]	-136,01	0,12241	
N	-628,4	Iyn* [m3]	0,55506	N	-599,95	Iyn* [m3]	0,13209
e [m]	-0,17414	σ_c [Kpa]	-670	e [m]	0,2267	σ_c [Kpa]	-710
yg*	0,675	σ_s [Kpa]	-3770	yg*	0,675	σ_s [Kpa]	-1280
		$\sigma_{s'}$ [Kpa]	-2440			$\sigma_{s'}$ [Kpa]	-10390
	σ_c [Mpa]	-3,3	-0,67		σ_c [Mpa]	-2,4	-0,71
3	σ_s [Mpa]	-16,5	-3,77	1	σ_s [Mpa]	-12	-1,28
4	$\sigma_{s'}$ [Mpa]	-7,8	-2,44	2	$\sigma_{s'}$ [Mpa]	-	-10,39

Calculations for 411+707 cross section case b

	411+707 h=1,35				411+707 h=1,35		
h [m]	1,35	Es [Mpa]	210000	h [m]	1,35	Es [Mpa]	210000
h/2 [m]	0,675	Ec [Mpa]	42000	h/2 [m]	0,675	Ec [Mpa]	42000
d [m]	1,3	alpha	5	d [m]	1,3	alpha	5
d' [m]	0,05	yn [m]	1,29802	d' [m]	0,05	yn [m]	0,44094
As [m2]	0,00643	b [m]	1	As [m2]	0,00643	b [m]	1
beta	1	e+h/2 [m]	0,41596	beta	1	e+h/2 [m]	-0,2551
M [KNm/m]	-356,905	0,4152		M [KNm/m]	-1266,9	-0,25574	
N	-1377,79	Iyn* [m3]	0,7791	N	-1362,11	Iyn* [m3]	0,05723
e [m]	0,25904	σ_c [Kpa]	-2023	e [m]	0,9301	σ_c [Kpa]	-1603
yg*	0,675	σ_s [Kpa]	-9727	yg*	0,675	σ_s [Kpa]	-32390
		$\sigma_{s'}$ [Kpa]	15,451			$\sigma_{s'}$ [Kpa]	71120
	σ_c [Mpa]	-2,04	-2,023		σ_c [Mpa]	-2,04	-1,603
11	σ_s [Mpa]	-5	-9,727	9	σ_s [Mpa]	-10,2	-32,39
12	$\sigma_{s'}$ [Mpa]	-10,2	0,01545	10	$\sigma_{s'}$ [Mpa]	-5,5	71,12

	411+707 h=1,7865				411+707 h=1,7865		
h [m]	1,7865	Es [Mpa]	210000	h [m]	1,7865	Es [Mpa]	210000
h/2 [m]	0,89325	Ec [Mpa]	42000	h/2 [m]	0,89325	Ec [Mpa]	42000
d [m]	1,7365	alpha	5	d [m]	1,7365	alpha	5
d' [m]	0,05	yn [m]	-8,1717908	d' [m]	0,05	yn [m]	0,762535
As [m2]	0,006434	b [m]	1	As [m2]	0,006434	b [m]	1
beta	1	e+h/2 [m]	4,27420967	beta	1	e+h/2 [m]	0,072354
M [KNm/m]	-3535,03	-2,78963		M [KNm/m]	-1100	0,073089	
N	-1045,57	Iyn* [m3]	-176,56619	N	-1340	Iyn* [m3]	0,194644
e [m]	3,38096	σ_c [Kpa]	-2898	e [m]	0,820896	σ_c [Kpa]	-264,3
yg*	0,89325	σ_s [Kpa]	-57000	yg*	0,89325	σ_s [Kpa]	-16930
		$\sigma_{s'}$ [Kpa]	259000			$\sigma_{s'}$ [Kpa]	23180
	σ_c [Mpa]	-2,6	-2,898		σ_c [Mpa]	-1,9	-0,2643
7	σ_s [Mpa]	-13	-57	5	σ_s [Mpa]	-9,5	-16,93
8	$\sigma_{s'}$ [Mpa]	-1	259	6	$\sigma_{s'}$ [Mpa]	-1,2	23,18

411+707 h=1,35

h [m]	1,35	Es [Mpa]	210000
h/2 [m]	0,675	Ec [Mpa]	42000
d [m]	1,3	alpha	5
d' [m]	0,05	yn [m]	1,502395
As [m2]	0,006434	b [m]	1
beta	1	e+h/2 [m]	0,487663
M [KNm/m]	245,788	0,487379	
N	-1312,01	Iyn* [m3]	1,199576
e [m]	-0,18734	σ_c [Kpa]	-469,5
yg*	0,675	σ_s [Kpa]	-1300
		$\sigma_{s'}$ [Kpa]	-7900
	σ_c [Mpa]	-2,1	-0,4695
3	σ_s [Mpa]	-10,5	-1,3
4	$\sigma_{s'}$ [Mpa]	0	-7,9

411+707 h=1,35

h [m]	1,35	Es [Mpa]	210000
h/2 [m]	0,675	Ec [Mpa]	42000
d [m]	1,3	alpha	5
d' [m]	0,05	yn [m]	0,767817
As [m2]	0,006434	b [m]	1
beta	1	e+h/2 [m]	0,18082
M [KNm/m]	594,237	0,180691	
N	-1202,47	Iyn* [m3]	0,176574
e [m]	-0,49418	σ_c [Kpa]	-620,4
yg*	0,675	σ_s [Kpa]	10630
		$\sigma_{s'}$ [Kpa]	-14350
	σ_c [Mpa]	-1,64	-0,6204
1	σ_s [Mpa]	-8	10,63
2	$\sigma_{s'}$ [Mpa]	-8,2	-14,35

Calculations for 411+348 cross section case c

411+707 h=1,35

h [m]	1,35	Es [Mpa]	210000
h/2 [m]	0,675	Ec [Mpa]	42000
d [m]	1,3	alpha	5
d' [m]	0,05	yn [m]	1,00038
As [m2]	0,00643	b [m]	1
beta	1	e+h/2 [m]	0,28169
M [KNm/m]	347,52	0,29896	
N	-883,58	Iyn* [m3]	0,36565
e [m]	-0,39331	σ_c [Kpa]	-1782
yg*	0,675	σ_s [Kpa]	-8380
		$\sigma_{s'}$ [Kpa]	3150
	σ_c [Mpa]	-1,5	-1,782
11	σ_s [Mpa]	-5	-8,38
12	$\sigma_{s'}$ [Mpa]	-7,5	3,15

411+707 h=1,35

h [m]	1,35	Es [Mpa]	210000
h/2 [m]	0,675	Ec [Mpa]	42000
d [m]	1,3	alpha	5
d' [m]	0,05	yn [m]	1,1498
As [m2]	0,00643	b [m]	1
beta	1	e+h/2 [m]	0,2437
M [KNm/m]	415,69	0,35981	
N	-963,801	Iyn* [m3]	0,54633
e [m]	-0,4313	σ_c [Kpa]	-667,8
yg*	0,675	σ_s [Kpa]	-9980
		$\sigma_{s'}$ [Kpa]	5030
	σ_c [Mpa]	-2,2	-0,6678
9	σ_s [Mpa]	-11	-9,98
10	$\sigma_{s'}$ [Mpa]	-7,5	5,03

411+707 h=1,7865

h [m]	1,7865	Es [Mpa]	210000
h/2 [m]	0,89325	Ec [Mpa]	42000
d [m]	1,7365	alpha	5
d' [m]	0,05	yn [m]	1,73822
As [m2]	0,00643	b [m]	1
beta	1	e+h/2 [m]	0,37605
M [KNm/m]	540,83	0,56108	
N	-1045,69	Iyn* [m3]	1,8423
e [m]	-0,5172	σ_c [Kpa]	-1670
yg*	0,89325	σ_s [Kpa]	-7760
		$\sigma_{s'}$ [Kpa]	3090
	σ_c [Mpa]	-2,9	-1,67
7	σ_s [Mpa]	-14,5	-7,76
8	$\sigma_{s'}$ [Mpa]	-2,9	3,09

411+707 h=1,7865

h [m]	1,7865	Es [Mpa]	210000
h/2 [m]	0,89325	Ec [Mpa]	42000
d [m]	1,7365	alpha	5
d' [m]	0,05	yn [m]	0,48686
As [m2]	0,00643	b [m]	1
beta	1	e+h/2 [m]	-0,48577
M [KNm/m]	1256,36	-0,53993	
N	-911,056	Iyn* [m3]	0,09484
e [m]	-1,37902	σ_c [Kpa]	-4600
yg*	0,89325	σ_s [Kpa]	-20700
		$\sigma_{s'}$ [Kpa]	57220
	σ_c [Mpa]	-2	-4,6
5	σ_s [Mpa]	-10	-20,7
6	$\sigma_{s'}$ [Mpa]	-4,2	57,22

	411+707 h=1,35				411+707 h=1,35		
h [m]	1,35	Es [Mpa]	210000	h [m]	1,35	Es [Mpa]	210000
h/2 [m]	0,675	Ec [Mpa]	42000	h/2 [m]	0,675	Ec [Mpa]	42000
d [m]	1,3	alpha	5	d [m]	1,3	alpha	5
d' [m]	0,05	yn [m]	0,49981	d' [m]	0,05	yn [m]	1,34032
As [m2]	0,00643	b [m]	1	As [m2]	0,00643	b [m]	1
beta	1	e+h/2 [m]	0,04891	beta	1	e+h/2 [m]	0,66215
M [KNm/m]	577,61	-0,10499		M [KNm/m]	11,73	0,43045	
N	-922,571	Iyn* [m3]	0,06873	N	-913,07	Iyn* [m3]	0,85622
e [m]	-0,62609	σ_c [Kpa]	-3127	e [m]	-0,01285	σ_c [Kpa]	-680
yg*	0,675	σ_s [Kpa]	-14340	yg*	0,675	σ_s [Kpa]	-3380
		$\sigma_{s'}$ [Kpa]	17960			$\sigma_{s'}$ [Kpa]	-3070
	σ_c [Mpa]	-2,4	-3,127		σ_c [Mpa]	-2,84	-0,68
3	σ_s [Mpa]	-12	-14,34	1	σ_s [Mpa]	-9	-3,38
4	$\sigma_{s'}$ [Mpa]	-4,8	17,96	2	$\sigma_{s'}$ [Mpa]	-14,2	-3,07

Calculations for 411+468 cross section case c

	411+707 h=1,35				411+707 h=1,35		
h [m]	1,35	Es [Mpa]	210000	h [m]	1,35	Es [Mpa]	210000
h/2 [m]	0,675	Ec [Mpa]	42000	h/2 [m]	0,675	Ec [Mpa]	42000
d [m]	1,3	alpha	5	d [m]	1,3	alpha	5
d' [m]	0,05	yn [m]	1,12966	d' [m]	0,05	yn [m]	0,40072
As [m2]	0,00643	b [m]	1	As [m2]	0,00643	b [m]	1
beta	1	e+h/2 [m]	0,19777	beta	1	e+h/2 [m]	0,43915
M [KNm/m]	-203,16	0,35197		M [KNm/m]	-112,22	-0,42017	
N	-425,71	Iyn* [m3]	0,51896	N	-475,81	Iyn* [m3]	0,05142
e [m]	0,47723	σ_c [Kpa]	-810	e [m]	0,23585	σ_c [Kpa]	-600
yg*	0,675	σ_s [Kpa]	4890	yg*	0,675	σ_s [Kpa]	-540
		$\sigma_{s'}$ [Kpa]	-11500			$\sigma_{s'}$ [Kpa]	-8720
	σ_c [Mpa]	-2,3	-0,81		σ_c [Mpa]	-1,36	-0,6
11	σ_s [Mpa]	-11,5	4,89	9	σ_s [Mpa]	-	-0,54
12	$\sigma_{s'}$ [Mpa]	-9,8	-11,5	10	$\sigma_{s'}$ [Mpa]	-6,8	-8,72

	411+707 h=1,7865				411+707 h=1,7865		
h [m]	1,7865	Es [Mpa]	210000	h [m]	1,7865	Es [Mpa]	210000
h/2 [m]	0,89325	Ec [Mpa]	42000	h/2 [m]	0,89325	Ec [Mpa]	42000
d [m]	1,7365	alpha	5	d [m]	1,7365	alpha	5
d' [m]	0,05	yn [m]	14,4095	d' [m]	0,05	yn [m]	1,2842
As [m2]	0,00643	b [m]	1	As [m2]	0,00643	b [m]	1
beta	1	e+h/2 [m]	0,50771	beta	1	e+h/2 [m]	4,91531
M [KNm/m]	194,62	4,77025		M [KNm/m]	1374,98	0,388	
N	-504,8	Iyn* [m3]	1009,1	N	-341,86	Iyn* [m3]	0,76155
e [m]	-0,38554	σ_c [Kpa]	-810	e [m]	-4,02206	σ_c [Kpa]	-3130
yg*	0,89325	σ_s [Kpa]	-11800	yg*	0,89325	σ_s [Kpa]	-42310
		$\sigma_{s'}$ [Kpa]	2340			$\sigma_{s'}$ [Kpa]	112100
	σ_c [Mpa]	-2,86	-0,81		σ_c [Mpa]	-2,9	-3,13
7	σ_s [Mpa]	-14,3	-11,8	5	σ_s [Mpa]	-14,5	-42,31
8	$\sigma_{s'}$ [Mpa]	-3,8	2,34	6	$\sigma_{s'}$ [Mpa]	-6,3	112,1

411+707 h=1,35

h [m]	1,35	Es [Mpa]	210000
h/2 [m]	0,675	Ec [Mpa]	42000
d [m]	1,3	alpha	5
d' [m]	0,05	yn [m]	1,15607
As [m2]	0,00643	b [m]	1
beta	1	e+h/2 [m]	0,16371
M [KNm/m]	241,19	0,36224	
N	-471,73	Iyn* [m3]	0,55506
e [m]	-0,51129	σ_c [Kpa]	-950
yg*	0,675	σ_s [Kpa]	-13590
		$\sigma_{s'}$ [Kpa]	6520
	σ_c [Mpa]	-3,3	-0,95
3	σ_s [Mpa]	-16,5	-13,59
4	$\sigma_{s'}$ [Mpa]	-7,8	6,52

411+707 h=1,35

h [m]	1,35	Es [Mpa]	210000
h/2 [m]	0,675	Ec [Mpa]	42000
d [m]	1,3	alpha	5
d' [m]	0,05	yn [m]	0,68461
As [m2]	0,00643	b [m]	1
beta	1	e+h/2 [m]	0,77393
M [KNm/m]	-45,81	0,12241	
N	-463,04	Iyn* [m3]	0,13209
e [m]	0,09893	σ_c [Kpa]	-410
yg*	0,675	σ_s [Kpa]	-2970
		$\sigma_{s'}$ [Kpa]	-6030
	σ_c [Mpa]	-2,4	-0,41
1	σ_s [Mpa]	-12	-2,97
2	$\sigma_{s'}$ [Mpa]	-	-6,03

Calculations for 411+707 cross section case c

411+707 h=1,35

h [m]	1,35	Es [Mpa]	210000
h/2 [m]	0,675	Ec [Mpa]	42000
d [m]	1,3	alpha	5
d' [m]	0,05	yn [m]	1,19321
As [m2]	0,00643	b [m]	1
beta	1	e+h/2 [m]	0,37677
M [KNm/m]	-280,166	0,37642	
N	-939,424	Iyn* [m3]	0,60868
e [m]	0,29823	σ_c [Kpa]	-1503
yg*	0,675	σ_s [Kpa]	-7200
		$\sigma_{s'}$ [Kpa]	666,2
	σ_c [Mpa]	-2,04	-1,503
11	σ_s [Mpa]	-5	-7,2
12	$\sigma_{s'}$ [Mpa]	-10,2	0,6662

411+707 h=1,35

h [m]	1,35	Es [Mpa]	210000
h/2 [m]	0,675	Ec [Mpa]	42000
d [m]	1,3	alpha	5
d' [m]	0,05	yn [m]	0,33043
As [m2]	0,00643	b [m]	1
beta	1	e+h/2 [m]	-1,05123
M [KNm/m]	-1034,41	-1,05122	
N	-599,232	Iyn* [m3]	0,0448
e [m]	1,72623	σ_c [Kpa]	-1603
yg*	0,675	σ_s [Kpa]	-25910
		$\sigma_{s'}$ [Kpa]	89600
	σ_c [Mpa]	-2,04	-1,603
9	σ_s [Mpa]	-10,2	-25,91
10	$\sigma_{s'}$ [Mpa]	-5,5	89,6

411+707 h=1,7865

h [m]	1,7865	Es [Mpa]	210000
h/2 [m]	0,89325	Ec [Mpa]	42000
d [m]	1,7365	alpha	5
d' [m]	0,05	yn [m]	-8,17179
As [m2]	0,00643	b [m]	1
beta	1	e+h/2 [m]	4,57613
M [KNm/m]	-2638,51	-2,78963	
N	-716,424	Iyn* [m3]	-176,566
e [m]	3,68288	σ_c [Kpa]	-2898
yg*	0,89325	σ_s [Kpa]	-42340
		$\sigma_{s'}$ [Kpa]	197900
	σ_c [Mpa]	-2,6	-2,898
7	σ_s [Mpa]	-13	-42,34
8	$\sigma_{s'}$ [Mpa]	-1	197,9

411+707 h=1,7865

h [m]	1,7865	Es [Mpa]	210000
h/2 [m]	0,89325	Ec [Mpa]	42000
d [m]	1,7365	alpha	5
d' [m]	0,05	yn [m]	1,00496
As [m2]	0,00643	b [m]	1
beta	1	e+h/2 [m]	0,25335
M [KNm/m]	-637,383	0,25349	
N	-996,07	Iyn* [m3]	0,38487
e [m]	0,6399	σ_c [Kpa]	-264,3
yg*	0,89325	σ_s [Kpa]	-9260
		$\sigma_{s'}$ [Kpa]	7120
	σ_c [Mpa]	-1,9	-0,2643
5	σ_s [Mpa]	-9,5	-9,26
6	$\sigma_{s'}$ [Mpa]	-1,2	7,12

411+707 h=1,35

h [m]	1,35	Es [Mpa]	210000
h/2 [m]	0,675	Ec [Mpa]	42000
d [m]	1,3	alpha	5
d' [m]	0,05	yn [m]	1,40564
As [m2]	0,00643	b [m]	1
beta	1	e+h/2 [m]	0,45367
M [KNm/m]	216,034	0,45364	
N	-976,061	Iyn* [m3]	0,98524
e [m]	-0,22133	σ_c [Kpa]	-469,5
yg*	0,675	σ_s [Kpa]	-510
		$\sigma_{s'}$ [Kpa]	-6390
	σ_c [Mpa]	-2,1	-0,4695
3	σ_s [Mpa]	-10,5	-0,51
4	$\sigma_{s'}$ [Mpa]	0	-6,39

411+707 h=1,35

h [m]	1,35	Es [Mpa]	210000
h/2 [m]	0,675	Ec [Mpa]	42000
d [m]	1,3	alpha	5
d' [m]	0,05	yn [m]	0,72926
As [m2]	0,00643	b [m]	1
beta	1	e+h/2 [m]	0,15549
M [KNm/m]	462,229	0,15539	
N	-889,744	Iyn* [m3]	0,1546
e [m]	-0,51951	σ_c [Kpa]	-620,4
yg*	0,675	σ_s [Kpa]	9154
		$\sigma_{s'}$ [Kpa]	-11200
	σ_c [Mpa]	-1,64	-0,6204
1	σ_s [Mpa]	-8	9,154
2	$\sigma_{s'}$ [Mpa]	-8,2	-11,2

Calculations for 411+348 cross section case d

411+707 h=1,35

h [m]	1,35	Es [Mpa]	210000
h/2 [m]	0,675	Ec [Mpa]	42000
d [m]	1,3	alpha	5
d' [m]	0,05	yn [m]	1,00038
As [m2]	0,00643	b [m]	1
beta	1	e+h/2 [m]	0,28169
M [KNm/m]	347,52	0,29896	
N	-883,58	Iyn* [m3]	0,36565
e [m]	-0,39331	σ_c [Kpa]	-1782
yg*	0,675	σ_s [Kpa]	-8380
		$\sigma_{s'}$ [Kpa]	3150
	σ_c [Mpa]	-1,5	-1,782
11	σ_s [Mpa]	-5	-8,38
12	$\sigma_{s'}$ [Mpa]	-7,5	3,15

411+707 h=1,35

h [m]	1,35	Es [Mpa]	210000
h/2 [m]	0,675	Ec [Mpa]	42000
d [m]	1,3	alpha	5
d' [m]	0,05	yn [m]	1,1498
As [m2]	0,00643	b [m]	1
beta	1	e+h/2 [m]	0,2437
M [KNm/m]	415,69	0,35981	
N	-963,801	Iyn* [m3]	0,54633
e [m]	-0,4313	σ_c [Kpa]	-667,8
yg*	0,675	σ_s [Kpa]	-9980
		$\sigma_{s'}$ [Kpa]	5030
	σ_c [Mpa]	-2,2	-0,6678
9	σ_s [Mpa]	-7,5	-9,98
10	$\sigma_{s'}$ [Mpa]	-11	5,03

411+707 h=1,7865

h [m]	1,7865	Es [Mpa]	210000
h/2 [m]	0,89325	Ec [Mpa]	42000
d [m]	1,7365	alpha	5
d' [m]	0,05	yn [m]	1,73822
As [m2]	0,00643	b [m]	1
beta	1	e+h/2 [m]	0,37605
M [KNm/m]	540,83	0,56108	
N	-1045,69	Iyn* [m3]	1,8423
e [m]	-0,5172	σ_c [Kpa]	-1343,93
yg*	0,89325	σ_s [Kpa]	-6,63479
		$\sigma_{s'}$ [Kpa]	-6526,35
	σ_c [Mpa]	-2,9	
7	σ_s [Mpa]	-14,5	-0,00663
8	$\sigma_{s'}$ [Mpa]	-2,9	-6,52635

411+707 h=1,7865

h [m]	1,7865	Es [Mpa]	210000
h/2 [m]	0,89325	Ec [Mpa]	42000
d [m]	1,7365	alpha	5
d' [m]	0,05	yn [m]	0,48686
As [m2]	0,00643	b [m]	1
beta	1	e+h/2 [m]	-0,48577
M [KNm/m]	1256,36	-0,53993	
N	-911,056	Iyn* [m3]	0,09484
e [m]	-1,37902	σ_c [Kpa]	-4600
yg*	0,89325	σ_s [Kpa]	-20700
		$\sigma_{s'}$ [Kpa]	57220
	σ_c [Mpa]	-2	-4,6
5	σ_s [Mpa]	-10	-20,7
6	$\sigma_{s'}$ [Mpa]	-4,2	57,22

	411+707 h=1,35				411+707 h=1,35		
h [m]	1,35	Es [Mpa]	210000	h [m]	1,35	Es [Mpa]	210000
h/2 [m]	0,675	Ec [Mpa]	42000	h/2 [m]	0,675	Ec [Mpa]	42000
d [m]	1,3	alpha	5	d [m]	1,3	alpha	5
d' [m]	0,05	yn [m]	0,49981	d' [m]	0,05	yn [m]	1,34032
As [m2]	0,00643	b [m]	1	As [m2]	0,00643	b [m]	1
beta	1	e+h/2 [m]	0,04891	beta	1	e+h/2 [m]	0,66215
M [KNm/m]	577,61	-0,10499		M [KNm/m]	11,73	0,43045	
N	-922,571	Iyn* [m3]	0,06873	N	-913,07	Iyn* [m3]	0,85622
e [m]	-0,62609	σ_c [Kpa]	-3127	e [m]	-0,01285	σ_c [Kpa]	-680
yg*	0,675	σ_s [Kpa]	-14340	yg*	0,675	σ_s [Kpa]	-3380
		$\sigma_{s'}$ [Kpa]	17960			$\sigma_{s'}$ [Kpa]	-3070
	σ_c [Mpa]	-2,4	-3,127		σ_c [Mpa]	-2,84	-0,68
3	σ_s [Mpa]	-12	-14,34	1	σ_s [Mpa]	-9	-3,38
4	$\sigma_{s'}$ [Mpa]	-4,8	17,96	2	$\sigma_{s'}$ [Mpa]	-14,2	-3,07

Calculations for 411+468 cross section case d

	411+707 h=1,35				411+707 h=1,35		
h [m]	1,35	Es [Mpa]	210000	h [m]	1,35	Es [Mpa]	210000
h/2 [m]	0,675	Ec [Mpa]	42000	h/2 [m]	0,675	Ec [Mpa]	42000
d [m]	1,3	alpha	5	d [m]	1,3	alpha	5
d' [m]	0,05	yn [m]	1,12966	d' [m]	0,05	yn [m]	0,40072
As [m2]	0,00643	b [m]	1	As [m2]	0,00643	b [m]	1
beta	1	e+h/2 [m]	0,35202	beta	1	e+h/2 [m]	-0,4194
M [KNm/m]	-201,62	0,35197		M [KNm/m]	-655,798	-0,42017	
N	-624,245	Iyn* [m3]	0,51896	N	-599,232	Iyn* [m3]	0,05142
e [m]	0,32298	σ_c [Kpa]	-323,7	e [m]	1,0944	σ_c [Kpa]	-1603
yg*	0,675	σ_s [Kpa]	-5050	yg*	0,675	σ_s [Kpa]	-16760
		$\sigma_{s'}$ [Kpa]	796			$\sigma_{s'}$ [Kpa]	42960
	σ_c [Mpa]	-2,04	-0,3237		σ_c [Mpa]	-2,04	-1,603
11	σ_s [Mpa]	-5	-5,05	9	σ_s [Mpa]	-10,2	-16,76
12	$\sigma_{s'}$ [Mpa]	-10,2	0,796	10	$\sigma_{s'}$ [Mpa]	-5,5	42,96

	411+707 h=1,7865				411+707 h=1,7865		
h [m]	1,7865	Es [Mpa]	210000	h [m]	1,7865	Es [Mpa]	210000
h/2 [m]	0,89325	Ec [Mpa]	42000	h/2 [m]	0,89325	Ec [Mpa]	42000
d [m]	1,7365	alpha	5	d [m]	1,7365	alpha	5
d' [m]	0,05	yn [m]	14,4095	d' [m]	0,05	yn [m]	1,2842
As [m2]	0,00643	b [m]	1	As [m2]	0,00643	b [m]	1
beta	1	e+h/2 [m]	4,76975	beta	1	e+h/2 [m]	0,38791
M [KNm/m]	-1722,87	4,77025		M [KNm/m]	-321,69	0,388	
N	-444,44	Iyn* [m3]	1009,1	N	-636,577	Iyn* [m3]	0,76155
e [m]	3,8765	σ_c [Kpa]	-2898	e [m]	0,50534	σ_c [Kpa]	-264,3
yg*	0,89325	σ_s [Kpa]	-27580	yg*	0,89325	σ_s [Kpa]	-4600
		$\sigma_{s'}$ [Kpa]	130800			$\sigma_{s'}$ [Kpa]	1690
	σ_c [Mpa]	-2,6	-2,898		σ_c [Mpa]	-1,9	-0,2643
7	σ_s [Mpa]	-13	-27,58	5	σ_s [Mpa]	-9,5	-4,6
8	$\sigma_{s'}$ [Mpa]	-1	130,8	6	$\sigma_{s'}$ [Mpa]	-1,2	1,69

411+707 h=1,35				411+707 h=1,35			
h [m]	1,35	Es [Mpa]	210000	h [m]	1,35	Es [Mpa]	210000
h/2 [m]	0,675	Ec [Mpa]	42000	h/2 [m]	0,675	Ec [Mpa]	42000
d [m]	1,3	alpha	5	d [m]	1,3	alpha	5
d' [m]	0,05	yn [m]	1,15607	d' [m]	0,05	yn [m]	0,68461
As [m2]	0,00643	b [m]	1	As [m2]	0,00643	b [m]	1
beta	1	e+h/2 [m]	0,3623	beta	1	e+h/2 [m]	0,12255
M [KNm/m]	186,724	0,36224		M [KNm/m]	299,984	0,12241	
N	-597,142	Iyn* [m3]	0,55506	N	-543,01	Iyn* [m3]	0,13209
e [m]	-0,3127	σ_c [Kpa]	-469,5	e [m]	-0,55245	σ_c [Kpa]	-620,4
yg*	0,675	σ_s [Kpa]	613,6	yg*	0,675	σ_s [Kpa]	7100
		$\sigma_{s'}$ [Kpa]	-4720			$\sigma_{s'}$ [Kpa]	-7300
	σ_c [Mpa]	-2,1	-0,4695		σ_c [Mpa]	-1,6	-0,6204
3	σ_s [Mpa]	-10,5	0,6136	1	σ_s [Mpa]	-8	7,1
4	$\sigma_{s'}$ [Mpa]	0	-4,72	2	$\sigma_{s'}$ [Mpa]	-8,2	-7,3

Calculations for 411+707 cross section case d

411+707 h=1,35				411+707 h=1,35			
h [m]	1,35	Es [Mpa]	210000	h [m]	1,35	Es [Mpa]	210000
h/2 [m]	0,675	Ec [Mpa]	42000	h/2 [m]	0,675	Ec [Mpa]	42000
d [m]	1,3	alpha	5	d [m]	1,3	alpha	5
d' [m]	0,05	yn [m]	1,12966	d' [m]	0,05	yn [m]	0,40072
As [m2]	0,00643	b [m]	1	As [m2]	0,00643	b [m]	1
beta	1	e+h/2 [m]	0,35202	beta	1	e+h/2 [m]	-0,4194
M [KNm/m]	-201,62	0,35197		M [KNm/m]	-655,798	-0,42017	
N	-624,245	Iyn* [m3]	0,51896	N	-599,232	Iyn* [m3]	0,05142
e [m]	0,32298	σ_c [Kpa]	-323,7	e [m]	1,0944	σ_c [Kpa]	-1603
yg*	0,675	σ_s [Kpa]	-5050	yg*	0,675	σ_s [Kpa]	-16760
		$\sigma_{s'}$ [Kpa]	796			$\sigma_{s'}$ [Kpa]	42960
	σ_c [Mpa]	-2,04	-0,3237		σ_c [Mpa]	-2,04	-1,603
11	σ_s [Mpa]	-5	-5,05	9	σ_s [Mpa]	-10,2	-16,76
12	$\sigma_{s'}$ [Mpa]	-10,2	0,796	10	$\sigma_{s'}$ [Mpa]	-5,5	42,96

411+707 h=1,7865				411+707 h=1,7865			
h [m]	1,7865	Es [Mpa]	210000	h [m]	1,7865	Es [Mpa]	210000
h/2 [m]	0,89325	Ec [Mpa]	42000	h/2 [m]	0,89325	Ec [Mpa]	42000
d [m]	1,7365	alpha	5	d [m]	1,7365	alpha	5
d' [m]	0,05	yn [m]	14,4095	d' [m]	0,05	yn [m]	1,2842
As [m2]	0,00643	b [m]	1	As [m2]	0,00643	b [m]	1
beta	1	e+h/2 [m]	4,76975	beta	1	e+h/2 [m]	0,38791
M [KNm/m]	-1722,87	4,77025		M [KNm/m]	-321,69	0,388	
N	-444,44	Iyn* [m3]	1009,1	N	-636,577	Iyn* [m3]	0,76155
e [m]	3,8765	σ_c [Kpa]	-2898	e [m]	0,50534	σ_c [Kpa]	-264,3
yg*	0,89325	σ_s [Kpa]	-27580	yg*	0,89325	σ_s [Kpa]	-4600
		$\sigma_{s'}$ [Kpa]	130800			$\sigma_{s'}$ [Kpa]	1690
	σ_c [Mpa]	-2,6	-2,898		σ_c [Mpa]	-1,9	-0,2643
7	σ_s [Mpa]	-13	-27,58	5	σ_s [Mpa]	-9,5	-4,6
8	$\sigma_{s'}$ [Mpa]	-1	130,8	6	$\sigma_{s'}$ [Mpa]	-1,2	1,69

	411+707 h=1,35				**411+707 h=1,35**		
h [m]	1,35	Es [Mpa]	210000	h [m]	1,35	Es [Mpa]	210000
h/2 [m]	0,675	Ec [Mpa]	42000	h/2 [m]	0,675	Ec [Mpa]	42000
d [m]	1,3	alpha	5	d [m]	1,3	alpha	5
d' [m]	0,05	yn [m]	1,15607	d' [m]	0,05	yn [m]	0,68461
As [m2]	0,00643	b [m]	1	As [m2]	0,00643	b [m]	1
beta	1	e+h/2 [m]	0,3623	beta	1	e+h/2 [m]	0,12255
M [KNm/m]	186,724	0,36224		M [KNm/m]	299,984	0,12241	
N	-597,142	Iyn* [m3]	0,55506	N	-543,01	Iyn* [m3]	0,13209
e [m]	-0,3127	σ_c [Kpa]	-469,5	e [m]	-0,55245		-620,4
yg*	0,675	σ_s [Kpa]	613,6	yg*	0,675		7100
		$\sigma_{s'}$ [Kpa]	-4720				-7300
	σ_c [Mpa]	-2,1	-0,4695		σ_c [Mpa]	-1,64	-0,6204
3	σ_s [Mpa]	-10,5	0,6136	1	σ_s [Mpa]	-8	7,1
4	$\sigma_{s'}$ [Mpa]	0	-4,72	2	$\sigma_{s'}$ [Mpa]	-8,2	-7,3

Calculations for 411+348 cross section case e

	411+707 h=1,35				**411+707 h=1,35**		
h [m]	1,35	Es [Mpa]	210000	h [m]	1,35	Es [Mpa]	210000
h/2 [m]	0,675	Ec [Mpa]	42000	h/2 [m]	0,675	Ec [Mpa]	42000
d [m]	1,3	alpha	5	d [m]	1,3	alpha	5
d' [m]	0,05	yn [m]	1,00038	d' [m]	0,05	yn [m]	1,1498
As [m2]	0,00643	b [m]	1	As [m2]	0,00643	b [m]	1
beta	1	e+h/2 [m]	0,29866	beta	1	e+h/2 [m]	0,35938
M [KNm/m]	134,87	0,29896		M [KNm/m]	126,642	0,35981	
N	-358,37	Iyn* [m3]	0,36565	N	-401,244	Iyn* [m3]	0,54633
e [m]	-0,37634	σ_c [Kpa]	-685,9	e [m]	-0,31562	σ_c [Kpa]	-667,8
yg*	0,675	σ_s [Kpa]	-1014	yg*	0,675	σ_s [Kpa]	434
		$\sigma_{s'}$ [Kpa]	-3259			$\sigma_{s'}$ [Kpa]	-3194
	σ_c [Mpa]	-1,5	-0,6859		σ_c [Mpa]	-2,2	-0,6678
11	σ_s [Mpa]	-5	-1,014	9	σ_s [Mpa]	-7,5	0,434
12	$\sigma_{s'}$ [Mpa]	-7,5	-3,259	10	$\sigma_{s'}$ [Mpa]	-11	-3,194

	411+707 h=1,7865				**411+707 h=1,7865**		
h [m]	1,7865	Es [Mpa]	210000	h [m]	1,7865	Es [Mpa]	210000
h/2 [m]	0,89325	Ec [Mpa]	42000	h/2 [m]	0,89325	Ec [Mpa]	42000
d [m]	1,7365	alpha	5	d [m]	1,7365	alpha	5
d' [m]	0,05	yn [m]	1,73822	d' [m]	0,05	yn [m]	0,48686
As [m2]	0,00643	b [m]	1	As [m2]	0,00643	b [m]	1
beta	1	e+h/2 [m]	0,56101	beta	1	e+h/2 [m]	-0,53995
M [KNm/m]	149,227	0,56108		M [KNm/m]	553,788	-0,53993	
N	-449,16	Iyn* [m3]	1,8423	N	-386,401	Iyn* [m3]	0,09484
e [m]	-0,33224	σ_c [Kpa]	-498,9	e [m]	-1,4332	σ_c [Kpa]	-2037
yg*	0,89325	σ_s [Kpa]	-2,218	yg*	0,89325	σ_s [Kpa]	-26140
		$\sigma_{s'}$ [Kpa]	-2430			$\sigma_{s'}$ [Kpa]	-9130
	σ_c [Mpa]	-2,9	-0,4989		σ_c [Mpa]	-2	-2,037
7	σ_s [Mpa]	-14,5	-0,00222	5	σ_s [Mpa]	-10	-26,14
8	$\sigma_{s'}$ [Mpa]	-2,9	-2,43	6	$\sigma_{s'}$ [Mpa]	-4,2	-9,13

	411+707 h=1,35				**411+707 h=1,35**		
h [m]	1,35	Es [Mpa]	210000	h [m]	1,35	Es [Mpa]	210000
h/2 [m]	0,675	Ec [Mpa]	42000	h/2 [m]	0,675	Ec [Mpa]	42000
d [m]	1,3	alpha	5	d [m]	1,3	alpha	5
d' [m]	0,05	yn [m]	0,49981	d' [m]	0,05	yn [m]	1,34032
As [m2]	0,00643	b [m]	1	As [m2]	0,00643	b [m]	1
beta	1	e+h/2 [m]	-0,10509	beta	1	e+h/2 [m]	0,43135
M [KNm/m]	300,66	-0,10499		M [KNm/m]	92,205	0,43045	
N	-385,418	Iyn* [m3]	0,06873	N	-378,429	Iyn* [m3]	0,85622
e [m]	-0,78009	σ_c [Kpa]	-1695	e [m]	-0,24365	σ_c [Kpa]	-528
yg*	0,675	σ_s [Kpa]	-13570	yg*	0,675	σ_s [Kpa]	-85,81
		$\sigma_{s'}$ [Kpa]	-7629			$\sigma_{s'}$ [Kpa]	-2590
	σ_c [Mpa]	-2,4	-1,695		σ_c [Mpa]	-2,84	-0,528
3	σ_s [Mpa]	-12	-13,57	1	σ_s [Mpa]	-9	-0,08581
4	$\sigma_{s'}$ [Mpa]	-4,8	-7,629	2	$\sigma_{s'}$ [Mpa]	-14,2	-2,59

Calculations for 411+468 cross section case e

	411+707 h=1,35				**411+707 h=1,35**		
h [m]	1,35	Es [Mpa]	210000	h [m]	1,35	Es [Mpa]	210000
h/2 [m]	0,675	Ec [Mpa]	42000	h/2 [m]	0,675	Ec [Mpa]	42000
d [m]	1,3	alpha	5	d [m]	1,3	alpha	5
d' [m]	0,05	yn [m]	1,12966	d' [m]	0,05	yn [m]	0,40072
As [m2]	0,00643	b [m]	1	As [m2]	0,00643	b [m]	1
beta	1	e+h/2 [m]	0,20768	beta	1	e+h/2 [m]	0,45289
M [KNm/m]	-67,71	0,35197		M [KNm/m]	-36,7	-0,42017	
N	-144,89	Iyn* [m3]	0,51896	N	-165,23	Iyn* [m3]	0,05142
e [m]	0,46732	σ_c [Kpa]	-270	e [m]	0,22211	σ_c [Kpa]	-190
yg*	0,675	σ_s [Kpa]	1480	yg*	0,675	σ_s [Kpa]	-370
		$\sigma_{s'}$ [Kpa]	-3860			$\sigma_{s'}$ [Kpa]	-2830
	σ_c [Mpa]	-2,3	-0,27		σ_c [Mpa]	-1,36	-0,19
11	σ_s [Mpa]	-11,5	1,48	9	σ_s [Mpa]	-	-0,37
12	$\sigma_{s'}$ [Mpa]	-9,8	-3,86	10	$\sigma_{s'}$ [Mpa]	-6,8	-2,83

	411+707 h=1,7865				**411+707 h=1,7865**		
h [m]	1,7865	Es [Mpa]	210000	h [m]	1,7865	Es [Mpa]	210000
h/2 [m]	0,89325	Ec [Mpa]	42000	h/2 [m]	0,89325	Ec [Mpa]	42000
d [m]	1,7365	alpha	5	d [m]	1,7365	alpha	5
d' [m]	0,05	yn [m]	14,4095	d' [m]	0,05	yn [m]	1,2842
As [m2]	0,00643	b [m]	1	As [m2]	0,00643	b [m]	1
beta	1	e+h/2 [m]	0,46721	beta	1	e+h/2 [m]	4,48994
M [KNm/m]	76,47	4,77025		M [KNm/m]	453,614	0,388	
N	-179,49	Iyn* [m3]	1009,1	N	-126,12	Iyn* [m3]	0,76155
e [m]	-0,42604	σ_c [Kpa]	-310	e [m]	-3,59669	σ_c [Kpa]	-590
yg*	0,89325	σ_s [Kpa]	-4480	yg*	0,89325	σ_s [Kpa]	-186
		$\sigma_{s'}$ [Kpa]	1290			$\sigma_{s'}$ [Kpa]	-8630
	σ_c [Mpa]	-2,86	-0,31		σ_c [Mpa]	-2,9	-0,59
7	σ_s [Mpa]	-14,3	-4,48	5	σ_s [Mpa]	-14,5	-0,186
8	$\sigma_{s'}$ [Mpa]	-3,8	1,29	6	$\sigma_{s'}$ [Mpa]	-6,3	-8,63

411+707 h=1,35

h [m]	1,35	Es [Mpa]	210000
h/2 [m]	0,675	Ec [Mpa]	42000
d [m]	1,3	alpha	5
d' [m]	0,05	yn [m]	1,15607
As [m2]	0,00643	b [m]	1
beta	1	e+h/2 [m]	0,24248
M [KNm/m]	70,09	0,36224	
N	-162,05	Iyn* [m3]	0,55506
e [m]	-0,43252	σ_c [Kpa]	-350
yg*	0,675	σ_s [Kpa]	-1880
		$\sigma_{s'}$ [Kpa]	850
	σ_c [Mpa]	-3,3	-0,35
3	σ_s [Mpa]	-16,5	-1,88
4	$\sigma_{s'}$ [Mpa]	-7,8	0,85

411+707 h=1,35

h [m]	1,35	Es [Mpa]	210000
h/2 [m]	0,675	Ec [Mpa]	42000
d [m]	1,3	alpha	5
d' [m]	0,05	yn [m]	0,68461
As [m2]	0,00643	b [m]	1
beta	1	e+h/2 [m]	0,77807
M [KNm/m]	-15,9	0,12241	
N	-154,27	Iyn* [m3]	0,13209
e [m]	0,10307	σ_c [Kpa]	-138
yg*	0,675	σ_s [Kpa]	-340
		$\sigma_{s'}$ [Kpa]	-740
	σ_c [Mpa]	-2,4	-0,138
1	σ_s [Mpa]	-12	-0,34
2	$\sigma_{s'}$ [Mpa]	-	-0,74

Calculations for 411+707 cross section case e

411+707 h=1,35

h [m]	1,35	Es [Mpa]	210000
h/2 [m]	0,675	Ec [Mpa]	42000
d [m]	1,3	alpha	5
d' [m]	0,05	yn [m]	2,88938
As [m2]	0,00643	b [m]	1
beta	1	e+h/2 [m]	0,4022
M [KNm/m]	-58,384	0,94779	
N	-214,019	Iyn* [m3]	8,38127
e [m]	0,2728	σ_c [Kpa]	-323,7
yg*	0,675	σ_s [Kpa]	-1554
		$\sigma_{s'}$ [Kpa]	48,17
	σ_c [Mpa]	-2,04	-0,3237
11	σ_s [Mpa]	-5	-1,554
12	$\sigma_{s'}$ [Mpa]	-10,2	0,04817

411+707 h=1,35

h [m]	1,35	Es [Mpa]	210000
h/2 [m]	0,675	Ec [Mpa]	42000
d [m]	1,3	alpha	5
d' [m]	0,05	yn [m]	0,35829
As [m2]	0,00643	b [m]	1
beta	1	e+h/2 [m]	2,06279
M [KNm/m]	-272,025	-0,71268	
N	-196,013	Iyn* [m3]	0,04692
e [m]	1,38779	σ_c [Kpa]	-1603
yg*	0,675	σ_s [Kpa]	-6890
		$\sigma_{s'}$ [Kpa]	21070
	σ_c [Mpa]	-2,04	-1,603
9	σ_s [Mpa]	-10,2	-6,89
10	$\sigma_{s'}$ [Mpa]	-5,5	21,07

411+707 h=1,7865

h [m]	1,7865	Es [Mpa]	210000
h/2 [m]	0,89325	Ec [Mpa]	42000
d [m]	1,7365	alpha	5
d' [m]	0,05	yn [m]	-14,3771
As [m2]	0,00643	b [m]	1
beta	1	e+h/2 [m]	-4,84692
M [KNm/m]	778,476	-4,84739	
N	-135,619	Iyn* [m3]	-975,542
e [m]	-5,74017	σ_c [Kpa]	-2898
yg*	0,89325	σ_s [Kpa]	-12240
		$\sigma_{s'}$ [Kpa]	63670
	σ_c [Mpa]	-2,6	-2,898
7	σ_s [Mpa]	-13	-12,24
8	$\sigma_{s'}$ [Mpa	-1	63,67

411+707 h=1,7865

h [m]	1,7865	Es [Mpa]	210000
h/2 [m]	0,89325	Ec [Mpa]	42000
d [m]	1,7365	alpha	5
d' [m]	0,05	yn [m]	3,74377
As [m2]	0,00643	b [m]	1
beta	1	e+h/2 [m]	1,23252
M [KNm/m]	-79,801	1,23252	
N	-235,214	Iyn* [m3]	18,0593
e [m]	0,33927	σ_c [Kpa]	-264,3
yg*	0,89325	σ_s [Kpa]	-1283
		$\sigma_{s'}$ [Kpa]	13,99
	σ_c [Mpa]	-1,9	-0,2643
5	σ_s [Mpa]	-9,5	-1,283
6	$\sigma_{s'}$ [Mpa]	-1,2	0,01399

	411+707 h=1,35				**411+707 h=1,35**		
h [m]	1,35	Es [Mpa]	210000	h [m]	1,35	Es [Mpa]	210000
h/2 [m]	0,675	Ec [Mpa]	42000	h/2 [m]	0,675	Ec [Mpa]	42000
d [m]	1,3	alpha	5	d [m]	1,3	alpha	5
d' [m]	0,05	yn [m]	0,95961	d' [m]	0,05	yn [m]	0,6992
As [m2]	0,00643	b [m]	1	As [m2]	0,00643	b [m]	1
beta	1	e+h/2 [m]	0,28037	beta	1	e+h/2 [m]	0,1334
M [KNm/m]	92,308	0,28095		M [KNm/m]	118,135	0,1337	
N	-233,91	Iyn* [m3]	0,3249	N	-218,124	Iyn* [m3]	0,13911
e [m]	-0,39463	σ_c [Kpa]	-469,5	e [m]	-0,5416	σ_c [Kpa]	-620,4
yg*	0,675	σ_s [Kpa]	837,1	yg*	0,675	σ_s [Kpa]	2669
		$\sigma_{s'}$ [Kpa]	-2225			$\sigma_{s'}$ [Kpa]	-2880
	σ_c [Mpa]	-2,1	-0,4695		σ_c [Mpa]	-1,64	-0,6204
3	σ_s [Mpa]	-10,5	0,8371	1	σ_s [Mpa]	-8	2,669
4	$\sigma_{s'}$ [Mpa]	0	-2,225	2	$\sigma_{s'}$ [Mpa]	-8,2	-2,88

APPENDIX B

Matlab code for 6x6 grid analysis case

```
B = 0.98271;
A = 1 - B;
alpha = 0.8412;
f = rand ([6 6])
x = zeros([6 6]);
for i=1:36 ;
  if f(i) >= 0.02
  x(i)= -1/alpha * log((f(i)-A/B))
  else
  x(i) = 6
  end
i=i+1;
end
```

Matlab code for 18x6 grid analysis case

```
B = 0.98271;
A = 1 - B;
alpha = 0.8412;
f = rand ([18 6])
x = zeros([18 6]);
for i=1:108 ;
  if f(i) >= 0.02
  x(i)= -1/alpha * log((f(i)-A/B))
  else
  x(i) = 6
  end
i=i+1;
end
```

Matlab code for 26x26 grid analysis case

```
B = 0.98271;
A = 1 - B;
alpha = 0.8412;
f = rand ([26 26])
x = zeros([26 26]);
for i=1:676 ;
  if f(i) >= 0.02
  x(i)= -1/alpha * log((f(i)-A/B))
  else
  x(i) = 6
  end
i=i+1;
end
```

APPENDIX C

Random numbers for the 26x26 grid analysis case

Random numbers (0-182/676)

0,815	0,743	0,655	0,616	0,166	0,431	0,338
0,906	0,392	0,163	0,473	0,602	0,911	0,900
0,127	0,655	0,119	0,352	0,263	0,182	0,369
0,913	0,171	0,498	0,831	0,654	0,264	0,111
0,632	0,706	0,960	0,585	0,689	0,146	0,780
0,098	0,032	0,340	0,550	0,748	0,136	0,390
0,278	0,277	0,585	0,917	0,451	0,869	0,242
0,547	0,046	0,224	0,286	0,084	0,580	0,404
0,958	0,097	0,751	0,757	0,229	0,550	0,096
0,965	0,823	0,255	0,754	0,913	0,145	0,132
0,158	0,695	0,506	0,380	0,152	0,853	0,942
0,971	0,317	0,699	0,568	0,826	0,622	0,956
0,957	0,950	0,891	0,076	0,538	0,351	0,575
0,485	0,034	0,959	0,054	0,996	0,513	0,060
0,800	0,439	0,547	0,531	0,078	0,402	0,235
0,142	0,382	0,139	0,779	0,443	0,076	0,353
0,422	0,766	0,149	0,934	0,107	0,240	0,821
0,916	0,795	0,258	0,130	0,962	0,123	0,015
0,792	0,187	0,841	0,569	0,005	0,184	0,043
0,959	0,490	0,254	0,469	0,775	0,240	0,169
0,656	0,446	0,814	0,012	0,817	0,417	0,649
0,036	0,646	0,244	0,337	0,869	0,050	0,732
0,849	0,709	0,929	0,162	0,084	0,903	0,648
0,934	0,755	0,350	0,794	0,400	0,945	0,451
0,679	0,276	0,197	0,311	0,260	0,491	0,547
0,758	0,680	0,251	0,529	0,800	0,489	0,296

Random numbers (182-364/676)

0,745	0,622	0,222	0,038	0,618	0,973	0,490
0,189	0,587	0,117	0,885	0,859	0,649	0,339

0,687	0,208	0,297	0,913	0,805	0,800	0,952
0,184	0,301	0,319	0,796	0,577	0,454	0,920
0,368	0,471	0,424	0,099	0,183	0,432	0,053
0,626	0,230	0,508	0,262	0,240	0,825	0,738
0,780	0,844	0,086	0,335	0,887	0,083	0,269
0,081	0,195	0,262	0,680	0,029	0,133	0,423
0,929	0,226	0,801	0,137	0,490	0,173	0,548
0,776	0,171	0,029	0,721	0,168	0,391	0,943
0,487	0,228	0,929	0,107	0,979	0,831	0,418
0,436	0,436	0,730	0,654	0,713	0,803	0,983
0,447	0,311	0,489	0,494	0,500	0,060	0,301
0,306	0,923	0,579	0,779	0,471	0,399	0,701
0,509	0,430	0,237	0,715	0,060	0,527	0,666
0,511	0,185	0,459	0,904	0,682	0,417	0,539
0,818	0,905	0,963	0,891	0,042	0,657	0,698
0,795	0,980	0,547	0,334	0,071	0,628	0,667
0,644	0,439	0,521	0,699	0,522	0,292	0,178
0,379	0,111	0,232	0,198	0,097	0,432	0,128
0,812	0,258	0,489	0,031	0,818	0,015	0,999
0,533	0,409	0,624	0,744	0,818	0,984	0,171
0,351	0,595	0,679	0,500	0,722	0,167	0,033
0,939	0,262	0,396	0,480	0,150	0,106	0,561
0,876	0,603	0,367	0,905	0,660	0,372	0,882
0,550	0,711	0,988	0,610	0,519	0,198	0,669

Random numbers (364-546/676)

0,190	0,906	0,53	0,67	0,24	0,66	0,40
0,369	0,880	0,33	0,84	0,92	0,42	0,45
0,461	0,818	0,11	0,34	0,27	0,84	0,37
0,982	0,261	0,61	0,78	0,77	0,83	0,76
0,156	0,594	0,78	0,68	0,19	0,26	0,63
0,856	0,023	0,42	0,01	0,29	0,61	0,77
0,645	0,425	0,09	0,60	0,09	0,58	0,93
0,376	0,313	0,27	0,39	0,58	0,54	0,97
0,191	0,161	0,15	0,92	0,68	0,87	0,19
0,428	0,179	0,28	0,00	0,55	0,26	0,14
0,482	0,423	0,44	0,46	0,43	0,32	0,70
0,121	0,094	0,53	0,42	0,64	0,12	0,09
0,590	0,599	0,46	0,46	0,65	0,94	0,53
0,226	0,471	0,88	0,77	0,68	0,65	0,53
0,385	0,696	0,52	0,32	0,64	0,48	0,86
0,583	0,700	0,94	0,78	0,95	0,64	0,48
0,252	0,639	0,64	0,47	0,21	0,54	0,39
0,290	0,034	0,96	0,04	0,71	0,65	0,67
0,617	0,069	0,24	0,18	0,24	0,54	0,74
0,265	0,320	0,68	0,72	0,12	0,72	0,52
0,824	0,531	0,29	0,47	0,61	0,52	0,35
0,983	0,654	0,67	0,15	0,45	0,99	0,15
0,730	0,408	0,70	0,34	0,46	0,22	0,59
0,344	0,820	0,07	0,61	0,66	0,11	0,26

0,584	0,718	0,25	0,19	0,77	0,11	0,04
0,108	0,969	0,22	0,74	0,35	0,06	0,75

Random numbers (546-676/676)

0,24	0,33	0,15	0,08	0,15
0,44	0,67	0,05	0,63	0,19
0,69	0,44	0,85	0,66	0,04
0,36	0,83	0,56	0,73	0,64
0,74	0,77	0,93	0,89	0,28
0,39	0,17	0,70	0,98	0,54
0,68	0,86	0,58	0,77	0,70
0,70	0,99	0,82	0,58	0,50
0,44	0,51	0,88	0,93	0,54
0,02	0,88	0,99	0,58	0,45
0,33	0,59	0,00	0,02	0,12
0,42	0,15	0,87	0,12	0,49
0,27	0,20	0,61	0,86	0,85
0,20	0,41	0,99	0,48	0,87
0,82	0,75	0,53	0,84	0,27
0,43	0,83	0,48	0,21	0,21
0,89	0,79	0,80	0,55	0,56
0,39	0,32	0,23	0,63	0,64
0,77	0,53	0,50	0,03	0,42
0,40	0,09	0,90	0,61	0,21
0,81	0,11	0,57	0,36	0,95
0,76	0,14	0,85	0,05	0,08
0,38	0,68	0,74	0,49	0,11
0,22	0,50	0,59	0,19	0,14
0,79	0,19	0,25	0,12	0,17
0,95	0,50	0,67	0,21	0,62

Swelling Pressures [Mpa] (0-182/676)

0,270	0,381	0,535	0,610	2,271	1,049	1,354
0,141	1,167	2,295	0,934	0,639	0,134	0,149
2,631	0,534	2,721	1,303	1,670	2,147	1,242
0,131	2,227	0,871	0,246	0,537	1,666	2,816
0,578	0,444	0,071	0,673	0,473	2,444	0,322
3,003	5,054	1,344	0,750	0,373	2,536	1,175
1,597	1,604	0,673	0,126	0,995	0,191	1,778
0,756	4,226	1,877	1,564	3,227	0,685	1,131
0,074	3,009	0,368	0,359	1,847	0,750	3,020
0,064	0,257	1,709	0,364	0,131	2,450	2,578
2,337	0,463	0,852	1,205	2,382	0,214	0,093
0,057	1,433	0,456	0,710	0,253	0,598	0,075
0,074	0,083	0,161	3,380	0,776	1,306	0,694
0,903	4,854	0,071	3,940	0,026	0,834	3,763
0,291	1,028	0,756	0,793	3,333	1,137	1,815
2,479	1,201	2,510	0,324	1,017	3,377	1,298
1,077	0,345	2,410	0,104	2,875	1,787	0,260

0,128	0,299	1,697	2,599	0,068	2,671	6,000
0,304	2,112	0,231	0,708	6,000	2,133	4,365
0,071	0,892	1,713	0,945	0,330	1,787	2,244
0,534	1,009	0,270	6,000	0,266	1,090	0,546
4,768	0,552	1,768	1,356	0,192	4,090	0,400
0,219	0,438	0,110	2,299	3,216	0,145	0,549
0,104	0,363	1,309	0,300	1,143	0,090	0,994
0,492	1,609	2,045	1,457	1,685	0,889	0,756
0,358	0,490	1,729	0,798	0,292	0,893	1,519

Swelling Pressures [Mpa] (182-364/676)

0,379	0,598	1,889	4,642	0,607	0,054	0,892
2,097	0,669	2,739	0,169	0,205	0,547	1,347
0,478	1,973	1,517	0,131	0,283	0,291	0,081
2,135	1,498	1,427	0,298	0,691	0,986	0,122
1,245	0,940	1,070	2,986	2,140	1,046	3,982
0,591	1,839	0,847	1,676	1,787	0,254	0,390
0,322	0,226	3,197	1,363	0,167	3,233	1,641
3,277	2,057	1,673	0,490	5,353	2,565	1,074
0,110	1,865	0,290	2,531	0,892	2,210	0,754
0,329	2,231	5,295	0,418	2,253	1,171	0,092
0,900	1,855	0,110	2,874	0,047	0,245	1,089
1,036	1,037	0,403	0,538	0,432	0,287	0,042
1,006	1,457	0,895	0,881	0,865	3,744	1,497
1,477	0,118	0,687	0,324	0,940	1,145	0,452
0,846	1,052	1,802	0,428	3,768	0,802	0,514
0,840	2,126	0,973	0,144	0,486	1,092	0,774
0,265	0,142	0,067	0,161	4,393	0,532	0,458
0,300	0,046	0,756	1,367	3,473	0,587	0,514
0,555	1,028	0,816	0,456	0,814	1,537	2,175
1,211	2,817	1,833	2,037	3,015	1,048	2,619
0,274	1,694	0,894	5,168	0,264	6,000	0,022
0,788	1,116	0,595	0,380	0,265	0,041	2,228
1,307	0,653	0,491	0,867	0,416	2,259	4,992
0,097	1,674	1,157	0,917	2,405	2,881	0,725
0,182	0,637	1,249	0,142	0,527	1,232	0,173
0,749	0,435	0,036	0,623	0,822	2,035	0,509

Swelling Pressures [Mpa] (364-546/676)

2,087	0,140	0,79	0,51	1,77	0,52	1,13
1,244	0,176	1,40	0,23	0,13	1,09	1,00
0,968	0,265	2,89	1,33	1,64	0,23	1,25
0,044	1,681	0,62	0,32	0,35	0,24	0,35
2,347	0,654	0,32	0,50	2,10	1,70	0,59
0,210	6,318	1,07	6,00	1,56	0,62	0,34
0,555	1,067	3,11	0,64	3,10	0,68	0,11
1,219	1,451	1,65	1,18	0,69	0,77	0,05
2,083	2,305	2,37	0,13	0,48	0,19	2,08
1,058	2,170	1,59	6,00	0,76	1,66	2,51

0,912	1,074	1,02	0,96	1,07	1,43	0,46
2,702	3,054	0,80	1,07	0,56	2,72	3,06
0,664	0,646	0,98	0,97	0,55	0,10	0,81
1,863	0,940	0,18	0,34	0,49	0,55	0,79
1,192	0,461	0,82	1,41	0,57	0,92	0,20
0,678	0,454	0,09	0,32	0,09	0,56	0,90
1,726	0,566	0,57	0,94	1,97	0,76	1,16
1,544	4,915	0,07	4,76	0,44	0,55	0,51
0,608	3,533	1,78	2,19	1,81	0,76	0,38
1,659	1,423	0,50	0,42	2,72	0,42	0,82
0,255	0,793	1,55	0,93	0,63	0,81	1,32
0,042	0,536	0,50	2,38	1,00	0,03	2,40
0,403	1,119	0,46	1,34	0,97	1,91	0,67
1,331	0,262	3,55	0,63	0,52	2,89	1,67
0,676	0,423	1,71	2,08	0,34	2,84	4,30
2,860	0,060	1,88	0,39	1,31	3,66	0,36

Swelling Pressures [Mpa] (546-676/676)

1,77	1,39	2,43	3,23	2,44
1,02	0,51	3,91	0,59	2,10
0,48	1,03	0,22	0,52	4,38
1,28	0,24	0,73	0,40	0,57
0,39	0,34	0,11	0,16	1,58
1,16	2,26	0,46	0,04	0,78
0,48	0,20	0,68	0,34	0,46
0,45	0,03	0,27	0,68	0,87
1,02	0,83	0,18	0,11	0,78
6,00	0,17	0,03	0,68	1,01
1,38	0,67	6,00	6,00	2,66
1,07	2,36	0,20	2,70	0,89
1,64	2,02	0,62	0,20	0,21
2,04	1,12	0,03	0,91	0,18
0,26	0,37	0,80	0,23	1,64
1,05	0,25	0,92	1,96	1,97
0,17	0,31	0,29	0,74	0,72
1,17	1,43	1,85	0,58	0,56
0,34	0,79	0,87	5,04	1,09
1,15	3,12	0,15	0,61	1,98
0,28	2,81	0,70	1,27	0,09
0,36	2,53	0,22	4,09	3,26
1,22	0,49	0,39	0,89	2,89
1,92	0,88	0,67	2,07	2,48
0,31	2,09	1,75	2,67	2,26
0,08	0,88	0,51	1,99	0,60

Swelling Forces [N] (0-182/676)

13231,08	18722,38	26270,68	29959,62	111466,33	51487,20	66467,72
6918,50	57292,48	112675,78	45862,30	31347,22	6600,36	7296,71
129126,43	26235,92	133551,76	63980,42	81984,99	105407,66	60986,44

6422,36	109323,44	42736,52	12063,86	26364,02	81787,55	138219,24
28390,10	21784,12	3477,38	33040,92	23228,52	119984,96	15810,77
147425,63	248109,29	65983,70	36813,71	18320,09	124472,51	57681,34
78404,59	78757,98	33040,55	6174,18	48850,41	9367,18	87278,67
37126,21	207457,02	92130,62	76785,42	158411,53	33615,23	55500,17
3616,10	147724,65	18071,77	17601,76	90687,06	36798,73	148223,66
3159,60	12595,17	83888,77	17876,28	6424,87	120252,01	126525,30
114722,68	22742,76	41822,11	59157,02	116946,27	10492,08	4583,67
2809,27	70352,94	22377,87	34862,05	12424,59	29376,47	3701,36
3637,21	4070,14	7904,97	165890,97	38075,32	64104,07	34083,85
44334,69	238276,50	3505,41	193408,40	1265,88	40957,18	184730,24
14298,09	50462,55	37089,39	38926,97	163611,11	55818,87	89106,70
121675,13	58978,37	123227,01	15893,83	49920,00	165778,50	63719,15
52864,46	16949,26	118296,99	5093,39	141126,88	87742,75	12759,33
6268,84	14678,11	83298,85	127589,54	3344,11	131116,56	294524,31
14903,12	103648,99	11358,58	34755,88	294524,31	104680,09	214266,64
3492,96	43789,76	84088,85	46363,63	16220,91	87733,21	110164,04
26211,88	49522,17	13263,21	294524,31	13042,55	53516,97	26820,88
234050,80	27080,41	86803,13	66576,60	9408,13	200745,88	19647,37
10765,25	21503,50	5396,45	112848,83	157872,61	7120,93	26947,56
5094,50	17800,42	64273,87	14746,85	56127,30	4411,19	48798,93
24146,20	78960,38	100390,10	71510,84	82727,12	43654,01	37112,17
17559,18	24060,86	84882,75	39185,01	14313,90	43853,04	74548,63

Swelling Forces [N] (182-364/676)

18597,02	29335,94	92717,96	227861,63	29801,70	2663,61	43799,25
102935,52	32858,17	134468,17	8289,46	10045,97	26832,34	66145,24
23440,82	96864,85	74474,34	6428,16	13911,02	14294,36	3982,08
104819,42	73526,43	70026,76	14604,32	33925,74	48413,19	5970,96
61113,06	46166,00	52518,18	146576,47	105026,83	51349,50	195488,50
29033,47	90271,37	41595,38	82247,19	87738,59	12460,93	19148,14
15812,65	11104,52	156937,32	66899,98	8199,14	158722,12	80540,89
160836,37	100990,06	82101,41	24058,64	262745,79	125917,43	52709,55
5388,62	91536,63	14243,38	124234,32	43772,83	108492,81	37017,23
16159,13	109505,57	259938,18	20511,31	110575,16	57493,64	4540,36
44158,32	91050,57	5422,67	141055,44	2316,12	12024,33	53447,37
50863,77	50886,08	19761,19	26393,53	21223,30	14068,62	2051,28
49359,12	71533,26	43932,73	43247,33	42481,27	183781,27	73483,53
72485,93	5774,29	33737,81	15902,68	46144,76	56207,49	22204,98
41518,02	51657,57	88437,86	21026,97	184952,92	39374,60	25250,72
41249,65	104362,18	47741,34	7054,75	23861,21	53585,29	37987,53
13018,88	6978,38	3270,59	7903,68	215642,74	26109,63	22461,09
14705,77	2251,33	37134,57	67119,62	170482,93	28807,91	25233,71
27265,86	50445,14	40036,03	22406,21	39976,49	75463,70	106742,48
59453,11	138271,34	89968,94	99995,49	148020,15	51453,74	128580,84
13461,63	83163,66	43896,97	253659,65	12980,90	294524,31	1090,48
38696,82	54778,44	29183,23	18646,69	13024,76	1990,19	109348,38
64143,52	32059,10	24110,87	42535,58	20410,88	110870,42	245043,86
4776,45	82165,90	56782,53	45018,99	118044,34	141413,54	35568,59
8913,28	31261,29	61287,60	6988,82	25859,56	60463,92	8511,95

36766,27	21347,57	1754,09	30565,16	40331,23	99895,66	24996,13

Swelling Forces [N] (364-546/676)

102434,3	6884,6	38866,0	25116,5	86977,8	25641,4	55399,4
61041,3	8661,5	68805,9	11098,6	6159,2	53679,0	49143,4
47493,6	13009,2	141801,4	65251,3	80554,3	11272,7	61558,5
2136,8	82520,9	30457,7	15790,3	16950,6	11914,2	17106,5
115228,4	32113,7	15921,8	24447,3	103035,4	83559,0	28815,3
10318,3	310138,3	52620,7	294524,3	76425,6	30212,1	16447,1
27224,3	52361,6	152546,8	31328,4	152316,1	33351,7	5167,1
59832,1	71212,7	81158,5	58148,5	33979,2	37807,3	2677,9
102268,9	113131,0	116395,3	6252,2	23739,1	9322,7	101898,2
51934,6	106512,6	77846,5	294524,3	37158,0	81556,7	123106,7
44754,5	52702,3	50277,1	47267,1	52294,4	70163,4	22619,0
132630,3	149893,9	39344,0	52492,0	27254,3	133427,1	150206,4
32606,3	31693,6	47930,0	47468,6	26959,4	4724,0	39543,4
91462,2	46165,9	8952,1	16588,1	24121,3	27151,1	38978,5
58489,7	22646,3	40394,5	69315,5	28065,7	45076,9	9928,4
33275,5	22308,5	4484,5	15468,4	4386,8	27733,4	44399,9
84702,5	27807,2	27884,5	46110,2	96500,0	37365,4	57101,3
75792,9	241268,4	3604,5	233886,6	21510,5	26987,8	24794,5
29857,7	173415,5	87535,5	107569,1	88718,2	37457,4	18873,3
81438,3	69867,8	24377,3	20467,3	133322,8	20526,3	40161,7
12528,7	38919,4	76087,9	45837,1	30818,2	39878,7	64674,0
2074,8	26330,4	24760,8	116797,9	48904,9	1411,0	117986,2
19767,9	54942,9	22715,9	65850,3	47757,7	93602,2	32955,9
65355,9	12847,5	174349,6	30809,8	25647,3	141689,5	82181,7
33163,9	20749,7	83963,7	101993,0	16578,4	139165,2	211073,5
140400,0	2928,4	92066,1	19102,1	64232,8	179682,2	17780,9

Swelling Forces [N] (546-676/676)

86994,47	68348,63	119048,76	158710,61	119541,54
49957,89	24809,34	191787,48	29000,73	102895,64
23351,89	50476,32	10654,24	25737,96	215125,17
62673,09	11872,45	35637,36	19808,61	28121,28
19271,26	16689,44	5374,36	7915,07	77655,98
56907,39	110837,22	22584,55	2096,59	38046,84
23734,52	9870,30	33295,70	16675,87	22713,95
21953,78	1640,54	13181,79	33434,68	42645,32
49971,21	40819,14	8704,87	5457,33	38360,80
294524,31	8349,15	1698,22	33575,20	49577,15
67732,07	32757,69	294524,31	294524,31	130779,01
52497,70	115927,26	9631,80	132490,03	43716,53
80274,47	99334,48	30299,76	9819,86	10494,38
100240,81	55042,37	1635,85	44469,46	9050,46
12721,06	18275,85	39282,52	11065,93	80268,95
51698,03	12441,43	45069,34	96356,77	96644,59
8114,64	15072,44	14218,59	36532,80	35164,25
57455,32	70076,00	91000,96	28625,59	27640,08

16669,24	38556,72	42769,27	247464,64	53551,75
56585,79	153246,38	7243,93	30089,57	97409,58
13687,43	137906,53	34141,16	62131,88	4213,53
17769,52	124362,29	11043,18	200968,09	159974,38
59649,65	24153,51	19084,81	43813,79	141748,28
94378,58	43124,64	32966,65	101737,18	121602,50
15038,89	102678,85	85979,99	131246,52	111147,28
4127,61	43145,56	25243,76	97558,88	29482,42